NASA-CR-198418

Three–Dimensional Turbopump Flowfield Analysis

Final Report

O. P. Sharma, K. A. Belford and R. H. Ni
United Technologies Corporation
Pratt & Whitney
Commercial Engineering

April 27, 1992

Prepared for
George C. Marshall Space Flight Center
National Aeronautics and Space Administration
Marshall Space Flight Center, AL 35812
Under Contract NAS8–36950

FOREWORD

The authors are grateful to Dr. Man Mohan Rai of the NASA Ames Research Center for providing the original version of the CFD code used in the present program and for his help in modularizing the code. The authors are thankful to Dr. Rai's colleagues Dr. Nateri Madavan and Dr. Akil Rangwala for sharing their unpublished results of evaluation of the code against UTRC Large Scale Rotating Rig data and for providing modifications to the code made to account for H–ratio effects. The authors are also grateful to Dr. Roger L. Davis and Dr. Daniel J. Dorney of the United Technologies Research Center for their helpful discussions for code debugging and for conducting extensive grid sensitivity studies in their investigation, funded by NAVAIR Contract #N00140–88–C–0677, using a version of the code utilized in the present program. The authors are thankful to the Pratt & Whitney management, in particular Dr. G. F. Pickett, Mr. L. R. Anderson, Dr. Seyf Tanrikut, Mr. Dan Minior and Mr. Jeff Bogoian for their continued support and encouragement during the course of the program. The authors appreciate continued technical discussions and dialogues with Dr. Helen McConnaughey, Dr. Luke Schutzenhoffer and Ms. Lisa Griffin of the NASA MSFC who ensured the focus of the present effort in developing a reliable design procedure for rocket turbopumps was not compromised by the time constraints in the program. This work was funded by NASA MSFC Contract #NAS8–36950 under the project management of Ms. Elaine Hamner, Ms. Irene Dolin and Ms. Janice Burrough, the authors appreciate the patience of the project management in allowing execution of the technical program in a cost effective manner. Dr. Helen McConnaughey and Ms. Lisa Griffin were the technical monitors of the program. Finally, the authors would like to thank NASA MSFC computer personnel for their support during the execution of the program.

TABLE OF CONTENTS

TABLE OF CONTENTS (Continued)

LIST OF ILLUSTRATIONS

LIST OF ILLUSTRATIONS (Continued)

LIST OF ILLUSTRATIONS (Continued)

LIST OF ILLUSTRATIONS (Continued)

LIST OF ILLUSTRATIONS (Continued)

LIST OF ILLUSTRATIONS (Continued)

LIST OF ILLUSTRATIONS (Continued)

LIST OF ILLUSTRATIONS (Continued)

LIST OF ILLUSTRATIONS (Continued)

SUMMARY

Development of a flow prediction method for rocket turbopumps is discussed in this report. A detailed description is given of the complex nature of the flowfield existing in turbopumps. Examples are given to illustrate that both physics based models and analytical calculation procedures based on Computational Fluid Dynamics (CFD) have resulted in progressive advancements of design procedures used in turbopumps. Limitations of the state-of-the-art design procedures are outlined for which the present work was conducted to significantly enhance the design methodology.

A CFD code developed at NASA ARC was used as the base code in the present work. In its initial form the CFD code could compute unsteady turbulent flow through an axial flow turbine stage. Governing equations and numerical procedure used in the CFD code is documented in detail. The turbulence model in the code was modified to facilitate computation of transitional flows and to account for extra rates of strain, such as rotation, three-dimensionality, surface curvature and surface roughness. Boundary conditions in the code were modified to facilitate computation of surface heat transfer coefficients and to allow computation through multistage turbomachines. The code was modified to permit simulations of flow through airfoil rows with flowpath convergence and divergence and to include radial flow turbomachines.

Extensive work was conducted to demonstrate that the CFD code yields good estimates of airfoil loadings, heat transfer coefficients, boundary layer parameters, losses, endwall secondary flows and tip leakage flows. Benchmark quality data, obtained from two- and three-dimensional cascades, are used in the code verification process. The ability of the base code to compute time-averaged and unsteady flow through a turbine stage had been previously demonstrated by the originator of the code at NASA ARC. Additional computations were conducted by NASA ARC personnel concurrent to the present program to demonstrate that the unsteady and time-averaged flow prediction capabilities of the code could be improved by utilizing more refined grids and by accounting for a more realistic airfoil count in axial flow turbines. To avoid duplication of work and to build on the enhanced strength of the code, work was conducted to demonstrate that the present code yields a more realistic estimate of unsteady loads in turbines than unsteady Euler codes; the latter codes are currently being used in the design procedures for rocket turbopumps.

Computations were conducted to demonstrate that the modified code with improved turbulence models, developed in the present program, yields realistic estimates of unsteady and time-averaged losses in multi-stage turbomachines. Work conducted in the present program and other simulations conducted by the authors during the program period indicated that the present code, operated in a two-dimensional mode (but modified to account for stream-tube variation effects), is a cost effective alternative to full three-dimensional calculations. This approach permits realistic predictions of unsteady loadings and losses for multistage machines, allowing design engineers more time for design optimization studies. The predictive capabilities of the present code were demonstrated by computing flow through a radial impeller and a multistage axial flow turbine.

The work conducted in the present program was supported by NASA MSFC Contract #NAS8-36950.

1. INTRODUCTION

Turbopumps for future rocket engines will require operating lives and performance levels well above those of present day units. Due to the very hostile environment that exists during the actual operation of a turbopump, reliable data that would permit identification of specific problems and thus guide future designs, is extremely difficult to obtain. In recognition of this situation, NASA has sponsored Computational Fluid Dynamics (CFD) computer code development programs which, when verified against basic data, may be used to identify ways to improve the current turbopumps and provide a basic understanding of the flow phenomena which could lead to better designs of future turbopumps for rocket engine applications. This report presents results from one of these programs, funded by NASA MSFC under contract # NAS8-36950 on the development, modification, verification and application of a CFD code for turbopump design application.

2. BACKGROUND

Although real flows in rocket turbopumps are highly unsteady, steady flow calculation methods are used during the design process. The unsteadiness is induced by the temporal and spatial variation of inlet temperatures and by aerodynamic interaction between rotating and stationary components. In the design process the effects of unsteadiness, at best, are accounted for through empirical correlations derived from available experimental data. Lack of physics in these empirical correlations invariably yield non–optimal designs requiring extensive efforts which add time and cost to the development process. Examples are given below to demonstrate that in addition to the fluctuations in the aerodynamic loads, unsteadiness affects time averaged losses and heat loads which must be accounted for in the design process.

The interaction which occurs in the SSME turbopump between the rotating pump impeller and the stator diffuser vane and also in the pump turbine between the rotor and the stator can generate unsteady forces through various mechanisms which occur at widely different time and length scales. Some of these mechanisms are summarized below (Greitzer (1987))

Types of Unsteady Flow		Extent	Typical Time Scale (sec)
Unsteadiness Due to:			
i)	Potential field interaction due to relative motion of airfoils	chord	5×10^{-5} sec
ii)	Wakes	chord	5×10^{-5} sec
iii)	Large scale vortical organized flow structures	chord/span	5×10^{-5} sec
iv)	Temperature distortions	gap/span	5×10^{-5} sec
v)	Turbulence	chord	
vi)	Rotating stall	circumference	5×10^{-1} sec
vii)	Surge	length	5×10^{-1} sec

Typical row assumed to have 60 airfoils at gap/chord of one and operating at 36000 RPM

These mechanisms are governed by different types of fluid dynamic phenomena. In order for any CFD code to capture these unsteady interactions, the responsible fluid dynamic phenomena tabulated above must be accurately modeled. A brief discussion on each of these phenomena, except rotating stall and surge, is given below. Rotating stall and surge typically occur in high pressure ratio compressors, and they may not contribute to the unsteadiness prevalent in the SSME turbopump. Unsteadiness due to turbulence is primarily embedded in the unsteadiness generated by wakes and large scale vortical organized structures; however, at the first row of airfoils, it can primarily be treated as a steady–state phenomenon using turbulence models in Reynolds–Averaged Navier–Stokes codes.

2.1 Potential Flowfield Interaction

The potential flowfield interaction in the turbopump components arises because the vane or the impeller is subject to a time–varying pressure field influence resulting from relative movement of adjacent airfoil rows. This time–varying force has a time scale on the order of the blade passing frequency and could cause structural fatigue in and of itself. In addition, the time–varying pressure field is capable of creating a transient flow disturbance, such as separation, in the vane or impeller passage; a possible interactive feedback mechanism could sustain or amplify the unfavorable interaction between the rotating and stationary components.

The potential interaction induced by relative motion of the adjacent airfoil rows is shown in Figure 2.1.1. This figure indicates that the pressure field (waves) due to the potential around an airfoil row extends both upstream and downstream of the airfoil. Typically the strength of the field decays over a length scale equal to the pitch/chord of the cascade. Unsteadiness effects due to relative motion of the pressure field, in both the upstream and the downstream rows increases with decreasing axial distance between adjacent rows.

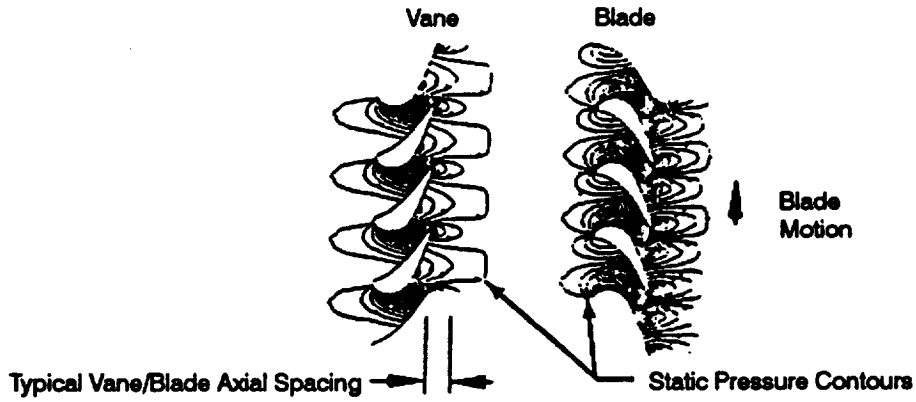

Figure 2.1.1 Potential Flow Pressure Gradients.

The magnitude of loading variation for a turbine stator and rotor at mean radius as measured in the United Technologies Research Center (UTRC) Large Scale Rotating Rig (LSRR) by Dring et al. (1982) is illustrated in Figure 2.1.2. The unsteady pressure variation on the stator caused by the upstream potential influence of the downstream rotor was as much as 15% of the steady stator exit dynamic pressure (Figure 2.1.2(a)). The pressure variations on the downstream rotor were measured when it was located at 15% axial chord downstream of the stator. The amplitudes of the pressure signals for the rotor were of the order of 80% of the relative steady state dynamic pressure. Data were also acquired when the gap between the upstream stator and downstream rotor was of the order of 60% chord of the upstream stator. The amplitudes of the unsteady pressure signals on the rotor at higher axial gap condition were measured to be about one–half those at the lower axial gap. The difference in the unsteady pressure amplitude on the rotor for the two axial gaps indicates a decay rate of pressure amplitude with distance which is far less than the rate of decay of potential influence. This implies that a large portion of the unsteadiness in pressure on the downstream rotor airfoil is due to wakes from the upstream rotor. A discussion on the physics of wakes as it affects downstream airfoil rows is given in the following subsection.

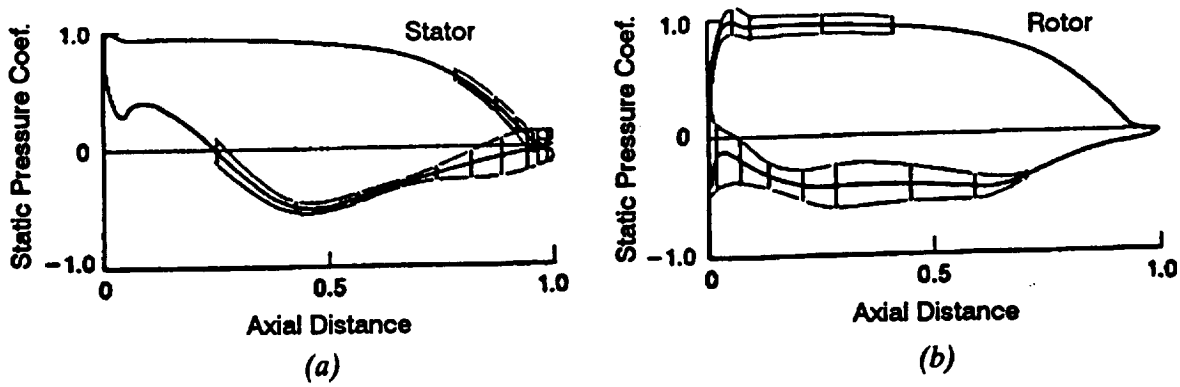

Figure 2.1.2 *Range of Instantaneous Pressure Distributions Measured in the United Technologies Research Center Large Scale Rotating Rig (UTRC LSRR) on Stator and Rotor Airfoils.*

The impact of potential flow interaction in a turbopump was numerically demonstrated by Rangwala et al. (1991) for the Generic Gas Generator (G3) turbine. Calculations were conducted for the mean section of the G3 turbine first stage, for three axial gaps between the first stator and the rotor, by using a two dimensional (2D) unsteady Navier–Stokes code. Results from these calculations (Fig.2.1.3) clearly show that time–averaged diffusion on the upstream stator is a function of the axial gap between the vane and the blade. The upstream vane is, therefore, affected by the downstream blade through the potential effect. The above calculations also showed that the turbine efficiency could be improved by up to 1% by operating the turbine at the larger gap. Although experimental data verifying these numerical results are not yet available, indications are that there is an optimum gap between adjacent airfoil rows.

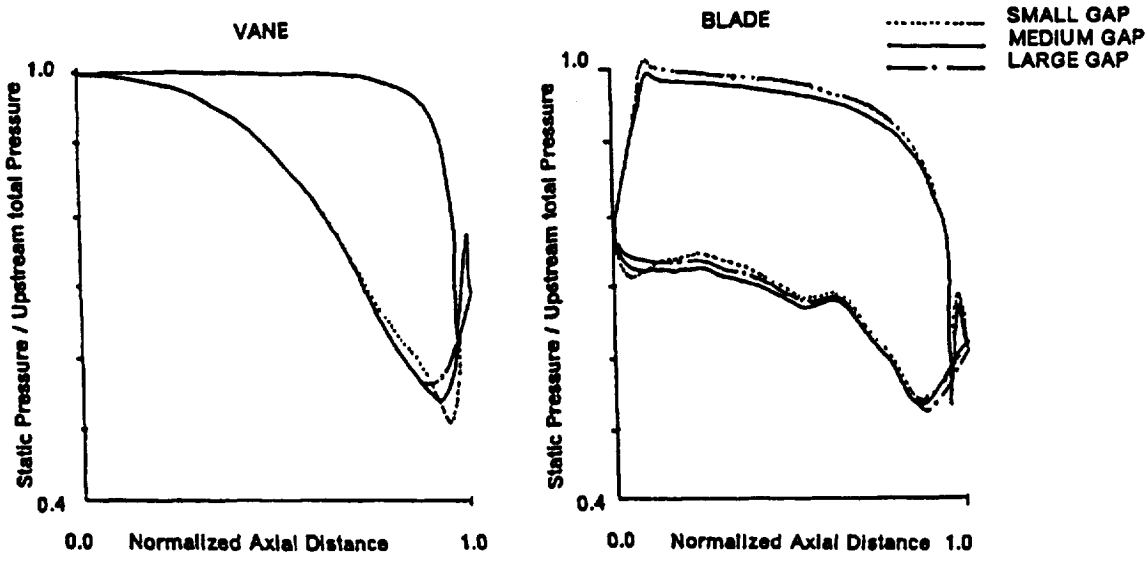

Figure 2.1.3 *Simulations (Rangwala et al. (1991)) Conducted for a Turbine Stage by Using a 2D Unsteady Navier–Stokes Code Show That Time–Averaged Diffusion on the Upstream Vane is Influenced by the Axial Gap Between the Vane and the Rotor.*

2.2 Wake & Temperature Streak Interaction

The circumferential variations in the velocity field downstream of the first stators for turbines are normally generated by the drag on the airfoil and endwall surfaces which causes a reduction in velocity and increases in the turbulence levels in the low velocity regions. In some flow situations, especially for airfoil rows downstream of a combustor, high velocity jets exist due to large circumferential gradients in temperatures. The effects of these upstream velocity variations can be simply illustrated through the use of velocity triangles (Butler et al. (1986)), as shown in Figure 2.2.1 for a turbine. This figure shows that the lower velocity fluid has a normal velocity component towards the suction side of the downstream airfoil indicating that the high turbulence, low momentum fluid from the upstream airfoil wake will migrate towards the suction side of the airfoil. In a similar manner, high velocity (high temperature) fluid will migrate towards the pressure side of the downstream airfoil. This preferential migration of fluid particles has three effects:

i) Alterations in the boundary layer characteristics of the airfoil through its effect on the transition process.

ii) Variation in the secondary flow generation for downstream passages.

iii) Redistribution of stagnation enthalpy.

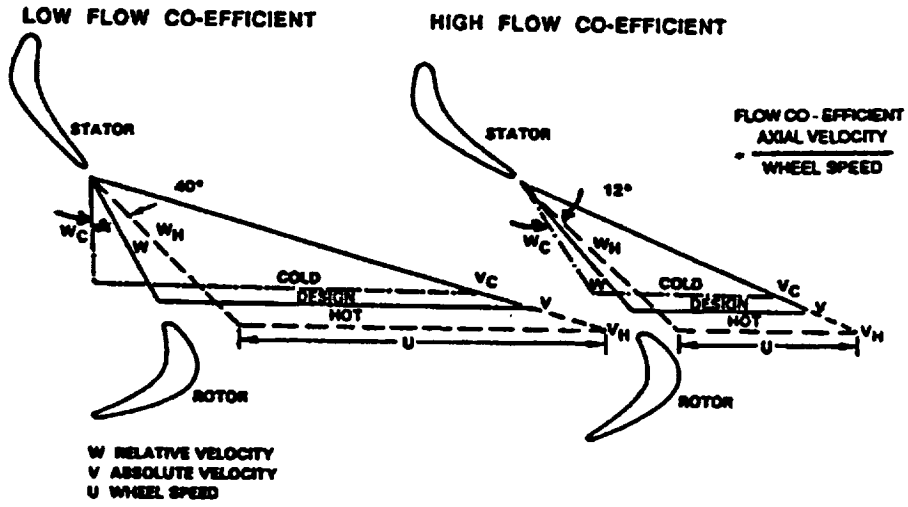

Figure 2.2.1 *Rotor Inlet Gas Temperature Distortion Causes Large Variation in Rotor Airfoil Incidence Angle. Simple Calculations Conducted for Hot to Cold Temperature Ratio of 1.7 Indicates Incidence Angle Variation of 12° and 40° for Typical High and Low Flow Coefficient.*

2.2.1 Effect of Upstream Wakes on Losses and Heat Loads

Detailed experimental investigations (Hodson (1983), Pfeil & Herbst (1979) Doorley & Oldfield (1984), Dring et al. (1982)) have been conducted to identify the influence of upstream periodic wakes on boundary layer characteristics. The characteristic of boundary layers on airfoil suction sides, affected by periodic movement of the upstream wakes, was clearly illustrated by Doorley & Oldfield (1984). Time resolved heat transfer data were acquired in this investigation in a stationary cascade at a low and a high background turbulence level with and without an upstream rotating rod that simulated wakes from upstream airfoils. These data, plotted in Figure 2.2.2(a), indicate that upstream wakes have relatively little effect on turbulent boundary layers and significant effects on laminar boundary layers. This figure shows that time–averaged heat transfer and losses for turbine airfoils, which normally have large regions of laminar flow in a steady flow environment, are expected to increase in an unsteady environment.

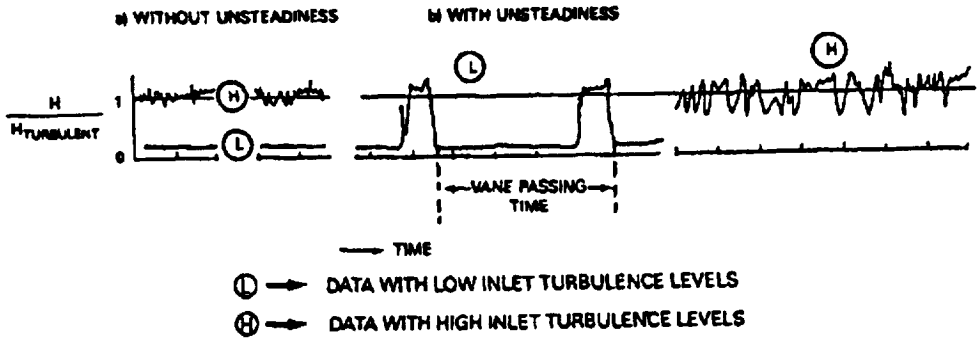

Figure 2.2.2(a) Measured Time–Resolved Heat Transfer on a Turbine Airfoil Suction Side (Doorly et al. (1984)) at Two Background Turbulence Levels in an Unsteady Environment Shows a Larger Effect on a Laminar Boundary Layer and Little Effect on a Turbulent Boundary Layer.

The time–averaged effect of upstream wakes on the boundary layer thickness and heat transfer coefficient for the suction sides of two separate rotor airfoils (Hodson (1983), Blair et al. (1988), Sharma et al. (1988)) are shown in Figure 2.2.2(b). Also shown in this figure are the data obtained for those airfoils in steady cascade configurations and calculated values from a boundary layer code. The steady cascade data are shown to yield good agreement with transitional calculations. The time–averaged data, however, lies between the transitional and fully–turbulent calculations. This figure indicates that the nature of transition is influenced by the periodic variation of turbulence imposed by wakes from upstream airfoil rows. In addition, losses and heat loads in an unsteady environment are larger than those measured in steady cascade configurations. For typical turbine airfoils, losses induced by unsteady effects may be on the order of 25% to 100% of the losses for those airfoils in a steady flow environment (Sharma et al. (1988)).

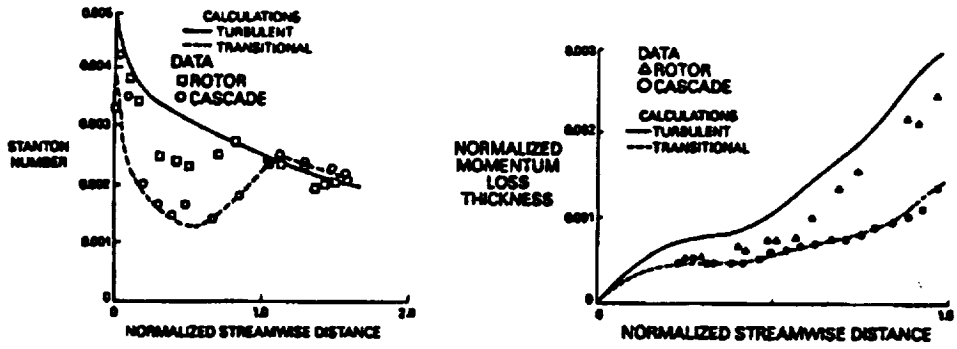

Figure 2.2.2(b) Measured Streamwise Distribution of Time–Averaged Stanton Number of Blair et al. (1988) and Sharma et al. (1988) and Boundary Layer Thickness of Hodson (1983) Show Larger Values in an Unsteady Environment Than in a Steady Cascade Configuration.

2.2.2 Effect of Upstream Wakes on Secondary Flows

In addition to affecting the characteristics of airfoil boundary layers, wakes from upstream airfoil rows also affect the generation of secondary flows (Sharma et al. (1983,88,90) as discussed below.

Unsteady experimental data for a rotor passage, obtained by using high response probes in the UTRC LSRR (Sharma et al. (1983)) are shown in Figure 2.2.3. This figure shows three instantaneous contour plots of relative total pressure coefficient upstream and downstream of the rotor passage. Large variations in the exit flow structures are seen in the figure for the three different inlet conditions. The exit flow field (Figure 2.2.3(a)) shows three distinct vortices due to the hub and tip secondary flows and the tip leakage effects. Without the tip leakage vortex, the flow field shown in Figure 2.2.3(a) is similar to the one expected for this airfoil in a steady cascade environment. The tip leakage vortex for the rotor shows least variation (Figures 2.2.3(a), (b), and (c)) indicating that the leakage phenomenon is not influenced by upstream circumferential distortions. The hub secondary flow vortex shows the largest variation transforming from a distinct structure in Figure 2.2.3(a) to a diffused structure in Figure 2.2.3(b), and becoming almost non–existent in Figure 2.2.3(c). This indicates that the secondary flow generation mechanisms, especially at the hub, are strongly influenced by the upstream circumferential distortions such as wakes. The overall variation in the size of the tip secondary flow vortex is smaller than that of the hub vortex but larger than the leakage vortex.

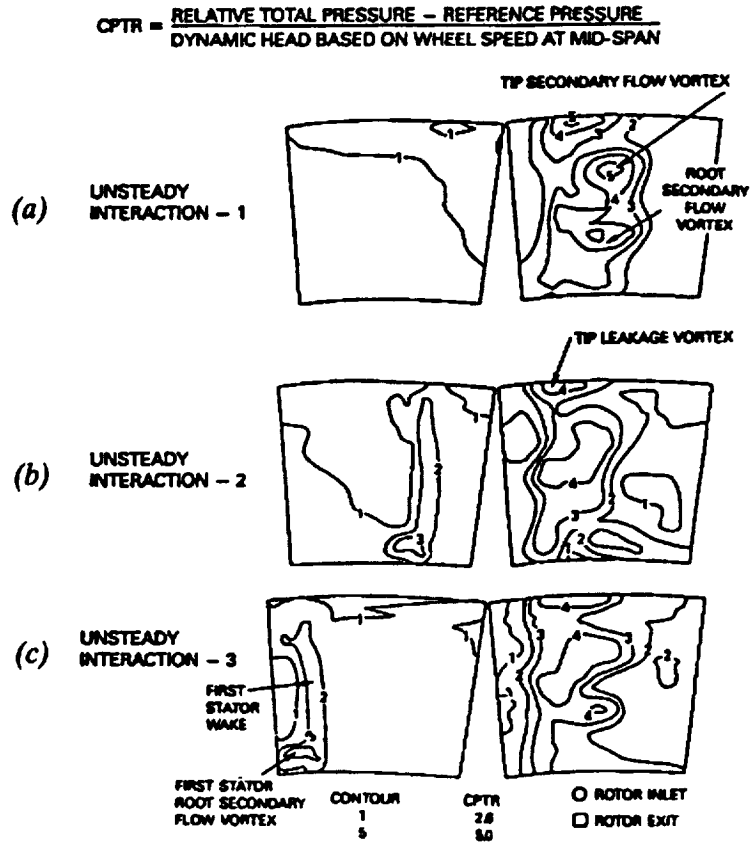

Figure 2.2.3 *Secondary Flow Structures Downstream of a Rotor (Sharma et al. (1988)) Obtained From Unsteady Measurements Show Large Variation in Their Size, Indicating Effects of Upstream Stator Wakes.*

The periodic variation in the size and strength of the secondary flow vortices observed in this experimental investigation shows almost 40% variation in the secondary flow losses for the rotor passage.

2.2.3 Effects of Upstream Temperature Streaks on Segregation of Hot and Cold Air in Turbine Rotors

Results from an experimental investigation, conducted to quantify the influence of burner induced hot streaks on segregation of hot and cold air in turbine rotors, are discussed below.

In this investigation, experimental data were acquired in the UTRC LSRR by introducing temperature streaks upstream of the first stator (Figure 2.2.4(a)). Two types of temperature profiles were generated upstream of the first stator, these being:

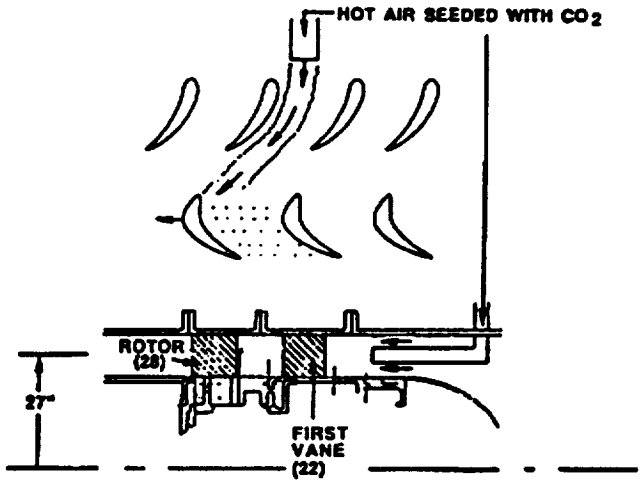

Figure 2.2.4(a) Schematics of the Experimental Apparatus Used to Simulate the Redistribution of Hot Streak in the Turbine Rotor (Butler et al. (1986)).

i) Hot streak with a circular cross–section to yield a temperature profile both in the radial and the circumferential direction, some of the results from this investigation were reported by Butler et al. (1986).

ii) Hot streak with a rectangular cross–section to yield a radially uniform profile that had temperature gradients mainly in the circumferential direction (Sharma et al. (1990)).

The hot air in these experiments was seeded with Carbon Dioxide (CO_2) to facilitate measurements of its migration in the turbine by using a gas sampling technique. The temperature patterns at the exit of the first stator for these tests are given in Figure 2.2.4(b) which indicates relatively small mixing in the first stator. This result is expected being compatible with the Munk and Prim (1947) principle. Spanwise distributions of axisymmetric CO_2 concentration profiles at inlet to the rotor,measured by using a rotating probe,for these two tests are given in Figure 2.2.4(c). The circular streak generate a parabolic concentration (temperature) profile, whereas the rectangular streak generated a radially uniform profile.

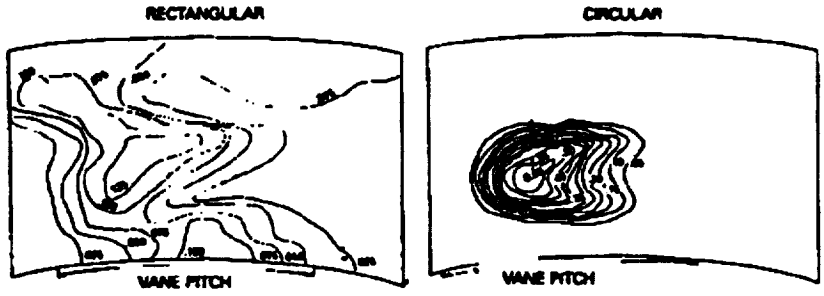

Figure 2.2.4(b) Contour Plots of Normalized CO_2 Concentration Downstream of the First Stator in the UTRC LSRR Obtained with Circular and Rectangular Hot Streaks; High Values Imply High Temperatures.

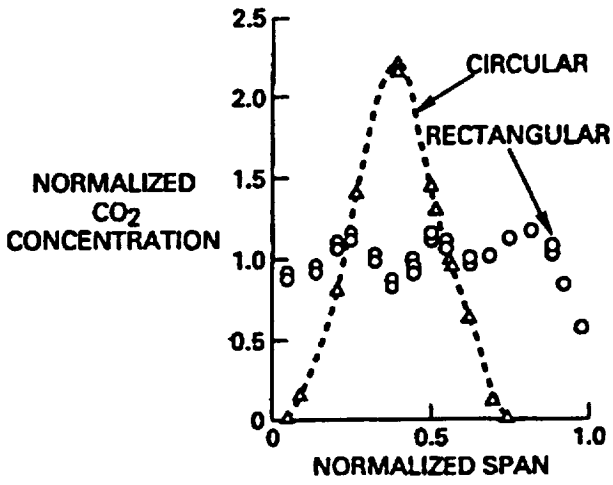

Figure 2.2.4(c) Spanwise Distribution of Normalized CO_2 Concentration Profiles (Indicators of Temperatures) Measured in the Rotor Frame for the Circular and Rectangular Hot Streaks.

Measured concentration of CO_2 on the rotor airfoil surfaces,for the rectangular hot streak, are shown in Figure 2.2.5. This figure indicates higher levels of CO_2 concentration on the rotor airfoil pressure side than on the suction side. Similar results were obtained with the circular hot streak as discussed by Butler et al. (1986). These results demonstrate that pressure sides of rotor airfoils operate at substantially higher temperatures than the suction sides when the incoming flow has a circumferentially non–uniform temperature profile.

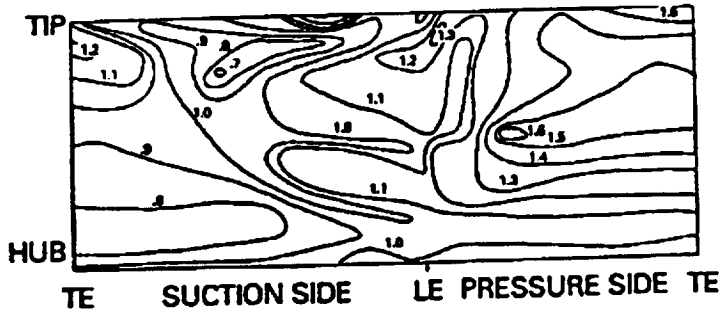

Figure 2.2.5 Larger Time–Averaged CO_2 Concentration (Temperatures) Measured on the Pressure Side of the Rotor Airfoil Relative to the Suction Side Indicate Segregation of Hot and Cold Air.

Interpretation of data obtained from an aircraft engine environment indicates that the pressure sides of first rotor airfoils in a high pressure turbine can operate anywhere between 100–700°F hotter than suction sides. These temperature differences between the two sides of airfoils can cause significant durability problems for airfoils. Large amounts of cooling air are required to accommodate these temperature levels resulting in reduced efficiency of the cycle and increased specific fuel consumption of aircraft engines.

2.3 Interaction Due to Large Scale Organized Vortical Flow Structures

The real flow in the turbopump turbines consists of large scale organized flow structures formed by viscous flows in large deflection airfoil rows. Although these flow structures may affect the unsteady flow fields in turbines more than either the potential or wake interaction, this phenomenon has not been discussed in the open literature until recently by Sharma et al. (1988,1990). Shortage of available data and complexity of the problem it introduces in the analytical treatment have contributed to this gap. Turbine cascade flow visualization experiments conducted in a water tunnel at University of Connecticut illustrate the organized structures formed in a simple configuration as shown in Figure 2.3.1. The flow structures formed in the cascade were visualized by utilizing hydrogen bubbles and laser lighting techniques. The deformation of two parallel horizontal lines of bubbles at the inlet and exit planes of the cascade is shown in the above figure. This figure clearly shows how the fluid particles contained between the two lines deform into vortical structures constituting almost 25% of the total airfoil passage. In a three dimensional unsteady flow field, these vortices should have a large influence on turbine performance, durability and structural integrity.

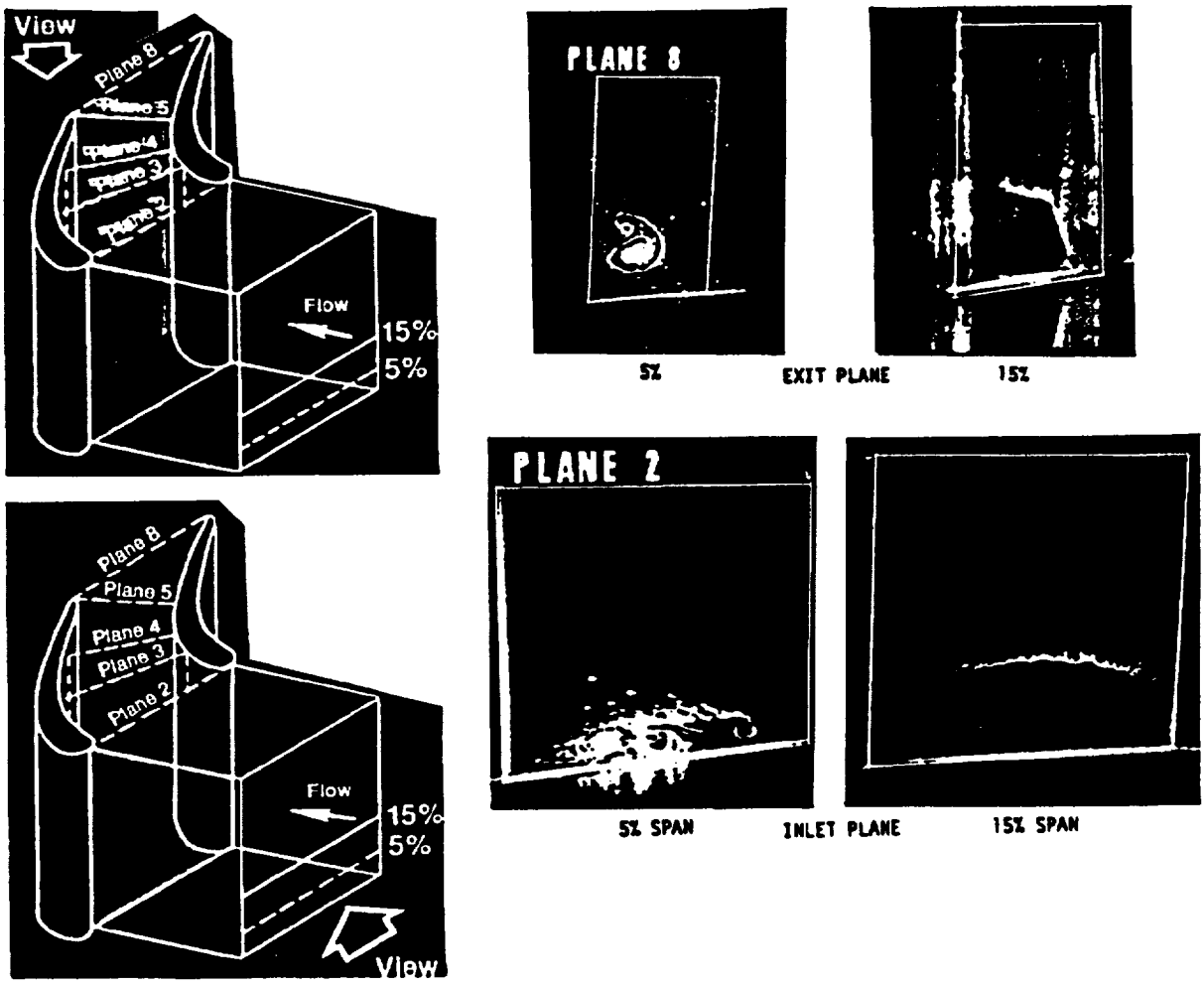

Figure 2.3.1 *Two Parallel Horizontal Lines Upstream of the Cascade Distort Into Vortical Structures at the Leading and Trailing Edges of the Cascade. Flow Visualization Tests Conducted at U. of Connecticut by Pratt & Whitney.*

The formation and development of these vortices in turbine cascade passages were extensively investigated at UTRC (Langston et al. (1977)) in a large scale cascade rig where detailed aerodynamic performance, loadings and external heat loads were measured. The effect of these flow structures on the airfoil loading is shown in Figure 2.3.2; data were obtained on the cascade airfoil for three different inlet boundary layer profiles resulting in three different magnitudes of secondary flow vortices. Large spanwise gradients in airfoil loadings are generated with an increase in the incoming boundary layer thickness. This also results in an increase of the size of the vortex. The variation in the pitch averaged gas angle profile at the exit of the cascade increases from 5 to 25 degrees for the two extreme inlet profiles. Since these angle variations are introduced by vortical motions, they would cause similar variation in the circumferential direction, thus causing unsteady incidence variation on the following row of airfoils. The circumferential distortions introduced by these vortices are two to three times larger than those introduced by 2D wakes.

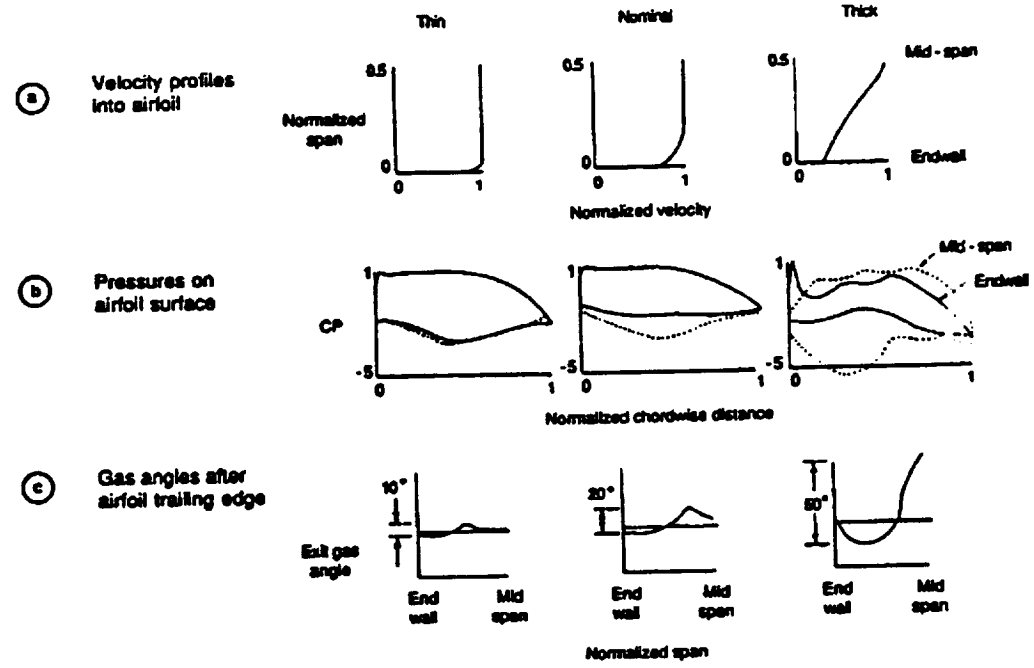

Figure 2.3.2 *Change in Airfoil Loadings and Exit Gas Angles as Affected by Cascade Inlet Boundary Layers Langston's Data (Langston et al. (1977), Sharma et al. (1990)).*

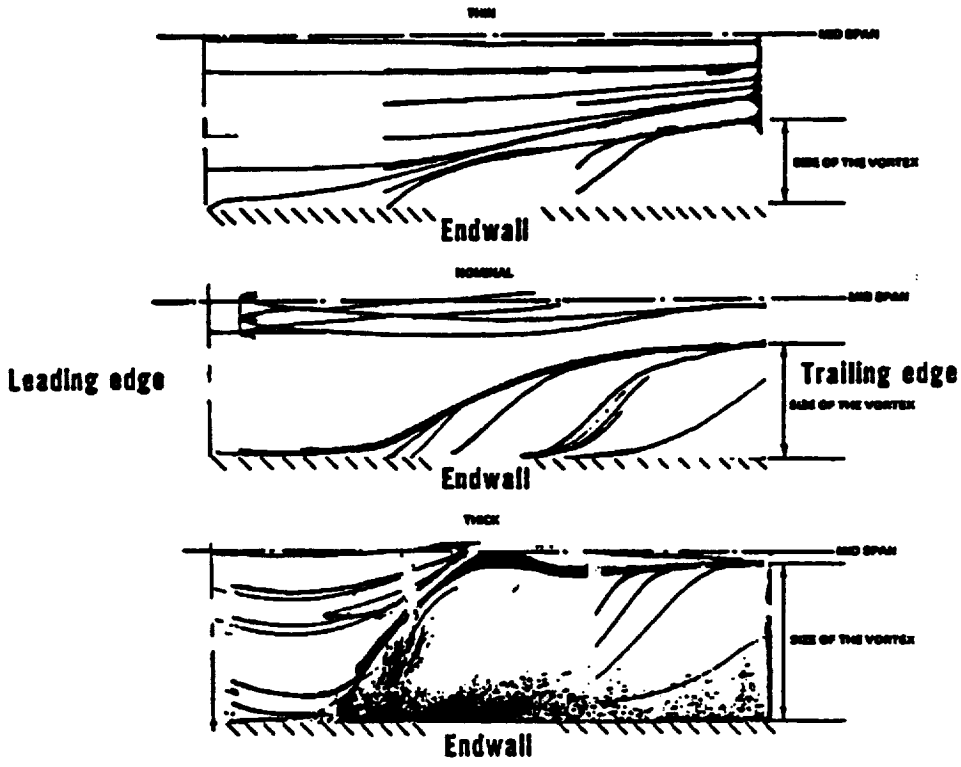

Figure 2.3.2 *Measured Streamline Patterns on the Airfoil Suction Side Indicating the Change in the Size of Secondary Flow Vortices Due to Inlet Boundary Layer.*

In addition to loading and exit angle variations the presence of secondary flow vortices also causes substantial effects on airfoil external heat loads as shown in Figure 2.3.3. This figure shows measured heat transfer coefficients on the midspan of the airfoil for thin and nominal inlet boundary layers; two different magnitudes of secondary flow vortices are represented. Although the airfoil loading at the midspan region for the two test conditions is the same, the heat load for the cascade with the larger secondary flow vortex is lower by 70%, indicating that the vortex causes substantial alterations to the structure of turbulence (Sharma & Graziani (1982)). The physical mechanisms governing the generation of secondary flow structures in steady cascade flows are well established (Langston et al. (1977) and Sharma & Butler (1986)), as depicted in Figure 2.3.4. The mechanisms governing the generation, development and transport of these vortices in unsteady turbomachinery environments, however, still require further work, especially from a predictive point of view. Extensive unsteady data acquired in the UTRC LSRR highlight important features of the secondary flow generation in the multistage turbine environment. These features have important implications on the development of analytical predictive models.

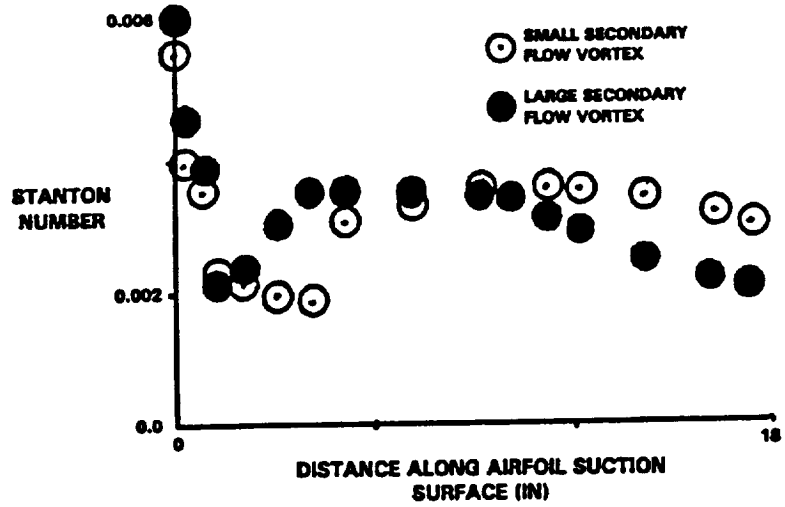

Figure 2.3.3 *Endwall Secondary Flow Vortex Affects External Heat Loads on Airfoil Suction Surface at Mid–Span (Sharma and Graziani (1982)). Midspan Loadings in the Two Tests are the Same.*

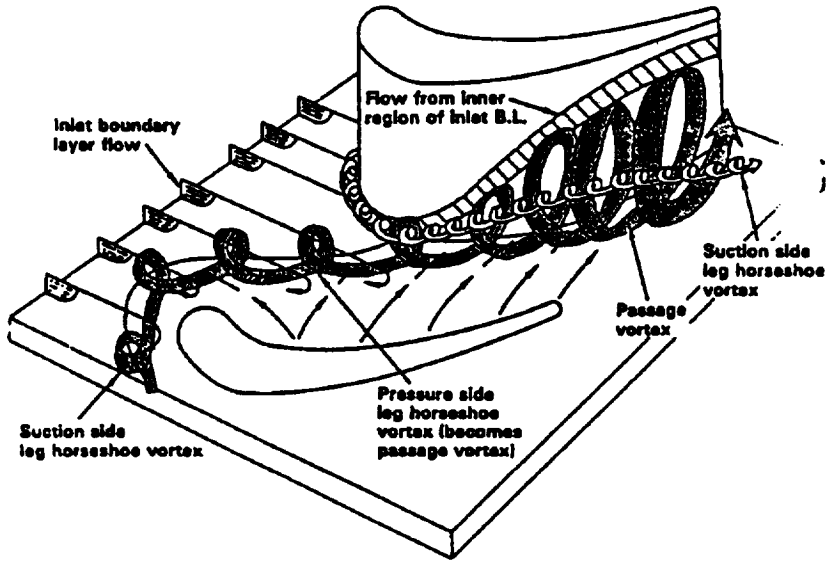

Figure 2.3.4 *Cascade Endwall Flow Structure (Sharma & Butler (1986))*

An example of large scale structures from the rotor influencing the flows in downstream stator airfoil rows is given in Figure 2.3.5. This figure shows the total pressure field downstream of a second stator which represents variations in the flowfield as one full rotor passage translates over one full second stator passage. The structures of the wakes and vortices of the second stator are only slightly affected by the upstream flow distortions, in contrast to information in Figure 2.2.3. Here, upstream flow distortions strongly influences the flow structure downstream of the rotor. A possible interpretation of the data shown in Figures 2.2.3 and 2.3.5 is that the effect of upstream flow distortions is enhanced by the rotation effects. The mid–passage flow region of the second stator, however, is strongly influenced by the upstream flow distortions. At certain time locations the vortices from the upstream rotor appear downstream of the second stator, completely unaffected by the stator.

Although these vortices contain fluid with large magnitudes of turbulence intensity and stresses, they show little evidence of mixing and thus indicate that these would have a large impact on the mid–span flow field of the second stator.

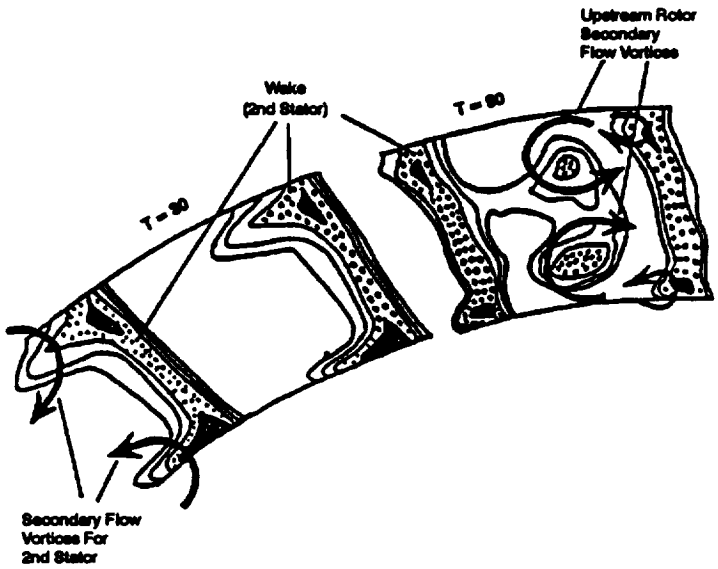

Figure 2.3.5 *Unsteady Instantaneous Total Pressure Loss Coefficient Downstream of the Second Stator Indicate that Rotor Secondary Flow Vortice Periodically Persist Through the Second Stator (Sharma and Syed (1991)).*

Measured time averaged heat transfer data obtained at the midspan location of this airfoil is shown in Figure 2.3.6, together with theoretical predictions that were based on measured midspan airfoil loadings. The streamwise gradients of the measured and predicted heat transfer coefficients on the airfoil suction side differ from each other in the turbulent region; influence of the secondary flow vortices convecting through the midspan region of the stator on the airfoil boundary layer is apparent.

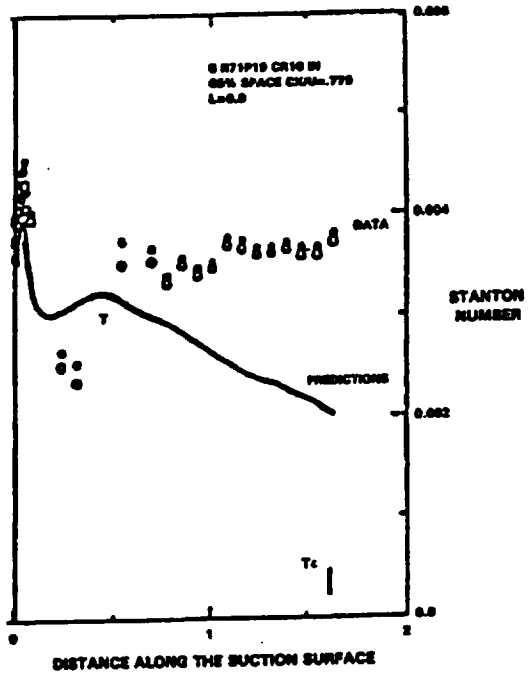

Figure 2.3.6 *Analytical Predictions Underestimate External Heat Load on the Second Stator Airfoil Suction Surface for Blair et al. (1989) tests. This Result is Opposite to the Experiments and Predictions in Steady Cascade Configurations in Figure 2.2.2(b) and 2.3.3.*

The discussion presented in this section clearly demonstrates that large scale organized structures constitute a significant portion of the overall flow field in multistage turbomachines. The incidence angles and unsteadiness induced by these structures are larger than those induced by wakes and potential interactions for typical rocket turbines. No model or discussion of the existence of these flow structures and their influence on the unsteady flow field have appeared in literature, indicating the complexity of the problem and infancy of the models. The development of a reliable prediction method, such as that discussed in the present program, will provide a valuable tool to turbopump designers, permitting optimization of the turbopump for improved durability, structural integrity and performance.

In summary, unsteadiness effects in turbomachinery are caused not only by potential flow and two dimensional wake interactions but also by large scale organized structure and temperature distortions. Of these phenomena, large scale organized structures have been given little attention in the overall turbomachinery design and analysis procedures. These structures can cause higher unsteadiness in the airfoil rows than either potential flows or wakes.

A review of the hierarchy of CFD codes used in the turbomachinery design and analyses modes is given in the following subsection, indicating how the work conducted under the present program permits improved analysis of turbopump flowfields to yield designs which are more efficient, durable and structurally sound.

2.4 Application of CFD Codes in Turbomachinery

Significant improvements in durability, structural integrity and performance of turbomachines have been realized over the past twenty years. One of the major contributors to these achievements has been the successful close coupling of analytical models describing the salient physical mechanism with state–of–the–art Computational Fluid Dynamics (CFD) codes. A brief review of the design process evolution with special emphasis on the use of CFD codes is given in the following subsection and schematically depicted in Figure 2.4.1. This will highlight how the work conducted under the present program has contributed to the enhancement of the current design process which will lead to improvements in durability, structural integrity and performance of rocket engine turbopump units.

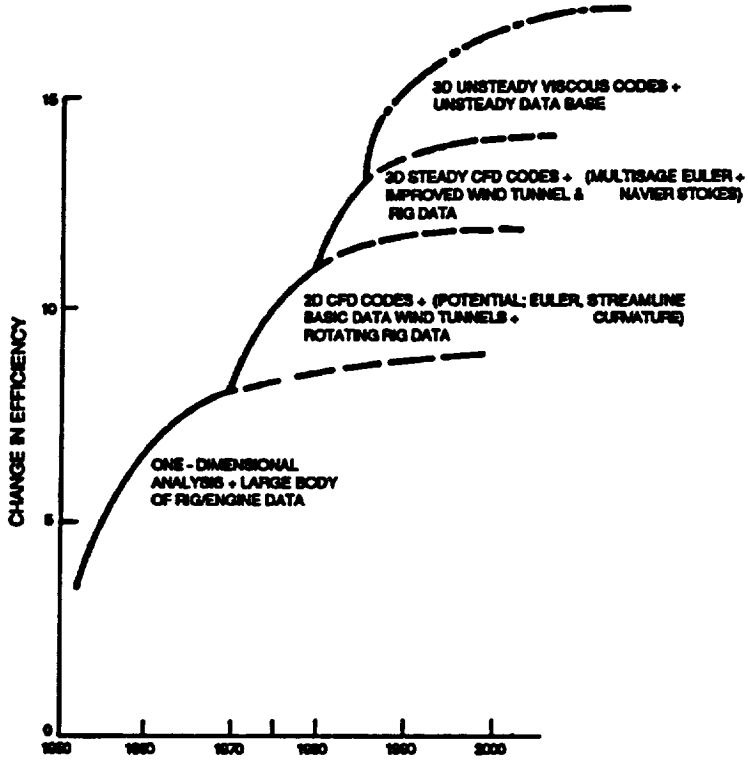

Figure 2.4.1 *Application of Computational Fluid Dynamics Codes Have Resulted in Improved Performance. Further Performance Improvements Are Possible With Unsteady Code Applications.*

2.4.1 State–of–the–Art

The actual flow fields in turbomachines are highly complex. They consist of laminar, transitional and turbulent boundary layers on airfoil surfaces and secondary flow vortices in the endwall regions. These vortices are formed by the incoming total pressure distortions in endwall boundary layers and tip leakage flows. These complex flow patterns are strongly influenced by three–dimensional pressure fields within the airfoil channels and relative movement of adjacent airfoils rows, as well as incoming time varying temperature patterns. The resultant flow field exhibits strongly viscous and highly time dependent characteristics, which necessarily create in transient thermal and aerodynamic loads on airfoil surfaces.

In the early stages of turbomachinery design, before the advent of sophisticated computer systems, engineers relied on one–dimensional concepts and simple correlations derived from

extensive experimental data to account for loss generation mechanisms. These correlations, albeit relatively crude, accounted for the various flow field characteristics in a global sense and allowed engineers to generate consistent designs. A large volume of data acquired during the process of turbomachinery development was used to establish design criteria for airfoil loadings and radial distribution of flow, as shown in Figure 2.4.2. This one–dimensional approach to turbomachinery design often resulted in expensive and time–consuming product development.

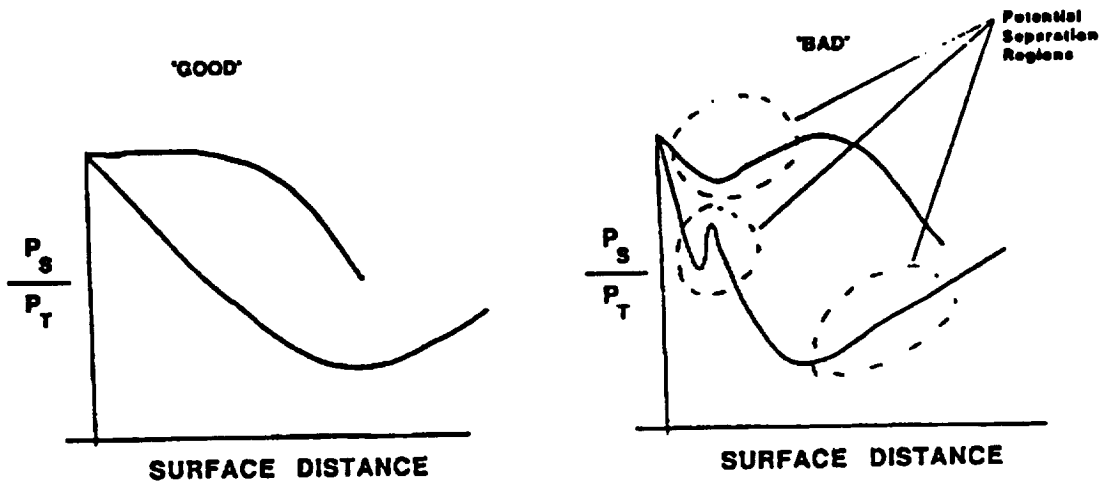

Figure 2.4.2 *Low Loss Airfoil Design Criteria Established Through Extensive Data Base Review. No Leading Edge Diffusion, Large Acceleration Regions, Small Diffusion Regions.*

2.4.2 First Generation of CFD Code for Turbomachinery

With the availability of computers in the mid 1960's, CFD codes were developed to assist in the turbomachinery design process. The first generation of CFD codes used in the design solved two–dimensional equations both in the blade–to–blade (Caspar et al. (1979), Denton (1975) Ni (1982)) and the radial direction (Novak & Hearsay (1976)). Initially, these codes were used to analyze flowfield to ensure that the design intention was achieved with reduced hardware testing. Two dimensional boundary layer codes were subsequently developed (Crawford & Kays (1976), McDonald & Fish (1972), Patankar & Spalding (1970) that permitted external heat load and aerodynamic loss calculations. Benchmark quality experiments (Blair & Werle (1980,81), Blair (1982), Sharma et al. (1982)), identifying the basic physics of boundary layers for typical turbine airfoils, were also conducted to develop improved turbulence models needed for the boundary layer codes.

An example of results from these experiments is shown in Figure 2.4.3, where the effect of mainstream pressure gradient on transitional boundary layers is quantified. A simple algebraic turbulence model developed on the basis of these data yielded a much better estimate of the external heat loads on turbine airfoils than the more complex K–E turbulence models shown in Figure 2.4.4. The 2D inviscid and boundary layer codes can then be utilized to optimize shape of an airfoil during design, as shown in Figure 2.4.5.

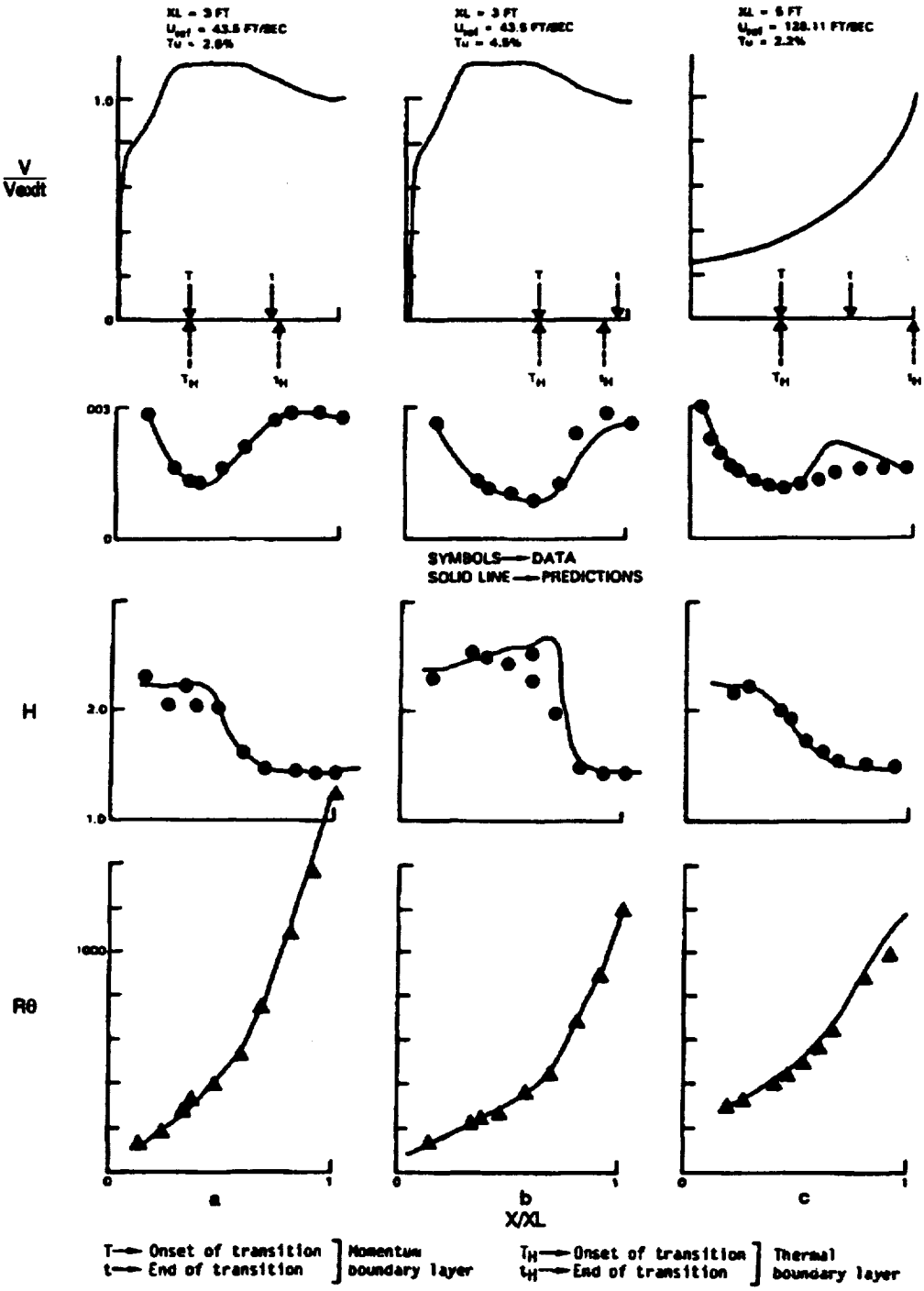

Figure 2.4.3 *Mainstream Pressure Gradient Effects More Pronounced on Thermal Boundary Layers Than on Momentum Boundary Layers in Transitional Region.*

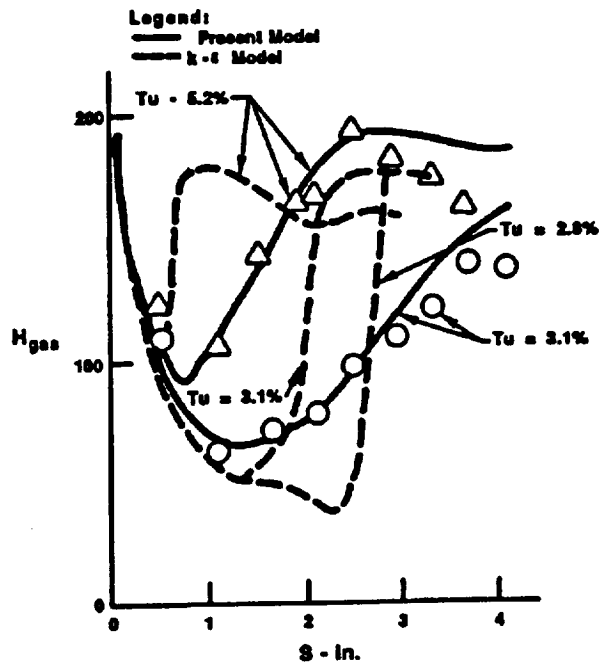

Figure 2.4.4 *Transition Model of Sharma (1986) Gives Better Estimate of Heat Load for Consigny and Richard's Airfoil (1982) Than the Launder–Jones (1972) Two Equation Model.*

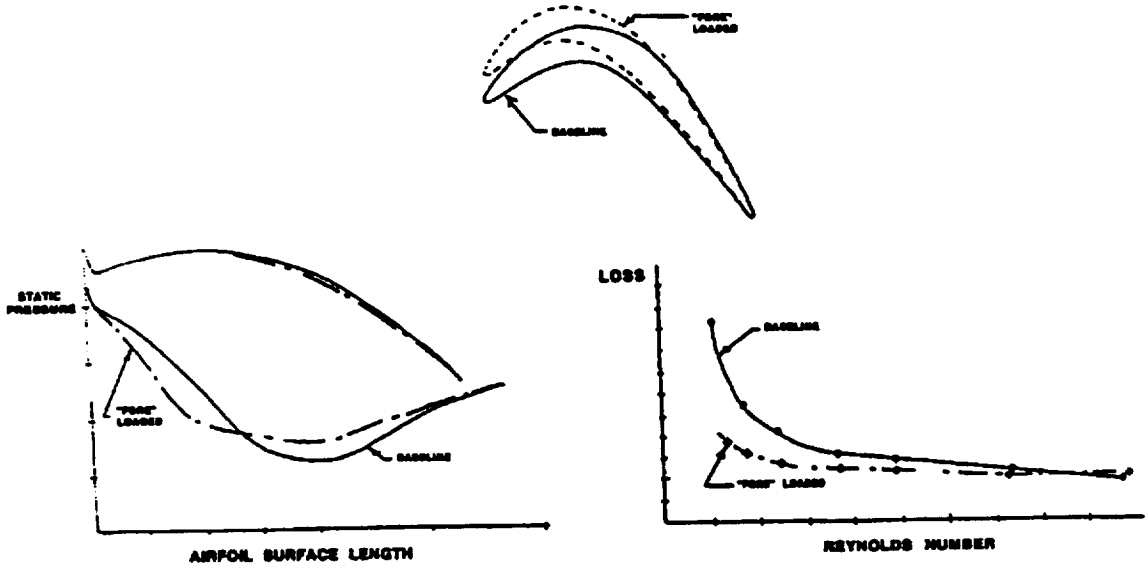

Figure 2.4.5 *2-D Viscous and Inviscid Codes Used to Optimize Shapes of Airfoil for Improved Performance.*

The use of boundary layer calculation methods and basic experimental data also allow qualitative estimates of the effect of unsteadiness on turbine airfoil boundary layer development. Several specific experiments (Dring et al. (1982), Pfeil and his co–workers (1979,82), Hodson (1983), Sharma et al. (1983,88,90), Langston et al. (1977), Joslyn et al. (1982)) contributed to the development of the unsteady loss prediction models. Results from one of these experiments shown in Figure 2.4.6

indicates that the time averaged loss on the airfoil in an unsteady environment is substantially higher than it would be for the same airfoil in a steady environment. In addition, the minimum and maximum losses in this experiment show good agreement with calculated results by utilizing transitional and fully turbulent boundary layer prediction models. The increase in time averaged loss can be related to reduced frequency (Schultz (1977), Sharma et al. (1988)) as shown in Figure 2.4.7. Quasi–steady models developed on the basis of these results yield excellent agreements with the steady and unsteady time averaged boundary layer data from Hodson (1983) and Pfeil & Herbst (1979) as indicated in Figure 2.4.8. It should be emphasized that a relatively simple model can yield good predictions for the effect of unsteadiness on airfoil boundary layers once the primary physical phenomenon has been identified through review of basic experimental data.

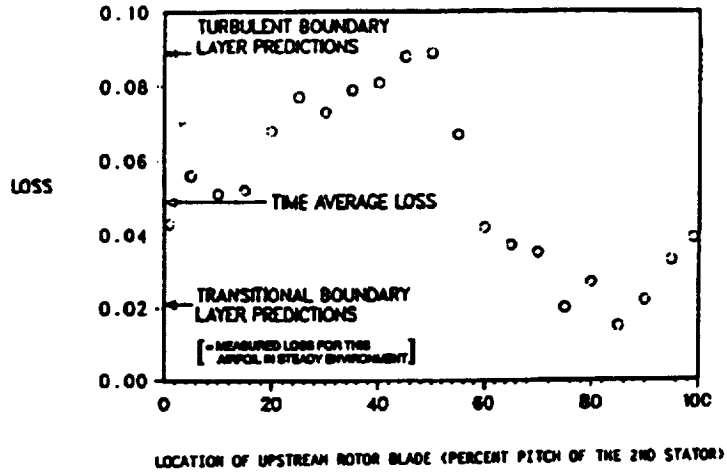

Figure 2.4.6 *Mid–Span Losses on the 2nd Stator as Influenced by the Unsteadiness Generated by the Upstream Rotor Airfoil Wake.*

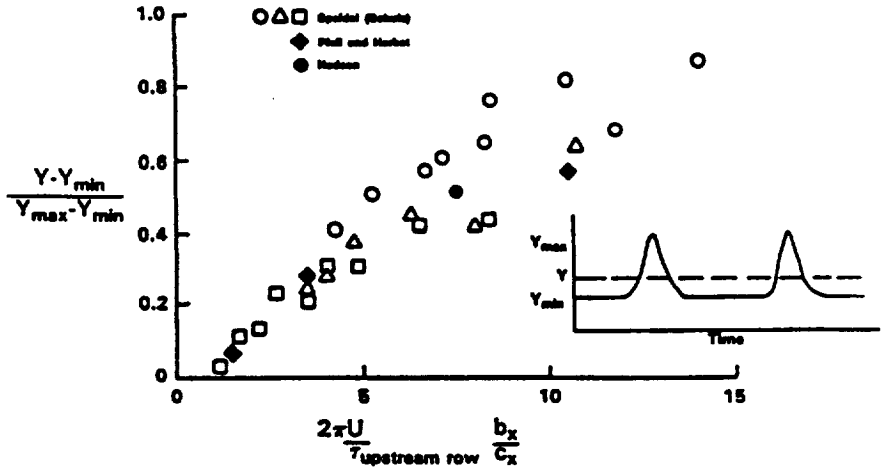

Figure 2.4.7 *Additional Time–Averaged Loss Generated Due to Unsteadiness Induced by Upstream Wakes can be Related to Reduced Frequency; Schultz (1977), Sharma et al. (1988, 90).*

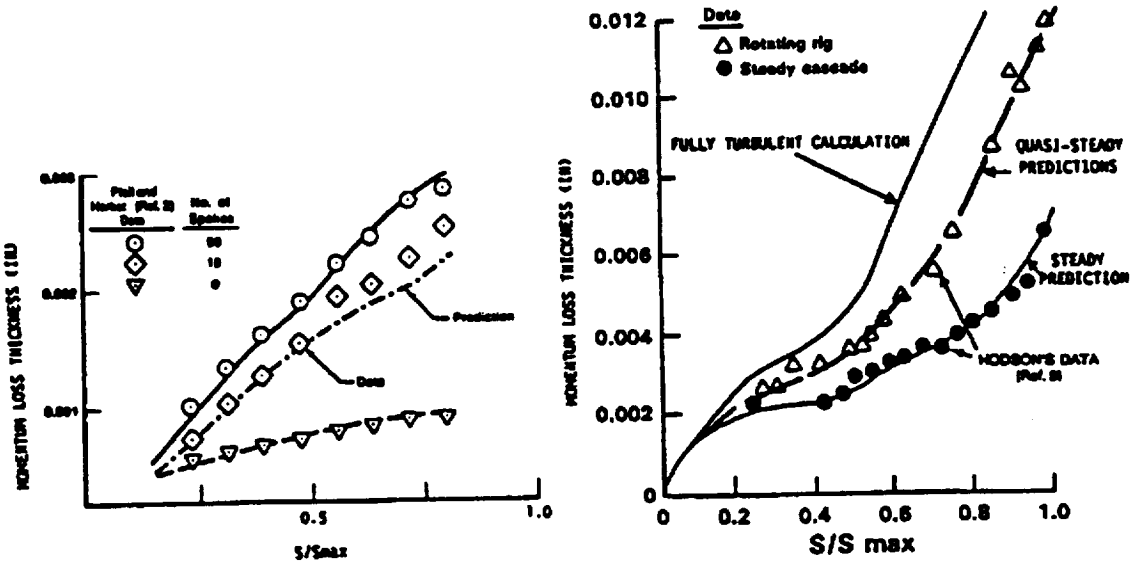

Figure 2.4.8 *Quasi-Steady Boundary Layer Code Gives Good Estimate of Extra Losses Generated Due to the Effect of Unsteadiness.*

The stable of 2D CFD codes for turbomachinery design application were completed with the development of 2D Navier–Stokes code (Davis et al. (1986)). This code permits realistic simulation of airfoil performance at off–design conditions where foil separation effects become important. An example of the application of this code to estimate loading distribution on an airfoil is shown in Figure 2.4.9 where the airfoil has a separation bubble on the airfoil pressure side. The Navier–Stokes code yields better agreement with experimental data than a 2D Euler flow solver because it simulates the effect of the separation bubble explicitly. It should be pointed out, however, that a good transition model is essential if good estimates of airfoil loadings are to be realized.

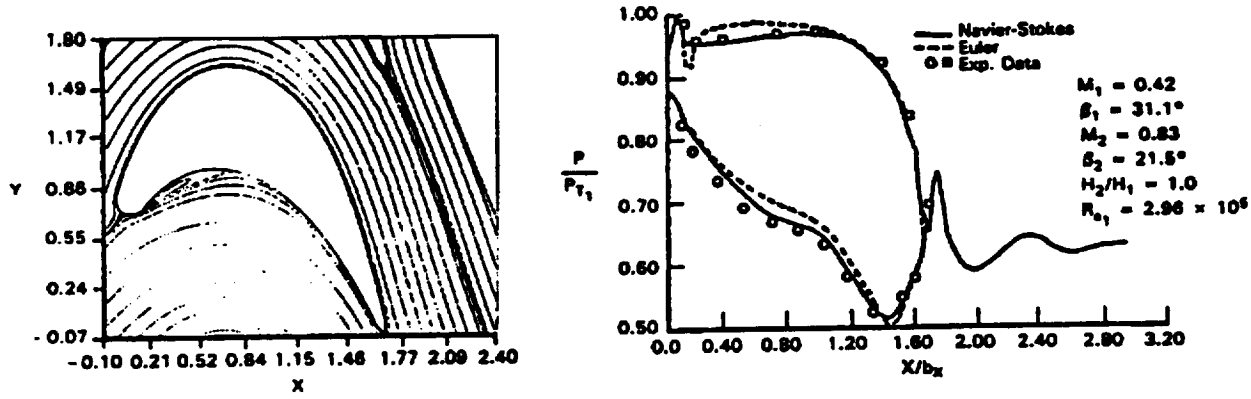

Figure 2.4.9 *2-D Navier–Stokes Code With Improved Transition Model Shows Separation Bubble on Airfoil Pressure Side and Predicts its Effect on Airfoil Loading.*

2.4.3 Second Generation of CFD codes for Turbomachinery

Three–dimensional Euler codes (Ni et al. (1989), Denton (1975)) and Navier–Stokes codes (Hah (1983), Rhie (1986)) represent the second generation of CFD codes utilized in the turbomachinery design process. Application of these codes represents the state–of–the–art in turbine design and analysis systems. Availability of 3D CFD codes to analyze flow through turbine airfoil rows has greatly enhanced the capabilities of the design engineer. In addition to providing the ability to compute flow through complex 3D geometries, these codes also permit calculation of secondary flows in turbine airfoil rows and thus provide a vehicle to control these flows; this can result in significant improvement in performance and durability of turbines.

The secondary flow prediction capability of the 3D CFD codes is demonstrated in Figure 2.4.10 where experimental data from Langston's Cascade (1977) are compared to theoretical predictions by utilizing both a Navier–Stokes code (Rhie (1986)) and an Euler code (Ni et al. (1989)). Both codes, run with measured inlet flow profiles, show good agreement with data in terms of airfoil loadings and surface streamline patterns, indicating the effects of secondary flows. The Navier–Stokes code was expected to yield good predictions for the three–dimensional flows since it solves viscous flow equations. Realistic predictions obtained by using an inviscid Euler code were, however, surprising because secondary flow behavior was expected to be induced by viscous effects not modeled by the code. Further investigations suggested that good agreement between data and predictions due to 3D codes was mainly influenced by the use of measured upstream flow profiles; the predicted magnitude of secondary flows changed dramatically as the upstream profile changed in both codes. Specification of upstream boundary condition thus becomes an important variable in the turbomachinery design and analysis process.

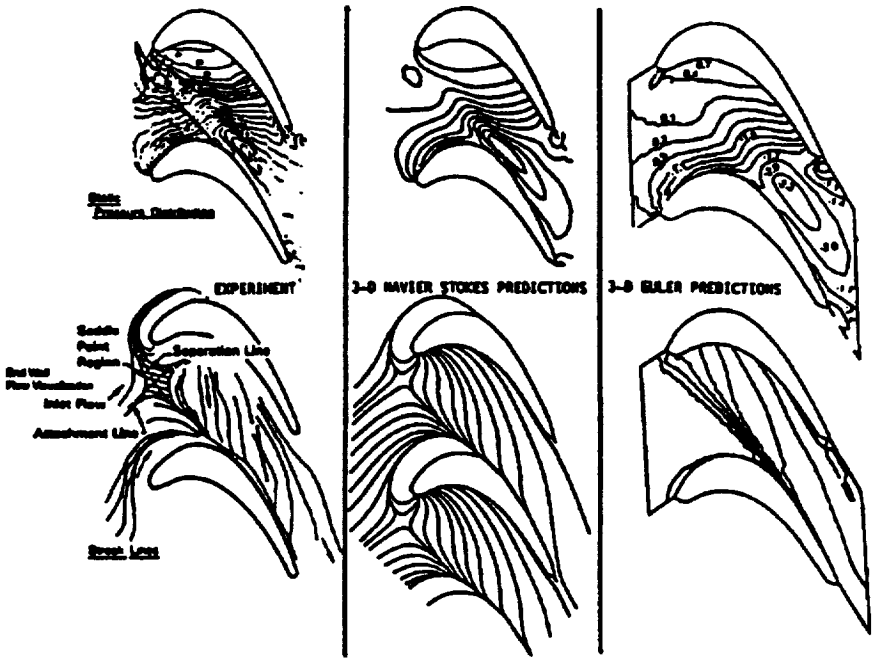

Figure 2.4.10(a) Both 3-D Euler and 3-D Navier–Stokes Code Yield Good Agreement with Langston's Cascade Data.

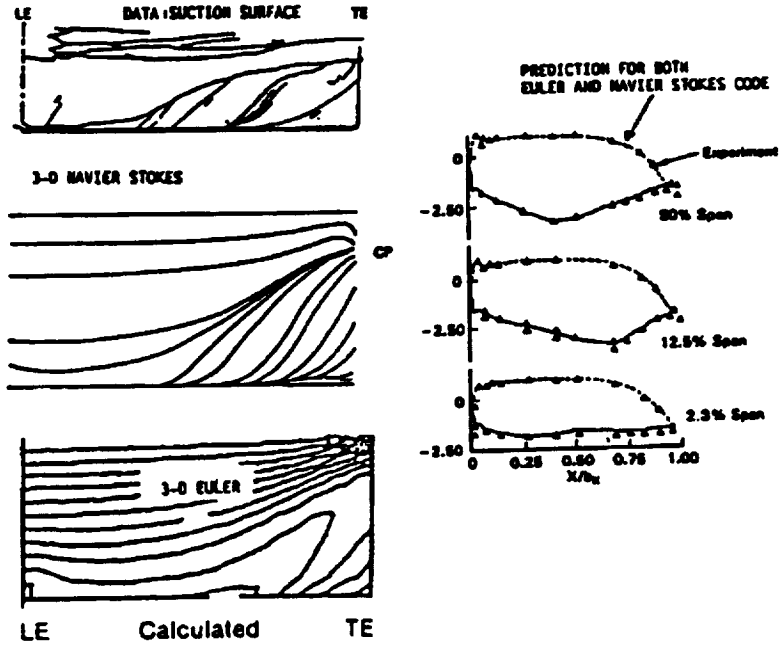

Figure 2.4.10(b) Both 3-D Euler and 3-D Navier-Stokes Code Show Good Agreement with Langston's Cascade Data for Suction Surface Streamlines and Loading Distributions on the Airfoil Surfaces.

Current turbines have closely spaced rows of airfoils. To analyze the flow through an airfoil row inside a multistage turbine, one must specify the boundary condition for that row which is difficult to obtain. To overcome this difficulty, multistage Euler codes have been developed (Ni et al. (1990) In these codes the flow downstream of each airfoil row is averaged at the interface plane (Figure 2.4.11) before information is transferred from an upstream to the downstream row during each solution iteration. All interstage boundary conditions are thus automatically provided by the code. Theoretical predictions from this code are compared against data measured in a two–stage turbine. Good agreement between data and predictions confirms the validity of the model. The measured airfoil loadings for the same experiment are compared to predictions in Figure 2.4.12 . Once again, excellent agreement is shown between the measured data and theoretical predictions. These multistage codes are routinely used in the design and analysis of the aircraft and SSME turbines.

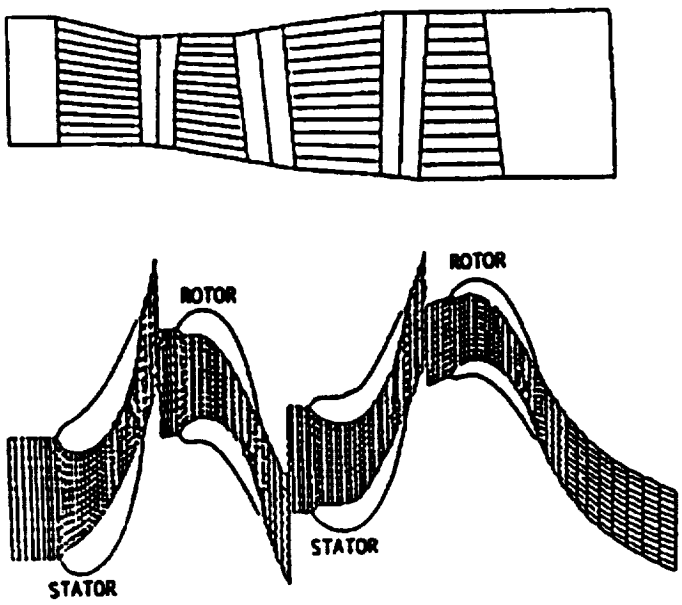

Figure 2.4.11 *Schematics of a Two–Stage Turbine Showing the Strategy Used in Computing 3-D Flows by Using Multi-Stage Euler Code. Flowfield Downstream of Each Airfoil Row is Averaged and Calculations are Conducted in Their Frame of Reference.*

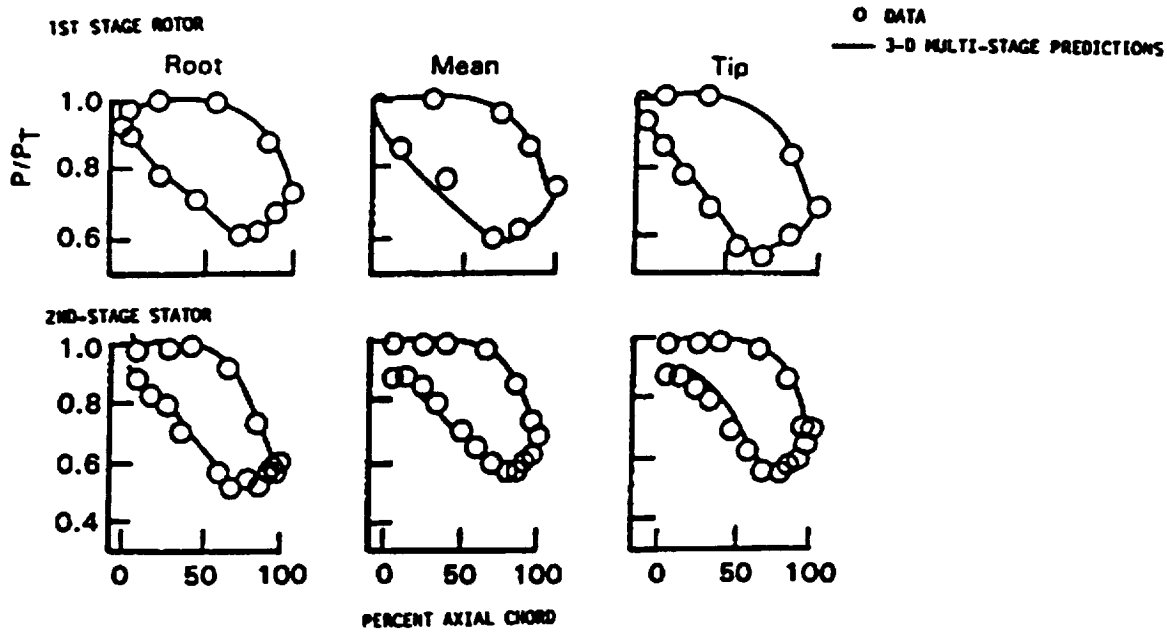

Figure 2.4.12 *Three–Dimensional Multi–Stage Euler Code Gives Good Estimates of Time–Averaged Loading for Airfoils in Unsteady Environment.*

The multistage calculation of Ni et al. (1989) described above facilitates steady state interaction between airfoil rows and provides good estimates of airfoil loadings, flow distributions and gap averaged total pressure and total temperature fields.

2.4.4 Future Direction

The 3D CFD codes described in the previous subsection provide necessary tools for designers to optimize turbomachines under "mean" (steady) flow conditions. However, as pointed out earlier, the actual flow fields in turbomachines are highly complex and unsteady. The airfoils undergo transient and periodic aerodynamic loads which affect life and performance. In order to further improve the durability and efficiency of the machine, more advanced flow prediction codes need to be developed.

Two specific aspects of the turbomachinery flow fields need further development: improved predictions of the viscous flow effects and a realistic account of the effects of unsteadiness.

The viscous flows in turbomachines are dominated by complex boundary layers having laminar, transitional and turbulent flow regimes. There are currently no methods available that can predict the breakdown of laminar flows into transitional, and subsequently turbulent flows without utilizing empiricism. Development of models that can account for mixing induced by turbulent flows from first principles, although highly desirable, is beyond the scope of the present program. Even if such a method could be developed, it would predict a flow structure similar to that shown in Figure 2.4.13(a) which shows a flow field downstream of the rotor in the absence of upstream distortions. The real flow in the rotor is influenced by wakes and vortices from the upstream stator airfoils (Figure 2.4.13(b)). The overall flow structure in Figure 2.4.13(b) is totally different from that in Figure 2.4.13(a), indicating that the effect of unsteadiness is more pronounced than the effect of viscosity. Further improvements in the turbomachinery flow field analysis are thus likely to come from unsteady flow analyses.

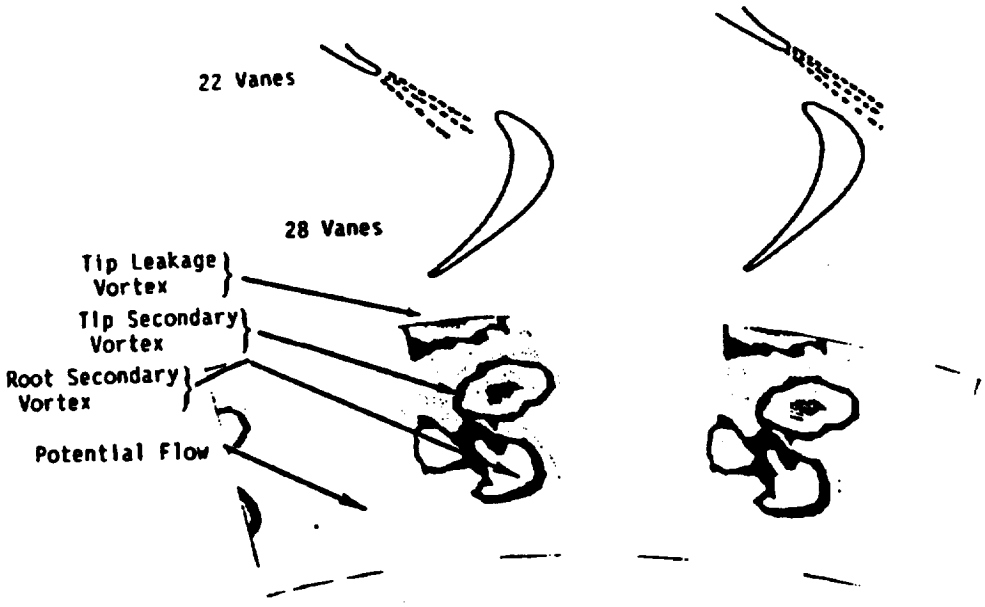

Figure 2.4.13(a) Rotor Exit Flow Total Pressure Loss Contours in the Absence of Upstream Wakes Show Distinct Organized Structures Similar to the Ones Measured in Cascades. A 3–D Steady Navier–Stokes Code With Best Turbulence Model Can Only Reproduce These Flow Structures.

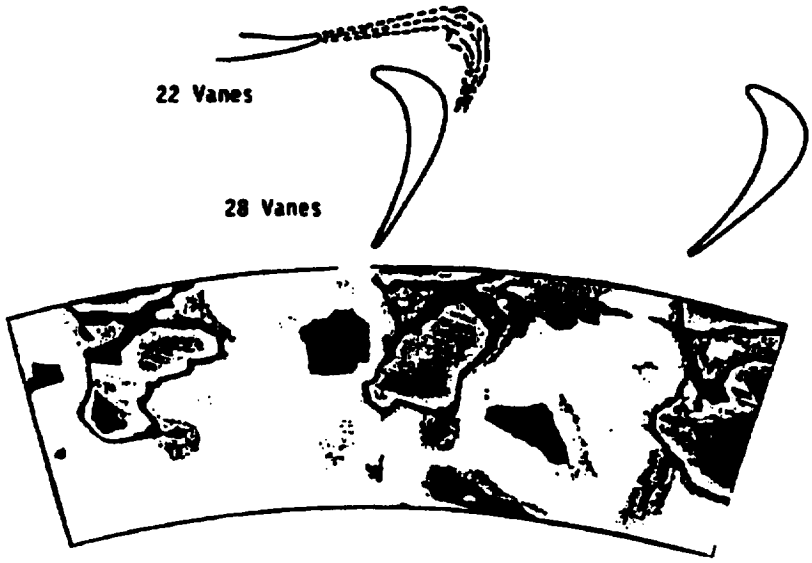

Figure 2.4.13(b) Rotor Exit Flow Total Pressure Contours As They Are Influenced By Wakes From Upstream Stator Row Airfoil Show Large Pulsation in the Organized Flow Structure. To Predict These Flows, Viscous Unsteady 3–D Code is Required.

Progress in computing three–dimensional unsteady flows has been reported by Rai (1987,89) where an innovative numerical scheme and a supercomputer (CRAY–XMP) were utilized to calculate three–dimensional viscous unsteady flows through a large scale model turbine. Some of his results are shown in Figure 2.4.14. Although the computational resources required for this exercise are large, Rai demonstrated that unsteady turbomachinery flow calculations are within the grasp of turbomachinery designers. Even though the geometry was simplified by assuming the same number of rotor and stator airfoil counts, the computation took 100 CPU hours on the CRAY–XMP computer. It is estimated, however, that a realistic case would require 1250 hours of CPU on the CRAY–XMP computer. Such requirements are not practical during a normal turbomachinery design process. In order to reduce these requirements, "smart" use of CFD codes must be adopted. Using the same approach as in the previous phases of the design system development, physical models, representing salient features of the flow field physics, must be developed from experiments. These models can then be incorporated into the unsteady, 3D viscous flow solvers, thus achieving improved accuracy with much reduced computational costs.

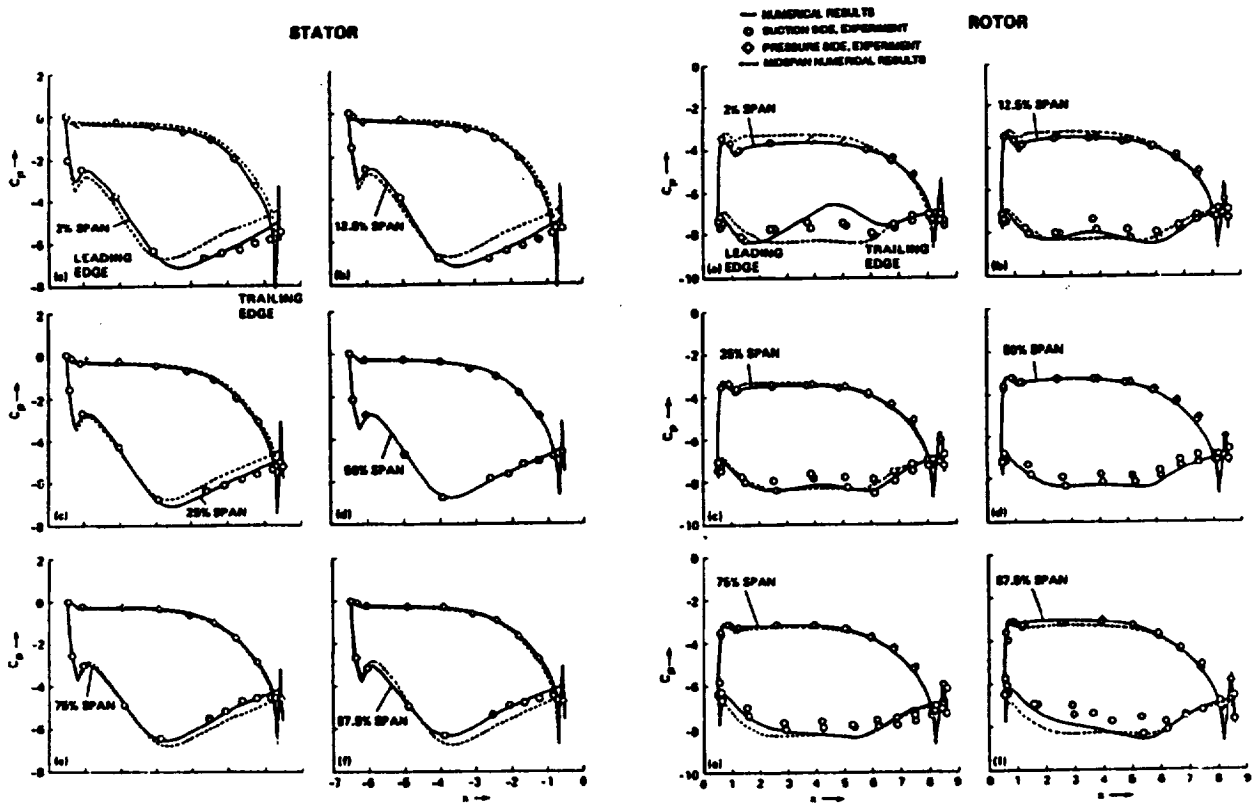

Figure 2.4.14(a) Rai's Unsteady Navier–Stokes Code Shows Good Agreement With Dring's LSRR Stator and Rotor Airfoils Time–Averaged Loading Data. Similar Predictions Have Been Obtained by Using 3–D Multi–Stage Euler Code (Ni et al. (1990)).

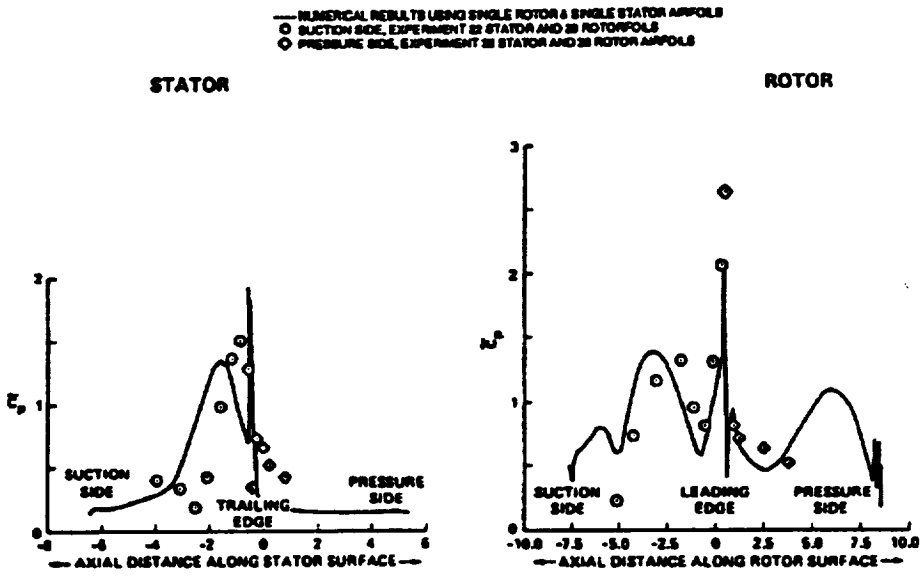

Figure 2.4.14(b) Comparison of Pressure Amplitude Data on the Stator and Rotor Airfoils at Mid–Span Between Rai's 3–D Unsteady Navier–Stokes Predictions and Dring's Experimental Data. An Improved Agreement Between Data and Predictions Indicated by Rai When He Used 3 Stator and 4 Rotor Airfoils in His 2–D Unsteady Navier–Stokes Simulation. In Experiment, Rotor and Stator Consist of 28 and 22 Airfoils Respectively.

Work conducted in the present program has been a step towards developing the third generation of CFD code application in the turbomachinery design process. The development and verification of a 3D unsteady viscous flow solver in a turbomachinery environment is essential before information from these codes can be utilized to improve durability, structural integrity and performance of rocket engine turbopumps. Theoretical treatment including a system of equations, boundary conditions and turbulence modeling used in the CFD code development is discussed in Section 3. Verification of the code against benchmark quality data is discussed in Section 4. The verified code is applied to two configurations to provide accurate estimates of flows in radial and axial machines in Section 5. Conclusions and recommendations for future work are discussed in Section 6.

3. THEORETICAL ANALYSIS

The CFD code used in the present program was originally developed by Rai (1987, 89) to simulate unsteady two– and three–dimensional viscous flows through a turbine stage. Detailed discussions of the governing equations, integration procedure, turbulence model and boundary conditions are given by Rai and Dorney et al. (1992) and are reproduced here for the sake of completeness of documentation. Modifications to turbulence models and boundary conditions developed under the present program are also discussed.

3.1 Governing Equations

The code is based on numerical solution of the time dependent, three–dimensional, Reynolds averaged Navier–Stokes equations. These equations can be written in Cartesian coordinates as:

$$Q_t + (F_i + F_v)_x + (G_i + G_v)_y + (H_i + H_v)_z = 0 \tag{3.1.1}$$

where

$$Q = \begin{bmatrix} \varrho \\ \varrho u \\ \varrho v \\ \varrho w \\ e_t \end{bmatrix} \tag{3.1.2}$$

$$F_i = \begin{bmatrix} \varrho u \\ \varrho u^2 + P \\ \varrho uv \\ \varrho uw \\ (e_t + P)u \end{bmatrix} \qquad F_v = -\begin{bmatrix} 0 \\ \tau_{xx} \\ \tau_{xy} \\ \tau_{xz} \\ \tau_{kx} \end{bmatrix} \tag{3.1.3}$$

$$G_i = \begin{bmatrix} \varrho v \\ \varrho uv \\ \varrho v^2 + P \\ \varrho vw \\ (e_t + P)v \end{bmatrix} \qquad G_v = -\begin{bmatrix} 0 \\ \tau_{yx} \\ \tau_{yy} \\ \tau_{yz} \\ \tau_{ky} \end{bmatrix} \tag{3.1.4}$$

$$H_i = \begin{bmatrix} \varrho w \\ \varrho uw \\ \varrho vw \\ \varrho w^2 + P \\ (e_t + P)w \end{bmatrix} \qquad H_v = -\begin{bmatrix} 0 \\ \tau_{zx} \\ \tau_{zy} \\ \tau_{zz} \\ \tau_{kz} \end{bmatrix} \tag{3.1.5}$$

and

$$
\begin{aligned}
\tau_{xx} &= 2\mu u_x + \lambda(u_x + v_x + w_z) \\
\tau_{xy} &= \mu(u_y + v_x) \\
\tau_{xz} &= \mu(u_z + w_x) \\
\tau_{yx} &= \tau_{xy} \\
\tau_{yy} &= 2\mu v_y + \lambda(u_x + v_y + w_z) \\
\tau_{yz} &= \mu(v_z + w_y) \\
\tau_{zx} &= \tau_{xz} \\
\tau_{zy} &= \tau_{yz} \\
\tau_{zz} &= 2\mu w_z + \lambda(u_x + v_y + w_z) \\
\tau_{hx} &= u\tau_{xx} + v\tau_{xy} + w\tau_{xz} + \gamma\mu P_r^{-1} e_x \\
\tau_{hy} &= u\tau_{yx} + v\tau_{yy} + w\tau_{yz} + \gamma\mu P_r^{-1} e_y \\
\tau_{hz} &= u\tau_{zx} + v\tau_{zy} + w\tau_{zz} + \gamma\mu P_r^{-1} e_z \\
e &= \frac{P}{\varrho(\gamma - 1)} \\
e_t &= \varrho e + \frac{\varrho(u^2 + v^2 + w^2)}{2}
\end{aligned}
\tag{3.1.6}
$$

For the present application, the second coefficient of viscosity is calculated using Stokes' hypothesis, $\lambda = -2/3\mu$. The equations of motion are completed by the perfect gas law which takes the form

$$P = \varrho RT \tag{3.1.7}$$

It is useful to non–dimensionalize the equations of motion so that certain parameters, such as the Reynolds and Mach numbers, can be varied independently. The non–dimensional variables chosen in this investigation are

$$
\begin{aligned}
x^* &= \frac{x}{L} \qquad & y^* &= \frac{y}{L} \qquad & t^* &= \frac{t}{L/V_\infty} \\
u^* &= \frac{u}{V_\infty} \qquad & v^* &= \frac{v}{V_\infty} \qquad & w^* &= \frac{w}{V_\infty} \\
\varrho^* &= \frac{\varrho}{\varrho_\infty} \qquad & P^* &= \frac{P}{\varrho V_\infty^2} \qquad & T^* &= \frac{T}{T_\infty} \\
& & \mu^* &= \frac{\mu}{\mu_\infty}
\end{aligned}
\tag{3.1.8}
$$

In addition, for the analysis of arbitrary geometries the equations of motion can be generalized by using body–fitted coordinates. Using the independent variable transformations

$$\begin{aligned} \tau &= t \\ \xi &= \xi(x,y,z,t) \\ \eta &= \eta(x,y,z,t) \\ \zeta &= \zeta(x,y,z,t) \end{aligned} \tag{3.1.9}$$

the body–fitted Cartesian coordinates in the physical domain become uniform coordinates in the computational domain. The transformation allows easier implementation of boundary conditions since the geometry surface lies along the boundaries of the computational domain. Upon applying the transformations and non–dimensionalizing, the three–dimensional Navier–Stokes equations can be written as (where the superscripts '*' have been omitted for clarity)

$$\tilde{Q}_\tau + (\tilde{F}_i + \mathrm{Re}^{-1}\tilde{F}_v)_\xi + (\tilde{G}_i + \mathrm{Re}^{-1}\tilde{G}_v)_\eta + (\tilde{H}_i + \mathrm{Re}^{-1}\tilde{H}_v)_\zeta = 0 \tag{3.1.10}$$

where

$$\begin{aligned} \tilde{Q} &= J^{-1}Q \\ \tilde{F}_i(Q,\xi) &= J^{-1}(\xi_t Q + \xi_x F_i + \xi_y G_i + \xi_z H_i) \\ \tilde{G}_i(Q,\eta) &= J^{-1}(\eta_t Q + \eta_x F_i + \eta_y G_i + \eta_z H_i) \\ \tilde{H}_i(Q,\zeta) &= J^{-1}(\zeta_t Q + \zeta_x F_i + \zeta_y G_i + \zeta_z H_i) \end{aligned} \tag{3.1.11}$$

The viscous fluxes are simplified by incorporating the thin layer assumption (Baldwin and Lomax (1978)). The thin layer assumption states that for high Reynolds number flows, the diffusion terms normal to a solid surface will be greater than those parallel to the surface. In the current study, viscous terms are retained in the direction normal to the hub/shroud surfaces (ς–direction) and in the direction normal to the blade surface (η–direction). Thus, the non–dimensionalized and transformed equations now become:

$$\tilde{Q}_\tau + (\tilde{F}_i)_\xi + (\tilde{G}_i + \mathrm{Re}^{-1}\tilde{G}_v)_\eta + (\tilde{H}_i + \mathrm{Re}^{-1}\tilde{H}_v)_\zeta = 0 \tag{3.1.12}$$

where

$$\tilde{G}_v = -\begin{bmatrix} 0 \\ K_1 u_\eta + K_2 \eta_x \\ K_1 v_\eta + K_2 \eta_y \\ K_1 w_\eta + K_2 \eta_z \\ K_1\left(P_r^{-1}(\gamma-1)^{-1}(a^2)_\eta + \left(\frac{q^2}{2}\right)_\eta\right) + K_2 K_3 \end{bmatrix} \tag{3.1.13}$$

$$\begin{aligned} K_1 &= \mu(\eta_x^2 + \eta_y^2 + \eta_z^2) \\ K_2 &= \frac{\mu}{3}(\eta_x u_\eta + \eta_y v_\eta + \eta_z w_\eta) \\ K_3 &= u\eta_x + v\eta_y + w\eta_z \\ q^2 &= u^2 + v^2 + w^2 \end{aligned} \tag{3.1.14}$$

The vector $\tilde{H}_v$ is obtained by replacing η with ς in Eqs. (3.1.13) and (3.1.15). If all the viscous terms are neglected, then the equations become the inviscid (Euler) equations of motion. The Jacobian of the transformation and the other metric quantities are given by Rai (1987, 89) and Pulliam and Steger (1985).

$$J^{-1} = x_\xi y_\eta z_\zeta + x_\zeta y_\xi z_\eta + x_\eta y_\zeta z_\xi - x_\xi y_\zeta z_\eta - x_\eta y_\xi z_\zeta - x_\zeta y_\eta z_\xi \tag{3.1.15}$$

$$\begin{aligned}
\xi_x &= J(y_\eta z_\zeta - y_\zeta z_\eta) & \eta_x &= J(z_\xi y_\zeta - y_\xi z_\zeta) \\
\xi_y &= J(z_\eta x_\zeta - z_\zeta x_\eta) & \eta_y &= J(x_\xi z_\zeta - z_\xi x_\zeta) \\
\xi_z &= J(x_\eta y_\zeta - y_\eta x_\zeta) & \eta_z &= J(y_\xi x_\zeta - x_\xi y_\zeta) \\
\zeta_x &= J(y_\xi z_\eta - z_\xi y_\eta) & \xi_t &= -x_\tau \xi_x - y_\tau \xi_y - z_\tau \xi_z \\
\zeta_y &= J(z_\xi x_\eta - x_\xi z_\eta) & \eta_t &= -x_\tau \eta_x - y_\tau \eta_y - z_\tau \eta_z \\
\zeta_z &= J(x_\xi y_\eta - y_\xi x_\eta) & \xi_t &= -x_\tau \zeta_x - y_\tau \zeta_y - z_\tau \zeta_z
\end{aligned} \tag{3.1.16}$$

The metric derivatives are evaluated using three point central differences in the interior of the computational domain and three point backward differences on the boundaries.

3.2 Integration Procedure

The governing equations of motion are integrated in time using the Approximate Factorization (AF) implicit technique developed by Beam and Warming (1977). Applying the AF technique for three–dimensional problems is accomplished by solving three one–dimensional operators, each requiring the inversion of a block tridiagonal matrix system with 5x5 blocks. Newtown iterations are applied within each global time step to increase stability and eliminate the linearization errors caused by the factorization process. To apply Newton's method, one starts with an initial guess for the solution and iterates according to:

$$\tilde{Q}^{p+1} = \tilde{Q}^p - \frac{f(\tilde{Q})}{f'(\tilde{Q})} \tag{3.2.1}$$

This method can be applied to the unsteady Navier–Stokes equations by setting

$$f(\tilde{Q}) = \tilde{Q}_\tau + (\tilde{F}_i)_\xi + (\tilde{G}_i + \mathrm{Re}^{-1}\tilde{G}_v)_\eta + (\tilde{H}_i + \mathrm{Re}^{-1}\tilde{H}_v)_\zeta \tag{3.2.2}$$

and

$$f'(\tilde{Q}) = \frac{\partial}{\partial \tilde{Q}}\left[\tilde{Q}_\tau + (\tilde{F}_i)_\xi + (\tilde{G}_i + \mathrm{Re}^{-1}\tilde{G}_v)_\eta + (\tilde{H}_i + \mathrm{Re}^{-1}\tilde{H}_v)_\zeta\right] \tag{3.2.3}$$

Noting that, for example,

$$\frac{\partial}{\partial \tilde{Q}}\left(\frac{\partial \tilde{F}_i}{\partial \xi}\right) = \frac{\partial}{\partial \xi}\left(\frac{\partial \tilde{F}_i}{\partial \tilde{Q}}\right) = \frac{\partial \tilde{A}}{\partial \xi'} \tag{3.2.4}$$

where $\tilde{A}$ is a Jacobian matrix, the factored, iterative, implicit integration algorithm can be defined by (Rai (1987, 89))

$$\left[I + \frac{\Delta\tau}{\Delta\xi}\left(\nabla_\xi \tilde{A}^+_{ijk} + \Delta_\xi \tilde{A}^-_{ijk}\right)\right]^p \left[I + \frac{\Delta\tau}{\Delta\eta}\left(\nabla_\eta \tilde{B}^+_{ijk} + \Delta_\eta \tilde{B}^-_{ijk} - \mathrm{Re}^{-1}\delta_\eta \tilde{M}\right)\right]^p$$

$$\left[I + \frac{\Delta\tau}{\Delta\zeta}\left(\nabla_\zeta \tilde{C}^+_{ijk} + \Delta_\zeta \tilde{C}^-_{ijk} - \mathrm{Re}^{-1}\delta_\zeta \tilde{N}\right)\right]^p \left(\tilde{Q}^{p+1}_{ijk} - \tilde{Q}^p_{ijk}\right)$$

$$= -\Delta\tau\left[\frac{\tilde{Q}^p_{ijk} - \tilde{Q}^n_{ijk}}{\Delta\tau} + \frac{(\hat{F}_i)^p_{i+1/2jk} - (\hat{F}_i)^p_{i-1/2jk}}{\Delta\xi}\right. \tag{3.2.5}$$

$$+ \frac{(\hat{G}_i)^p_{ij+1/2k} - (\hat{G}_i)^p_{ij-1/2k}}{\Delta\eta} - \frac{(\hat{G}_v)^p_{ij+1/2k} - (\hat{G}_v)^p_{ij-1/2k}}{\mathrm{Re}\,\Delta\eta}$$

$$\left. + \frac{(\hat{H}_i)^p_{ijk+1/2} - (\hat{H}_i)^p_{ijk-1/2}}{\Delta\zeta} - \frac{(\hat{H}_v)^p_{ijk+1/2} - (\hat{H}_v)^p_{ijk-1/2}}{\mathrm{Re}\,\Delta\zeta}\right]$$

where

$$\tilde{A}^\pm = \left(\frac{\partial \tilde{F}_i}{\partial \tilde{Q}}\right)^\pm \quad \tilde{B}^\pm = \left(\frac{\partial \tilde{G}_i}{\partial \tilde{Q}}\right)^\pm \quad \tilde{C}^\pm = \left(\frac{\partial \tilde{H}_i}{\partial \tilde{Q}}\right)^\pm \tag{3.2.6}$$

$$\tilde{M}^\pm = \left(\frac{\partial \tilde{G}_v}{\partial \tilde{Q}}\right)^\pm \quad \tilde{N}^\pm = \left(\frac{\partial \tilde{H}_v}{\partial \tilde{Q}}\right)^\pm \tag{3.2.7}$$

and Δ, ∇, and δ represent forward forward, backward, and central difference operators. In equation (2.21), $\tilde{Q}^p$ is an approximation to $\tilde{Q}^{n+1}$. The quantities $\hat{F}_i, \hat{G}_i, \hat{H}_i, \hat{G}_v$, and $\hat{H}_v$ are numerical fluxes which are consistent with the physical fluxes $\tilde{F}_i, \tilde{G}_i, \tilde{H}_i, \tilde{G}_v$, and $\tilde{H}_v$. If p = 0 then $\tilde{Q}^p = \tilde{Q}^n$, and when the equation is iterated to convergence $\tilde{Q}^p = \tilde{Q}^{n+1}$. As the left hand side of equation (3.2.5) is driven to zero, the linearization and factorization errors associated with the AF technique are also driven to zero. If only one iteration is used then the integration scheme reverts to the conventional AF type scheme (Beam and Warming (1977)). Typically, unsteady calculations require two to three iterations per global time step to reduce the residual of the density by three orders of magnitude (Rai (1987, 89), Dorney et al. (1992)).

The inviscid numerical fluxes $\hat{F}_i, \hat{G}_i$, and $\hat{H}_i$ are discretized using Roe's scheme (Roe (1981)). The numerical fluxes are then evaluated from a family of high accuracy representations of the fluxes developed in Chakravarthy and Osher (1985). For example,

$$(\hat{F}_i)_{i+1/2jk} = (\tilde{F}_i)_{i+1/2jk} - \frac{(1-\phi)}{4}\Delta F^-_{i+3/2jk} - \frac{(1+\phi)}{4}\Delta F^-_{i+1/2jk} + \frac{(1+\phi)}{4}\Delta F^+_{i+1/2jk} + \frac{(1-\phi)}{4}\Delta F^+_{i-1/2jk} \tag{3.2.8}$$

where $(\tilde{F}_i)_{i+1/2jk}$ is the first order accurate upwind flux given by

$$(\tilde{F}_i)_{i+1/2jk} = \frac{1}{2}[(\tilde{F}_i)_{ijk} + (\tilde{F}_i)_{i+1jk}] - \frac{1}{2}(\Delta F^+_{i-1/2jk} - \Delta F^-_{i+1/2jk}) \tag{3.2.9}$$

and the additional terms in Eq. (3.2.8) are used to increase the order of accuracy. The third order accurate upwind biased difference scheme is used for interior grid points and either first or second order accurate upwind differencing is used at boundary points.

The flux differences ($\Delta F^{\pm}$) in Eqs. (3.2.8) and (3.2.9) are calculated using Roe's scheme and are given by

$$\Delta F^{\pm}_{i+1/2jk} = \tilde{A}^{\pm}_{i+1/2jk} \times (Q_{i+1jk} - Q_{ijk}) \tag{3.2.10}$$

The flow variables needed to determine $\tilde{A}^{\pm}$ between grid points (i + 1/2, j, k) are calculated using Roe's averaging formulae:

$$u_{i+1/2jk} = \frac{u_{ijk}\sqrt{\varrho_{ijk}} + u_{i+1jk}\sqrt{\varrho_{i+1jk}}}{\sqrt{\varrho_{ijk}} + \sqrt{\varrho_{i+1jk}}}$$

$$v_{i+1/2jk} = \frac{v_{ijk}\sqrt{\varrho_{ijk}} + v_{i+1jk}\sqrt{\varrho_{i+1jk}}}{\sqrt{\varrho_{ijk}} + \sqrt{\varrho_{i+1jk}}} \tag{3.2.11}$$

$$w_{i+1/2jk} = \frac{w_{ijk}\sqrt{\varrho_{ijk}} + w_{i+1jk}\sqrt{\varrho_{i+1jk}}}{\sqrt{\varrho_{ijk}} + \sqrt{\varrho_{i+1jk}}}$$

$$(h_t)_{i+1/2jk} = \frac{(h_t)_{ijk}\sqrt{\varrho_{ijk}} + (h_t)_{i+1jk}\sqrt{\varrho_{i+1jk}}}{\sqrt{\varrho_{ijk}} + \sqrt{\varrho_{i+1jk}}}$$

where h_t is the total enthalpy and is defined as

$$h_t = \frac{e_t + P}{\varrho} \tag{3.2.12}$$

The Jacobian matrix $\tilde{A^{\pm}}$ can be written as:

$$\tilde{A^{\pm}} = T_{\xi}^{-1} \Lambda_{\xi}^{\pm} T_{\xi} \tag{3.2.13}$$

where T_{ξ} and T_{ξ}^{-1} are eigenvectors and which can be expressed as (Pulliam and Steger (1985)):

$$T_{\xi} = \begin{bmatrix} \tilde{\xi}_x & \tilde{\xi}_y \\ \tilde{\xi}_x u & \tilde{\xi}_y u - \tilde{\xi}_z \varrho \\ \tilde{\xi}_x v + \tilde{\xi}_z \varrho & \tilde{\xi}_y v \\ \tilde{\xi}_x w - \tilde{\xi}_y \varrho & \tilde{\xi}_y w + \tilde{\xi}_z \varrho \\ \tilde{\xi}_x R_1/(\gamma - 1) + \varrho(\tilde{\xi}_z v - \tilde{\xi}_y w) & \tilde{\xi}_y R_1/(\gamma - 1) + \varrho(\tilde{\xi}_z w - \tilde{\xi}_z u) \end{bmatrix} \tag{3.2.14}$$

$$\begin{bmatrix} \tilde{\xi}_z & R_2 & R_2 \\ \tilde{\xi}_z u + \tilde{\xi}_y \varrho & R_2(u + \tilde{\xi}_z a) & R_2(u - \tilde{\xi}_z a) \\ \tilde{\xi}_z v - \tilde{\xi}_z \varrho & R_2(v + \tilde{\xi}_z a) & R_2(v - \tilde{\xi}_z a) \\ \tilde{\xi}_z w & R_2(w + \tilde{\xi}_z a) & R_2(w - \tilde{\xi}_z a) \\ \tilde{\xi}_z R_1(\gamma - 1) + \varrho(\tilde{\xi}_y u - \tilde{\xi}_z v) & R_2[(R_1 + a^2)/(\gamma - 1) + R_4 a] & R_2[(R_1 + a^2)/(\gamma - 1) + R_4 a] \end{bmatrix}$$

$$T_{\xi}^{-1} = \begin{bmatrix} \tilde{\xi}_x(1 - R_1/a^2) - (\tilde{\xi}_z v - \tilde{\xi}_y w)/\varrho & \tilde{\xi}_x(\gamma - 1)u/a^2 \\ \tilde{\xi}_y(1 - R_1/a^2) - (\tilde{\xi}_z w - \tilde{\xi}_z u)/\varrho & \tilde{\xi}_y(\gamma - 1)u/a^2 - \tilde{\xi}_z/\varrho \\ \tilde{\xi}_z(1 - R_1/a^2) - (\tilde{\xi}_y u - \tilde{\xi}_z v)/\varrho & \tilde{\xi}_z(\gamma - 1)u/a^2 + \tilde{\xi}_y/\varrho \\ R_3(R_1 - R_4 a) & -R_4[(\gamma - 1)u - \tilde{\xi}_z a] \\ R_3(R_1 + R_4 a) & -R_4[(\gamma - 1)u + \tilde{\xi}_z a] \end{bmatrix} \tag{3.2.15}$$

$$\begin{bmatrix} \tilde{\xi}_x(\gamma - 1)v/a^2 + \tilde{\xi}_z/\varrho & \tilde{\xi}_x(\gamma - 1)w/a^2 - \tilde{\xi}_y/\varrho & -\tilde{\xi}_x(\gamma - 1)/a^2 \\ \tilde{\xi}_y(\gamma - 1)v/a^2 & \tilde{\xi}_y(\gamma - 1)w/a^2 - \tilde{\xi}_z/\varrho & -\tilde{\xi}_y(\gamma - 1)/a^2 \\ \tilde{\xi}_z(\gamma - 1)v/a^2 - \tilde{\xi}_z/\varrho & \tilde{\xi}_z(\gamma - 1)w/a^2 & -\tilde{\xi}_z(\gamma - 1)/a^2 \\ -R_3[(\gamma - 1)v - \tilde{\xi}_y a] & -R_3[(\gamma - 1)w - \tilde{\xi}_z a] & R_3(\gamma - 1) \\ -R_3[(\gamma - 1)v + \tilde{\xi}_y a] & -R_3[(\gamma - 1)w + \tilde{\xi}_z a] & R_3(\gamma - 1) \end{bmatrix}$$

$$R_1 = \frac{\gamma - 1}{2}(u^2 + v^2 + w^2) \quad R_2 = \varrho/(a\sqrt{2}) \quad R_3 = 1/(\varrho a\sqrt{2}) \quad R_4 = (\xi_x u + \xi_y v + \xi_z w)/\varkappa \tag{3.2.16}$$

$$\tilde{\xi}_x = \xi_x/\varkappa \qquad \tilde{\xi}_y = \xi_y/\varkappa \qquad \tilde{\xi}_z = \xi_z/\varkappa \qquad \varkappa = \sqrt{\xi_x^2 + \xi_y^2 + \xi_z^2}$$

The eigenvectors for the $\tilde{B}$ and $\tilde{C}$ matrices can be obtained by replacing ξ in Eqs. (3.2.14) and (3.2.15) with η and ς. The matrix containing the eigenvalues of the Jacobian matrix is given by

$$\Lambda_\xi^{\pm} = \begin{bmatrix} \lambda_1^{\pm} & 0 & 0 & 0 & 0 \\ 0 & \lambda_2^{\pm} & 0 & 0 & 0 \\ 0 & 0 & \lambda_3^{\pm} & 0 & 0 \\ 0 & 0 & 0 & \lambda_4^{\pm} & 0 \\ 0 & 0 & 0 & 0 & \lambda_5^{\pm} \end{bmatrix} \tag{3.2.17}$$

where

$$\begin{aligned} \lambda_{1,2,3} &= \xi_t + \xi_x u + \xi_y v + \xi_z w \\ \lambda_4 &= \lambda_1 + \varkappa a \\ \lambda_5 &= \lambda_1 - \varkappa a \end{aligned} \tag{3.2.18}$$

The superscripts '$\pm$' in the previous equations refer to the contributions from the downstream and upstream running characteristic waves. To prevent expansion shocks, the eigenvalues in Eq. (3.2.18) are replaced by a nonvanishing, continuously differentiable approximation which can be written as (Yee et al. (1985)):

$$\tilde{\lambda}_n^{\pm} = \begin{cases} \frac{1}{2}\left[\left(\lambda_n^2/\delta\right) + \delta\right] & |\lambda_n| < \delta \\ |\lambda_n| & |\lambda_n| \geq \delta \end{cases} \tag{3.2.19}$$

where $n = 1,5$

The flow variables needed to determine the viscous fluxes, $\tilde{G}_v$ and $\tilde{H}_v$, are evaluated using standard central differences. For example,

$$\begin{aligned} (\tilde{G}_v)_{ij+1/2k} &= f(Q_{ij+1/2k}, (Q_n)_{ij+1/2k}) \\ Q_{ij+1/2k} &= \frac{1}{2}(Q_{ijk} + Q_{ij+1k}) \\ (Q_n)_{ij+1/2k} &= Q_{ij+1k} - Q_{ijk} \end{aligned} \tag{3.2.20}$$

The corresponding viscous flux Jacobian, $\tilde{M}$, can be written as (Pulliam and Steger (1985))

$$\tilde{M} = J^{-1} \begin{bmatrix} 0 & 0 & 0 & 0 & 0 \\ m_{21} & S_1\partial_\eta(\varrho^{-1}) & S_2\partial_\eta(\varrho^{-1}) & S_3\partial_\eta(\varrho^{-1}) & 0 \\ m_{31} & S_2\partial_\eta(\varrho^{-1}) & S_4\partial_\eta(\varrho^{-1}) & S_5\partial_\eta(\varrho^{-1}) & 0 \\ m_{41} & S_3\partial_\eta(\varrho^{-1}) & S_5\partial_\eta(\varrho^{-1}) & S_6\partial_\eta(\varrho^{-1}) & 0 \\ m_{51} & m_{52} & m_{53} & m_{54} & S_0\partial_\eta(\varrho^{-1}) \end{bmatrix} \tag{3.2.21}$$

where

$$m_{21} = -S_1\partial_\eta(u/\varrho) - S_2\partial_\eta(v/\varrho) - S_3\partial_\eta(w/\varrho)$$

$$m_{31} = -S_2\partial_\eta(u/\varrho) - S_4\partial_\eta(v/\varrho) - S_5\partial_\eta(w/\varrho)$$

$$m_{41} = -S_3\partial_\eta(u/\varrho) - S_5\partial_\eta(v/\varrho) - S_6\partial_\eta(w/\varrho)$$

$$\begin{aligned} m_{51} = & -S_0\partial_\eta[-(e_t/\varrho^2) + (u^2+v^2+w^2)/\varrho] \\ & - S_1\partial_\eta(u^2/\varrho) - S_4\partial_\eta(v^2/\varrho) - S_6\partial_\eta(w^2/\varrho) \\ & - 2S_2\partial_\eta(uv/\varrho) - 2S_3\partial_\eta(uw/\varrho) - 2S_5\partial_\eta(vw/\varrho) \end{aligned} \qquad (3.2.22)$$

$$m_{52} = -S_0\partial_\eta(u/\varrho) - m_{21} \qquad m_{53} = -S_0\partial_\eta(v/\varrho) - m_{31}$$

$$m_{54} = -S_0\partial_\eta(w/\varrho) - m_{41}$$

$$S_0 = \gamma\mu\,\mathrm{Pr}^{-1}(\eta_x^2 + \eta_y^2 + \eta_z^2) \qquad S_1 = \mu[(4/3)\eta_x^2 + \eta_y^2 + \eta_z^2]$$

$$S_2 = (\mu/3)\eta_x\eta_y \qquad S_3 = (\mu/3)\eta_x\eta_z$$

$$S_4 = \mu[\eta_x^2 + (4/3)\eta_y^2 + \eta_z^2] \qquad S_5 = (\mu/3)\eta_y\eta_z$$

$$S_6 = \mu[\eta_x^2 + \eta_y^2 + (4/3)\eta_z^2]$$

The viscous flux Jacobian, $\tilde{N}$ can be obtained by replacing η in Eqs. (3.2.21) and (3.2.22) with ς. The equations of motion and solution procedure used in the two–dimensional computational procedure are a direct subset of the equations developed above, except that the inviscid fluxes are calculated using Osher's (1981) approximate Riemann solver.

3.3 Turbulence/Transition Model

The original version of the CFD code used in the present program contained a simple turbulence model which facilitated reasonable predictions in an unsteady flow environment. Limitations of this model were that it assumed fully turbulent flows on airfoil and endwall surface whereas in reality flow is transitional on airfoil surfaces especially in available benchmark quality experiments against which this code was planned to be verified. Appropriate modifications were, therefore, made to the turbulence model to allow transitional flow calculations. Additional modifications were also made to account for free stream turbulence level, surface roughness and extra rates of strain to allow realistic predictions in the complex flow environment of the rocket turbopump. All of these modifications were made in the context of the base turbulence model, these modifications are, however, of generic nature and would still be applicable if a higher order turbulence model was implemented in the code. The scope of the present program limited implementation of the higher order turbulence model in the code which is needed to obtain further reliable predictions from the code.

An eddy viscosity formulation is used in the code to model the effect of turbulence. Effective viscosity and effective turbulent conductivity are defined as:

$$\text{Effective viscosity} = \mu = \mu_L + \mu_T \tag{3.3.1}$$

$$\text{Effective conductivity} = \frac{\varkappa}{C_p} = \frac{\mu_L}{\text{Pr}_L} + \frac{\mu_T}{\text{Pr}_T} \tag{3.3.2}$$

Pr_L and Pr_T are the laminar and turbulent Prandtl numbers respectively.

3.3.1 Baldwin–Lomax Turbulence Model

Turbulence model developed by Baldwin–Lomax (1978) was used in the original CFD code used in the present program.

In the Baldwin–Lomax (B–L) model turbulent eddy viscosity μ_T is described by

$$\mu_T = \begin{cases} \mu_{T_{inner}} & s \le s_{crossover} \\ \mu_{T_{outer}} & s > s_{crossover} \end{cases} \tag{3.3.3}$$

where s is the distance normal to the solid surface and $s_{crossover}$ is the smallest value at which $\mu_{T_{inner}} = \mu_{T_{outer}}$. In the inner region, the eddy viscosity is calculated using the Prandtl–Van Driest formulation

$$\mu_{T_{inner}} = \varrho l^2 |\omega| \tag{3.3.4}$$

where

$$l = ksD$$

and (3.3.5)

$$D = 1 - exp(-y^+/A^+)$$

and the magnitude of the vorticity, $|\omega|$ can be written as:

$$|\omega| = \sqrt{(u_y - v_x)^2 + (v_z - w_y)^2 + (w_x - u_z)^2}$$

$$\begin{aligned} v_x &= v_\xi \xi_x + v_\eta \eta_x + v_\zeta \zeta_x \\ w_x &= w_\xi \xi_x + w_\eta \eta_x + w_\zeta \zeta_x \\ u_y &= u_\xi \xi_y + u_\eta \eta_y + u_\zeta \zeta_y \\ w_y &= w_\xi \xi_y + w_\eta \eta_y + w_\zeta \zeta_y \\ u_z &= u_\xi \xi_z + u_\eta \eta_z + u_\zeta \zeta_z \\ v_z &= v_\xi \xi_z + v_\eta \eta_z + v_\zeta \zeta_z \end{aligned} \tag{3.3.6}$$

and y^+ is the law–of–the–wall coordinate

$$y^+ = \frac{\sqrt{\varrho_w \tau_w} s}{\mu_w} \tag{3.3.7}$$

In the outer region the eddy viscosity is calculated using

$$\mu_{T_{outer}} = KC_{cp}\rho F_{wake}F_{Kleb}(s) \tag{3.3.8}$$

where K is the Clauser constant, C_{cp} is an additional constant and F_{wake} is described by

$$F_{wake} = \min(s_{max}F_{max}, C_{wk}s_{max}q_{dif}^2/F_{max}) \tag{3.3.9}$$

The term F_{max} is the maximum value of F(s) along a given computational grid line normal to the surface and

$$F(s) = s|\omega|D \tag{3.3.10}$$

The Klebanoff intermittency factor, $F_{Kleb}(s)$ is given by:

$$F_{Kleb}(s) = (1 + 5.5((sC_{Kleb})/s_{max})^6)^{-1} \tag{3.3.11}$$

and q_{dif} is the difference between the maximum and minimum velocity in the profile. The vorticity and velocity are calculated in the appropriate reference frame (i.e., in the absolute reference frame for stationary surfaces and in the relative frame for moving surfaces). The constants used in the B–L turbulence model are:

$$\begin{aligned} A^+ &= 26 & C_{cp} &= 1.6 \\ C_{Kleb} &= 0.3 & C_{wk} &= 0.25 \\ k &= 0.4 & K &= .0168 \end{aligned} \tag{3.3.12}$$

The Baldwin–Lomax turbulence model is based upon two–dimensional boundary layer data and as such, is not well suited for corner flows such as those at the blade/endwall juncture.

Originally, the treatment used to implement this turbulence model in the corner regions (Rai (1989)) was the technique proposed by Hung and Buning (1984). In this technique, the turbulence model is computed separately for each endwall and the blade surface. The mixing length in the corner region is computed depending on the computational indices of a given node. For instance, consider the case when the J=constant computational lines run normal to the blade and the K=constant lines run normal to the endwall. For any computational node whose J–wise index is less than its K–wise index, the normal distance is defined as the distance from the blade surface to the grid point and the parallel distance is defined as the distance from the endwall to the grid point. The mixing length for the inner region of the boundary layer is then calculated as

$$l = 2sn/(s + n + \sqrt{(s^2 + n^2)}) \tag{3.3.13}$$

where s is the parallel distance and n is the normal distance. The eddy viscosity is then based on the flow variables along a computational grid line from the airfoil surface to the grid point under consideration. Likewise, for any computational node whose J–wise index is greater than its K–wise index, the parallel distance is measured from the blade surface to the grid point and the normal distance is measured from the endwall to the grid point. The eddy viscosity is then based on the flow variables along a computational grid line from endwall to the grid point. Two significant problems arise from this particular three–dimensional implementation of the Baldwin–Lomax turbulence model. First, the eddy viscosity distribution in the corner regions is discontinuous across the J=K computational lines and can cause large gradients to occur in the velocity field. Secondly, this particular blending is dependent upon the computational grid density and stretching in both

directions. It was found, based upon numerical simulations, that flow solutions in the blade/endwall region were extremely sensitive to changes in the computational grid structure.

A blending function was then used to smoothly vary the eddy viscosity distribution between the blade and endwall. Separate eddy viscosity distributions are computed for the blade and endwall surfaces along the computational lines which run normal to each surface, respectively. The eddy viscosity in the corner flow regions is then computed based upon the following blending function according to the work of Vatsa and Wedan (1988)

$$\mu_T = \frac{l_{ew}^2 \mu_{T_b} + l_b^2 \mu_{T_{ew}}}{l_b^2 + l_{ew}^2} \tag{3.3.14}$$

where l_b is the distance from the blade surface to a given node, $l_e w$ is the distance from the endwall surface to the node, and μ_{Tb} and μ_{Tew} are the eddy viscosities computed from the separate blade and endwall flows, respectively. This type of blending creates a smooth eddy viscosity distribution in the corner regions.

3.3.2 Turbulence Model for Surface Roughness

The need to model surface roughness effects was illustrated by tests conducted at NASA MSFC for the SSME turbine (Boynton et al. (1992)). Significant improvement in the performance of the turbine was achieved by polishing the hardware currently used in the SSME. Surface roughness erodes the effect of viscous damping near the wall causing an increase in mixing length in the inner part of the boundary layer. A model proposed by van Driest (1956) can be used to account for this phenomena. The modified damping function due to surface roughness is given as:

$$Dm = D + Dr \tag{3.3.15}$$

Dm = damping term for modifying turbulent viscosity

D = damping term for smooth surface (equation 3.3.5)

$Dr = -60\, y^+/r^+A^+$

y^+ is defined in equation (3.3.7)

A^+ is defined in equation (3.3.12)

r^+ can be obtained by using surface roughness height instead of 's' in equation (3.3.7)

Predictive capabilities of this model were demonstrated in a publication by Blair (1992) through comparison against data obtained on a smooth and rough airfoil as a part of the NASA MSFC contract # NAS8–37351 as indicated in Figure 3.3.1.

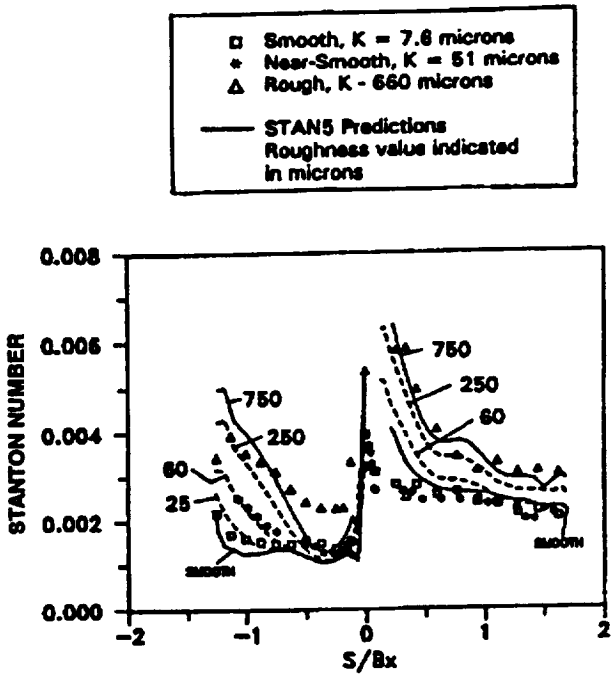

Figure 3.3.1 *Comparison of Midspan Rotor Airfoil Heat Transfer Distributions Obtained at Re = 5.8 x 10^5 and β_1 = 40° with STAN5 Predictions for Various Wall Roughness Values.*

3.3.3 Turbulence Model for Extra Rates of Strain

Extra rates of strain such as streamline curvature, system rotation and streamtube contraction ratio have been known to have significant effects on the structure of turbulence as discussed by Bradshaw (1973), Johnston (1970) and Sharma and Graziani (1982). A solution of Reynolds stress transport equations is actually needed to resolve these effects properly, but the development of closure models for these equations is still in infancy. Simpler models are, therefore, needed to capture the effects of these flow features for engineering application. Modifications to turbulence model developed in the present program are based on the work of Sharma and Graziani (1982), who utilized Towsend's hypothesis (1956) which states that the turbulent kinetic energy and Reynolds shear stress are related by a constant in the inner part of the turbulent boundary layer. One can, therefore, capture these effects of extra rates of strain by interrogating the transport equation for turbulent kinetic energy and the total Reynolds shear stress. Modified turbulent viscosity can be fairly accurately estimated as the ratio of the generation terms for the Reynolds shear stress equation to the production terms for the turbulent kinetic energy transport equation. No empirical constant is required in this approach and it yields fairly good results for flows in the presence of extra rates of strain.

For incompressible flows production terms for the three normal stresses and the turbulent kinetic energy are given below in Cartesian coordinate with rotation in the axial, tangential and normal direction:

$$P\left(\frac{\overline{u^2}}{2}\right) = -\overline{u^2}\,\frac{\partial U}{\partial x} - \overline{uv}\left(\frac{\partial U}{\partial y} - 2\Omega z\right) - \overline{uw}\left(\frac{\partial U}{\partial z} + 2\Omega y\right) \tag{3.3.16}$$

$$P\left(\frac{\overline{v^2}}{2}\right) = -\overline{v^2}\,\frac{\partial V}{\partial y} - \overline{uv}\left(\frac{\partial V}{\partial x} + 2\Omega z\right) - \overline{vw}\left(\frac{\partial V}{\partial z} - 2\Omega x\right) \tag{3.3.17}$$

$$P\left(\frac{\overline{w^2}}{2}\right) = -\overline{w^2}\ \frac{\partial W}{\partial z} - \overline{vw}\left(\frac{\partial W}{\partial y} + 2\Omega x\right) - \overline{uw}\left(\frac{\partial W}{\partial x} - 2\Omega y\right) \qquad (3.3.18)$$

Adding the above three equations yields production terms for the turbulent kinetic energy ($K = \frac{\overline{u^2}}{2} + \frac{\overline{v^2}}{2} + \frac{\overline{w^2}}{2}$):

$$P(K) = -\overline{u^2}\frac{\partial U}{\partial x} - \overline{v^2}\frac{\partial V}{\partial y} - \overline{w^2}\frac{\partial W}{\partial z} - \overline{uv}\left(\frac{\partial U}{\partial y} + \frac{\partial V}{\partial x}\right) - \overline{vw}\left(\frac{\partial V}{\partial z} + \frac{\partial W}{\partial y}\right) - \overline{uw}\left(\frac{\partial U}{\partial z} + \frac{\partial W}{\partial x}\right) \qquad (3.3.19)$$

It is apparent from the above four equations that whereas each individual normal stress component is affected by rotation ($\Omega x, y, z$), total turbulent kinetic energy is unchanged indicating that turbulence models based on turbulent kinetic energy transport equation would fail to capture the effect of rotation explicitly. Since rotation terms change the distribution of energy in various components, they could either enhance or reduce mixing and, therefore, losses and heat loads in turbomachines.

Generation terms for the diagonal components of Reynolds shear stress are given below to show a more complex effect of rotation in turbulent flows, effects of streamtube contraction and streamline curvatures are also present in these terms but these are not apparent due to the use of the coordinate system:

$$G(\overline{uv}) = \overline{uv}\left(\frac{\partial U}{\partial x} + \frac{\partial V}{\partial y}\right) + \overline{v^2}\left(\frac{\partial U}{\partial y} + \frac{\partial V}{\partial x}\right) + \left(\overline{u^2} - \overline{v^2}\right)\left(\frac{\partial V}{\partial x} + 2\Omega z\right) + \overline{vw}\left(\frac{\partial U}{\partial z} + 2\Omega y\right) + \overline{uw}\left(\frac{\partial V}{\partial z} - 2\Omega x\right) \qquad (3.3.20)$$

$$G(\overline{uw}) = \overline{uw}\left(\frac{\partial U}{\partial x} + \frac{\partial W}{\partial z}\right) + \overline{u^2}\left(\frac{\partial U}{\partial z} + \frac{\partial W}{\partial x}\right) + \left(\overline{w^2} - \overline{u^2}\right)\left(\frac{\partial W}{\partial x} + 2\Omega y\right) + \overline{vw}\left(\frac{\partial U}{\partial y} - 2\Omega z\right) + \overline{uv}\left(\frac{\partial W}{\partial y} + 2\Omega x\right) \qquad (3.3.21)$$

$$G(\overline{vw}) = \overline{vw}\left(\frac{\partial V}{\partial y} + \frac{\partial W}{\partial z}\right) + \overline{w^2}\left(\frac{\partial W}{\partial y} + \frac{\partial V}{\partial z}\right) + \left(\overline{v^2} - \overline{w^2}\right)\left(\frac{\partial W}{\partial y} + 2\Omega x\right) + \overline{uw}\left(\frac{\partial V}{\partial x} + 2\Omega z\right) + \overline{uv}\left(\frac{\partial W}{\partial x} - 2\Omega y\right) \qquad (3.3.22)$$

A generation term for the magnitude of the diagonal stress (defined as $\tau = \sqrt{\overline{uv}^2 + \overline{vw}^2 + \overline{uw}^2}$) can be deduced from the above three equations by multiplying equations (3.3.20), (3.3.21) and (3.3.22) by $\overline{uv}/\tau, \overline{uw}/\tau$ and $\overline{vw}/\tau$, respectively, as shown below:

$$G(\tau) = TERM\ ① + TERM\ ② + TERM\ ③ \qquad (3.3.23)$$

where

$$TERM\ ① = \frac{\left(\overline{uv}\ \overline{v^2} + \overline{uw}\ \overline{vw}\right)}{\tau}\left(\frac{\partial U}{\partial y} + \frac{\partial V}{\partial x}\right) + \frac{\left(\overline{uw}\ \overline{u^2} + \overline{uv}\ \overline{vw}\right)}{\tau}\left(\frac{\partial W}{\partial x} + \frac{\partial V}{\partial z}\right) + \frac{\left(\overline{vw}\ \overline{w^2} + \overline{uv}\ \overline{uw}\right)}{\tau}\left(\frac{\partial V}{\partial z} + \frac{\partial W}{\partial y}\right)$$

$$TERM\ ② = \frac{\overline{uv}\ \left(\overline{u^2} - \overline{v^2}\right)}{\tau}\left(\frac{\partial V}{\partial x} + 2\Omega z\right) + \frac{\overline{uw}\ \left(\overline{w^2} - \overline{u^2}\right)}{\tau}\left(\frac{\partial V}{\partial z} + 2\Omega y\right) + \frac{\overline{vw}\ \left(\overline{v^2} - \overline{w^2}\right)}{\tau}\left(\frac{\partial W}{\partial y} + 2\Omega x\right)$$

$$TERM\ ③ = \frac{\overline{uv^2}}{\tau}\left(\frac{\partial U}{\partial x} + \frac{\partial V}{\partial y}\right) + \frac{\overline{uw^2}}{\tau}\left(\frac{\partial U}{\partial x} + \frac{\partial W}{\partial z}\right) + \frac{\overline{vw^2}}{\tau}\left(\frac{\partial V}{\partial y} + \frac{\partial W}{\partial z}\right)$$

TERM ② in the above equation represents a generation of Reynolds shear stress due to the effects of rotation and curvature. This turbulence generation mechanism is not present in the turbulent kinetic energy production terms as indicated by the absence of rotation terms in equation (3.3.19).

TERM ③ represents the generation of Reynolds shear stress due to the effect of streamtube convergence and divergence.

TERM ① represents the direct generation of Reynolds shear stress. It was pointed out by Bradshaw (1968) that the generation of Reynolds shear stress is also affected by the pressure–velocity correlation terms present in the complete Reynolds shear transport equation. In the absence of extra rates of strain for equilibrium turbulent boundary layer flows, generation of turbulence given by equation (3.3.19) and by *TERM* ① modified to account for pressure–velocity correlation have to be the same, therefore, direct generation of Reynolds shear stress can be written as:

$$\textit{TERM}\ ① \ + \ \text{Extra terms from pressure} - \text{velocity correlation} = \frac{\tau}{K} P(K) \tag{3.3.24}$$

Generation of the diagonal component of Reynolds shear stress can now be written as:

$$\begin{aligned} G(\tau) &= \frac{\tau}{K} P(K) + (\textit{TERM}\ ② + \textit{TERM}\ ③) \\ &= \frac{\tau}{K} P(K) \left[1 + \frac{K}{\tau} \frac{(\textit{TERM}\ ② + \textit{TERM}\ ③)}{P(K)} \right] \end{aligned} \tag{3.3.25}$$

This equation shows that production terms in the turbulent kinetic energy equation or other turbulence mixing equations must be modified to properly account for the effects of extra rates of strain. These modifications have invariably been conducted by using ad hoc expressions, present analysis indicates that these can be exactly deduced from turbulence transport equations.

In equilibrium turbulent boundary layer flows, production and dissipation terms in the turbulent kinetic energy transport equation balance each other. Dissipation and generation terms in the Reynolds shear stress transport equation must, therefore, also balance each other in equilibrium boundary layer flows. Using Bradshaw's (1968) model for dissipation terms, the behavior of Reynolds shear stress transport equation can be expressed as:

$$\begin{aligned} G(\tau) &= \frac{\tau}{K} \ (\text{Dissipation}) \\ &= \frac{\tau}{K} \frac{(\tau)^{3/2}}{L_0} \end{aligned} \tag{3.3.26}$$

where

L_0 = dissipation length

By substituting equation (3.3.26) in equation (3.3.25) results in:

$$P(K)\left[1 + \frac{K}{\tau}\,\frac{(TERM\ ② + TERM\ ③}{P(K)}\right] = \frac{\tau^{3/2}}{L_0} \tag{3.3.27}$$

or

$$\tau = \left[L_0\,\frac{P(K)}{\tau}\right]^2\left[1 + \frac{K}{\tau}\,\frac{(TERM\ ② + TERM\ ③}{P(K)}\right]^2 \tag{3.3.28}$$

In the absence of *TERM* ② and *TERM* ③ , it can be shown that

$$\tau \equiv \left[-\overline{u\mu_j}\right] = \mu_T\left(\frac{\partial Ui}{\partial xj} + \frac{\partial Uj}{\partial xi}\right) \tag{3.3.29}$$

μ_T in this equation can, therefore, be modified to account for *TERM* ② and *TERM* ③ as:

$$\mu_{T_m} = \mu_T\left(1 + \frac{2K}{\tau}\,RiQ,R + \frac{2K}{\tau}\,Ri_{3D}\right) \tag{3.3.30}$$

where

μ_{T_m} = modified turbulent viscosity

μ_T = turbulent viscosity from Baldwin – Lomax model discussed in Section 3.3.1

and

RiQ,R = Richardson number for rotation & curvature = $\dfrac{\text{TERM ②}}{\text{P(K)}}$

Ri_{3D} = Richardson number for three – dimensionality = $\dfrac{\text{TERM ③}}{\text{P(K)}}$

Impact of these modifications can be illustrated in boundary layer flows for two–dimensional rotating ducts and at the line of symmetry in cascades.

In two–dimensional boundary layers experimental data (Klebanoff (1954)) indicates that $\frac{K}{\tau} = \frac{10}{3}$, $\overline{u^2} = K, \overline{v^2} = 0.4K$ and $\overline{w^2} = 0.6K$.

In two–dimensional rotating ducts, equation (3.3.26) simplifies to:

$$\mu_{T_m} = \mu_T\left(1 + \frac{40}{3}\,\frac{2\Omega z}{\frac{\partial U}{\partial y}}\right)$$

which is almost exactly the same as deduced by Johnston (1971) from experimental data.

For boundary layer flows at the line of symmetry equation (3.3.26) simplifies to:

$$\mu_{T_m} = \mu_T\left(1 - \frac{20}{3}\,\frac{\frac{\partial W}{\partial z}}{\frac{\partial U}{\partial y}}\right)$$

which was used by Sharma & Graziani (1982) to yield good estimates of heat loads on the suction side of a turbine cascade at the mid–span as indicated in Figure 3.3.2.

Modification to turbulent viscosity suggested by equation (3.3.26) are generic and can be implemented in one– or two–equation turbulence models almost exactly in the form presented by the equation.

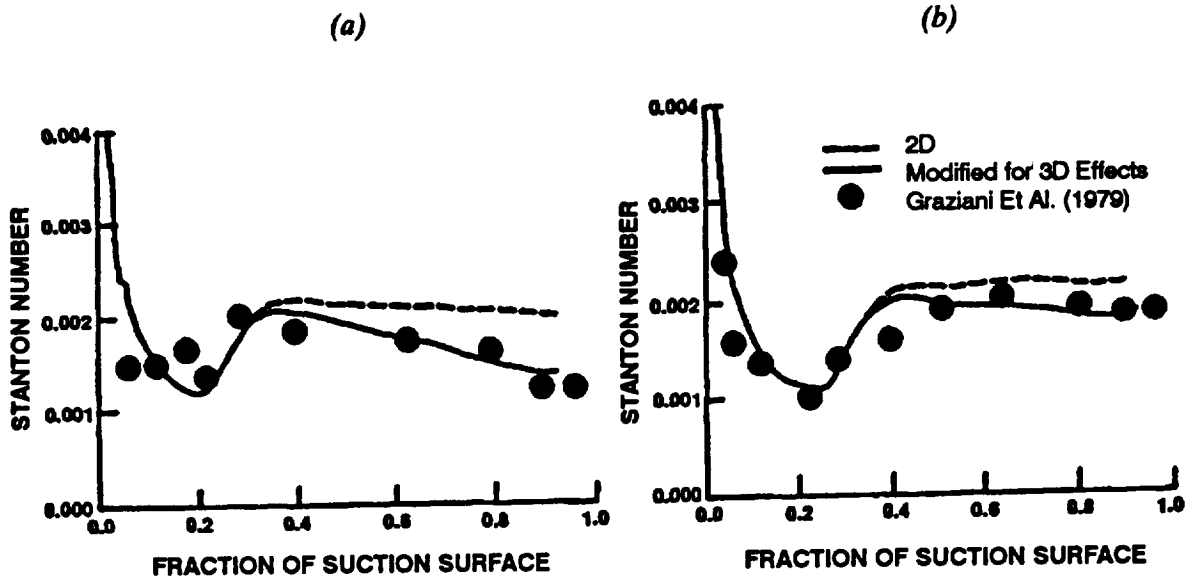

Figure 3.3.2 *Turbulence Model Modified to Account for Extra Rates of Strain (Sharma & Graziani (1982)) Yields Good Estimate of Midspan Stanton Number on Langston's Turbine Airfoil.*
(a) Nominal Inlet Boundary Layer to the Cascade.
(b) Thin Inlet Boundary Layer to the Cascade (Refer to Figure 2.3.2 for the Magnitudes of Flow Convergence at the Cascade Airfoil Midspan).

3.3.4 Transition Model

Although all boundary layer flows start in a laminar mode, they become turbulent by passing through a transitional region, the regions of laminar and transitional flows are only significant in turbomachinery operating under a Reynolds number of about one million. For rocket applications Reynolds numbers are invariably larger than ten million and these applications transition plays a small role on the overall development of the viscous flows. A knowledge of the transitional region was, however, essential during the code verification and application part of this program since most of the available data used in these tasks were acquired at moderate Reynolds numbers where laminar and transitional regions were significant. Transition models were, therefore, implemented in the CFD code to accomplish the defined tasks.

In three–dimensional flow situations, the transition from the laminar to the turbulent state was assumed to be instantaneous. The transition point was specified along grid lines to simulate the physics of the flowfield.

For two–dimensional and unsteady flow computations the onset of transition was determined by using a correlation based on the work of Mayle (1991) and Hourmuziadis (1990). According to this correlation, onset of transition occurs when the local boundary layer momentum loss thickness Reynolds number exceeds a critical Reynolds number.

$$R\theta c = 40/\sqrt{Tu} \tag{3.3.24}$$

where

$R\theta c$ = Critical Reynolds number.

and

Tu = Local turbulence level which needs to be specified as input to the computer code for single airfoil row or for the first row of the stage, it is automatically calculated for the following rows.

Numerical computations are conducted by modifying the turbulent viscosity in the transitional region by using the approach suggested by Sharma (1987).

$$\begin{aligned} \mu_{TM} &= F^{*}\mu_T \\ \mu_{TM} &= \text{Modified turbulent viscosity} \\ \mu_T &= \text{Turbulent viscosity calculated in Section 3.3.1} \\ F &= \text{Intermittency factor having a value of zero in laminar regions and a value of 1 in fully turbulent region} \\ &= 1 - \exp\left(- (R\theta^{2.5} - R\theta c^{2.5})/R\theta c^{2.68}\right) \\ R\theta &= \text{Reynolds number based on momentum loss thickness of the boundary layer.} \end{aligned} \tag{3.3.25}$$

3.4 Boundary Conditions

3.4.1 Inlet Boundary Condition

In the following expressions, u, v, w are velocities in the x−, y−, and z−directions, p is static pressure, ϱ is density, c is speed of sound, s is entropy, and h is total enthalpy, α is arctan(v/u) and ϕ is arctan(w/u); boldface type indicates a new updated value, subscript 0 indicates an initial value, and subscripts of 1 and 2 indicate a current value at inlet and one point downstream of inlet, respectively.

The following boundary conditions were available in the original version of the Rai code (Rai (1989)):

$$\text{Reimann invariant 1} = R_1 = u_0 + \frac{2}{\gamma - 1}\left(\frac{\sqrt{\gamma p_0}}{\sqrt{\varrho_0}}\right) \tag{3.4.1}$$

$$\text{Reimann invariant 2} = R_2 = u_2 - \frac{2}{\gamma - 1}\left(\frac{\sqrt{\gamma p_2}}{\sqrt{\varrho_2}}\right) \tag{3.4.2}$$

$$\begin{aligned} u_1 &= (R_1 + R_2)/2 \\ v_1 &= v_0 \\ w_1 &= w_0 \end{aligned} \tag{3.4.3}$$

$$c_1 = \frac{\gamma - 1}{4}(R_1 - R_2) \tag{3.4.4}$$

$$s_1 = s_0 \tag{3.4.5}$$

$$\begin{aligned} \varrho_1 &= \left(\frac{c_1}{\gamma s_1}\right)^{1/(\gamma-1)} \\ p_1 &= \frac{\varrho_1 c_1^2}{\gamma} \end{aligned} \tag{3.4.6}$$

The following modifications were made to, in effect, hold inlet total pressure, in addition to reducing the stiffness of the boundary condition:

First define the variable h' as follows:

$$h' = \frac{2c^2}{\gamma - 1} + u^2 = 2h - (v^2 + w^2) \tag{3.4.7}$$

Assuming $h_1 = h_0$, that is, inlet total enthalpy is held at its initial value,

$$h'_1 = 2h_0 - (v_1^2 + w_1^2) \tag{3.4.8}$$

It can be shown that (3.4.8), together with the assumption

$$u_1 - \frac{2c_1}{\gamma - 1} = u_2 - \frac{2c_2}{\gamma - 1} = R_2\,, \tag{3.4.9}$$

yields:

$$\frac{2}{\gamma - 1}\left(1 + \frac{2}{\gamma - 1}\right) c_1^2 + \frac{4R_2}{\gamma - 1}\, c_1 - \left(h'_1 - R_2^2\right) = 0 \tag{3.4.9a}$$

This is a quadratic equation for c_1 that can be solved with the quadratic formula. Then,

$$u_1 = R_2 + \frac{2c_1}{\gamma - 1} \tag{3.4.10}$$

$$v_1 = u_1 \tan(\alpha_0)$$
$$w_1 = u_1 \tan(\phi_0)$$

$$s_1 = s_0$$

$$\varrho_1 = \left(\frac{c_1}{\gamma s_1}\right)^{1/(\gamma-1)} \tag{3.4.11}$$

$$p_1 = \frac{\varrho_1 c_1^2}{\gamma} \tag{3.4.12}$$

3.4.2 Surface Boundary Conditions

The surface boundary conditions in Rai code (Rai (1989)) were a first–order adiabatic wall condition, that is, in addition to the no–slip condition for velocity, zero normal pressure and density gradients were imposed. Options were added to specify either wall temperature or heat flux on the surfaces, which modified the density condition.

The specified wall temperature condition that was implemented was developed by Griffin (1990). It requires an additional input file containing adiabatic wall temperatures on the surfaces, and the wall temperature is prescribed as a percentage of the adiabatic wall temperature. The percentage is input in the RAIJOB shell script. The adiabatic wall temperature file can be obtained by running RAI3DS with the adiabatic wall condition; the file will get written out in routine WALTMP, which will also read the file if the option to specify wall temperature is chosen. The UNICOS jobstream will need modification to assign these files to the file environment.

The following is the derivation of the second–order density condition allowing specified heat flux. Here, Q is heat flux, k is the coefficient of thermal conductivity, R is the specific gas constant, T is temperature, p is static pressure, ϱ is density, and y is distance from the wall.

Assume

$$Q = -k\frac{dT}{dy} = -k\frac{d\left(\frac{p}{\varrho R}\right)}{dy} = \frac{-k\left(\frac{dp}{dy}\right)\varrho - p\left(\frac{d\varrho}{dy}\right)}{R\quad\varrho^2} \tag{3.4.13}$$

Assuming a zero normal pressure gradient, this yields

$$Q = \frac{kp}{R\varrho^2}\left(\frac{d\varrho}{dy}\right) \quad \Rightarrow \quad \frac{d\varrho}{dy} = \frac{\varrho^2 Q'}{p}, \quad \text{where } Q' = \frac{QR}{k} \tag{3.4.14}$$

Now assume that ϱ is some quadratic function of y, given by

$$\varrho = ay^2 + by + c \tag{3.4.15}$$

Then, values of ϱ at y1, y2, and y3 are given by the system

$$\begin{aligned} ay_1^2 + by_1 + c &= \varrho_1 \\ ay_2^2 + by_2 + c &= \varrho_2 \\ ay_3^2 + by_3 + c &= \varrho_3 \end{aligned} \tag{3.4.16}$$

Assuming y_1 is zero, that is, at the wall, the system reduces to

$$b = \frac{(\varrho_2 - \varrho_1)y_3^2 - (\varrho_3 - \varrho_1)y_2^2}{y_2y_3^2 - y_2^2y_3}$$

Differentiating the quadratic equation for ϱ,

$$\frac{d\varrho}{dy} = 2ay + b \qquad \Rightarrow \qquad \frac{d\varrho}{dy} = b \quad \text{at the wall.}$$

From the previous expression for $\frac{d\varrho}{dy}$,

$$\frac{(\varrho_2 - \varrho_1)y_3^2 - (\varrho_3 - \varrho_1)y_2^2}{y_2y_3^2 - y_2^2y_3} = \frac{\varrho^2Q'}{p}$$

Algebraically solving for ϱ_1,

$$\varrho_1 = \frac{\varrho_2y_3^2 - \varrho_3y_2^2}{y_3^2 - y_2^2} - \frac{\varrho^2Q'(y_2y_3^2 - y_2^2y_3)}{p(y_3^2 - y_2^2)} \quad . \tag{3.4.17}$$

The values of p and ϱ at y_2 are used in the implementation of the condition. To define the value of Q' (note the solver will expect the given heat flux value to be properly nondimensionalized and to contain the factors of R and k), divide the dimensional Q by the dimensional k, and use a value of 1.0 for R to be consistent with the solver's nondimensionalization scheme. This will result in a value with units of degrees over length. Divide the resultant value by the inlet total temperature and convert the remaining length unit to inches to obtain the value of Q' in inches. This is what should be input to the RAIJOB shell script as discussed by Belford (Appendix A).

4. CODE VERIFICATION

The predictive capability of the numerical solution procedure (code) can be verified by comparing the results from the code with:

- Results from exact calculation methods for an unsteady multistage turbomachine
- A complete set of unsteady experimental data for a multistage turbomachine
- A series of experimental data set from benchmark quality experiments which simulate various aspects of multistage turbomachines.

Exact calculation methods for an unsteady multistage turbomachine are not yet available. In addition, a complete set of experimental unsteady data for a realistic turbomachine is also not available. The verification of the code in the present program was, therefore, conducted by comparing its predictions with data from benchmark quality experiments which simulated pertinent aspects of multistage turbomachines. These comparisons, discussed below, clearly demonstrate that the code provides accurate estimates of loadings, losses and heat loads for airfoil rows both in a steady and in an unsteady flow environment. This indicates that the code will provide accurate and reliable estimates of flow fields in a multistage turbomachine and it can be used in the design process to improve the performance and durability of turbopumps used in the rocket propulsion system.

4.1 Verification of the 2D Steady Aspect of the Code

Predictive capabilities of the code in a two-dimensional steady flow environment were verified by comparing theoretical predictions with experimental data obtained at the mean section of three linear cascades and two airfoil rows in a stage environment. Although flow through the airfoil rows in a stage environment is unsteady in a strict sense, simple assumptions are made to treat the flow as steady to demonstrate that steady flow assumptions do yield fairly accurate estimates of the performance and heat load characteristics of airfoil rows. This exercise indicates that appropriate assumptions permit cost effective evaluation of airfoil geometries in a multistage turbomachinery; computational resources required to execute a steady flow simulation are almost two orders of magnitudes lower than those needed to execute an unsteady flow simulation.

Representative grids used in the 2D code verification are shown in Figure 4.1.1. Nominally they contained 101*21 points in the inner grid and 50*31 points in the outer grid. An extensive evaluation of the effect of the grid points on the accuracy of loss and heat transfer predictions was conducted as part of work funded by the Naval Air Systems Command under NAVAIR Contract #N00140-88-C-0677 at the United Technologies Research Center by Dorney, Davis and Edwards (1992). Since the base CFD code in this effort was the same as that used in the present program, results from the NAVAIR Contract are directly applicable to the present program. The focus in the present program is to achieve engineering accuracy of the solution using minimum computer resources without compromising the technical results.

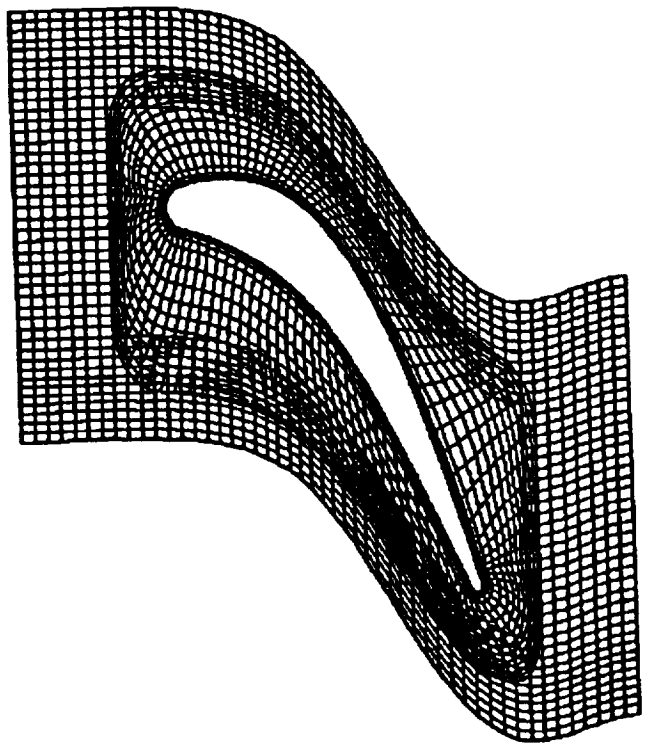

Figure 4.1.1 A RAI3DC Stator Grid

4.1.1 Kopper's Cascade

The first 2D test case termed as Kopper's cascade was tested in the United Technologies Research Center (UTRC) Variable Density Supersonic Plane Cascade Wind Tunnel. This cascade had an aspect ratio of 2.37 and pitch to chord ratio of 0.8925. The air entered the cascade with an inlet angle of 31.1 degrees and a Mach number of 0.4187. The Reynolds number based on axial chord (1.268 inches) and exit velocity was 500,000 and it was tested with a pressure ratio (exit static pressure/upstream total pressure) of 0.625. At the operating condition this airfoil had a separation bubble on the airfoil pressure side which affected the airfoil loading distribution on both the pressure and the suction sides. This configuration was used in the code verification process to demonstrate that accurate simulation of the transition process is essential to capture relevant features of the flow field. Theoretical calculations were conducted both in a transitional and a fully turbulent mode.

Theoretical predictions from the code are compared against experimental data for airfoil surface static pressure distributions (Figure 4.1.2). Results from transitional calculations exhibit excellent agreement with the experimental data while the fully turbulent calculations miss experimental behavior in the middle 40% of the airfoil.

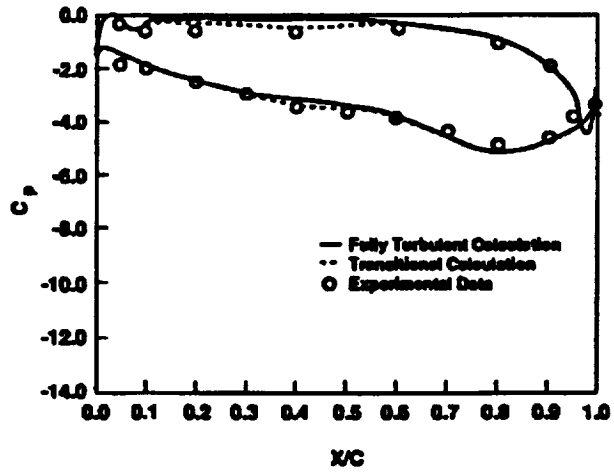

Figure 4.1.2 Airfoil Pressure Distribution for Kopper's Cascade

The nature of the flow near the surface of the airfoil can be more clearly highlighted through review of the streaklines around the airfoil streaklines generated from the fully turbulent calculations and the transitional calculations are shown in Figure 4.1.3. Both calculations predicted separation near the pressure side of the airfoil as indicated in this figure; however, the separation bubble predicted by the transitional calculation is larger and better defined, yielding better agreement with the pressure distribution data on both the pressure and the suction sides of the airfoil as indicated in Figure 4.1.2.

Figure 4.1.3 Predicted Streaklines Near Kopper's Airfoil.
(a) Fully Turbulent Calculation,
(b) Transitional Calculation.

4.1.2 Hodson's Cascade

The second 2–D test cascade termed as Hodson's Cascade was tested at the Whittle Laboratory at Cambridge University in U.K. This linear cascade contained seven airfoils with an aspect ratio of 3.0 and a pitch to chord ratio of 0.698. Test conditions involved ambient air entering the cascade at

approximately 58.89 ft/sec. The Reynolds number based on axial chord (3.2 inches) and exit velocity was 315,000. Additional details are given by Hodson (1983).

This airfoil had a small separation bubble on the airfoil suction side downstream of the maximum velocity point. Comparisons of predictions with experimental data for this cascade were made to verify the boundary layer and the transition prediction capability of the code. Calculations were conducted both in a transitional and a fully turbulent mode.

Measured airfoil surface static pressure coefficients are compared to theoretical predictions in Figure 4.1.4. Although both fully turbulent and transitional calculations show good agreement with the data, transitional calculations show slightly better agreement with the data on the airfoil suction side.

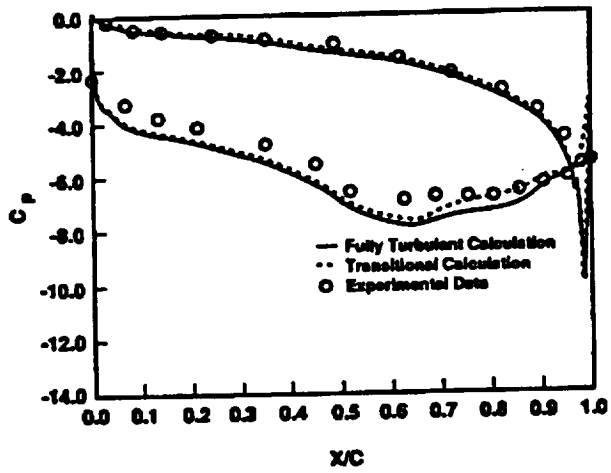

Figure 4.1.4 Airfoil Pressure Distribution for Hodson's Cascade

Measured boundary layer parameters on the airfoil suction side are compared to theoretical predictions in Figure 4.1.5. Plots of boundary layer momentum loss thickness are presented in Figure 4.1.5a. Results from transitional calculations exhibit excellent agreement with the data, showing improvement over fully turbulent calculations. Figure 4.1.5b shows a comparison of predicted and measured shape factor (displacement thickness/momentum loss thickness). Again results from transitional calculations agree more closely with the data, although the transitional results appear to overshoot the data in the trailing edge region. This overshoot is a result of the integration method used in calculating the integral parameters, the displacement and the momentum loss thicknesses. The definition of these parameters calls for integration along lines normal to the surface. The grid lines are normal to the surface near the airfoil but become quite skewed away from the surface at the trailing edge. A better method of integration would be to interpolate the results from the calculations onto a grid which has normal lines at the trailing edge before calculating the boundary layer integral parameters. Such a method would provide even better agreement with the experimental data than that indicated in Figure 4.1.5.

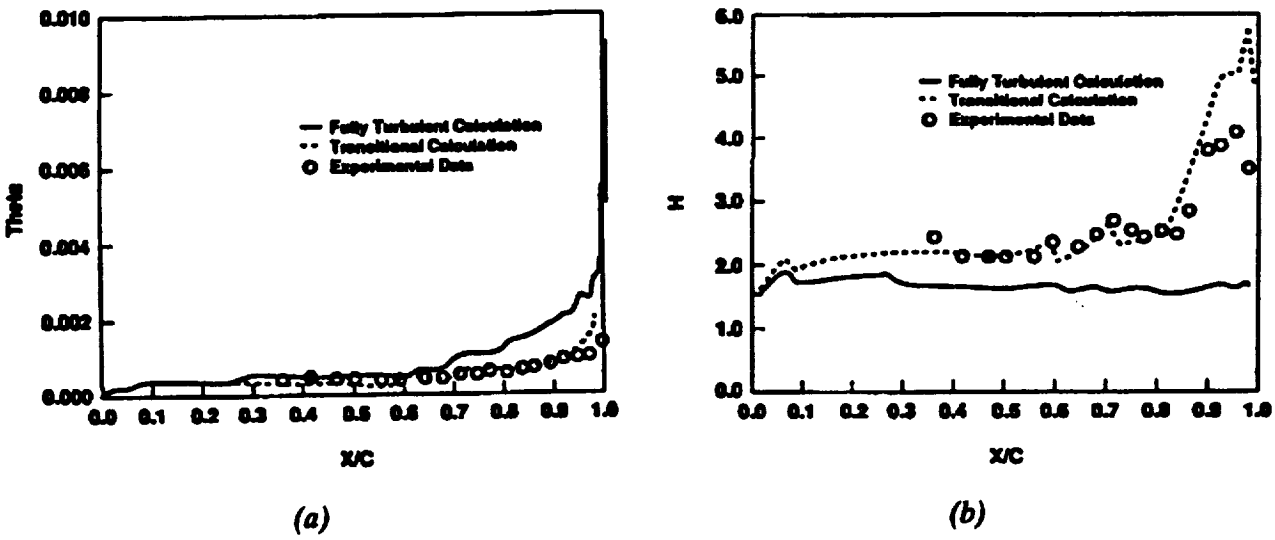

(a) (b)

Figure 4.1.5 *Boundary Layer Parameters for Hodson's Cascade.*
(a) Momentum Thickness,
(b) Shape Factor

4.1.3 Dring's Stator (Midspan)

The third 2D test configuration termed as Dring's Stator (midspan) was tested at UTRC as the first row of the 1½ stage large scale rotating rig (LSRR). Although flow in this airfoil row is affected both by three–dimensionality (due of radial pressure gradient) and unsteadiness (induced by relative movement of the downstream rotor), these effects are not very pronounced and a two–dimensional simulation yields fairly reasonable estimates of flow through the midspan of the airfoil. The aspect ratio for this annular cascade is 1.0118 and pitch to chord ratio at midspan of 1.3. Test conditions involved ambient air at approximately 75 ft/sec. The Reynolds number based on axial chord (6 inches) and exit velocity is 612,000. Additional details are given by Blair et al. (1988).

Detailed heat transfer data are available at the mean section of this airfoil. Comparisons of predictions with experimental data for this configuration were made to verify the heat load prediction capability of the code. Calculations were conducted both in a transitional and a fully turbulent mode.

Measured airfoil surface static pressure coefficients are compared to theoretical predictions in Figure 4.1.6 showing excellent agreement between data and predictions; both transitional and fully turbulent calculations yielded identical predicted values for static pressures.

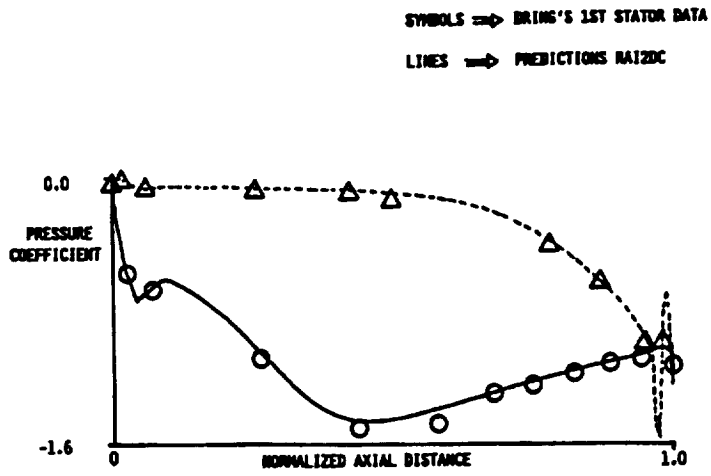

Figure 4.1.6 *2D Steady Version of the Code (RAI2DC) Developed to Verify the Code Against Basic Data*

Measured heat transfer coefficient (Stanton number) distributions along the midspan of the airfoil are compared theoretical predictions in Figure 4.1.7. Fully turbulent calculations are found to overestimate the heat transfer coefficients on the pressure side and over initial 60% of the suction side. The transitional calculations are, however, found to yield excellent agreement with the data over both sides of the airfoil. This figure illustrates need to model transitional nature of the boundary layer to accurately estimate heat loads on airfoil rows.

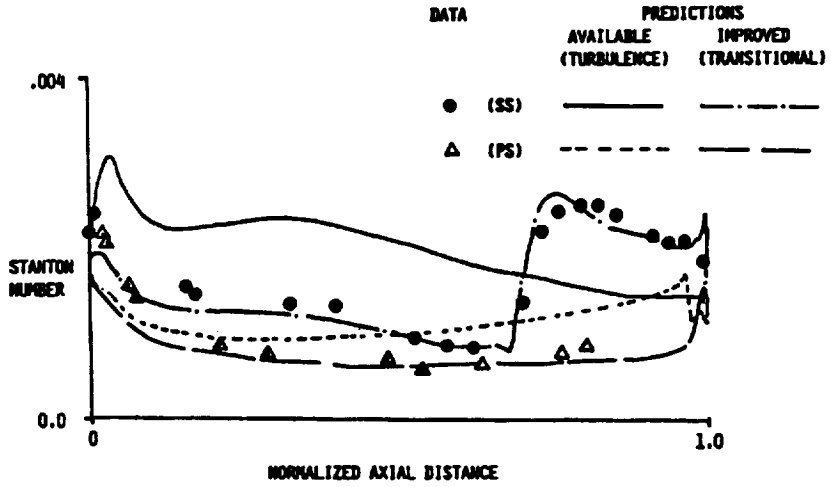

Figure 4.1.7 *Transition Model in the Code (RAI2DC) Provides Improved Estimates of Dring's Stator Airfoil Surface Stanton Number*

4.1.4 Dring's Rotor (Midspan)

The fourth 2D test configuration termed as Dring's rotor (midspan) was tested at the UTRC as the rotor in the 1½ stage LSRR. Flowfield on this airfoil is strongly affected by unsteadiness due to rotation of the rotor relative to the adjacent stators. Measured time–averaged experimental heat transfer and static pressure data on this airfoil, however, indicated that both of these parameters were unaffected when the rotor was placed at two distinct distances (15% and 65% axial chord) downstream of the first stator. This result showed that it was possible to simulate the flow through this airfoil by assuming a steady flow assumption. Only fully turbulent calculations were conducted because of the

presence of a relatively large inlet turbulence level generated by the upstream stator. The aspect ratio of this rotor is 0.9464 and pitch to chord ratio at midspan of 1.01. Test conditions involved almost ambient total pressure with an axial velocity of 75 ft/sec and a relative inlet angle of 40.6 degrees. The Reynolds number based on axial chord (6 inches) and exit velocity is 525,000. Additional details are given by Blair et al. (1988).

Measured airfoil surface static pressure coefficients are found to be in good agreement with theoretical predictions as shown in Figure 4.1.8(a). Fully turbulent calculations modified to account for free stream turbulence level and surface curvature are found to yield better agreement with the airfoil surface Stanton number (heat transfer coefficient) data (Figure 4.1.8(b)) than the base turbulence model available in the original Rai code. This result indicates that steady flow simulations can yield fairly reliable estimates of time–averaged loadings and heat loads on airfoil rows operating in an unsteady flow environment; appropriate modifications are, however, needed to the turbulence model to account for physical variables existing in the flowfield.

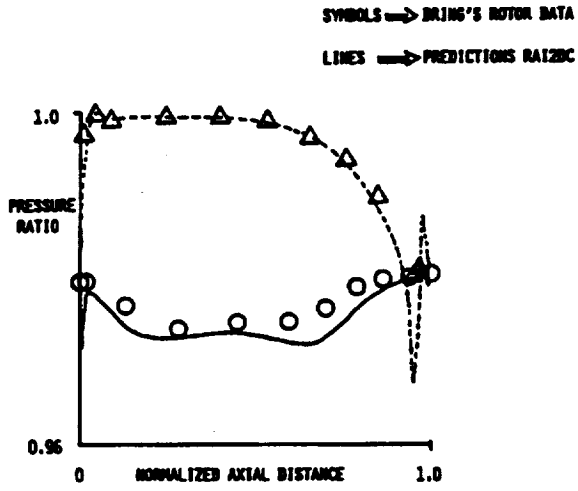

Figure 4.1.8(a) 2D Steady Cascade Version of the RAI Code (RAI2DC) Developed to Verify the Code Against Basic Data

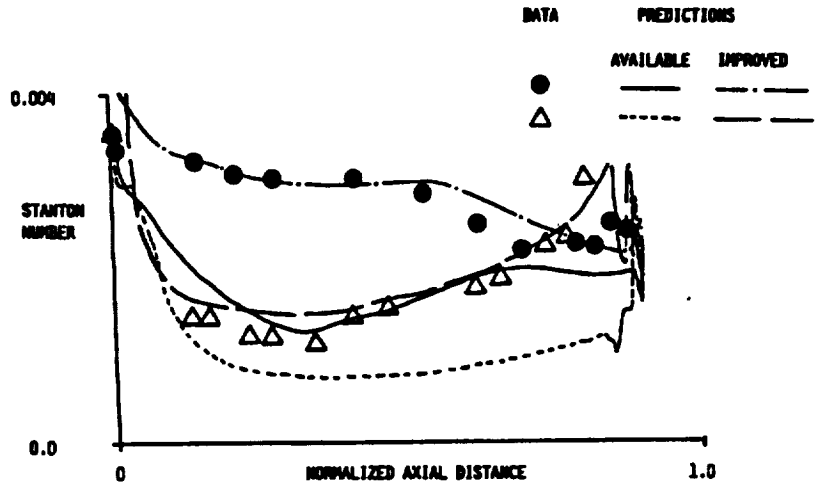

Figure 4.1.8(b) Improved Turbulence Model Yields Better Agreement with Rotor Stanton Number Data Than Available Model in the RAI Code

4.1.5 Transonic Cascade

The transonic flow prediction capability of the code was verified by comparing calculations to data obtained for a Pratt & Whitney Transonic Cascade. This cascade, tested in the UTRC Variable Density Plane Cascade Wind Tunnel, had an aspect ratio of 4 and pitch to chord ratio of 0.647. The air entered the cascade at an inlet angle of 48.5 degrees and a Mach number of 0.48. The Reynolds number based on axial chord (1.5 inches) and exit velocity was 760,000 and it was tested with a pressure ratio (exit static/upstream total pressure) of 0.528. Calculations were conducted both in a transitional and a fully turbulent mode. The shape of the airfoil and airfoil surface static pressure distributions are shown in Figure 4.1.9. Both transitional and fully turbulent calculations are shown to yield good agreement with the experimental data except in the trailing edge region. The inability of the code to predict pressures in the trailing edge region can be attributed to the thin layer assumptions used in the solution procedure. The calculations are, however, found to yield good estimates of lift on the airfoil indicating that it would provide accurate predictions of flows around transonic airfoils.

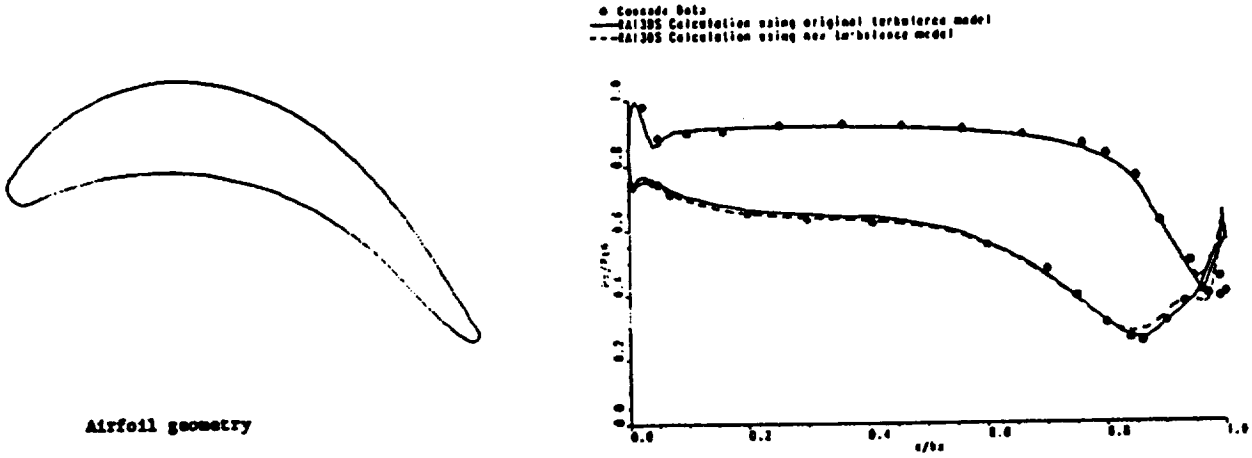

Figure 4.1.9 *Airfoil Geometry and Measured and Predicted Loadings on the Pratt & Whitney Transonic Cascade.*

4.1.6 Energy Efficient Engine (E^3) Turbine Lightweight Cascade

The ability of a 2D version of the Rai code [TOMCAT2 – Dorney, et al. (1992)] to compute flow for an airfoil over a range of incidence angles was verified by comparing its predictions against data obtained by Sharma et al. (1982). Results from this verification effort, conducted under NAVAIR Contract #N00140–88–C–0677 at UTRC, are shown here to demonstrate the predictive capabilities of the code. Grids used in these calculations, containing 101*71 points for the inner grid and 41*21 points for the outer grid are shown in Figure 4.1.10. Measured airfoil surface static pressure distributions compared to theoretical predictions from TOMCAT–2 and from VISCAS steady Navier–Stokes developed by Davis et al. (1986) in Figure 4.1.11 (a through f) over a range of incidence angles. Results indicate excellent agreement between data and predictions. Predicted total pressure losses for the airfoil are compared to the experimental data in Figure 4.1.12. Overestimates of losses at the design and the negative incidence angles are due to the assumption of fully turbulent flow in the analysis whereas in the experiment airfoil had large regions of laminar and transitional flows; turbulent flow at positive incidence angles is appropriate since leading edge separation bubbles induce transition in separation regions.

Comparisons of experimental data with theoretical predictions shown in this subsection clearly demonstrate that this code provides accurate estimates of airfoil loadings, losses and heat loads. The 2D predictive capabilities of the code are, therefore, verified.

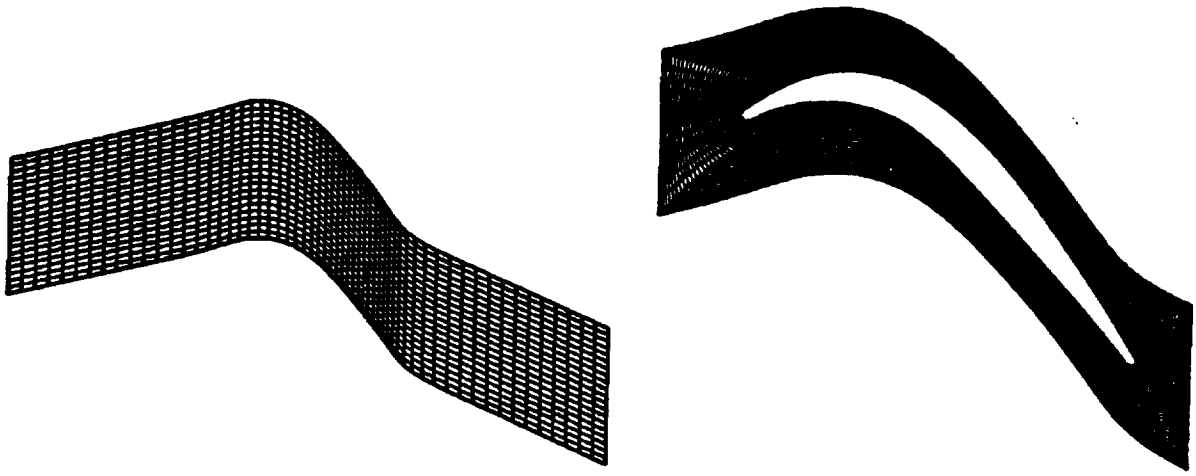

a: Outer H–grid *a: Inner O–grid*

Figure 4.1.10 Viscous Computational Grid for E^3 Lightweight Turbine Blade

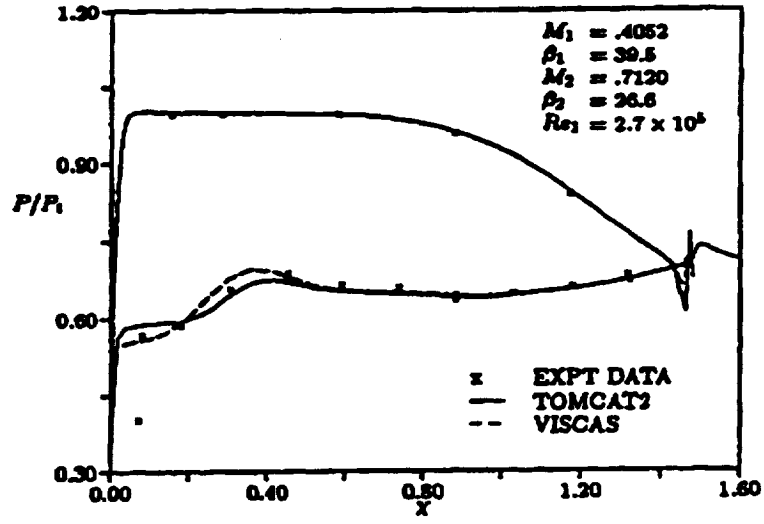

Figure 4.1.11a Pressure Distribution for E^3 Turbine Blade, 10° Incidence

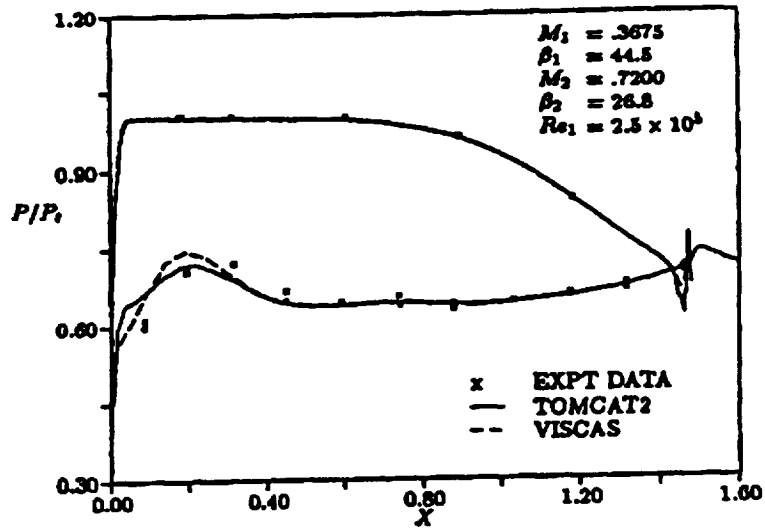

Figure 4.1.11b Pressure Distribution for E^3 Turbine Blade, 5° Incidence

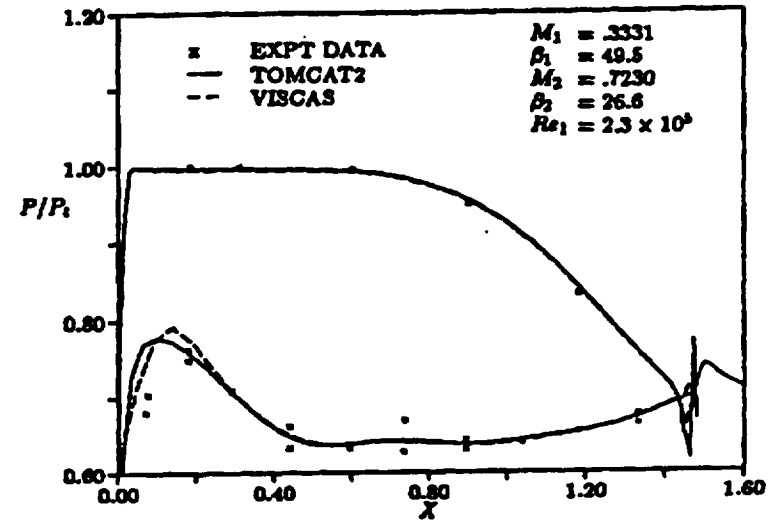

Figure 4.1.11c Pressure Distribution for E^3 Turbine Blade, 0° Incidence

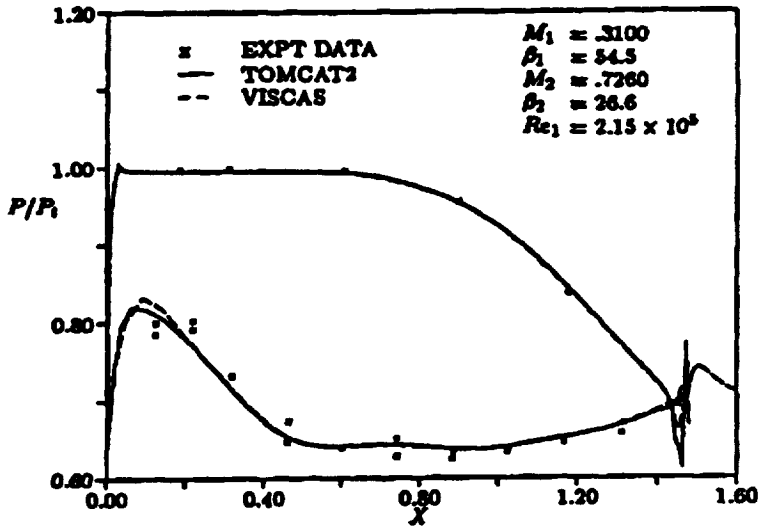

Figure 4.1.11d Pressure Distribution for E^3 Turbine Blade, $-5°$ Incidence

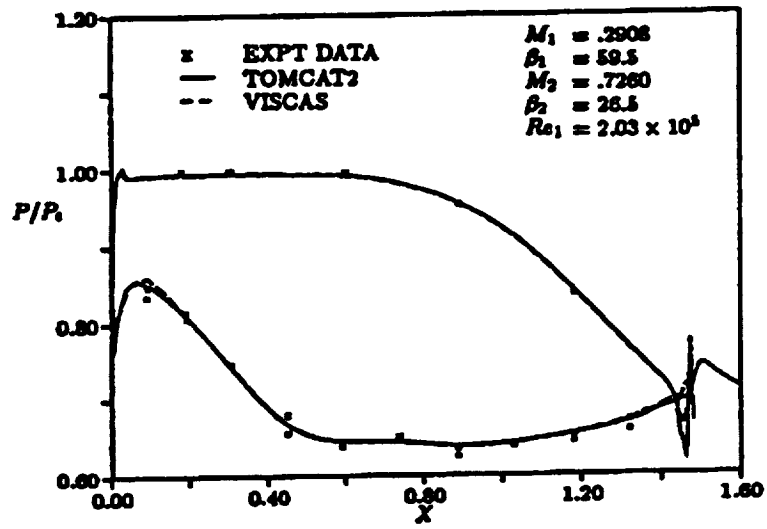

Figure 4.1.11e Pressure Distribution for E^3 Turbine Blade, $-10°$ Incidence

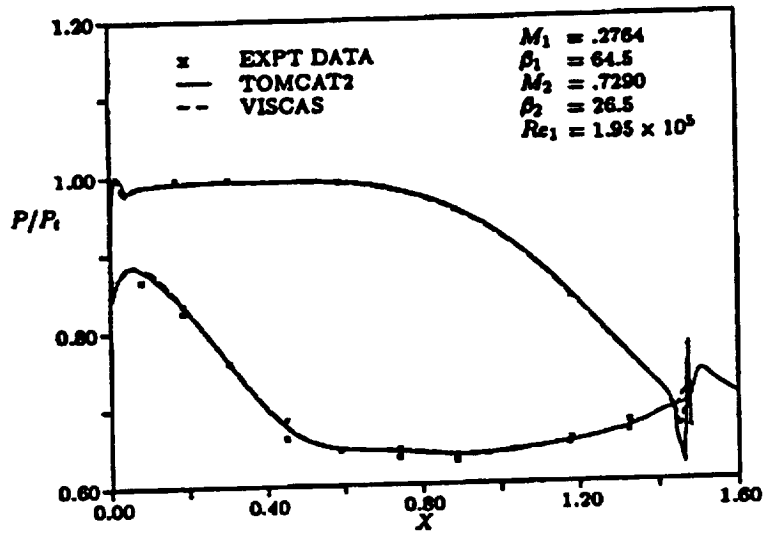

Figure 4.1.11f Pressure Distribution for E^3 Turbine Blade, −15° Incidence

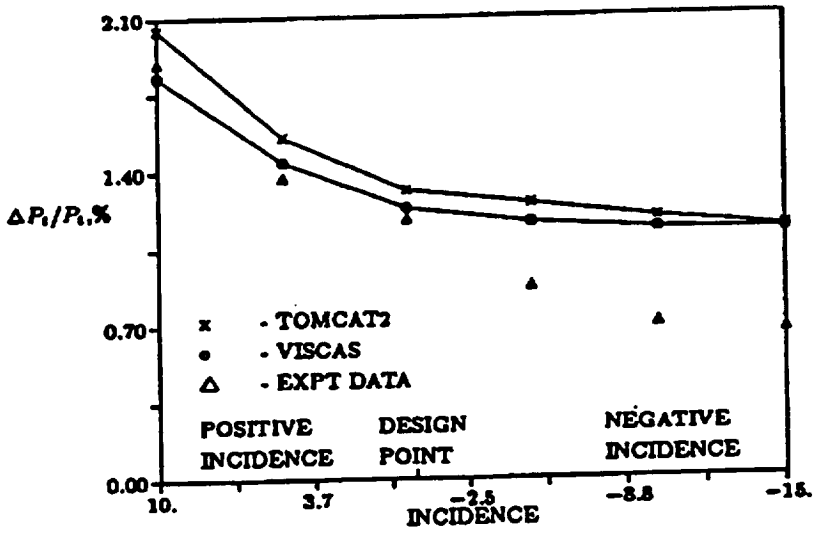

Figure 4.1.12 Total Pressure Loss Map for E^3 Lightweight Turbine Blade

4.2 Verification of the 3D Steady Aspect of the Code

Predictive capabilities of the code in a three−dimensional steady flow environment were verified by comparing theoretical predictions with benchmark quality experimental data obtained for an annular and a linear cascade. The emphasis of this effort was to demonstrate that the code provides reliable estimates of loadings, secondary flows and heat loads both on airfoil surfaces and endwalls. Studies were conducted to quantify the number of grid points on the pertinent features of the three−dimensional flowfields in cascades. Limitations of computer resources on the NASA MSFC CRAY−XMP computer did not permit establishment of a grid independent solution; further evaluation of the impact on the grid numbers on the flowfield was, therefore, conducted as a part of

the NAVAIR Contract #N00140–88–C–0677 at UTRC using a version of the Rai code (Dorney, et al. (1992)) and one of the linear cascade geometries used in the present program. Highlights of the results from the NAVAIR contract are also discussed to demonstrate the predictive capabilities of the code. The impact of the number of iterations on the predicted flowfield was also investigated to identify degree of convergence needed to establish ultimate levels of losses and heat loads. A detailed discussion on the 3D code verification effort conducted under the present program was presented by Griffin and Belford (1990) and Griffin, Belford, Sharma and Ni (1991) in international conferences.

4.2.1 Dring's Annular Cascade – UTRC LSRR First Stator

Detailed aerodynamic data consisting of spanwise airfoil loading distributions, midspan heat transfer coefficients, and flowfield information downstream of the stator are available for the UTRC LSRR first stator. Comparisons between predictions and experimental data are made to verify the heat transfer, secondary flows, and performance prediction capabilities of the code. The code was run in a 3–D annular mode, and calculations were performed assuming a transitional flow over the airfoil surfaces.

Airfoil Pressure Distributions. Comparisons of the calculated and experimentally measured airfoil pressure coefficients are shown in Figure 4.2.1 for the 2%, 50%, and 98% spanwise locations. The pressure coefficient is defined as

$$C_p = \frac{P - P_{T_R}}{1/2\rho_\infty \omega^2}$$

The agreement between the measured and computed results is excellent and is consistent with the results reported by Rai (1987).

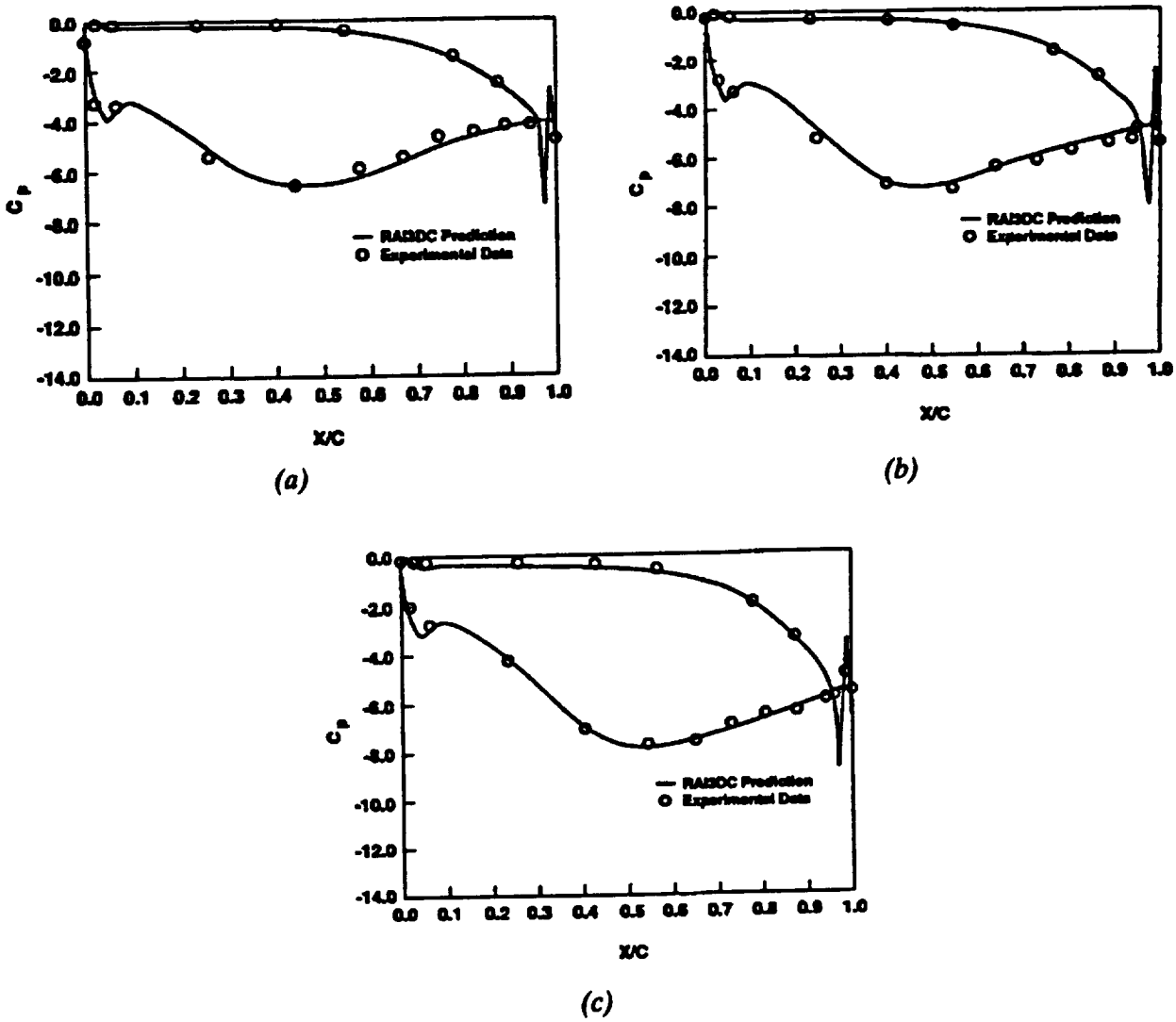

Figure 4.2.1 *Airfoil Pressure Distribution for UTRC LSRR First Stator for the (a) 2%, (b) 50%, and (c) 98% Spanwise Locations.*

Secondary Flows

Secondary flow structure can be seen in plots of exit total pressure contours. The vortex structures contain fluid from both the endwall and airfoil boundary layers, and consequently represent regions of low total pressure. Exit total pressure contours for the LSRR first–stage stator are shown in Figure 4.2.2. The total pressure was measured and computed at a location of 17% of the airfoil chord aft of the stator trailing edge. Figure 4.2.2a shows the experimentally measured contours. Figure 4.2.2b shows total pressure contours calculated using a fairly coarse outer grid (the outer grid's dimensions were 50 x 31 x 25) and an inlet total pressure that was constant across the span. The predicted results show qualitative features of the measured data. Both show the passage vortices, and the migration of these vortices toward the midspan. However, the computed vortices are closer to their respective endwalls than those that were measured. The measured and predicted low total pressure regions compare well in terms of local loss. The maximum local loss of the tip secondary flow was measured to be $C_{PTL} = -1.5$ and predicted to be -1.7. The maximum local loss of the hub

secondary flow was measured at −2.5 and computed to be −2.1. The calculation yielding the contours in Figure 4.2.2c used the same grid as in the previous calculation, but a measured (spanwise−varying) inlet total pressure was imposed. The inlet boundary layer was measured to be 8.3% of the span at the hub and 11.67% at the casing. The locations of the computed and experimentally measured hub passage vortices are now in closer agreement. The calculated casing passage vortex, although it has migrated further midspan, is still nearer the casing endwall than was measured. The shapes of the calculated passage vortices now more closely resemble the shapes of the measured vortices. The maximum local loss of the hub secondary flow was −2.2. Additional spanwise planes were added to the grid in an effort to better resolve the endwall effects (as was done by Madavan et al., 1991). Figure 4.2.2d shows the exit total pressure contours calculated using the refined grid (50 x 31 x 31) and the measured inlet total pressure profile. This calculation produced results with much greater resolution. The maximum local loss of the tip secondary flow was still predicted to be −1.7, and the predicted maximum local loss of the hub secondary flow was −2.3. The casing endwall vortex computed with the relatively fine grid is located further from the casing than its coarse grid counterpart, but nearer the casing than the measured vortex. Additional refinement in the spanwise direction is expected to further improve the calculated location of the casing vortex. However, due to computer memory limitations, additional spanwise refinement was not attempted during this study. One possible explanation for the discrepancy between prediction and measurement at the casing is the effect of concave curvature. Extra rates of strain introduced by normal pressure gradients, such as those due to surface curvature, have been shown to have large effects on viscous boundary layer development (Sharma and Graziani, 1982). The effect of surface curvature was not modeled in these calculations.

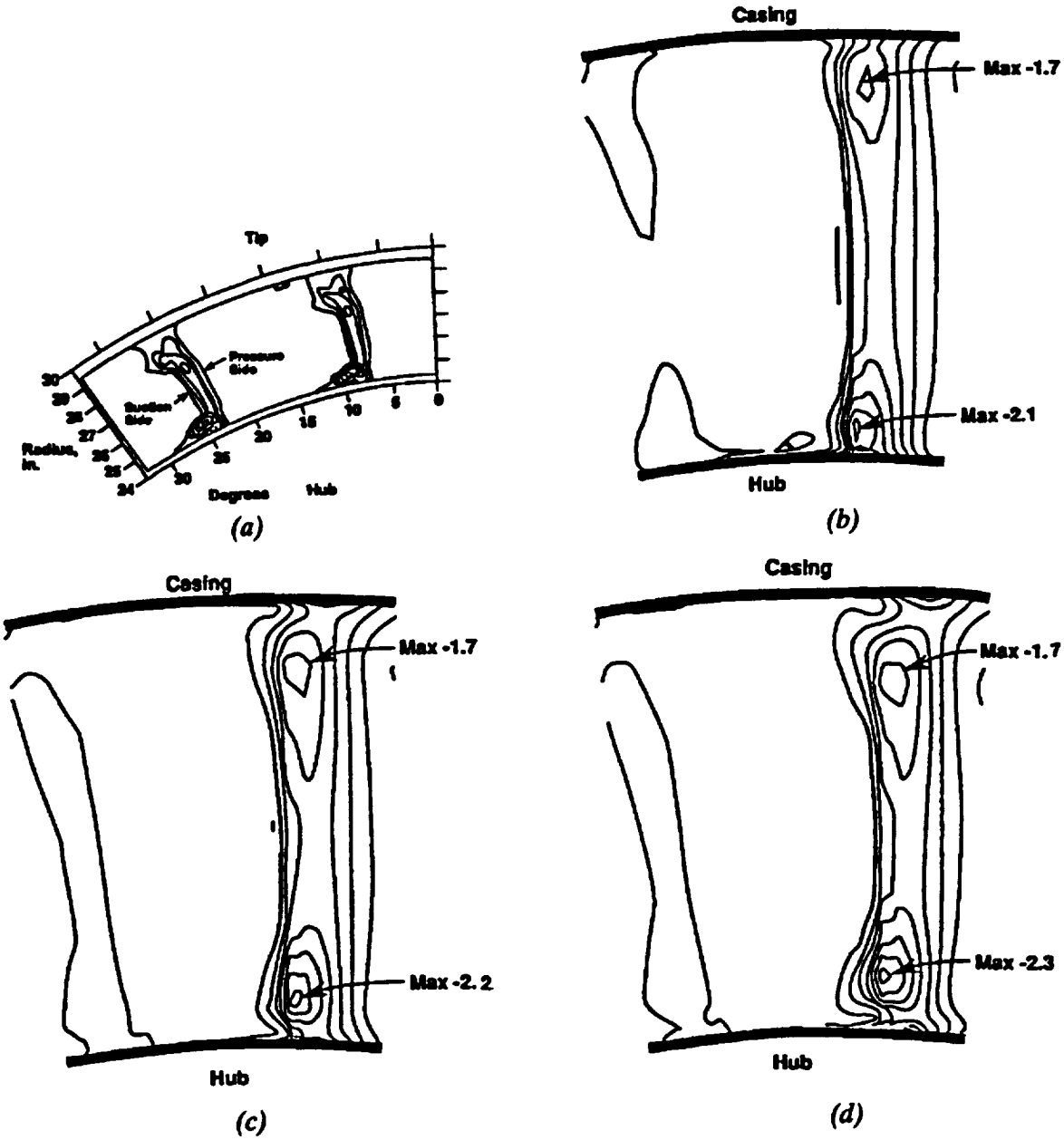

Figure 4.2.2 *Total Pressure Contours Downstream of the UTRC LSRR First Stator.*
(a) Experimentally Measured (Sharma, et al., 1985),
(b) Coarse Grid/Constant Inlet Total Pressure Calculation,
(c) Coarse Grid/Measured Inlet Total Pressure Calculation, and
(d) Spanwise–Refined Grid/Measured Inlet Total Pressure Calculation

Total Pressure Loss

A typical measure of performance for internal flows is the total pressure loss through the passage. Comparisons of computed and measured total pressure loss through the LSRR first–stage stator are presented in Figure 4.2.3. Total pressure loss coefficient is defined as

$$C_{pTL} = \frac{P_{TO} - P_{Te}}{1/2\rho_o\omega^2} \quad ,$$

where P_{Te} is circumferentially averaged at each spanwise plane. The stator "exit" total pressure was computed and measured at a location 17% aft of the stator trailing edge. Figure 4.2.3a shows total pressure loss calculated using the relatively coarse grid that was discussed in the secondary flows section. A total pressure that was constant across the span was imposed at the inlet. Corresponding experimental data is also shown. Features represented by the measured loss data are predicted by RAI3DC. Both the experimental and computed results display the maxima and minima associated with the endwall secondary flows, but the computed and measured magnitudes and locations of these features do not agree very well. That this would be the case was highly predictable after observing the trends of the computed exit total pressure contours. For the coarse grid/constant inlet total pressure calculation, both the hub and casing passage vortices are positioned closer to their respective endwalls than the experimentally indicated location. The measured casing boundary layer is much thicker than the computed boundary layer. The calculation and experimental data agree reasonably well in the midspan region (the pressure loss coefficient at midspan was measured to be 0.14 and predicted to be 0.17). In an attempt to more accurately model the stator boundary layers and reduce the artificial loss generated in the grid overlap region, the outer grid was refined in the circumferential direction as was suggested by Rangwalla (1989). For a two–dimensional calculation, Rangwalla increased the number of circumferential grid lines from 31 to 71 and produced a midspan total pressure loss coefficient of 0.13. Unfortunately, due to limitations in computer memory in this study, it was not feasible to increase the number of circumferential planes by more than 120% as was done by Rangwalla. Grids containing a 20%, 40%, and 60% increase in the number of circumferential planes were generated. However, calculations using each of these grids yielded negligible differences in pressure loss. Apparently, the grid must be greatly refined in the circumferential direction in order to achieve any benefit in total pressure loss prediction.

Predicted total pressure loss in Figure 4.2.3b was calculated using the coarse grid and the measured inlet total pressure profile. The magnitude of the computed and measured maxima and minima are now in close agreement (except at 20% span where the code fails to predict the low total pressure loss for all cases and actually predicts a decrease in total pressure loss from 20% span to midspan). The predicted location of the relatively high loss region associated with the hub passage vortex more closely matches the data than the results of constant inlet total pressure case. The predicted location of the loss region coinciding with the casing vortex moved slightly toward the midspan. The computed casing boundary layer appears to be slightly thinner than in the previous case. Figure 4.2.3c shows pressure loss coefficients calculated wit the spanwise–refined grid and measured inlet total pressure profile. The computed and measured magnitude and location of the relatively high loss region associated with the hub vortex are not in excellent agreement. The predicted location of the loss region corresponding to the casing endwall vortex, though it has moved further from the casing, still exhibited poor agreement with the measured location. The reason for this poor agreement is thought to be due to the effects of surface curvature, as was discussed in the secondary flows section.

It must be mentioned that predicting total pressure loss required a relatively large amount of computer time. Although the airfoil loading predictions were converged after the residuals had dropped three orders of magnitude, and the Stanton numbers were converged after a residual drop of four orders of magnitude, the total pressure loss calculation required a drop in residuals of six

orders of magnitude. In addition, when a spanwise–varying inlet total pressure profile was imposed, a very small time step (one–fifth the size of the time step used in a constant inlet total pressure calculation) had to be employed to enable the solution to converge. Naturally, using the small time step increased the run time.

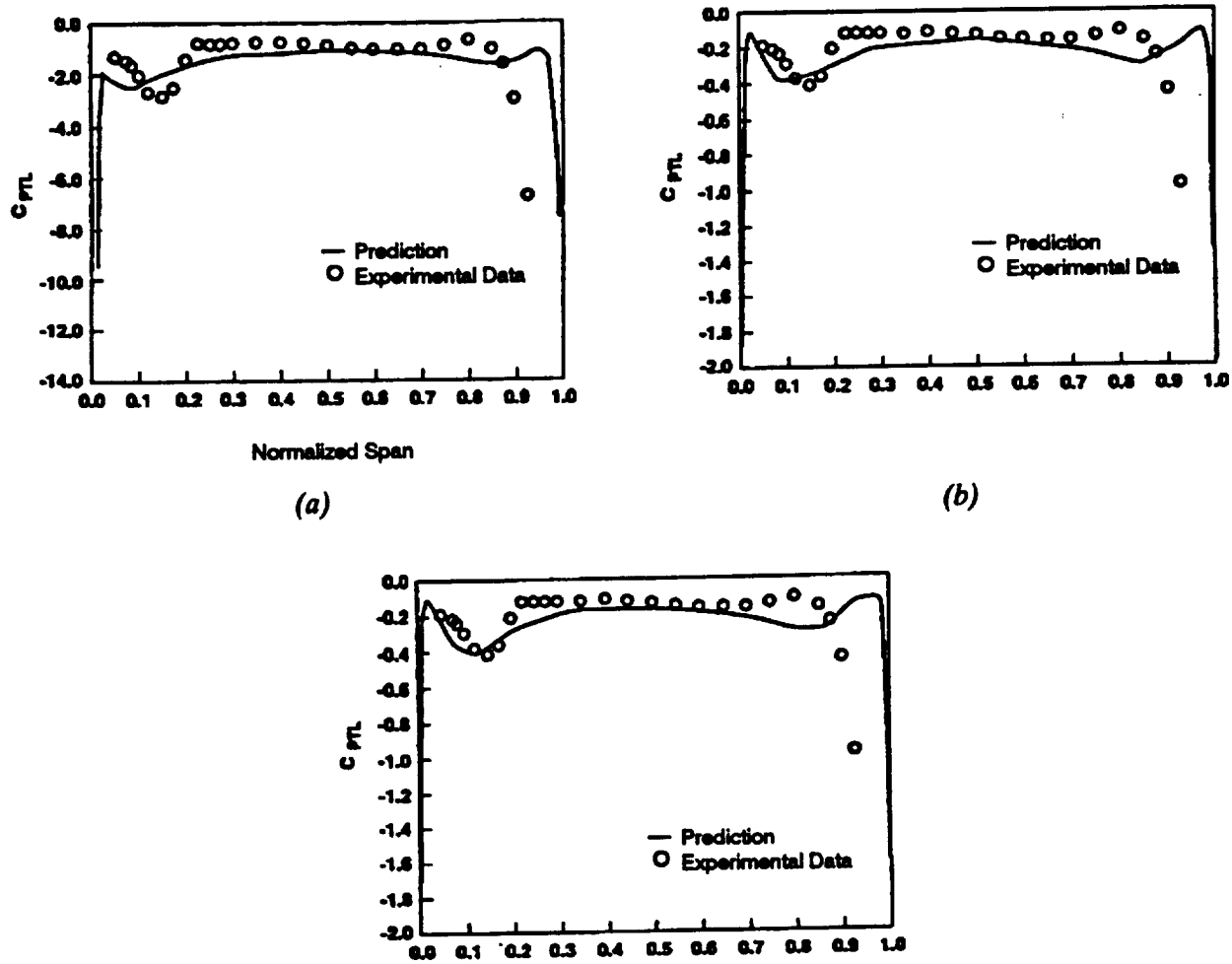

Figure 4.2.3 *Total Pressure Loss Through the UTRC LSRR First Stator.*
(a) Coarse Grid/Constant Inlet Total Pressure Calculation,
(b) Coarse Grid/Measured Inlet Total Pressure Calculation, and
(c) Spanwise–Refined Grid/Measured Inlet Total Pressure Calculation.

Thermal Results

A comparison between measured and computed midspan Stanton numbers is shown in Figure 4.2.4. The Stanton number is defined as

$$St = \frac{q''}{\rho_\infty U_\infty c_p (T_s - T_w)} .$$

Agreement between the prediction and experimental data is excellent.

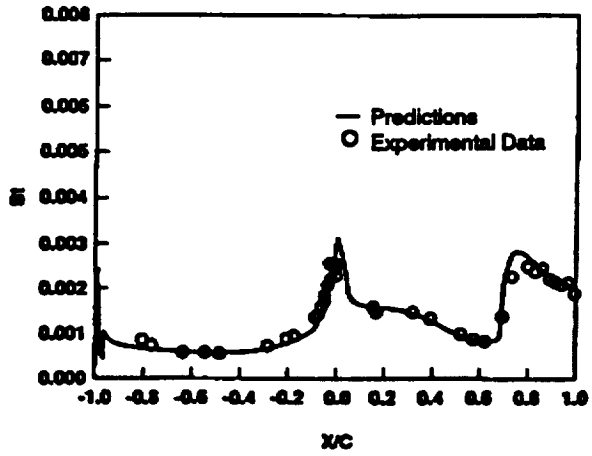

Figure 4.2.4 Stanton Numbers for the Midspan of the UTRC LSRR First Stator.

Stanton number contours for the airfoil surface are presented in Figure 4.2.5. The pressure surface shows contour lines typical of a 2–D flow. The contours near the endwalls are attributed to the assumption of fully turbulent flow within 20% of the endwalls and not to secondary flows. The suction surface heat transfer, on the other hand, exhibits effects of a 3–D flow except for a region on either side of midspan which is primarily two–dimensional. Relatively high values of Stanton number and a steep gradient are seen at the leading edge and transition location on the suction surface. Additional regions of high heat transfer are located downstream of the leading edge near the endwalls. A very steep gradient is noticed at that location. This region coincides with the 3–D flow of the passage vortices as they move from the endwalls onto the airfoil suction surface.

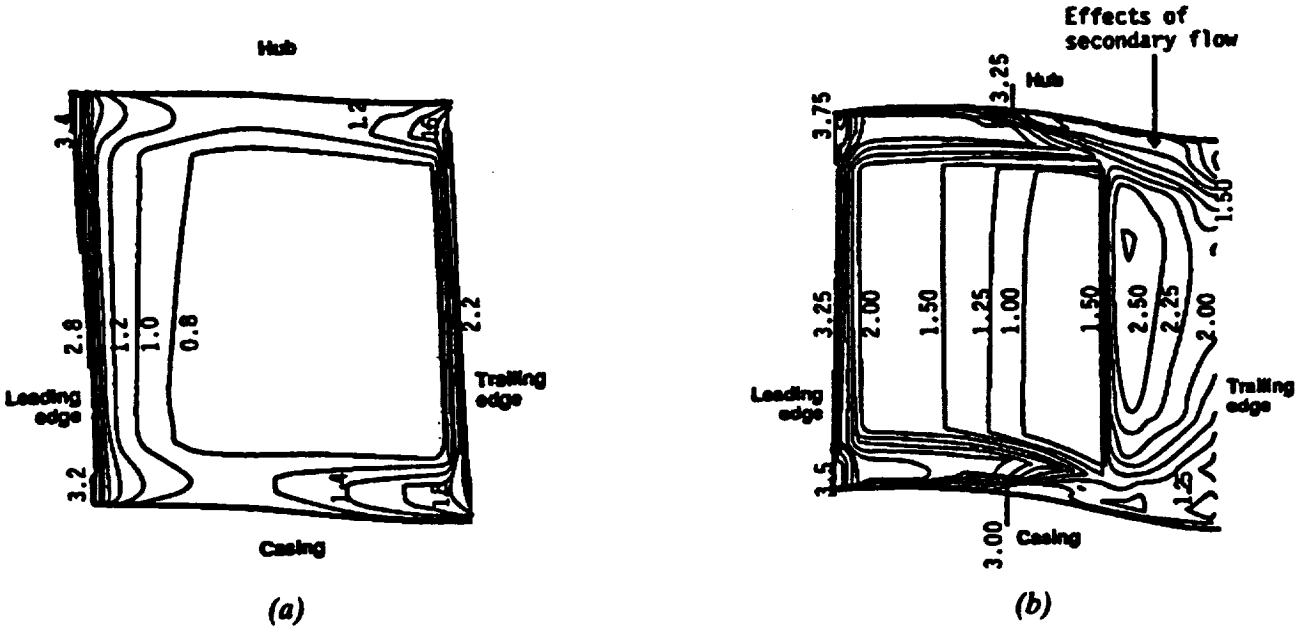

Figure 4.2.5 Predicted Stanton Number (St x 10^3) Contours for the UTRC LSRR First Stator Surface.
(a) Pressure Surface,
(b) Suction Surface.

Stanton numbers for the endwalls are shown in Figure 4.2.6. The Stanton number contours upstream of the stator are basically parallel to the airfoil leading edge. This pattern implies the approach of a 2–D boundary layer. An area of high heat transfer is located at the stator leading edge where the passage vortices cause a rapid transport of fluid perpendicular to the endwalls.

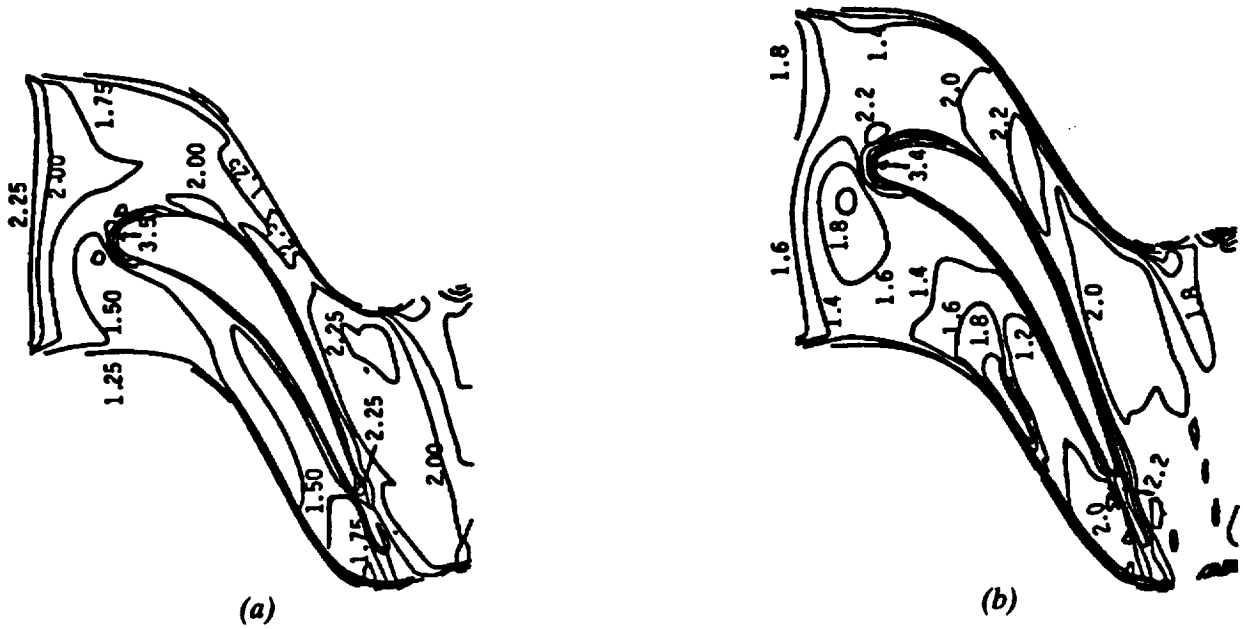

Figure 4.2.6 *Predicted Stanton Number (St x 10^3) Contours for the UTRC LSRR First Stator Endwalls.*
(a) Hub,
(b) Casing.

4.2.2 Langston Cascade

Langston cascade represents one of the best documented benchmark quality data for an airfoil row representative of a turbine environment. Detailed aerodynamic experimental data were acquired for this cascade by Langston et al. (1977) at the UTRC in a large scale low speed cascade tunnel with three incoming profiles consisting of thin (1.8% of the span), nominal (13.6% of the span) and thick (50% of the span) boundary layers. Surface heat transfer coefficient data were subsequently acquired on this airfoil by Graziani et al. (1980) for the thin and the nominal inlet boundary layers. This cascade was tested with an aspect ratio of 1.08 and a pitch to chord ratio of 0.955. Test conditions involved ambient air entering the cascade at approximately 98 ft/sec. The Reynolds number based on axial chord (11.08 inches) and inlet velocity was 565,000. Additional details are given by Langston and Graziani. This test case was chosen to verify the loading, secondary flow and heat load prediction capabilities of the code. A grid refinement study was conducted to determine the sensitivity of predictions to grid points in the spanwise direction. The code was run with grids having ranges of 31 to 49 points in the spanwise direction for the thin inlet boundary layer. A line of symmetry condition was imposed in the code for the nominal inlet boundary layer case and the code was run with girds having ranges of 16 to 39 points up to the midspan. The calculations were conducted both in a transitional and a fully turbulent mode. Most of the results discussed below were obtained with the finest grid and with calculations conducted in a transitional mode.

Surface Static Pressures and Surface Streamlines

A comparison of measured and predicted airfoil surface static pressures is shown in Figures 4.2.7 and 4.2.8 for the thin and the nominal inlet boundary layer. Excellent agreement is shown between experimental data and predictions. Figures 4.2.9 and 4.2.10 show a comparison of the measured and predicted surface static pressure coefficients at the endwall for the thin and the nominal inlet boundary layers respectively. Excellent agreement is shown between the data and predictions for the thin inlet boundary layer case. For the nominal inlet boundary layer, however, predicted results show larger impact of secondary flows than experimental measurements indicating an overestimation of secondary flows.

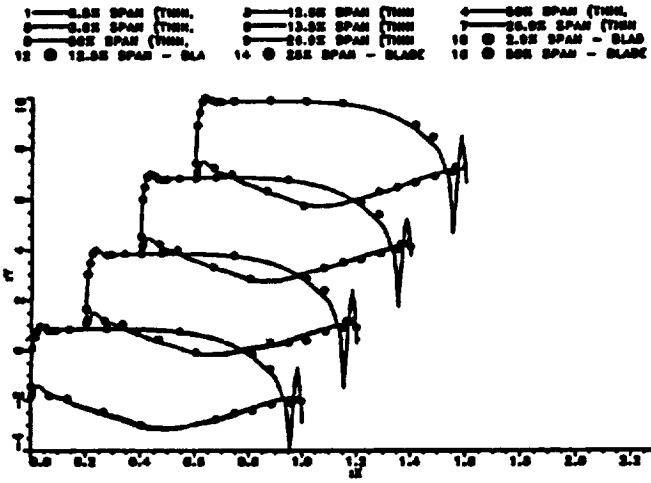

Figure 4.2.7 *RAI3DC Code Yields Excellent Agreement with the Airfoil Loadings at Various Spanwise Locations Measured by Graziani et al. (1980) for the Thin Incoming Boundary Layer*

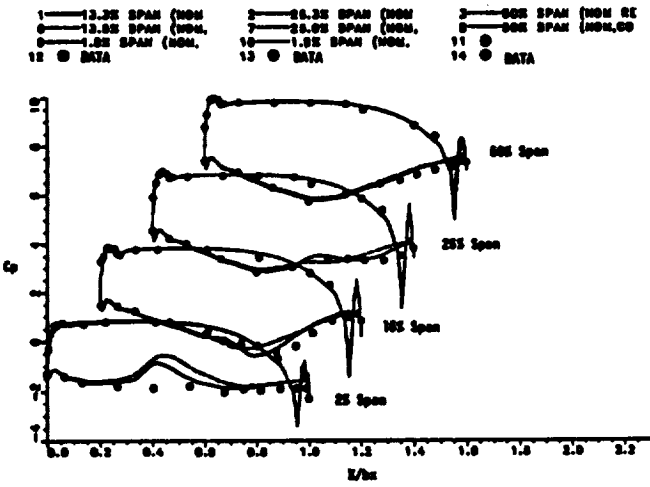

Figure 4.2.8 *RAI3DC Code Yields Good Agreement with the Airfoil Loadings at Various Spanwise Locations Measured by Langston et al. (1977) for the Nominal Incoming Boundary Layer*

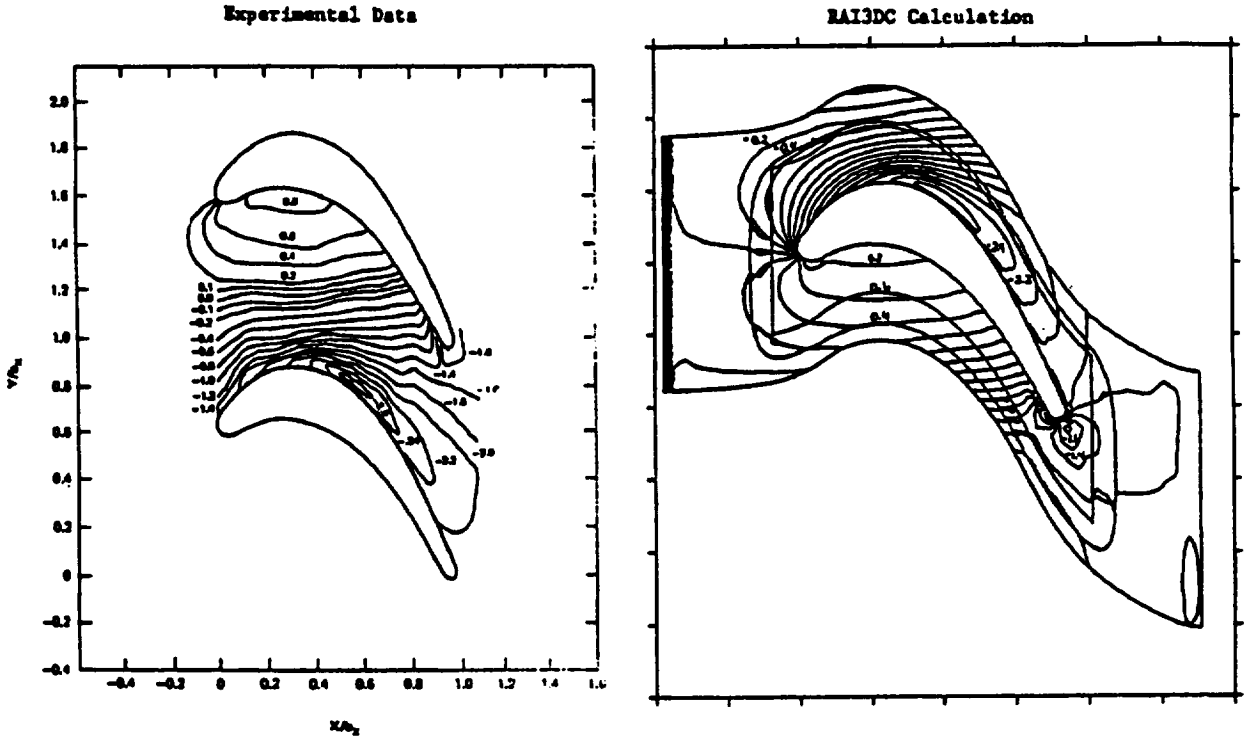

Figure 4.2.9 Endwall C_p Contours Thin Boundary Layer

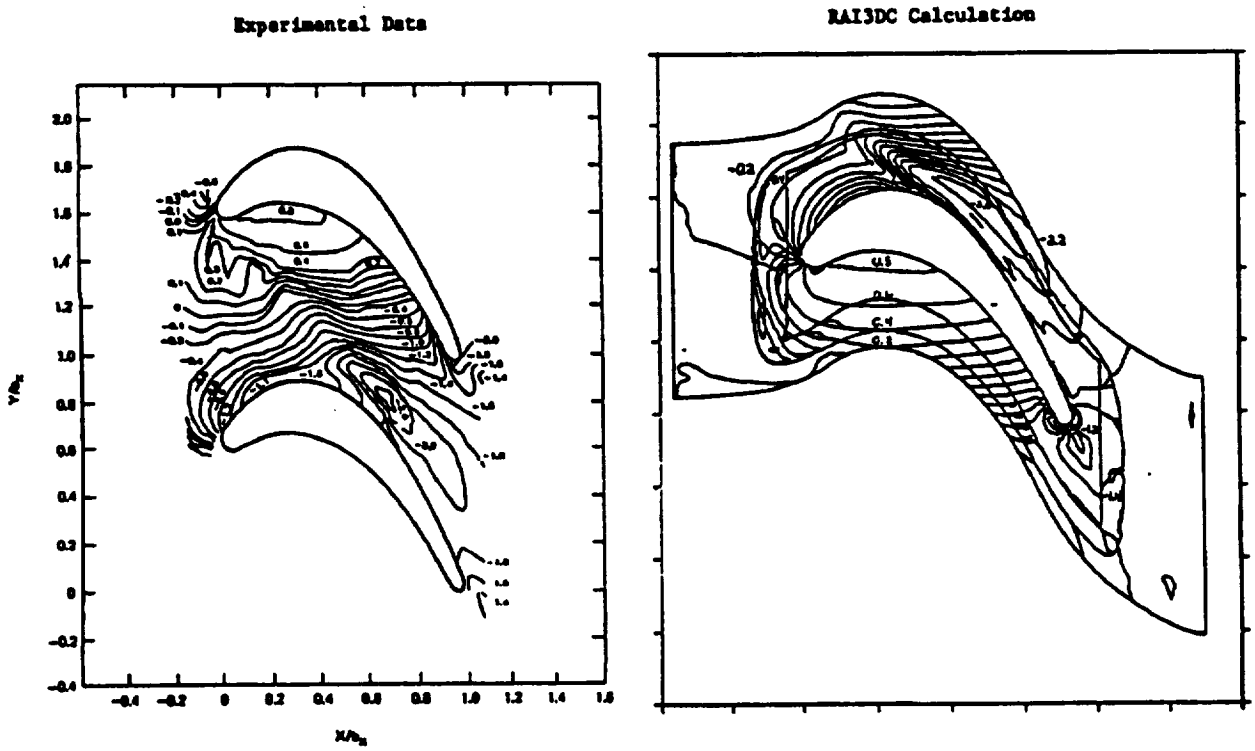

Figure 4.2.10 Endwall C_p Contours Nominal Boundary Layer

Figures 4.2.11 and 4.2.12 show a comparison of the measured and predicted streaklines on the airfoil suction sides for the thin and the nominal boundary layer cases. This comparison also indicates that whereas the thin boundary layer case is fairly well predicted; secondary flows for the nominal boundary layer case are overestimated which results in larger spanwise penetration of the separation line on the airfoil suction surface.

Thin Inlet Boundary Layer

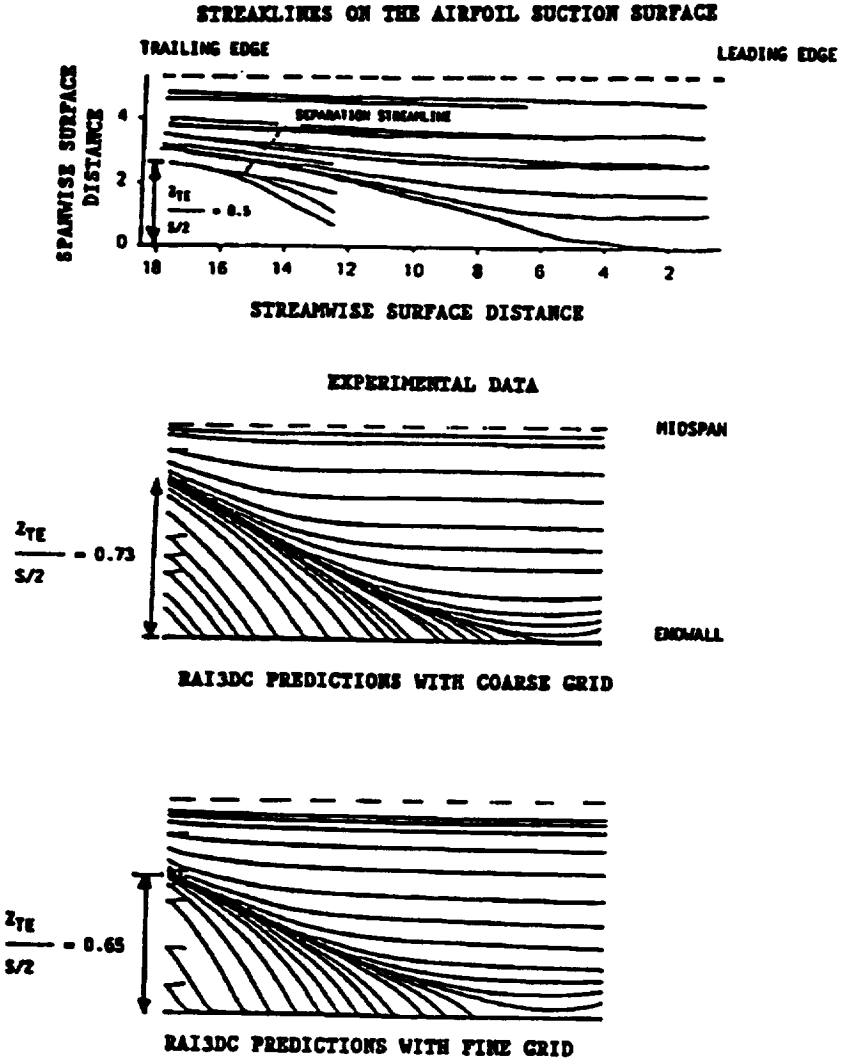

Figure 4.2.11 *Theoretical Predictions Overestimate the Penetration of Separation Line on the Airfoil Suction Surface. A Possible Solution May Be to Increase the Number of Grid Points in the Spanwise Direction.*

Nominal Inlet Boundary Layer

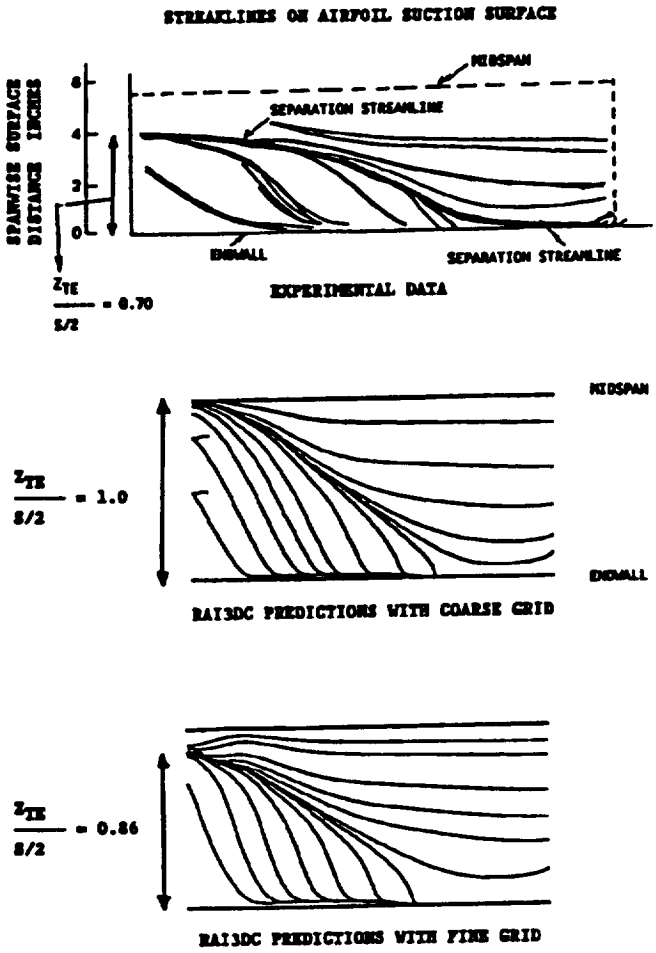

Figure 4.2.12 *Penetration of the Separation Line on the Airfoil Suction Surface Overpredicted by the RAI3DC Cascade Code. Increasing the Number of Grid Points in the Spanwise Direction has a Favorable Effect on the Penetration Height at the Trailing Edge of the Airfoil Suction Side.*

Secondary Flows and Total Pressure Loss

A comparison of the measured and computed total pressure loss coefficient at 10% axial chord downstream of the trailing edge of the cascade is shown in Figures 4.2.13 and 4.2.14 for the thin and the nominal inlet boundary layers. Excellent agreement is demonstrated for the thin inlet boundary layer case for the shapes and levels of pressure contours. Predicted loss contours for the nominal boundary layer case, although they show similar behavior as the experimental data, indicate a large wake at the midspan and higher maximum total pressure loss coefficient than the experimental data.

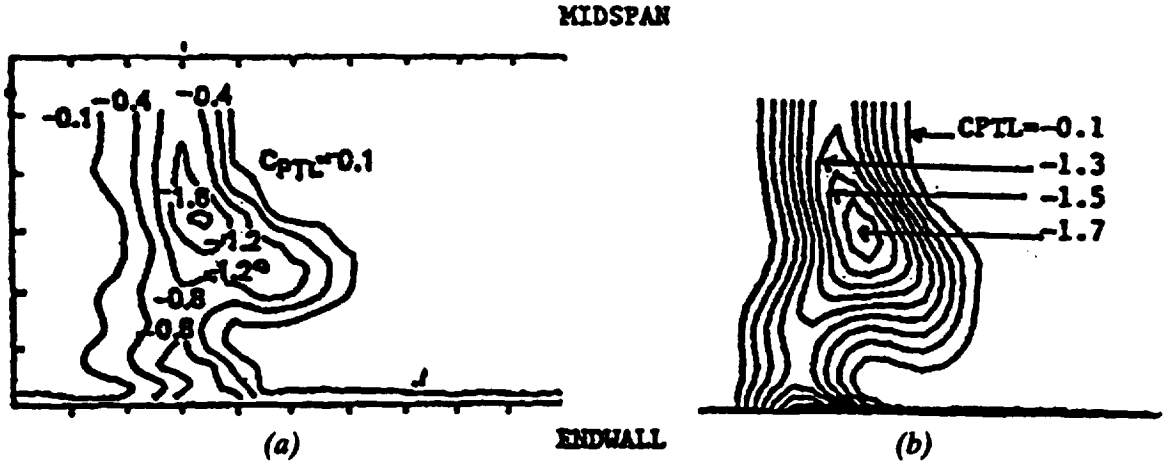

Figure 4.2.13 *Total Pressure Loss Contours Downstream of Langston's Cascade for Thin Inlet Boundary Layer.*
(a) Experimental (Graziani et al., 1980),
(b) Predicted.

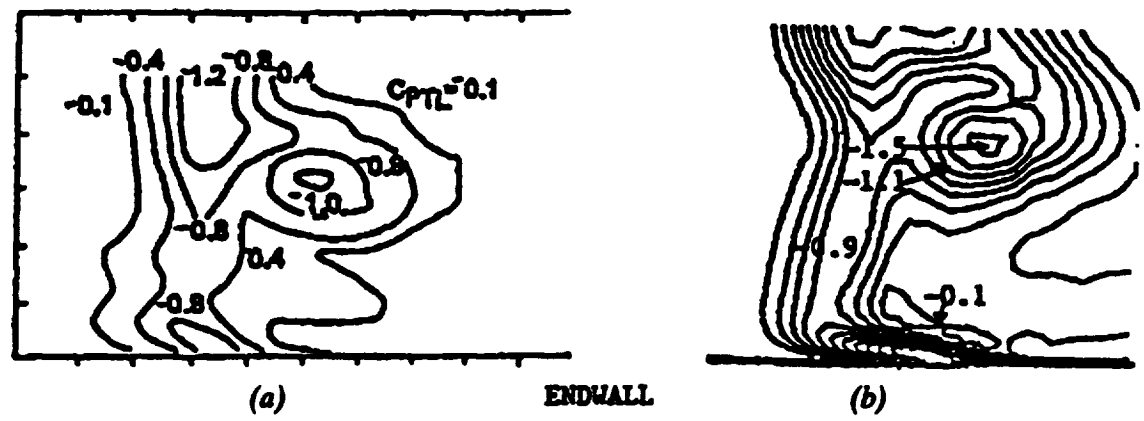

Figure 4.2.14 *Total Pressure Loss Contours Downstream of Langston's Cascade, Nominal Inlet Boundary Layer.*
(a) Experimental (Langston et al. (1977)),
(b) Prediction.

Predicted gap–averaged total pressure loss coefficients for the two inlet boundary layer cases are compared to the experimental data in Figures 4.2.15 and 4.2.16. Overall agreement between data and predictions is good except at the midspan for the nominal inlet boundary layer case. The agreement between data and predictions should improve if additional grid points are used in the inner grid and the effect of dilation induced by the secondary flow is accounted for through improvements in the turbulence model as suggested by Sharma and Graziani (1982). Limitations of computer storage available at the NASA MSFC CRAY–XMP computer did not permit further refinement of the grid especially in the airfoil surface normal direction. The effect of grid refinement on the predicted results was, however, conducted as a part of the NAVAIR contract #N00140–88–C–0677 at UTRC by Dorney et al. (1982) by using a version of the Rai code for the thin inlet boundary layer

case by utilizing the NAS super computers and large storage super mini workstations. Results from Dorney's work, shown in Figure 4.2.17, indicate that almost 30% further increase in grid points are needed to provide an accurate estimate of profile and secondary losses in cascades. Significant improvements in computer resources, especially by using super workstations, have been achieved since the present computations were conducted. Execution of reliable loss computations for turbine cascades is now within the reach of design engineers. It should be pointed out here that the code gives reliable results, provided the grid resolution is adequate.

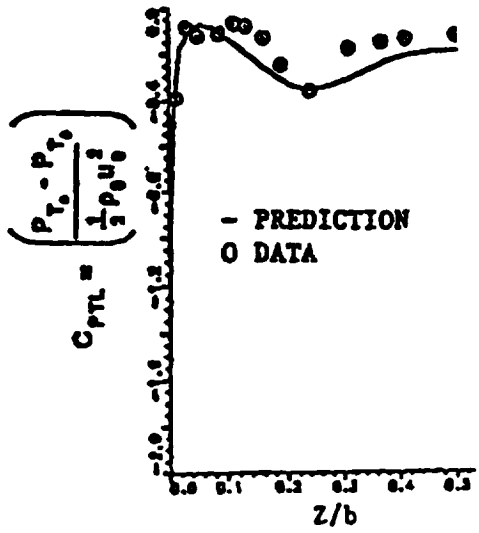

Figure 4.2.15 *Total Pressure Loss, Gap Averaged, Langston's Cascade*

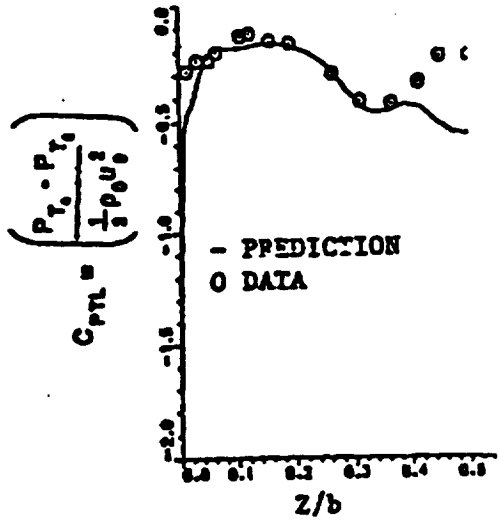

Figure 4.2.16 *Total Pressure Loss, Gap Averaged, Through Langston's Cascade, Nominal Inlet Boundary Layer*

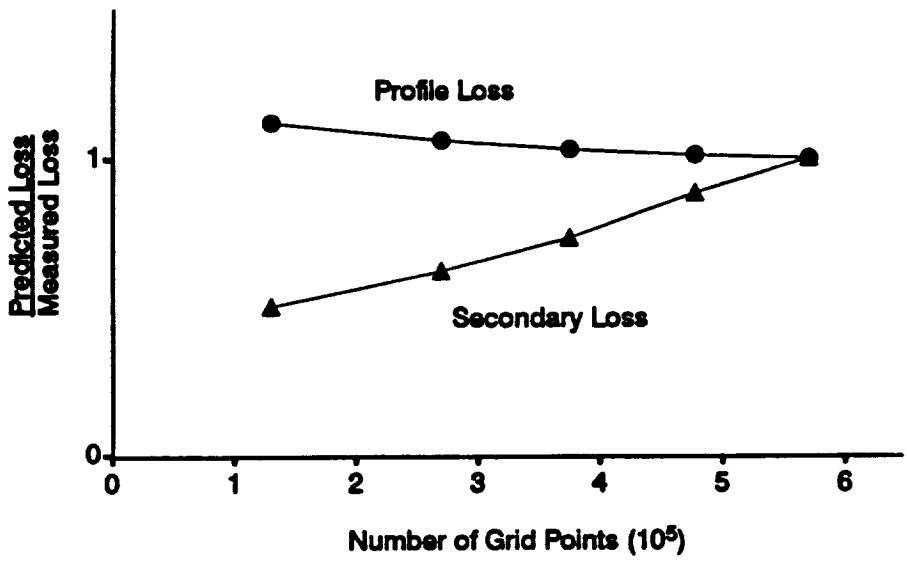

Figure 4.2.17 *Grid Refinement Study Conducted by Dorney et al., (1992) Indicates Almost 550,000 Grid Points Are Needed to Accurately Resolve Losses in Turbine Cascades*

Surface Heat Transfer Coefficients

Measured and predicted heat transfer coefficients at the midspan of the airfoil for the thin and the nominal boundary layer cases are compared in Figure 4.2.18. The agreement between experimental data and predictions is fairly good; this agreement should improve with an increased number of grid points in the surface normal direction as pointed out above and as demonstrated by Dorney et al. (1992).

Distributions of Stanton number measured over the airfoil surfaces and endwalls for the two boundary layer cases are shown in Figures 4.2.19 through 4.2.22. Qualitative agreement is shown between the experimental data and theoretical predictions. Improvements in turbulence/transition models and increased number of grid points should further improve the agreement between data and predictions.

Comparison of experimental data with theoretical predictions shown in this section clearly demonstrates the predictive capabilities of the Rai code. Lack of good agreement between the experimental data and theoretical prediction can invariably be attributed to the limitations of grid points used in the present effort. For engineering design execution, however, this code, even with limited grid resolution, provides excellent results which should allow use of the code in the design execution process for optimizing airfoil rows in rocket propulsion systems.

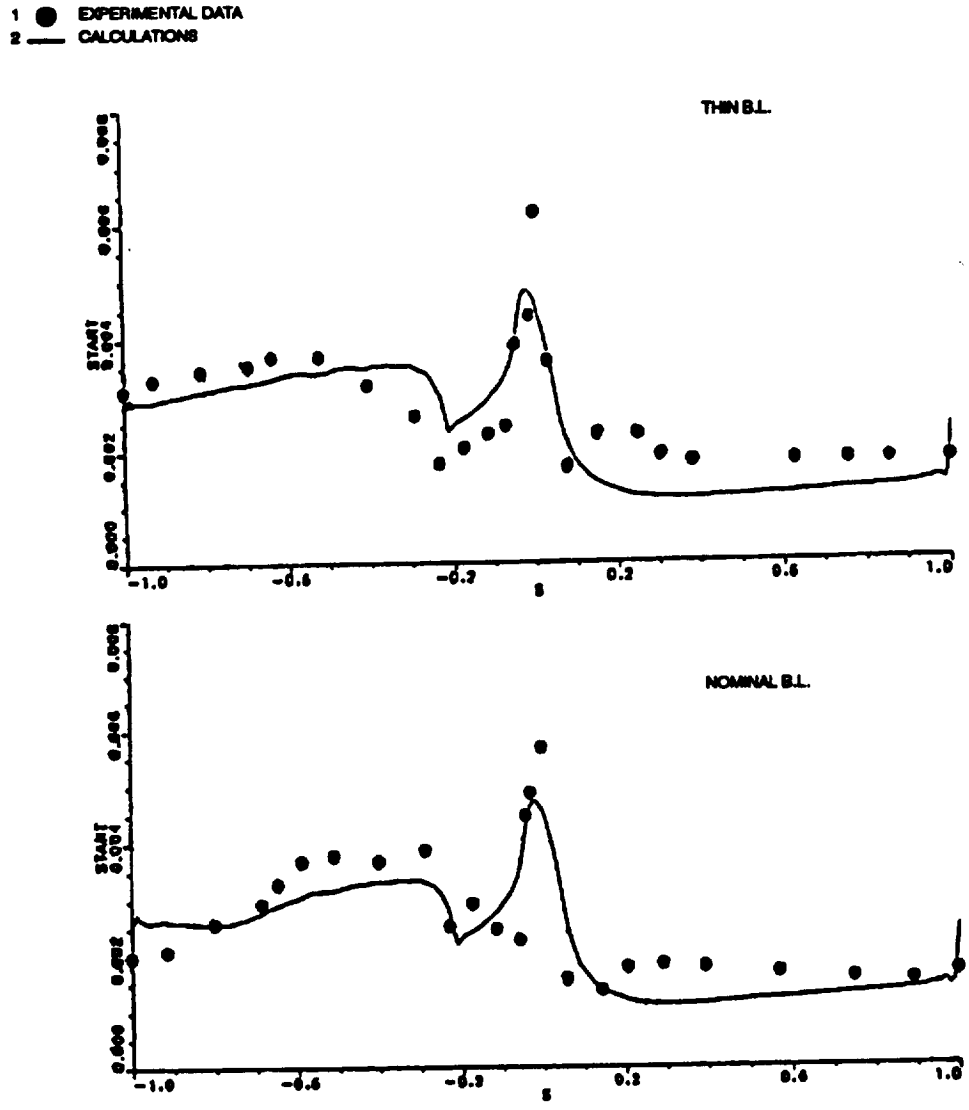

Figure 4.2.18 Midspan Stanton Number

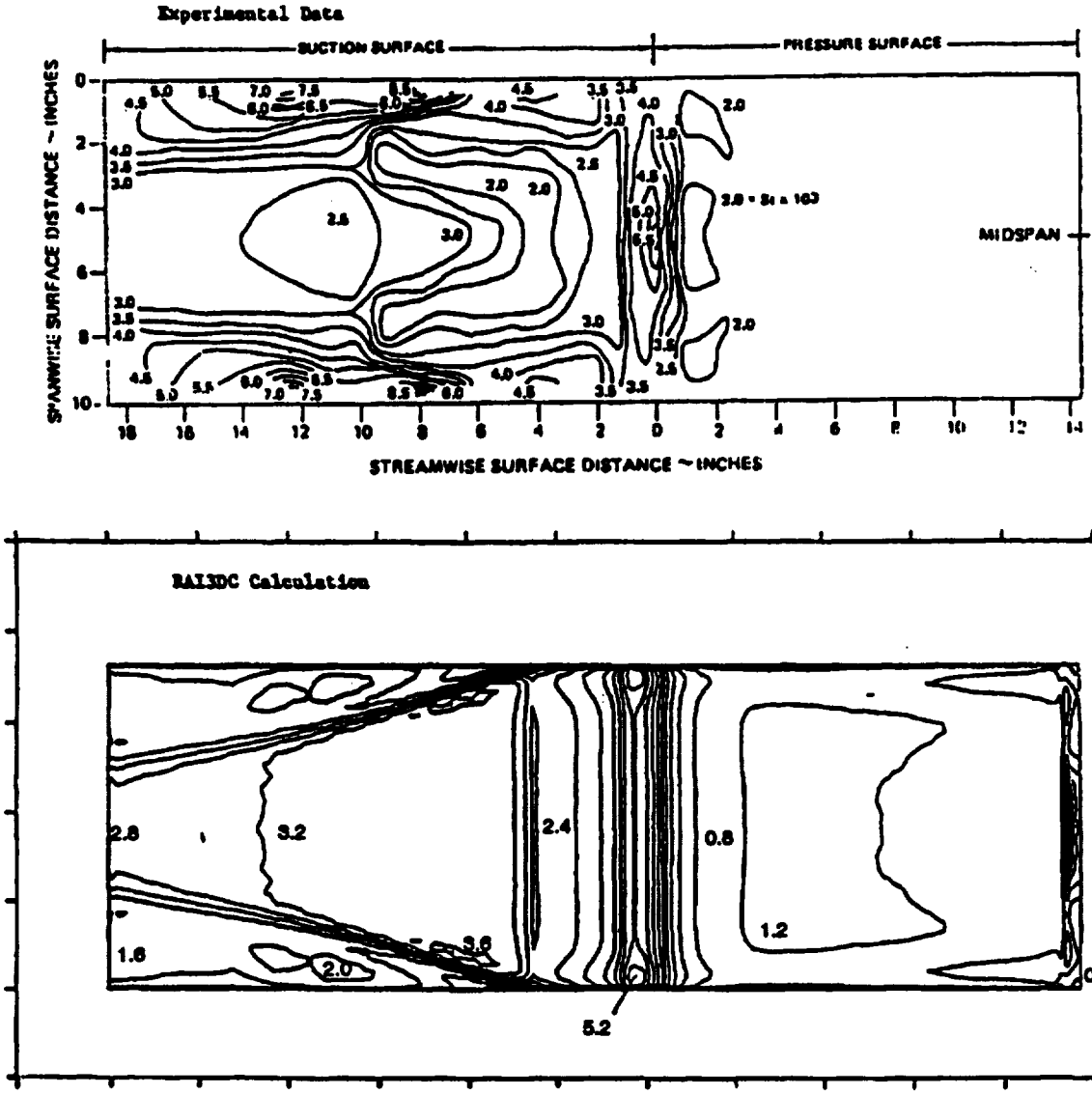

Figure 4.2.19 Blade Surface Stanton Number Contours Thin Boundary Layer

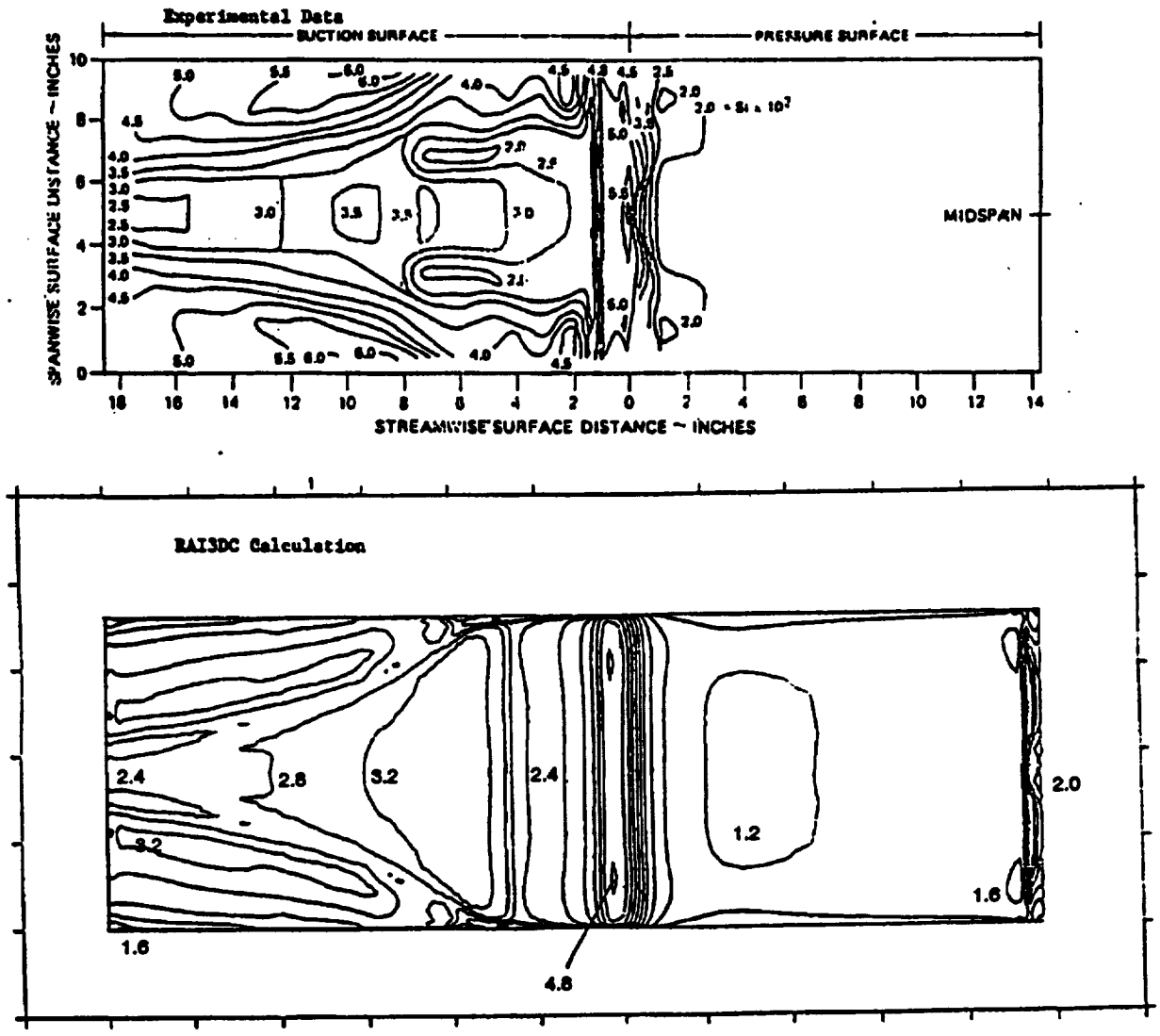

Figure 4.2.20 *Blade Surface Stanton Number Contours*
Nominal Boundary Layer

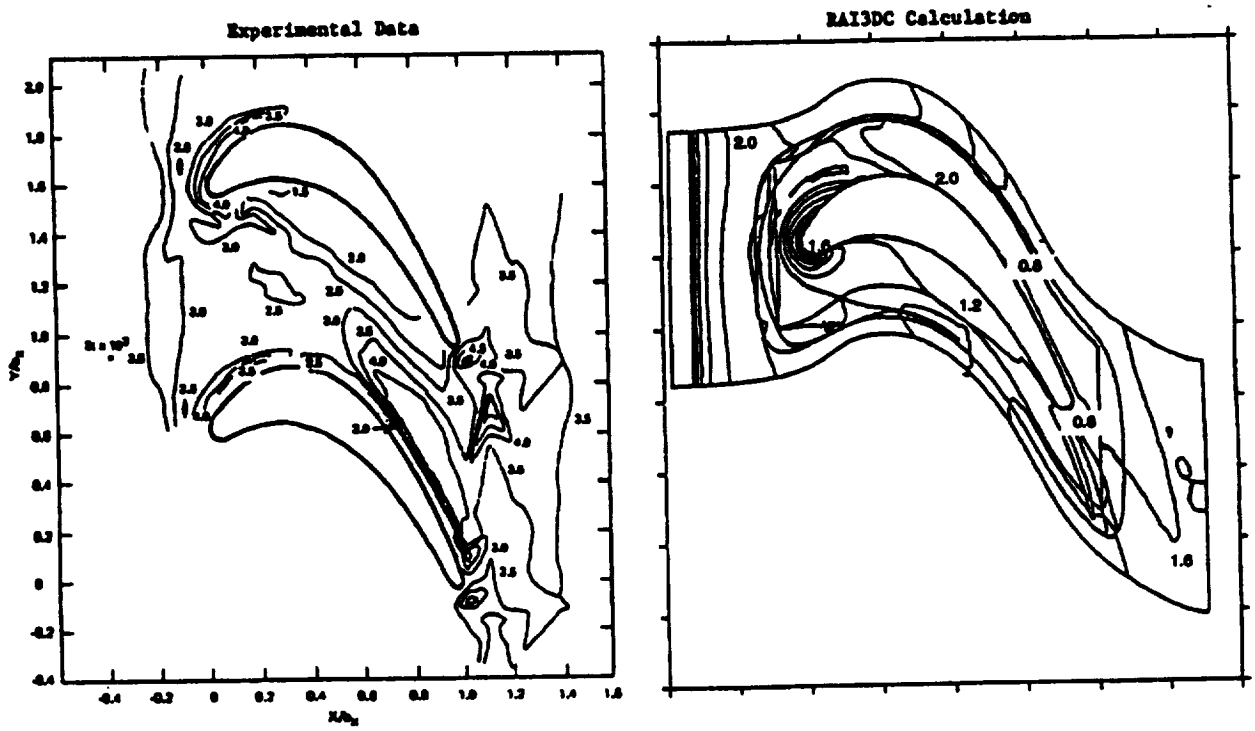

Figure 4.2.21 *Endwall Stanton Number Contours*
Thin Boundary Layer

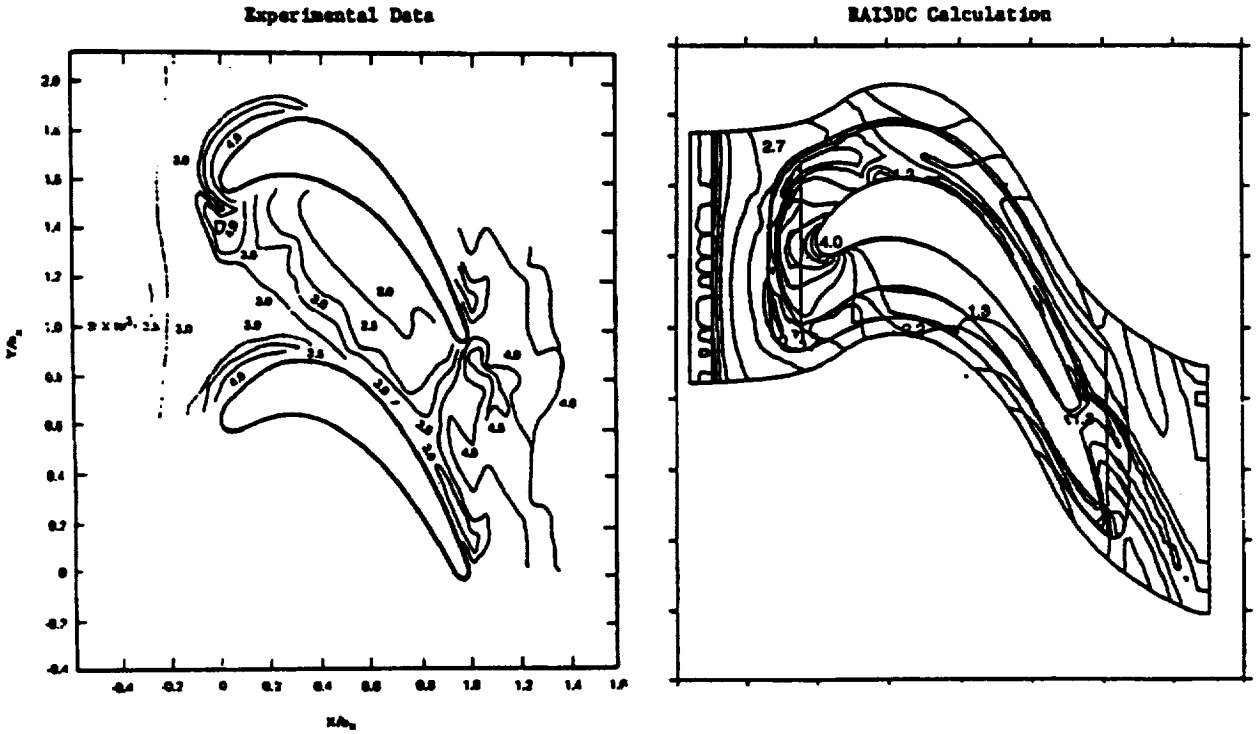

Figure 4.2.22 *Endwall Stanton Number Contours*
Nominal Boundary Layer

4.3 Tip Leakage Prediction Aspect of the Code

Although initial version of the Rai code (ROTOR3) allows computations in the tip clearance region, these calculations did not provide stable results as noted by Rai (1987). Tip clearance levels used in computations by Madavan et al. (1989) were lower and by Dorney et al. (1992) were larger than the experimental results to yield stable overall solution. A study was conducted in the present program to verify the tip leakage flow prediction capabilities of the code.

Flow was simulated in the Langston cascade with tip clearance flows on one of the endwalls. Experimental data was available from this configuration from detailed measurements conducted by Dishart and Moore (1989). Computations were conducted with 39 points in the spanwise direction; which included 9 grid points in the tip clearance region containing 2.1% of the span. Initial calculations indicated insufficient grid resolution to resolve the overall flowfield but limitation of available computer storage space, on the NASA MSFC CRAY–XMP computer, did not permit inclusion of additional grid points. The calculations were, therefore, run to convergence to establish the level of accuracy achieved for the tip flows.

A comparison of measured and predicted streaklines near the tip endwall for this configuration is shown in Figure 4.3.1. The predicted results yield fairly accurate description of the flow behavior near the endwalls. Separation and reattachment streaklines are fairly accurately predicted by the code; migration of flow from the pressure to the suction side is also well predicted. Measured total pressure loss contours 40% of the axial chord downstream of the cascade are compared to the present theoretical predictions in Figure 4.3.2. The predicted results indicate a stronger endwall passage vortices than measured results, these results are similar to the ones discussed in the previous subsection for the nominal inlet boundary layer. The predicted secondary flow structures tend to merge into a high loss region which affects the convection of the tip leakage vortex. Distinct tip leakage vortex is, however, predicted as indicated in Figure 4.3.2 at the 10% and the 40% axial chord locations. The predicted tip clearance vortex is smaller than the experimental data primarily due to the influence of larger than measured secondary flow structures. This exercise indicates that the code with a larger number of grid points in the spanwise direction will provide accurate simulation of tip clearance flows.

It should be pointed out here that the tip clearance flows are dominated by inviscid migration of flows where the viscosity plays only a limited role. This point is illustrated in Figure 4.3.3 where the flow in a low turning cascade (Yaras et al. (1989)) was simulated by Staubach (1990) by utilizing an Euler code with 51 grid points in the spanwise direction. Good agreement between the measured data and Euler predictions demonstrates the need to use an increased number of grid points for tip clearance simulation; the need to account for viscous effects is not as important as originally anticipated.

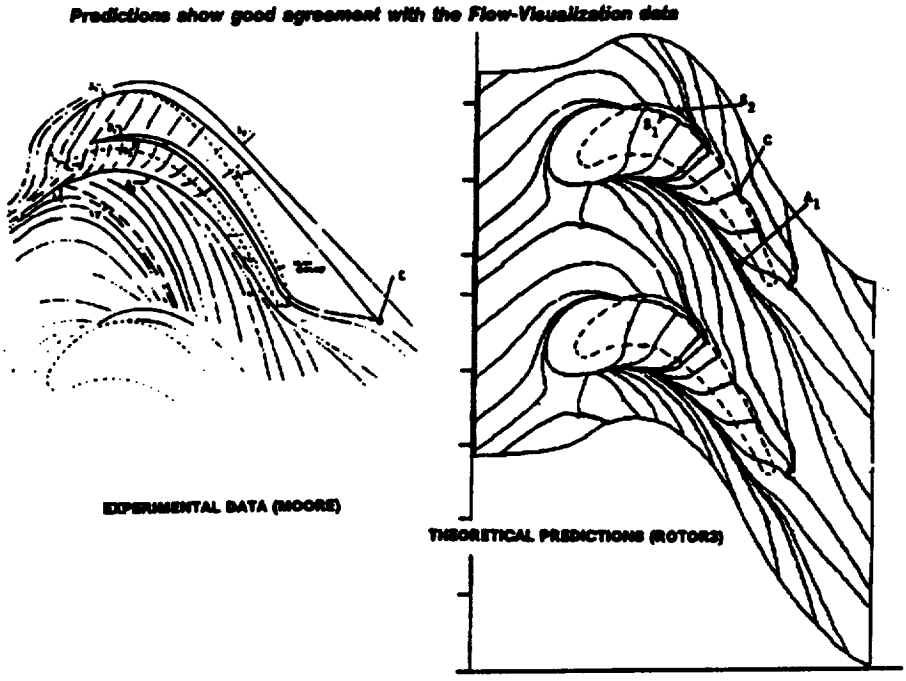

Figure 4.3.1 *Tip Leakage Flow Predictive Capabilities of the Rotor Code Verified*

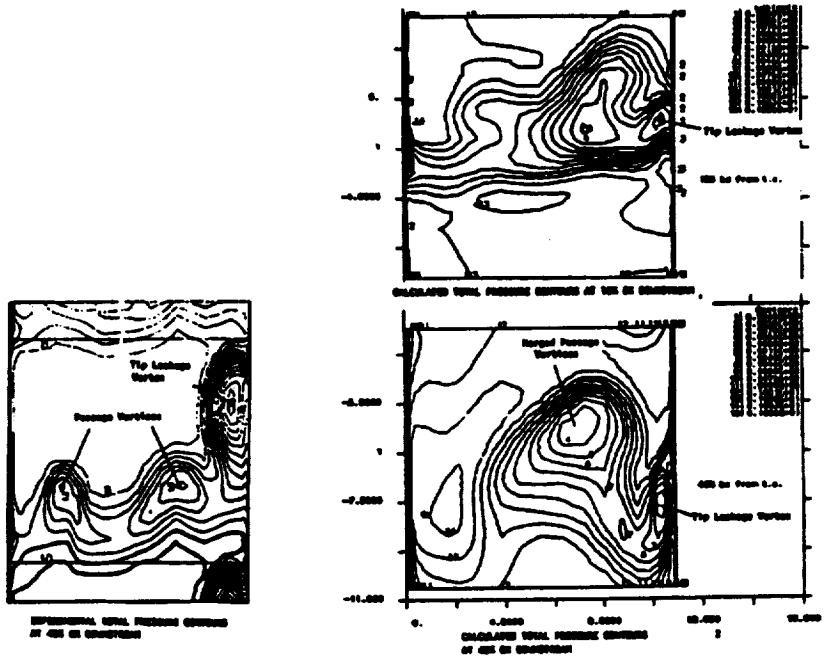

Figure 4.3.2 *Comparison of Calculated and Experimental Exit Total Pressure Contours*

C-2

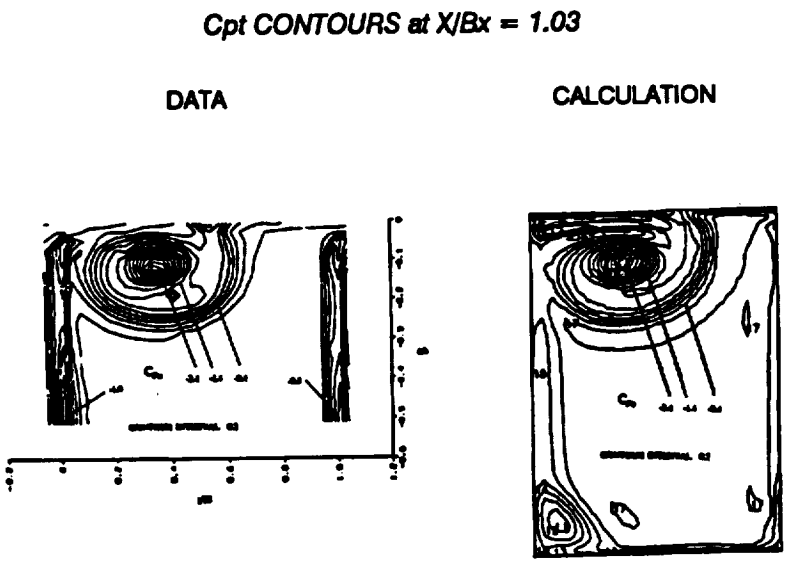

Figure 4.3.3 *3D Euler Calculation with 51 Grid Points in Spanwise Direction Can Resolve Tip Leakage Vortex (Staubach (1990)).*

4.4 Unsteady Flow Prediction Aspect of the Code

In addition to predicting the time–averaged loadings, surface streaklines and total pressure losses, an unsteady code must provide predictions of the following four well established unsteady flow features to ensure its proper verification:

- unsteady pressure amplitudes on airfoils
- segregation of hot and cold air in rotor passages
- periodic elimination of rotor secondary flow vortices
- unsteady variation in the transition point on downstream row airfoils and unsteady loss variation

A number of simulations have been conducted in literature by using the code used in the present program to demonstrate its predictive capabilities. Results from some of these simulations are discussed below to provide evidence of the code verification.

Rai (1987, 1989), Rai and Madavan (1988) and Madavan et al (1991) have provided sufficient comparisons with experimental data to demonstrate that the code provides accurate estimates of time–averaged flows for a turbine stage. Most detailed results for the UTRC LSRR were obtained by Madavan et al (1991) by using almost 1.43 million grid points to simulate three–dimensional flow through 3 vane and 4 blade passages; the experimental rig contains 22 vanes and 28 blades. Madavan et al. (1991) compared their results with those obtained by Madavan et al. (1989), which used 0.41 million grid points and utilized 1 vane and 1 blade to simulate the flow through the same rig. Results from these publications, shown in Figures 4.4.1 through 4.4.4, clearly demonstrate that the code, with multi–passage simulation, provides very accurate predictions for:

- spanwise distribution of time–averaged airfoil loadings (Figure 4.4.1),
- amplitudes of unsteady pressures at midspan (Figure 4.4.2),

- time–averaged streaklines on airfoil surfaces (Figure 4.4.3), and
- time–averaged total pressure loss contours at the exit of the vane and the blade (Figure 4.4.4).

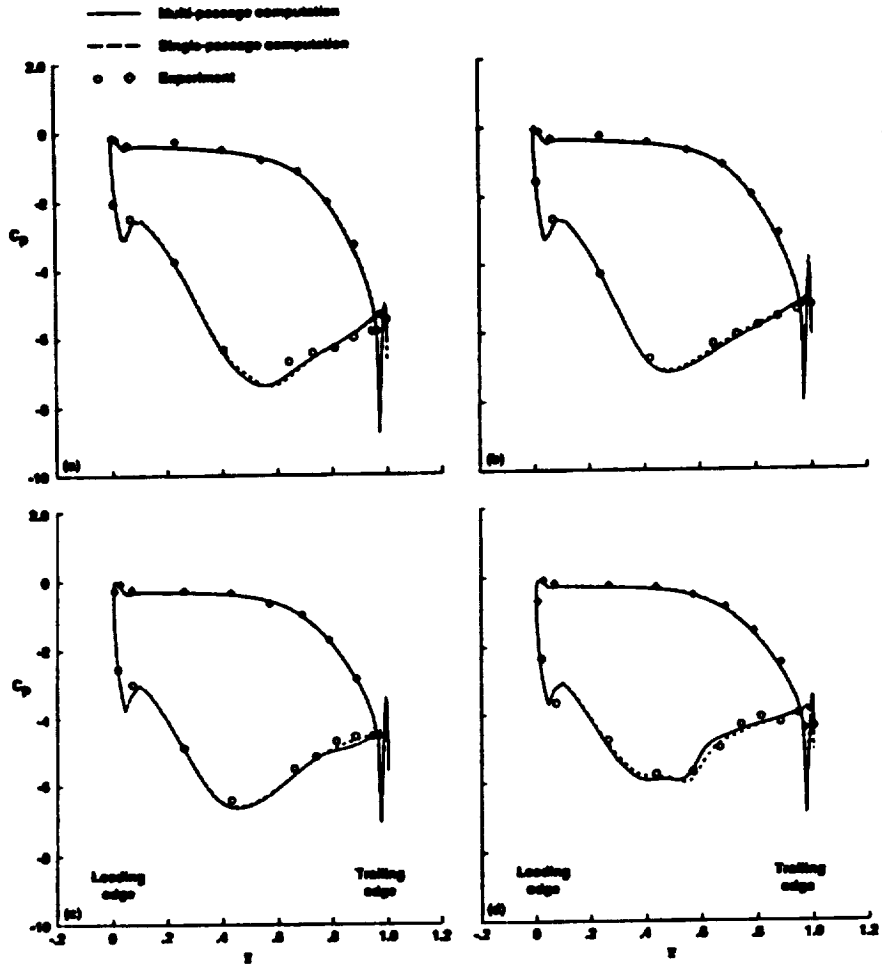

Figure 4.4.1(a) *Spanwise Variation of Time–Averaged Pressure Distributions on the Stator.*
(a) 2% Span;
(b) 25% Span;
(c) 75% Span;
(d) 98% Span.
(Madavan et al. (1989, 91) Computations)

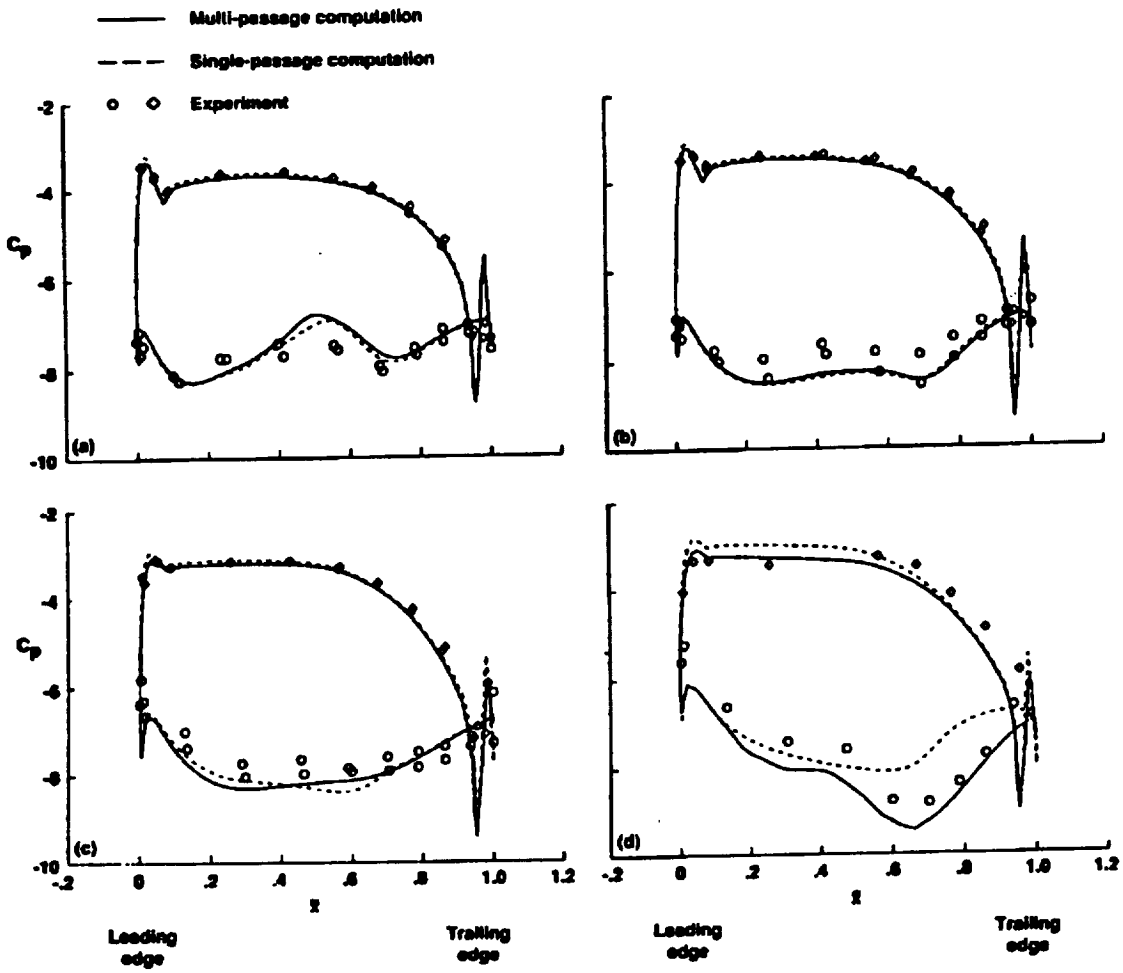

Figure 4.4.1(b) Spanwise Variation of Time–Averaged Pressure Distributions on the Rotor.
(a) 2% Span;
(b) 25% Span;
(c) 75% Span;
(d) 98% Span.

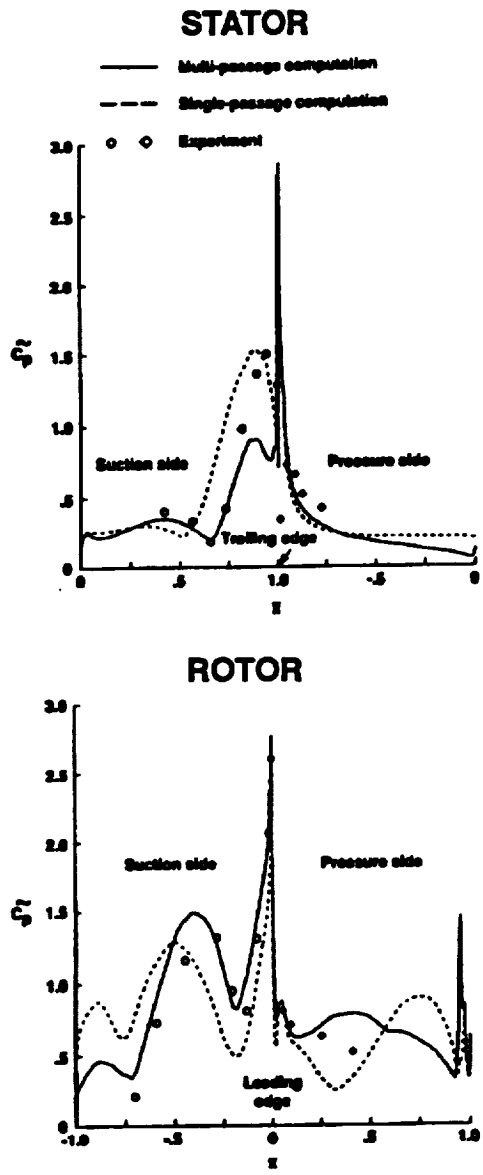

Figure 4.4.2 *Pressure Amplitude Distribution on the Rotor at Midspan (Madavan et al. (1989, 91) Computations)*

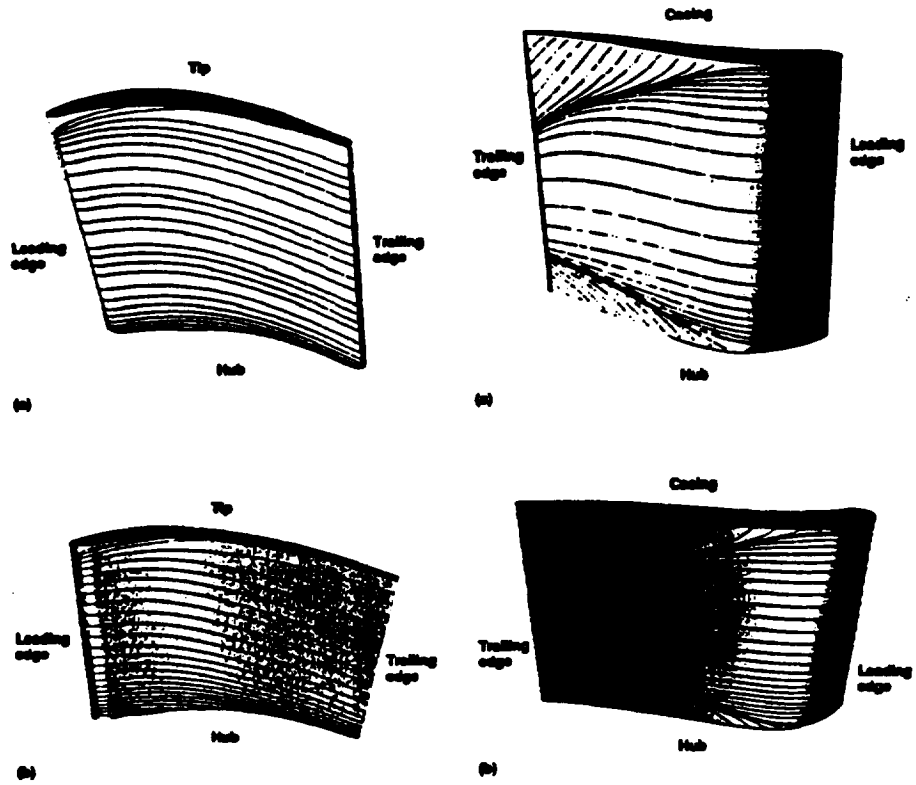

Figure 4.4.3(a) *Stator Surface Flow Visualization. Time–Averaged Limiting Streamlines From*
(a) Single–Passage Computations; and
(b) Multi–Passage Computations.
(Madavan et al. (1991))

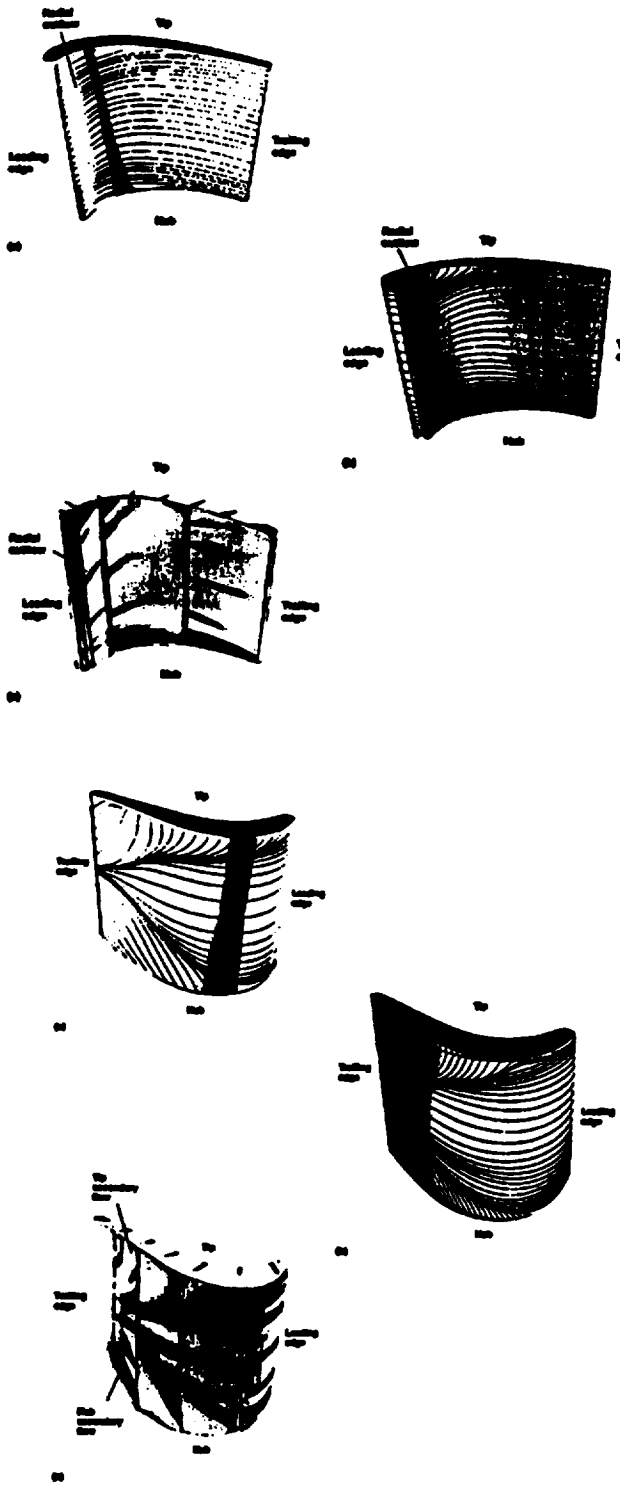

Figure 4.4.3(b) *Rotor Surface Flow Visualization. Time–Averaged Limiting Streamlines From*
(a) Single–Passage Computations;
(b) Multi–Passage Computations; and
(c) Experimental Results.
(Madavan et al. (1991))

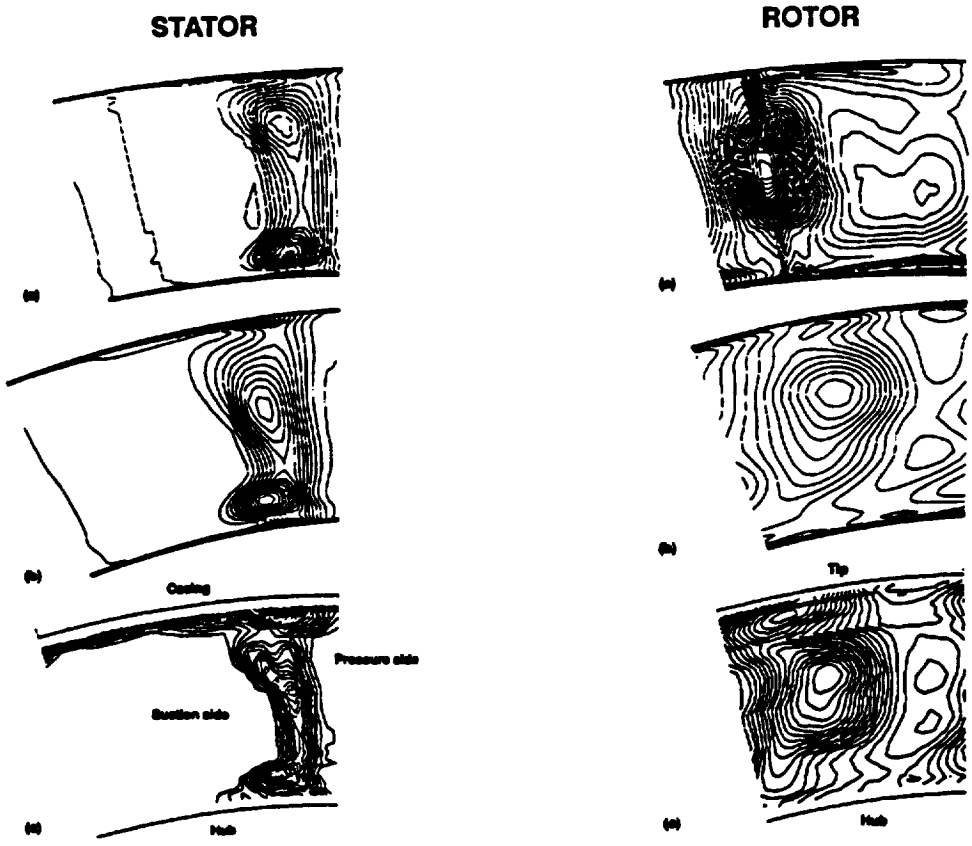

Figure 4.4.4 *Relative Total Pressure Contours at the Exit to the Stator and the Rotor.*
(a) Single–Passage Computations;
(b) Multi–Passage Computations; and
(c) Experimental Results.
(Madavan et al. (1989, 91) Computations)

The multipassage simulation, conducted with 51 spanwise grid points and with correct tip clearance levels also captures the tip leakage vortex structure which was not previously captured with a smaller tip clearance level by Rai.

Pressure sides of turbine rotors operating in the presence of circumferentially inlet temperature profiles tend to have higher surface temperatures on the airfoil pressure sides than the time–averaged temperature at the rotor inlet. This flow phenomena, experimentally documented by Butler et al (1986), Sharma et al (1990) and Roback and Dring (1991), illustrates that the hot and cold stream of fluid tend to segregate in a turbine rotor. A number of unsteady numerical simulations (Rai and Dring (1990), Ni et al (1988), Ni and Sharma (1988), Krouthen and Giles (1988), Dorney et al (1991, 1992), Takahashi and Ni (1990, 1991) have been conducted to predict this flow phenomena. One of the most accurate simulations of this effect was conducted by Dorney, Davis and Sharma (1991) by using a 2D version of the code used in the present program. Results from this publication clearly demonstrate that segregation of hot and cold fluid in turbine rotors is an unsteady two–dimensional phenomena and it is well predicted by the code used in the present program as demonstrated by excellent agreement between experimental data and theoretical predictions in Figure 4.4.5.

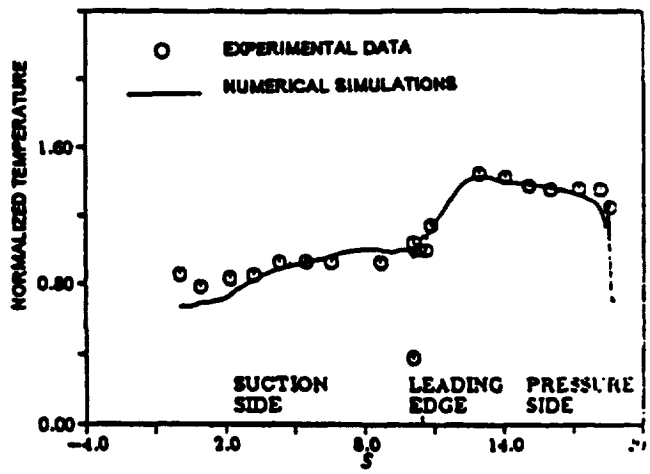

Figure 4.4.5 ***A Radially Uniform Incoming Two-Dimensional Hot Streak Yields Higher Surface Temperature on the Pressure Side and Lower Temperatures on the Suction Side (Dorney et al. (1991)) Indicating Segregation of the Hot and Cold Air in Turbine Rotors.***

Periodic elimination of the rotor secondary flow vortices due to the interaction between the upstream vane and the downstream blade flowfield, experimentally documented by Sharma et al. (1983), was initially envisioned to be viscous effect. Unsteady, three-dimensional flow simulations conducted by an inviscid Euler code, however, were found to be sufficient to predict this flow feature as indicated in Figure 4.4.6 from Ni and Sharma (1989). It can, therefore, be safely concluded that an unsteady Navier Stokes code (like the one used in the present program) will predict this phenomena. Further expensive simulations are not needed to demonstrate this prediction capability. Review of existing numerical results from Madavan et al (1991) should clearly illustrate this flow behavior.

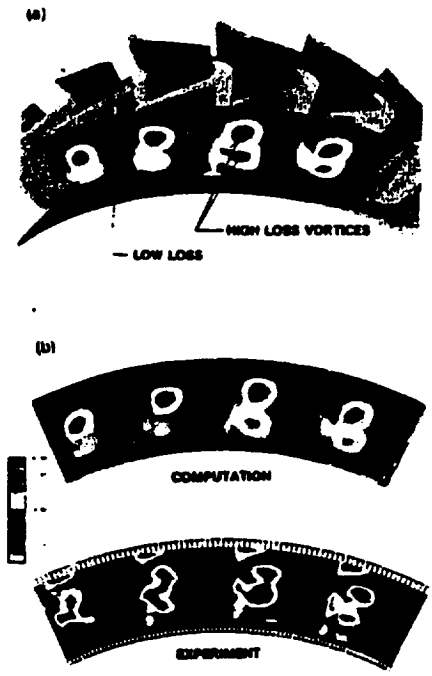

Figure 4.4.6 *Relative Total Pressure at Exit of the Rotor from Both the Unsteady Simulation and Experimental Data Indicate That the Unsteady Euler Code (Ni & Sharma (1990)) is Sufficient to Predict Experimental Behavior.*

Periodic variation of the onset and the extent of transition has been observed by Pfeil & Herbst (1978), Doorley and Oldfield (1984) for an unsteady flow simulation in a linear cascade and by Hodson (1983) in a turbine rotor. This phenomena is most pronounced in moderate and low Reynolds number flow situations in the turbine and it should have little effect on the rocket turbines where Reynolds numbers are very high. An unsteady transition model has been implemented in the present code as discussed in Section 3 of the present report. Flow simulations were conducted for the UTRC LSRR by using this transition model. Large leading edge overspeed for the rotor, however, always tripped the boundary layer to a turbulent state. This effect, therefore, cannot be illustrated in this subsection of the report. Code application results shown in Section 5.2 do, however, discuss the impact of this phenomena on the overall unsteady and time–averaged losses.

Two– and three–dimensional flow simulations were conducted in the present program for the UTRC LSRR rotor. Measured flow properties from the upstream stator (vane) were specified as inlet boundary conditions. Results of the two–dimensional calculations are similar to those obtained by Rai (1987) and Madavan et al. (1991) and some of these results are shown in Figures 4.4.7 and 4.4.8. Three–dimensional flow calculations were also conducted for the rotor by using a uniform upstream and measured upstream boundary conditions from the stator exit. Limitations of the available computer storage on the NASA MSFC XMP contained the spanwise grid density to 39. In addition, a fully converged solution has not yet been achieved so the results are not discussed. Even converged results from these simulations are not expected to be any superior to those obtained by Madavan et al (1991) because of fewer number of grid points used in the present simulation. It should, however, be pointed out that verification of the unsteady flow predictive capabilities of the code has been demonstrated by results shown in this section.

In summary, results shown in this section clearly demonstrate the predictive capabilities of the code used in this program. The code provides accurate estimates of losses, heat loads, loadings, unsteady pressure amplitudes, secondary flows, tip leakage vortices and segregation of the hot and

cold air in turbine passages. The only requirement for accurate predictions is proper grid resolution and computer resources to ensure convergence of calculations.

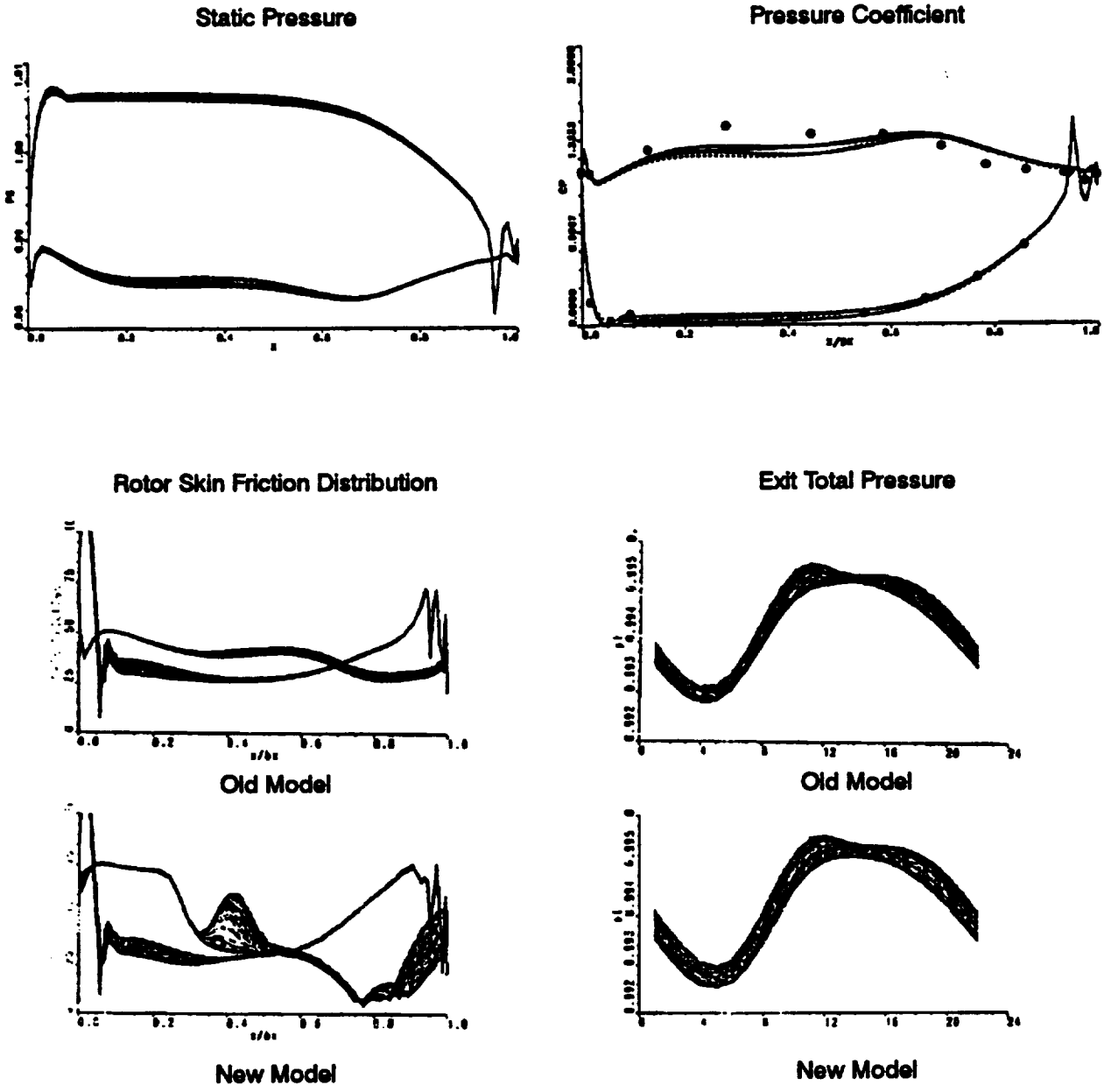

Figure 4.4.7 *Unsteady Two–Dimensional Computations for the UTRC LSRR Rotor Indicating Unsteadiness in Static Pressure, Skin Friction and Losses. Larger Effects Indicated Using Transitional Model Developed in the Present Program.*

Computational Grid

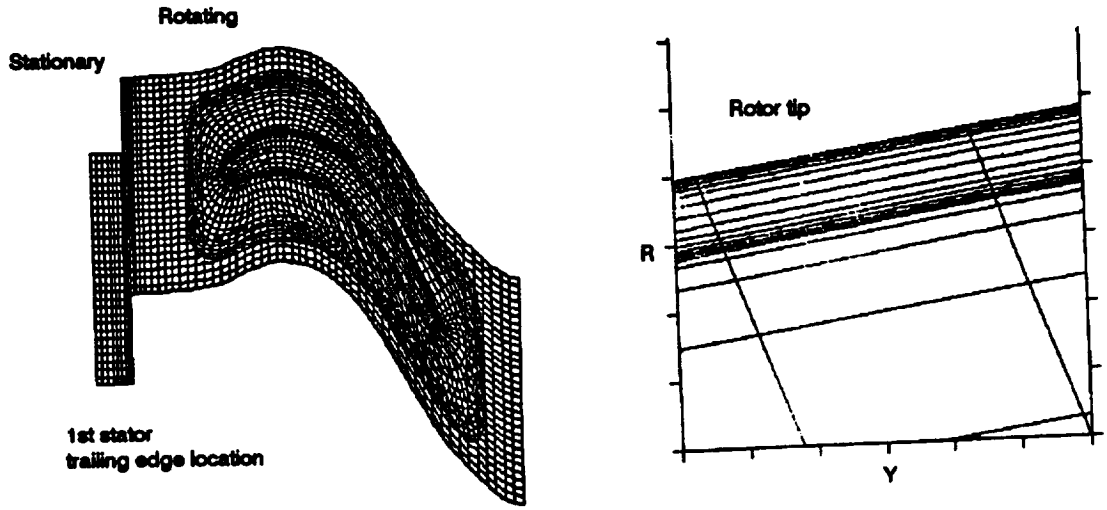

Steady vs. Unsteady Inlet Profile

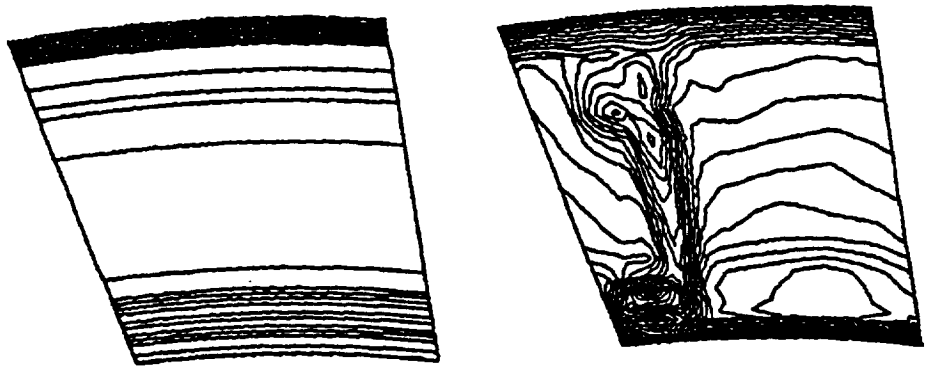

Figure 4.4.8a *Computational Grid and Inlet Profiles Used in Simulating Steady and Unsteady 3D Flows Through the UTRC Rotor.*

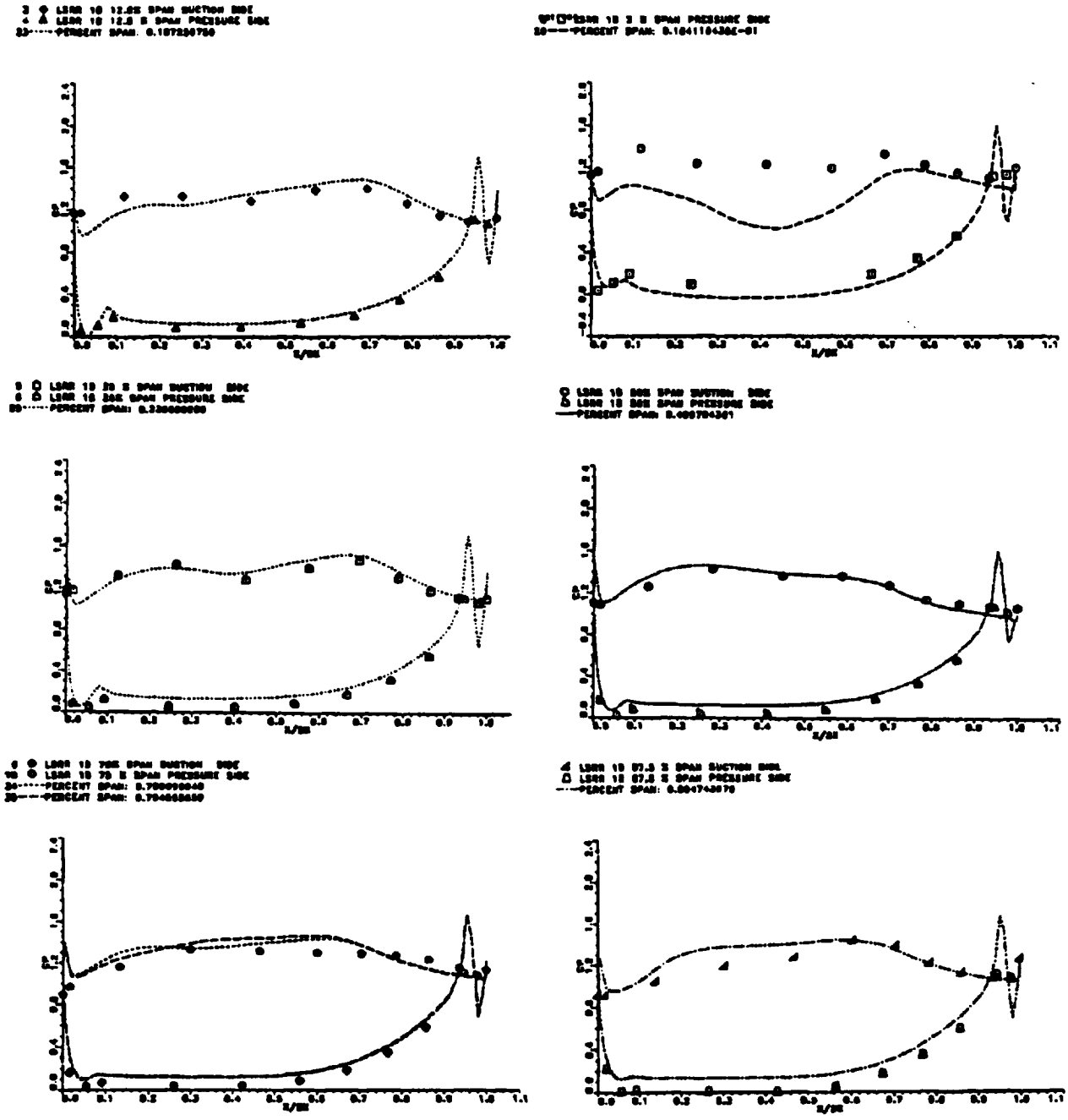

Figure 4.4.8b *A Comparison of Measured and Predicted Time–Averaged Airfoil Surface Static Pressure Coefficients for the UTRC LSRR Rotor Indicating Good Agreement.*

5. CODE APPLICATION

The verified CFD code was applied to simulate flow through two configurations to demonstrate that it can be used to compute the flow through both axial and radial turbomachines. This exercise indicates that the CFD code developed under the present program can be applied in the design optimization studies for rocket turbopumps to yield high performance and improved durability hardware. The results obtained from this exercise are discussed below.

5.1 Railly's Radial Impeller

Railly's impeller (Ekerol & Railly (1982)) was selected as one of the configurations in the code application task of the program to show that the code will provide accurate estimates of flows in radial (centrifugal) machines. This impeller is a low speed radial cascade with an outer diameter of 45 inches as shown schematically in Figure 5.1.1. Air enters this impeller radially after passing through a vaneless inducer which directs the flow from the axial to the radial direction. Large contraction in the inducer ensures uniform flow at the impeller inlet. The pitch to chord ratio of the impeller is 0.78 and the Reynolds number, based on radial chord (7.72 inches) and an exit relative velocity of 433,000. The span of the impeller is constant (3.5 inches). The airfoils are shrouded to ensure absence of leakage flows.

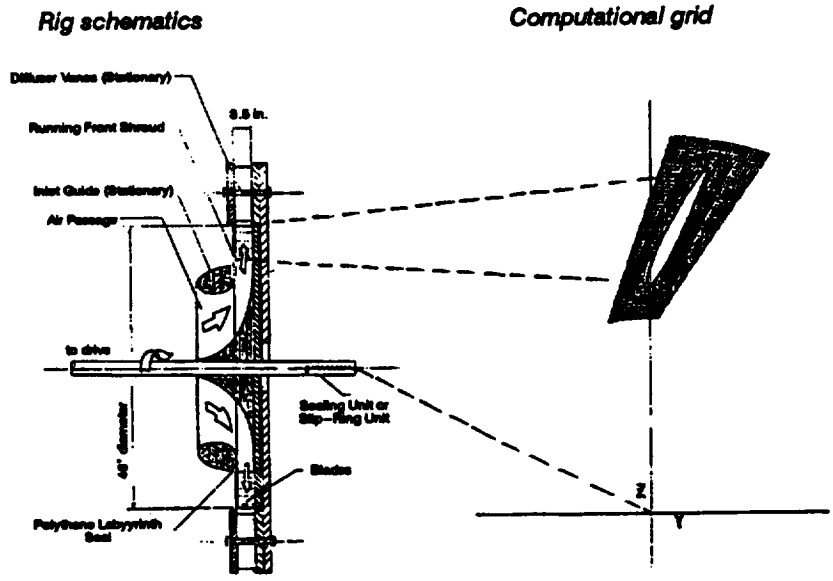

Figure 5.1.1 Code Application – Railly's Impeller.

Calculations were conducted in a fully turbulent mode by assuming a two–dimensional flow at the mid–span; effects of endwall boundary layers were accounted for through the use of stream–tube contraction ratio. Computational grids used in the code are shown in Figure 5.1.2. Predicted streaklines indicate separation of the flow on the airfoil suction side as indicated in Figure 5.1.3. Measured boundary layer thickness distribution along the airfoil suction side is shown in Figure 5.1.4. Experimental data indicate a large gradient in the boundary layer thickness around 66% of the chord on the airfoil suction side which is in close proximity of the onset of the separation zone predicted by the code (Figure 5.1.3) This comparison indicates that the code provides an accurate estimate for one of the most dominant features of the flowfield in radial impellers. Three–dimensional flow simulations were also initiated for this impeller; the solution was, however, not run to convergence due to the unavailability of computer resources.

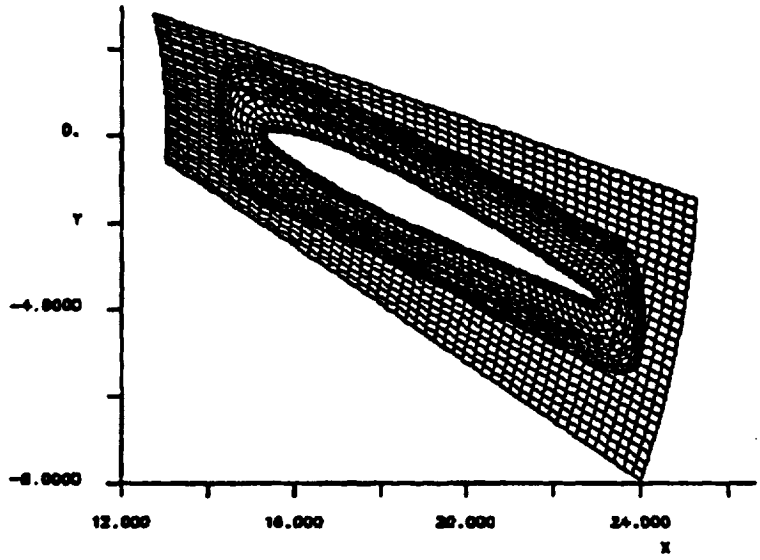

Figure 5.1.2 Grid Used in the Simulation.

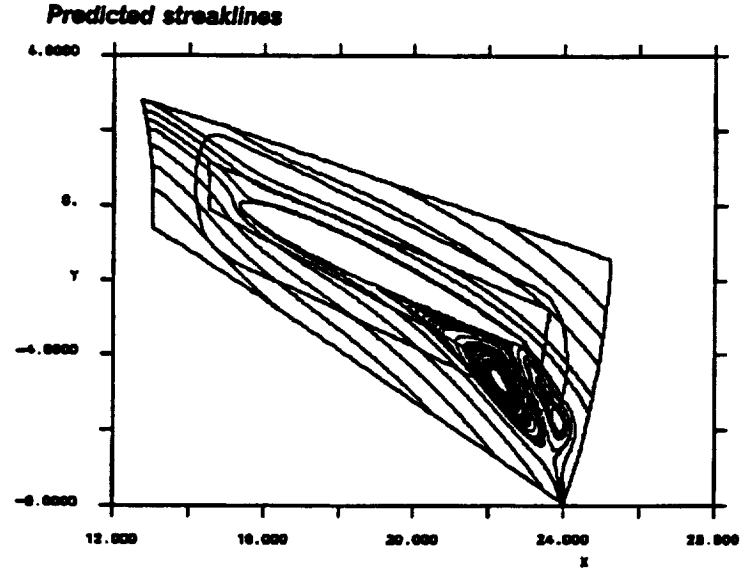

Figure 5.1.3 Code Application – Railly's Impeller (2D Steady Calculation).

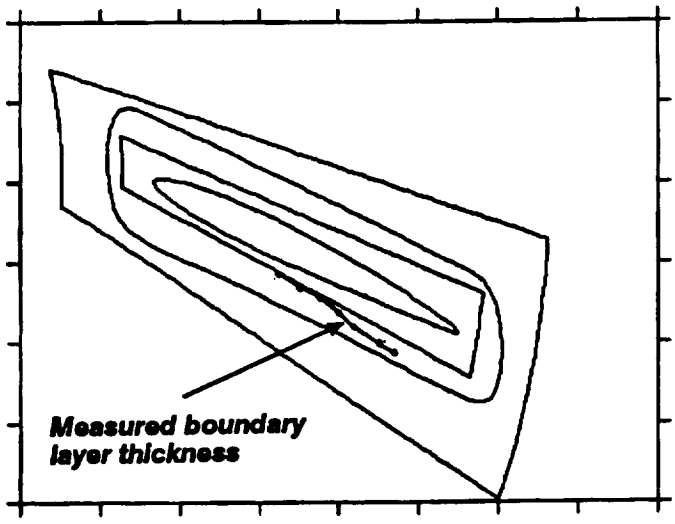

Figure 5.1.4 *Code Application – Railly's Impeller (2D Steady Calculation).*

5.2 Pratt & Whitney Full Scale Turbine

This configuration was selected to demonstrate that the CFD code used in the present program provides a more accurate estimate of unsteady loads on airfoils than the Euler code; the latter code is extensively used in the current design process for turbomachines.

The need to establish the relative accuracy of the unsteady loading prediction capability of an Euler and a Navier–Stokes code became apparent in the design of the Space Shuttle Main Engine (SSME) alternate turbopump development (ATD) high pressure oxygen turbopump (HPOT) and high pressure fuel turbopump (HPFTP) turbine blades. Analysis of the first stage blades of each turbine indicated possible resonance problems in crucial operating ranges of the turbopumps. Unsteady aerodynamic simulations were conducted for the two turbines (Griffin & Rowey(1993)) to support further investigations of the dynamic responses of the first stage turbine blades. These simulations were conducted at the mean radius of the two turbines by utilizing two dimensional unsteady Euler (Ni et al (1990)) and Navier Stokes (Gundy–Burlet et al(1991)) codes. Both codes were found to yield almost identical time–averaged loadings. Unsteady axial and tangential loadings for the first blades of the two turbines were, however, found to be very different as shown in Figure 5.2.1, which also shows a comparison of the time–average loadings for the two first blades. The unsteady loads predicted by the Navier–Stokes code were almost an order of magnitude larger than those predicted by the Euler code. The main objective of the present application is to evaluate the unsteady loading prediction capabilities of the unsteady Euler and Navier Stokes codes for a subsonic axial flow turbine.

A brief discussion of the experimental turbine rig, where appropriate data are available to verify the predictive capabilities of the two codes, is given below.

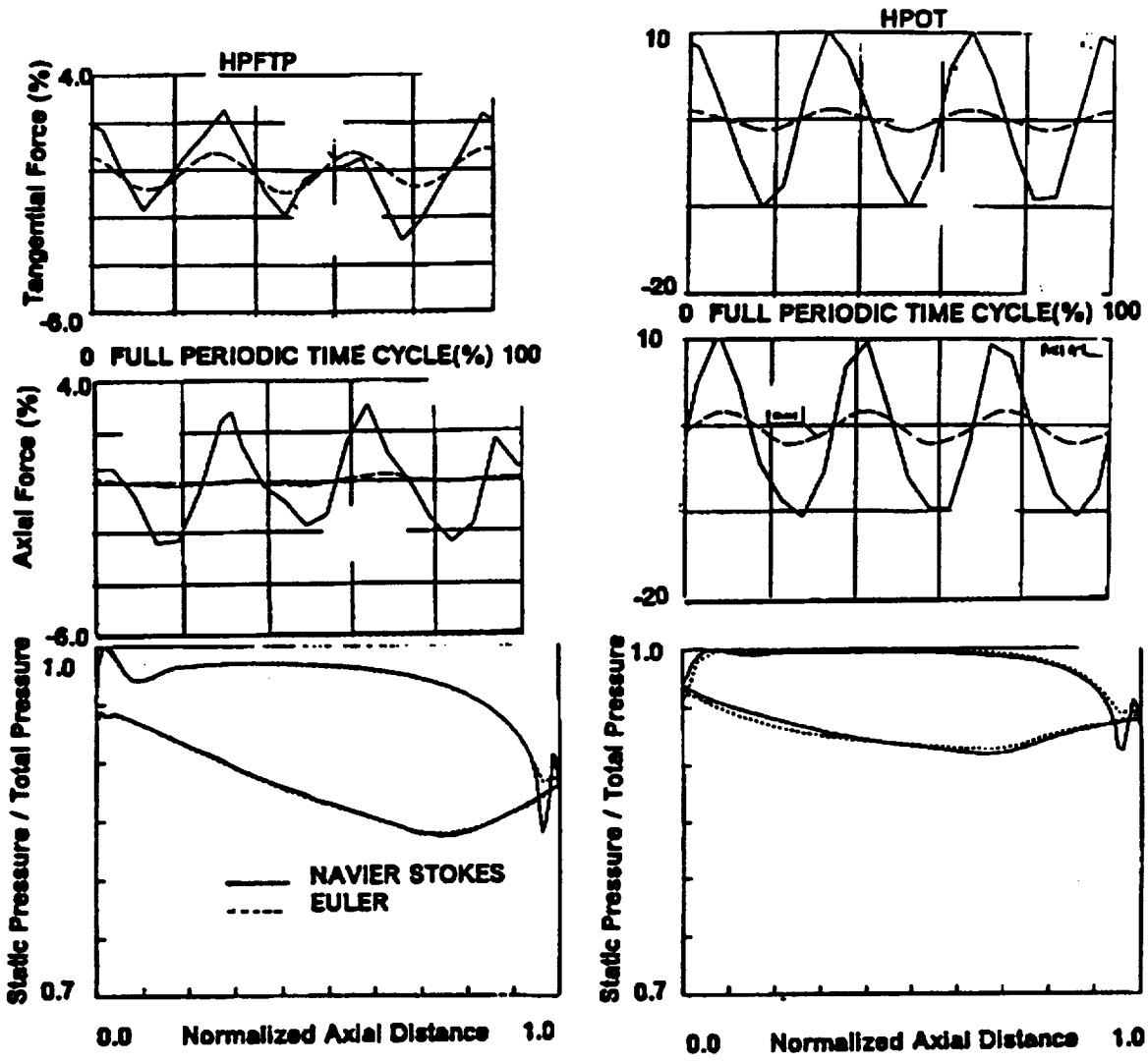

Figure 5.2.1 *Numerical Simulations Conducted For The HPOT And HPFTP Turbines (Griffin & Rowey (1993)) By Using Two–Dimensional Unsteady Euler And Navier–Stokes Codes Show:*
I) Almost Identical Time–averaged Loadings; But
II) Smaller Unsteady Loads From The Euler Code Than Those From The Navier–Stokes Code.

Experimental Rig

The experimental rig consists of a two stage turbine operating at an overall pressure ratio of 4.5 and a Reynolds number of about 700,000 for the first stage stator. The schematics of the rig and measurement locations are shown in Figure 5.2.2. Airfoil surface static pressures are measured at various spanwise locations for all airfoil rows. Overall two stage turbine performance is measured by traversing the flow at the exit of the turbine, using pressure and temperature rakes in four quadrants. Leading edge Kiel head probes at the second stator inlet are used to define the first stage performance. Unsteady total pressure data are acquired downstream of the turbine to quantify interaction between

airfoil rows. Laser Doppler Velocimetry (LDV) is used to acquire unsteady velocity data in between the airfoil rows.

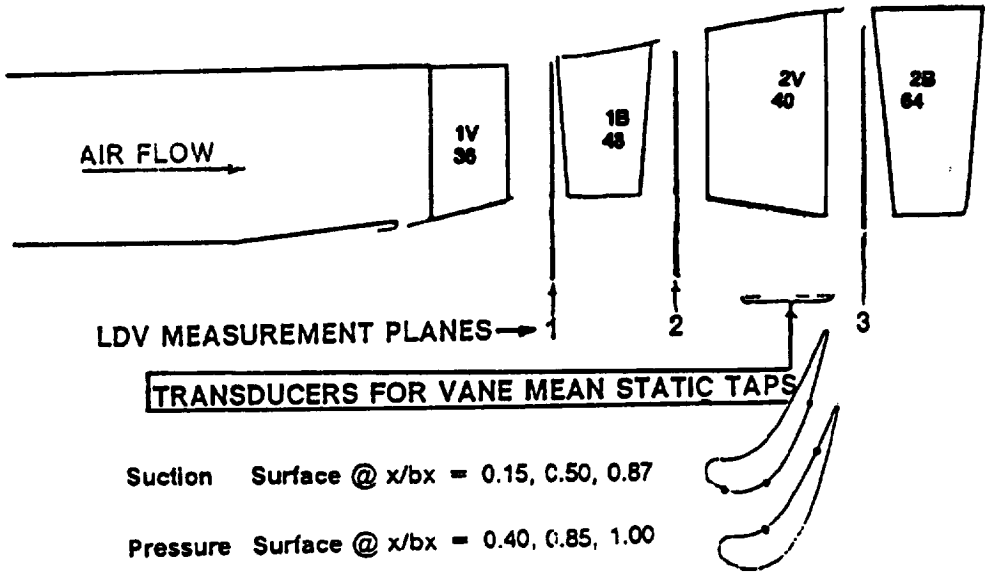

Figure 5.2.2 *Schematics of the Two–Stage Turbine Rig Along With the Measurement Locations.*

Unsteady surface static pressures were measured at several locations at the mid–span of the second stator. The measurements were obtained using infinite tube probes coupled to conventional airfoil surface static pressure taps. The infinite tube probe technique permits unsteady measurements to be made on the surface of the airfoil without altering the surface contours, as would be required with the installation of surface mounted high–response pressure transducers. It also removes the transducers from direct contact with the flow field, thus providing a more durable high–response instrumentation system.

In this application, the unsteady static pressures were obtained at six locations in a stator passage. Measurements were made at 15%, 50%, and 87% chord on the suction side of one airfoil and at 40%, 85% and 100% chord on the pressure side of an adjacent airfoil. The infinite tube probes were located outside the turbine case 16 to 20 inches from the pressure taps, resulting in a usable frequency response of up to 11 kHz at the rig operating pressures and temperatures. This is above the rotor blade passing frequencies of 6 to 7 kHz but not adequate to capture any higher harmonics. (Note: work is currently in progress to reduce the sense tube line lengths to improve the response of the probes to over 20 kHz).

To determine the pressure fluctuations at the airfoil surface measurement location, the data from the infinite tube probes must be compensated for the attenuation and phase shift in the connecting lines. Typically, one hundred revolutions of data are acquired for each test point. Each revolution of data is then frequency compensated using the technique described by Nyland et al(1971). The compensated data is then ensemble averaged to produce the average periodic and random components of the data for one rotor revolution. Levels of periodic unsteadiness are obtained by examining the fluctuations of the periodic signals and levels of random unsteadiness are obtained by examining the mean levels of the random signals.

Solution Procedures (CFD Codes & Models)

Euler Code

Three dimensional multistage unsteady Euler flow solver, developed by Ni (1989,90), is used to conduct inviscid numerical simulations. This solver utilizes an explicit time–accurate finite volume numerical scheme with the cell–vertex centered solution algorithm to integrate the unsteady Euler equations to provide a solution for flow in multistage turbomachines. The scheme is second order accurate both in time and space on a smooth computational mesh. Detailed numerical equations for implementing the scheme and methods for applying various types of boundary conditions are given in Ni et al(1989). For time–accurate simulations of multistage flow, a cubic interpolation method is used for transfer of flow information across the interface boundaries dividing stationary and rotating airfoil rows as discussed by Ni et al (1989,90). A surface drag force model similar to the one described by Denton(1990), is used to provide the effect due to viscosity near airfoil and endwall surfaces. The boundary conditions applied for the present simulations are flow tangency on solid surfaces, prescribed spanwise and tangential distributions of total pressure, total temperature and flow angles at inlet to the multistage turbine. The number of grid points used in simulations and their distributions along with the operating conditions are given in Figures 5.2.3 & 5.2.4 for the two– and three–dimensional simulations.

Figure 5.2.3 *Computational Grid Used to Simulate Two–Dimensional Unsteady Flow Through the First Rotor and Second Stator of the Rig.*

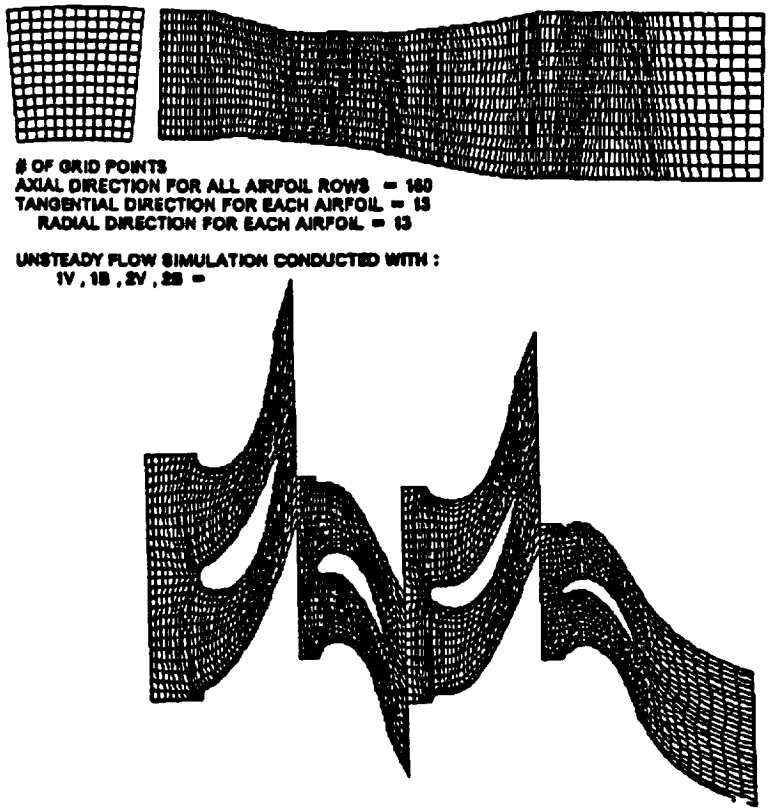

Figure 5.2.4 *Computational Grid Used to Simulate Three–Dimensional Steady and Unsteady Flow Through the Multistage Two–Stage Rig by Using the Euler Code.*

Navier–Stokes Code

Two–dimensional version of the three–dimensional unsteady Navier Stokes code, developed by Rai (1989), is used to conduct the viscous numerical simulation. The numerical procedure consists of a time marching, implicit, third order spatially accurate, upwind, finite difference scheme. The inviscid fluxes in the code are discretized according to the scheme developed by Osher (1982). The viscous fluxes are calculated using standard central differences. An alternative direction, approximate–factorization technique is used to compute the time rate change in the primary variables. In addition, an inner Newton iteration is used to increase stability and to reduce linearization errors. The code is modified to account for the 'stream–tube' ('H–Ratio') effects in a manner proposed Rangwalla et al (1991).

The two–layer Baldwin–Lomax (1978) turbulence model is used to compute the turbulent viscosity. This turbulence model is modified to account for the transitional nature of the airfoil suction surface boundary layer by using the intermittency factor approach suggested by Sharma (1987).

Modified Turbulent Viscosity = F * Turbulent Viscosity B–L

F = Intermittency Factor

= 1.–exp (–(Rθ**2.5–Rθc**2.5))/Rθc**2.68)

Rθ = Reynolds Number based on momentum loss thickness of the airfoil boundary layer

Rθc = Critical Reynolds Number = 40/Tu**0.5

Tu = Free stream turbulence level

Free stream turbulence level is calculated by using entropy value at the edge of the stator boundary layer. Circumferential variation of flow properties at the interface between the rotor and the second stator is used to determine a relation between entropy and turbulence for application in the second stator. Turbulence level is specified as an input value to the rotor.

Multiple zonal grids are used to discretize the rotor/stator flow field and to facilitate relative motion of the rotor (Rai(1989)). A combination of O– and H–grid sections are generated in the blade–to– blade direction extending upstream of the rotor leading edge to downstream of the stator trailing edge. Algebraically generated H–grids are used in the region upstream of the leading edge to downstream of the trailing edge and in the inter blade region. The O–grids, which are body fitted to the surfaces of the airfoils and generated by using elliptic solution procedure, are used to properly resolve the viscous flow in blade passages and to facilitate application of algebraic turbulence models. Computational lines within the O–grids are stretched in the blade–normal direction with a fine spacing at the wall Figure 5.2.5 illustrates the grid topology used in the present simulation. Boundary conditions used in the current simulation are no slip condition on solid surfaces; prescribed spanwise and tangential distributions of total pressure, radial and tangential flow angles; and Reimann invariant at the inlet; prescribed static pressure at the exit.

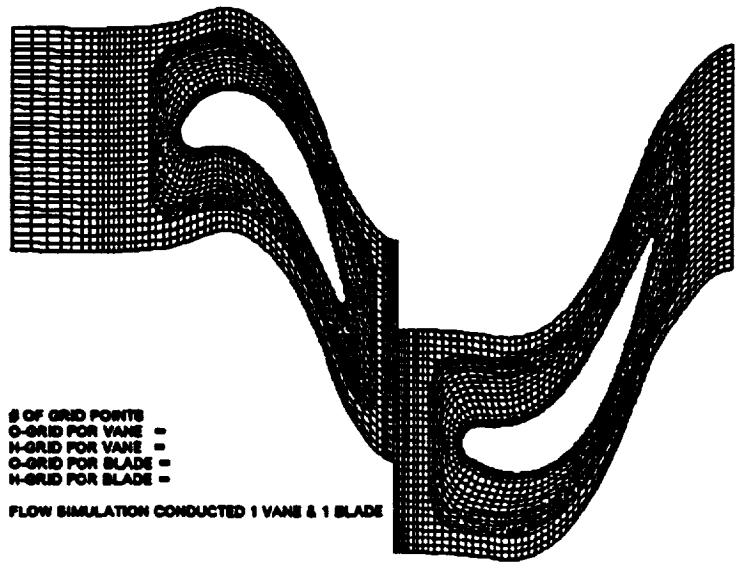

Figure 5.2.5 *Computational Grid Used to Simulate Viscous Flow Through the Rotor and the Stator by Using an Unsteady Navier–Stokes Code.*

Discussion of Results

Unsteady two–dimensional flow simulations were initially conducted to evaluate the steady and unsteady loading prediction capabilities of the Euler and the Navier–Stokes codes. Predicted envelope of unsteady surface static pressures on the stator from these simulations are shown in Figure 5.2.6. It is apparent from this figure that the Navier Stokes code predicts larger magnitudes of unsteady pressures than the Euler code over the entire airfoil surface. This result is similar to that obtained in ATD turbines as shown in Figure 5.2.1. A comparison of the experimental data with predicted results indicates that even the Navier–Stokes code underestimates the unsteady pressures on the airfoil. In addition, analysis of numerical results indicates that the two–dimensional simulation of the turbine has yielded a lower inlet Mach number and a larger negative incidence angle for the stator than these were present in the experiment.

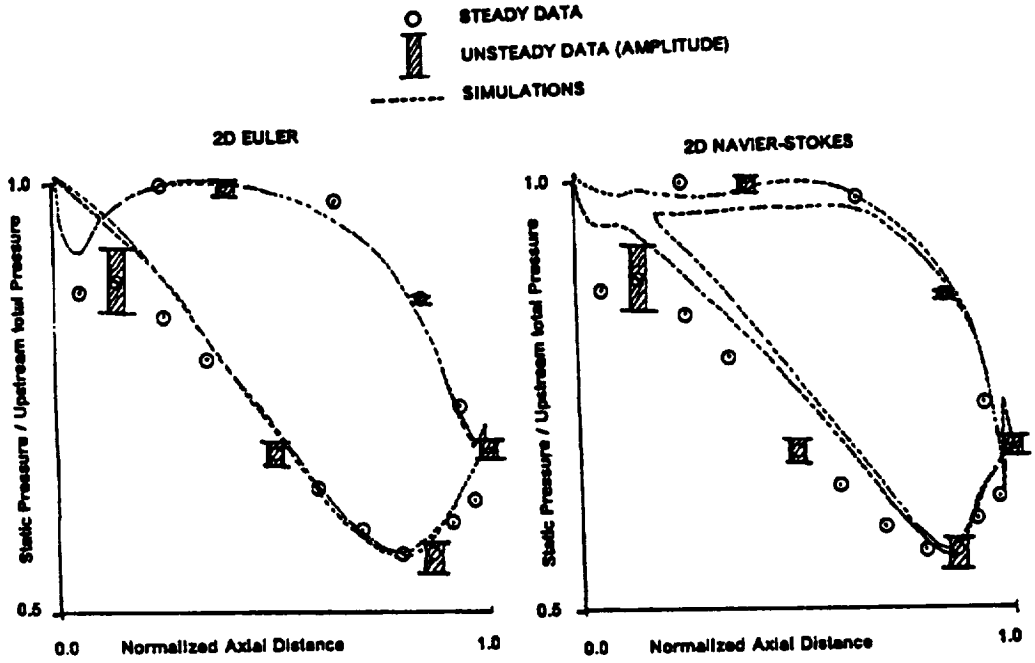

Figure 5.2.6 *Two–Dimensional Unsteady Flow Simulations Show Larger Levels of Unsteadiness From The Navier–Stokes Code Than Those From The Euler Code. Both Simulations, However, Do Not Accurately Model The Inlet Condition To The Stator.*

A review of the steady three–dimensional multistage Euler flow simulations of the entire two stage turbine showed that the mid–span region of the second stator was strongly influenced by the endwall secondary flows and flowpath divergence. These steady simulations yielded excellent agreement with the time–averaged loadings on airfoil surfaces, predicted results at the mid–span of the first rotor and the second stator are compared to the experimental data in Figure 5.2.7. Unsteady three–dimensional flow simulations were then conducted for the two stage turbine using the Euler code. Predicted envelope of unsteady pressures for the second stator from this simulation is shown in Figure 5.2.8, amplitudes of measured unsteady pressures are also identified in this figure. Results shown in this figure indicate that the 3D Euler code predicts larger amplitudes of unsteady pressures on the second stator than the 2D code primarily because it provides more realistic inlet flow conditions to the second stator. The predicted magnitudes of unsteady pressure are, however, still lower than the experimental data.

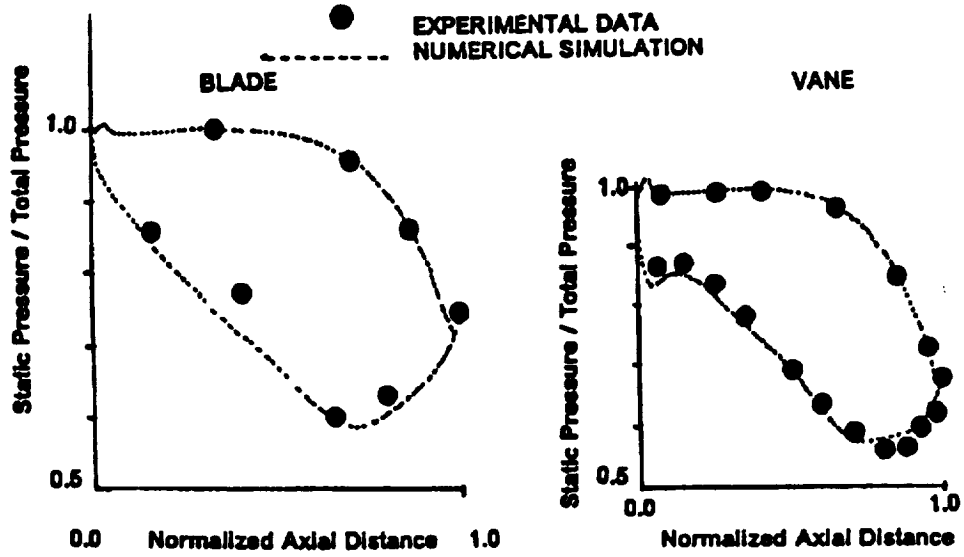

Figure 5.2.7 *Three–Dimensional Steady Multistage Euler Code Yields Good Agreement with the Airfoil Loading Data for the Rotor and the Stator.*

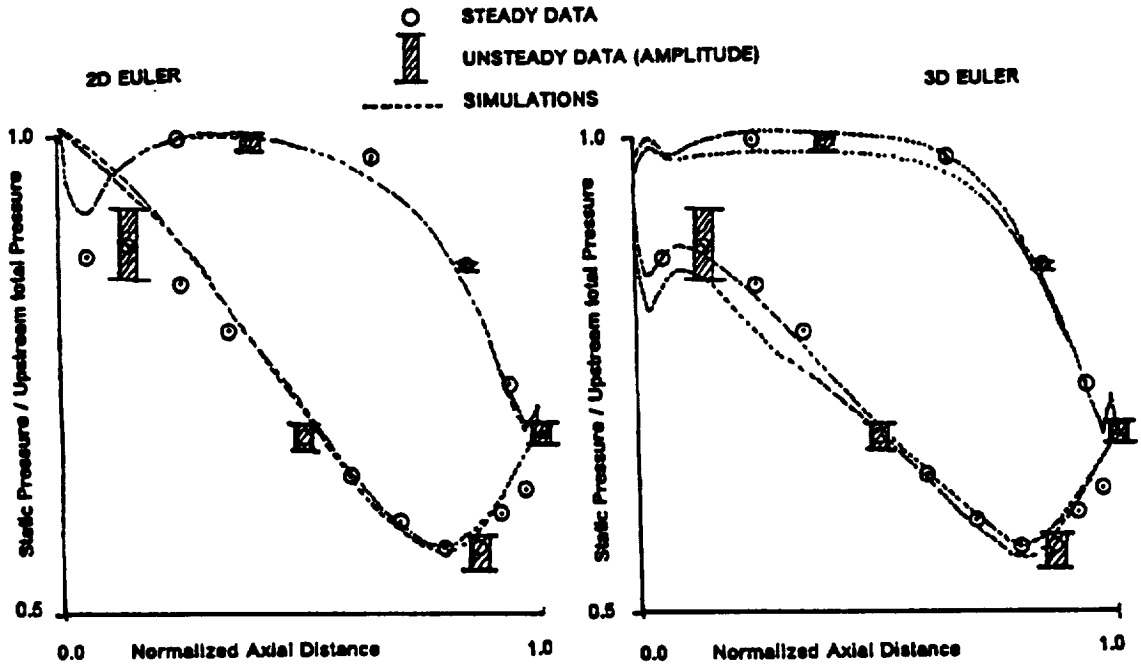

Figure 5.2.8 *Three–Dimensional Multistage Unsteady Euler Code Predicts Higher Unsteadiness Than the 2D Code, But it Still Underestimates Unsteady Pressure Amplitudes on the Airfoil Suction Side.*

One is tempted to conclude at this stage that only a 3D unsteady Navier Stokes code can provide accurate predictions of unsteady pressures in this experiment. Computational resources required to execute a 3D unsteady Navier Stokes for this configuration are, however, prohibitive. The approach undertaken in the present investigation was to use the two–dimensional unsteady Navier Stokes code which was modified to account for the endwall flow effects through the use of 'steam tube' (H–ratio)

variation. The distribution of stream tube variation was calculated from the numerical results obtained from the 3D steady multistage Euler flow simulation.

Steady two–dimensional flow simulations were first obtained by using the cascade version of the unsteady Navier Stokes code for the rotor and the stator with the 'H–ratio' variation calculated above. Calculated airfoil surface static pressure distributions from these cascade simulations are compared to the experimental data obtained by using steady pneumatic instrumentation in Figure 5.2.9. Good agreement is shown between the experimental data and predictions.

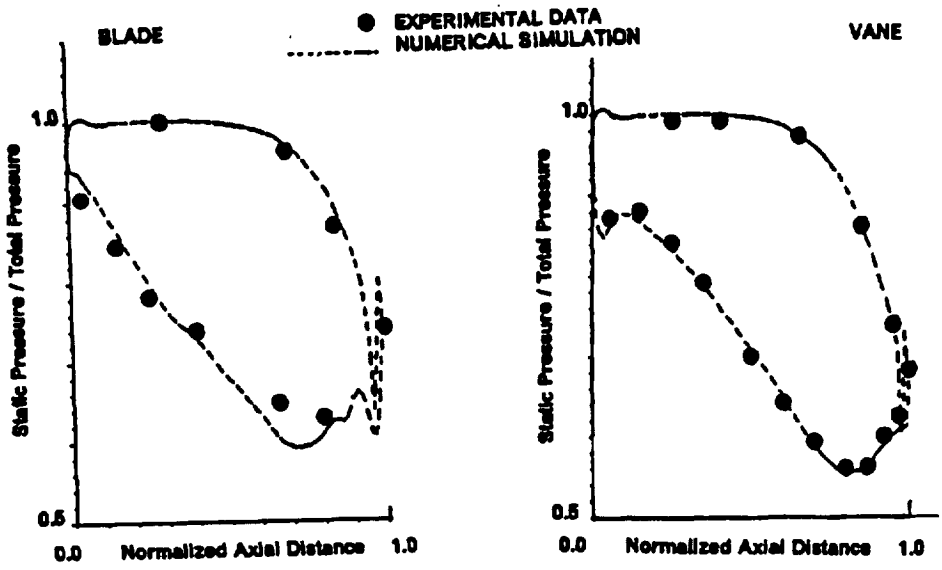

Figure 5.2.9 *Steady Loadings on the Rotor and the Second Stator Well Predicted by 2D Steady Navier Stokes Code Modified to Account for "H–ratio" Effect.*

Two–dimensional unsteady flow simulations were then conducted for the rotor and the second stator by using the 2D Navier Stokes code modified for the 'H–ratio' effect. The predicted envelope of unsteady pressure from this simulation for the stator is compared to the experimental data in Figure 5.2.10. Measured amplitudes of unsteady pressures are also identified in this figure. Good agreement between the unsteady experimental data and predictions for the stator clearly demonstrates that a Navier–Stokes code is needed to estimate unsteady loads in turbine rows. This result also shows that a two–dimensional code, modified to account for 'H–ratio' effects, is a cost effective alternative to three–dimensional unsteady Navier Stokes codes, at least for estimating the levels of unsteady loads on airfoil surfaces.

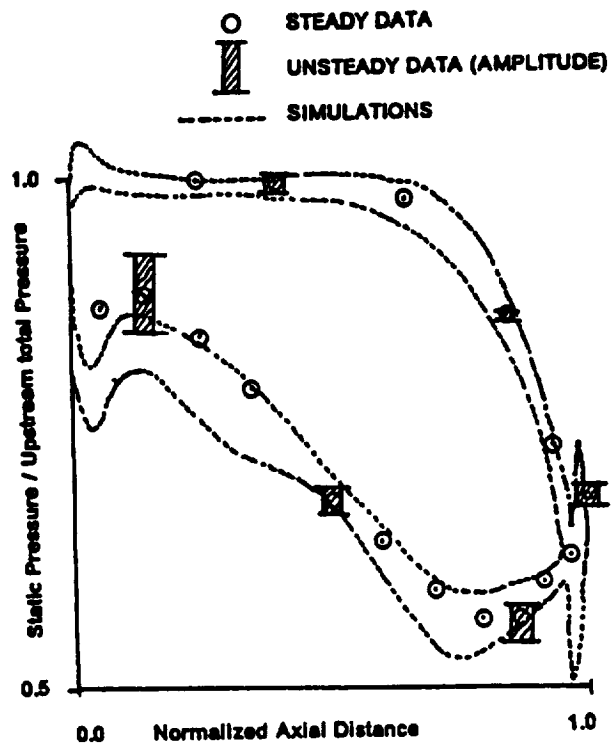

Figure 5.2.10 *Envelope of Loadings on the Stator Predicted by Using 2D Unsteady Navier–Stokes Code with "H–ratio" Modifications; Amplitudes of Unsteady Pressures on the Airfoil Suction Side Fairly Well Predicted.*

Numerical results from the above unsteady flow simulation were processed to establish the levels of unsteady losses for the second stator as it was affected by the unsteady interaction with the upstream rotor. Periodic variation in the loss for the second stator is shown in Figure 5.2.11. The second stator is found to yield almost 50% higher time–averaged loss in the unsteady flow environment than the loss calculated for that airfoil in a steady flow environment. The predicted increase in the time–averaged loss for this airfoil is similar to that measured by Hodson (1983) as shown in Figure 5.2.12. The predicted periodic variation in unsteady losses is similar to those experimentally measured for the second stator in the UTRC LSRR as shown in Figure 5.2.13. Results from this application indicate:

- An unsteady Navier Stokes code provides a more accurate estimate of unsteady loads in a multistage turbine environment than an Unsteady Euler code.

- 2D unsteady Navier Stokes codes, modified to account for 'H–ratio' effect, are a cost effective alternative to more expensive and computer intensive 3D unsteady Navier Stokes codes to estimate unsteady loads in turbines.

- Time–averaged losses for airfoils in an unsteady flow environment are larger than estimated for those airfoils in a steady flow environment and unsteady Navier Stokes codes can model this flow phenomena accurately.

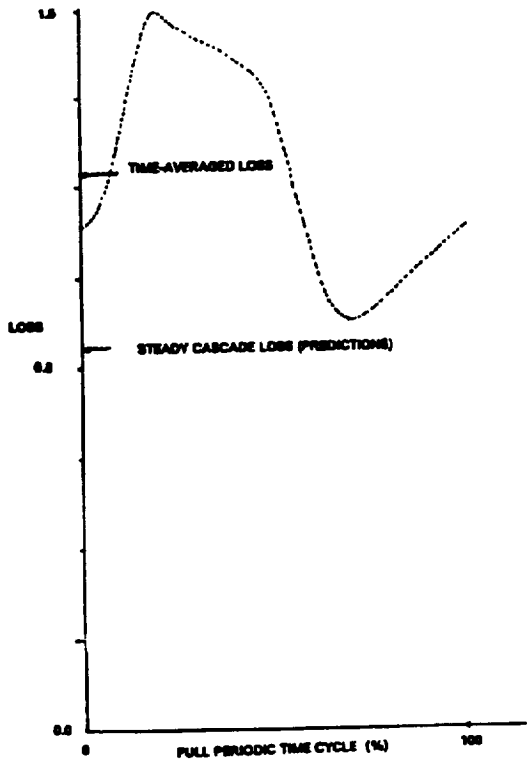

Figure 5.2.11 *Two–Dimensional Unsteady Navier–Stokes Code Predicts Periodic Variation in Loss for the Stator as it is Influenced by the Upstream Rotor. Time–averaged Loss for the Stator is Almost 50% Larger Than Calculated for this Airfoil in a Steady Flow Environment.*

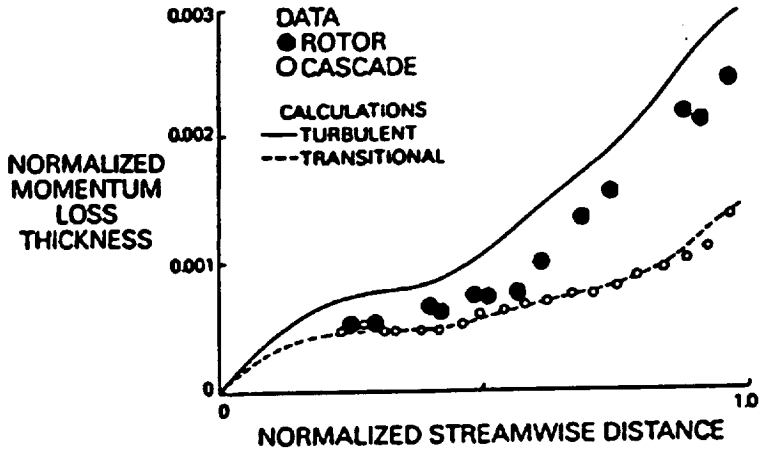

Figure 5.2.12 *Measured Streamwise Distribution of Time–Averaged Boundary Layer Momentum Loss Thickness (Hodson (1983)) Show Larger Values For Rotors (Unsteady Environment) Than Those Measured For The Same Airfoil Sections In a Steady Cascade Environment. The Rotor Data Are Bracketed By The Transitional and Fully Turbulent Calculations (Sharma et al. (1988)).*

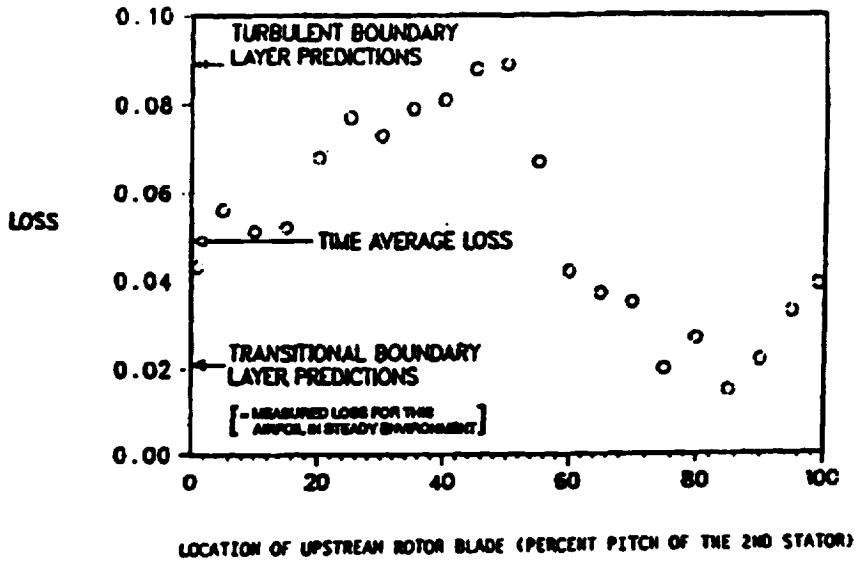

Figure 5.2.13 *Mid–Span Losses On The 2nd Stator As Influenced By The Unsteadiness Generated By The Upstream Rotor Airfoil Wake.*

6. CONCLUSIONS AND FUTURE DIRECTION

CFD code developed by Rai (1987) at NASA ARC has been modified to account for transitional flows on airfoil surfaces. Improved turbulence models have been implemented in the code to facilitate account of physical phenomena such as surface roughness, rotation, turbulence level and extra rates of strain on the development of viscous flows in turbopumps. This code has been shown to yield good estimates of:

- Airfoil loadings, heat loads, losses and secondary flows in a two– and a three–dimensional steady flow environment (Griffin and Belford (1990), Griffin et al. (1990)).
- Tip leakage flows.
- Unsteady loads, time–averaged loadings and flowfield in an unsteady flow environment.
- Unsteady variation of losses and increased time–averaged loss than measured for airfoils in a steady flow environment.
- Flow separation in a radial impeller.

Grid sensitivity studies conducted, in the present program and those conducted by Dorney et al. (1992) by using a version of the present CFD code, indicate that almost 550,000 grid points are needed to accurately estimate profile and secondary losses in turbines.

Studies conducted in the present program and those conducted by other investigators using versions of the present code can predict following known effects of unsteadiness in turbine stages:

- Segregation of hot and cold air in turbine rotors (Dorney, Davis and Sharma (1990)).
- Periodic elimination of rotor secondary flow vortices in a turbine stage (Ni and Sharma (1990)).
- Amplitudes of unsteady pressures in a turbine stage (Rai and Madavan (1989)). Present code yields more realistic estimates of unsteady loads than an unsteady Euler code (Sharma et al. (1992)).
- Time–averaged losses are higher in an unsteady flow environment than measured for the same airfoil in a steady flow environment (Sharma et al. (1992)).

Future work in this area needs to focus in numerical investigations to isolate and identify loss generation mechanisms to provide guidance to designers. These investigation may focus on identifying:

- Loss production mechanisms due to secondary flows in airfoil rows.
- Loss production and control mechanisms due to tip leakage flows.
- Loss production due to steady and unsteady flow interactions in multi–stage machines.

REFERENCES

Baldwin, B. S., and Lomax, H., "Thin Layer Approximation and Algebraic Model for Separated Turbulent Flow," AIAA Paper 78–257, Huntsville, Ala., 1978.

Beam, R. M. and Warming, R. F., "An Implicit Factored Scheme for the Compressible Navier–Stokes Equations," AIAA Paper 77–645, 1977.

Blair, M. F. and Werle, M. J., "The Influence of Free Stream Turbulence on Zero Pressure Gradient Fully Turbulent Boundary Layer", UTRC/R80–914388–12, Sept 1980.

Blair, M. F. and Werle, M. J., "Combined Influence of Free–Stream Turbulence and Favorable Pressure Gradients on Boundary Layer Transition and Heat Transfer", UTRC/R81–914388–17, March 1981.

Blair, M. F., "Influence of Free Stream Turbulence on Boundary Layer Transition in Favorable Pressure Gradients", Journal of Engineering for Power, Vol. 104, No. 4, Oct. 1982, pp 743–750.

Blair, M. F., "An Experimental Study of Heat Transfer in a Large–Scale Turbine Rotor Passage," ASME Paper #92–GT–195, 1992.

Blair, M. F., Dring, R. P. and Joslyn, H. D., "The Effects of Turbulence and Stator–Rotor Interactions on Turbine Heat Transfer Part I, Design Operating Conditions", ASME Paper #88–GT–125, 1988.

Boynton, J. L., Tabibzadeh, R. and Hudson, S. T., "Investigation of Rotor Blade Roughness Effects on Turbine Performance," ASME Paper #92–GT–297, 1992.

Bradshaw, P., "Outlook for Three–Dimensional Procedures," AFOSR–IFP–Stanford Conference, Thermoscience Division, Stanford University, California, 1968.

Bradshaw, P., "Effect of Streamline Curvature on Turbulent Flow," AGARD–CP–169, 1973.

Butler, T. L., Sharma, O. P., Joslyn, H. D., and Dring, R. P, 1989, "Redistribution of an Inlet Temperature Distortion in an Axial Flow Turbine Stage,: Journal of Propulsion and Power, Vol. 5, pp.64–71, 1989.; also AIAA Paper No. 86–1468, 1986.

Caspar, J. C., Hobbs, D. E., and Davis, R. L., "The Calculation of Two–Dimensional Compressible Potential Flow in Cascades Using Finite Area Techniques," AIAA Paper 79–0007, Jan. 1979.

Chakravarthy, S. and Osher, S., 1982, "Numerical Experiments with the Osher Upwind Scheme for the Euler Equations," AIAA Paper #82–0975, 1982.

Chakravarthy, S. R., Szema, K–Y, Goldberg, U. C., and Gorski, J. J., "Application of a New Class of High Accuracy TVD Schemes to the Navier–Stokes Equations," AIAA Paper 85–165, Reno, Nev., 1985.

Consigny, H. and Richards, B. E, "Short Duration Measurements of Heat Transfer Rate to a Gas Turbine Rotor Blade", Journal of Engineering for Power, Vol. 104, No. 2 July 1982, pp 542–551.

Crawford, M. E., and Kays, W. M., "STAN–5––A Program for Numerical Computation of Two Dimensional Internal and External Boundary Layer Flows," NASA CR–2742, 1976.

Davis, R. L., Ron–Ho Ni, and Carter J. E., "Cascade Viscous Flow Analysis Using the Navier–Stokes Equations," AIAA Paper 86–0033, Reno, Nev., 1986.

Dean, R. C., "On the Necessity of Unsteady Flow in Fluid Machines," ASME J. Basic Eng., March 1959, pp. 24–28.

Denton, J. D., "A Time Marching Method for Two and Three Dimensional Blade to Blade Flow," A. R. C. R. & M 3775, 1975.

Denton, J. D., "The Use of a Distributed Body Force to Simulate Viscous Flow in 3D Flow Calculations," ASME Paper # 86–GT–144, 1986.

Denton, J., "Calculation of Three–Dimensional Viscous Flows Through Multistage Turbine;, ASME Paper # 90–GT–19, 1990.

Dishart, P. D. and Moore, J., "Tip Leakage Losses in a Linear Turbine Cascade," ASME Paper #89–GT–56, 1989.

Doorly, D. J., Oldfield, M. L. G., and Scrivener, C. T. J., 1985, "Wake–Passing in a Turbine Rotor Cascade," Heat Transfer and Cooling in Gas Turbines, AGARD–CP–390, pp. 7–1 to 7–8, 1985.

Dorney, D.J., Davis, R.L. and Sharma, O.P., "Two–Dimensional Inlet Temperature Profile Attenuation in a Turbine Stage ", ASME Paper #91–GT–408, 1991.

Dorney, D. J., Davis, R. L. and Edwards, D. E., "Investigation of Hot–Streak Migration and Film Cooling Effects on Heat Transfer in Rotor/Stator Interacting Flows," N00140–88–C–0677–Report 1, UTRC Report 91–29, April 1992.

Dring, R. P., Joslyn, H. D., Hardin, L. W., and Wagner, J. H., "Turbine Rotor–Stator Interaction," Journal of Engineering for Power, Vol. 104, Oct. 1982.

Ekerol, H. and Railly, J. W., "A Theory for Boundary Layer Growth on the Blades of a Radial Impeller Including Endwall Influence," ASME Paper #82–GT–90, 1982.

Graziani, R. A., Blair, M. F., Taylor, J. R., and Mayle, R. E., "An Experimental Study of Endwall and Airfoil Surface Heat Transfer in a Large Scale Turbulent Blade Cascade," ASME Journal of Engineering for Power, Vol. 102, No. 2, April 1980, pp. 257–267.

Greitzer, E. M., "An Introduction to Unsteady Flow in Turbomachines," Lecture #7, MIT, Cambridge, 1987 (private communication to O. P. Sharma).

Griffin, L. W. and McConnaughey, H. V., "Prediction of the Aerodynamic Environment and Heat Transfer for Rotor–Stator Configurations," ASME Paper #89–GT–89, 1989.

Griffin, L. W. and Belford, K. A., "Prediction of the Aerodynamic and Thermal Environment in Turbines," ASME Paper #ASME–GT–227, 1990.

Griffin, L. W., Belford, K. A., Sharma, O. P. and Ni, R. H., "3D Turbopump Flowfield Analysis – Validation of the Steady Cascade Version of ROTOR3," Presented at the 1990 ETO Meeting in Huntsville, Alabama, 1990.

Griffin, L., and Rowey, R., "Analyses of Turbine Blades for Space Shuttle Main Engine – Part 1: Aerodynamic Environment," Paper to be Presented at the 1993 ASME Gas Turbine Meeting.

Gundy–Burlet, K. L., "Computations of Unsteady Multistage Compressors Flows in a Workstation Environment," ASME Paper #91–GT–336, 1991.

Hah, C., "A Navier–Stokes Analysis of Three–Dimensional Turbulent Flows Inside Turbine Blade Rows at Design and Off–Design Conditions; ASME Paper #83– GT–40, 1983.

Hodson, H. P., "The Development of Unsteady Boundary Layers in the Rotor of an Axial–Flow Turbine", AGARD Conference Proceedings No. 351, Viscous Effects in Turbomachines, 1983.

Hodson, H. P., "Measurements of Wake Generated Unsteadiness in the Rotor Passages of Axial Flow Turbines", ASME Paper 84–GT–189, 1984.

Hodson, H. P., "An Inviscid Blade–to–Blade Prediction of a Wake–Generated Unsteady Flow", ASME Paper 84–GT–43, 1984.

Hourmuziadis, J., "Aerodynamic Design of Low Pressure Turbines," Blading Design for Axial Turbomachines, AGARD Lecture Series #167, 1989.

Huber, F. W.; Rowey, R. J.; and Ni, R–H.: Application of 3D Flow Computation to Gas Turbine Aerodynamic Design. AIAA–85–1216, 1985.

Hung, C. M. and Buning, P. G., "Simulation of Blunt–Fin Induced Shock Wave and Turbulent Boundary Layer Interaction," AIAA Paper 84–0457, January, 1984.

Johnston, J. P., "The Effects of Rotation on Boundary Layers in Turbomachinery Rotors," Report MD–24, Thermosciences Division, Department of Mechanical Engineering, Stanford University, Stanford, California, 1970.

Jones, W. P. and Launder, B. E. "The Calculation of Low–Reynolds Number Phenomenon with a Two–Equation Model of Turbulence", International Journal of Heat and Mass Transfer, Vol. 16, 1973, pp 1119–1130.

Joslyn, H. D., Dring, R. P., and Sharma, O. P., "Unsteady Three–Dimensional Turbine Aerodynamics," ASME Paper 82–GT–161, April 1982.

Kerrebrock, J. L. and Mikolajczak, A. A "Intra–Stator Transport of Rotor Wakes and Its Effect on Compressor Performance," ASME J. Eng. for Power, Oct. 1970, pp. 359–370.

Klebanoff, P. S., "Characteristics of Turbulence in a Boundary Layer with Zero Pressure Gradient," NACA Report #1247, 1955.

Kopper, F., Stoeffler, R., and Dring, R.P., United Technologies Internal Report, 1977.

Krouthen, B., and Giles, M., "Numerical Investigation of Hot Streaks in Turbines," AIAA Paper 88–3015, July 1988.

Langston, L. S., Nice, M. L., and Hooper, R. M., "Three–Dimensional Flow Within a Turbine Cascade Passage," ASME Journal of Engineering for Power, Jan. 1977, pp. 21–28.

Madavan, N. K., Rai, M. M. and Gavali, S., "Grid Refinement Studies of Turbine Rotor–Stator Interaction," AIAA Paper No. 89–0325, 1989.

Madavan, N. K., Rai, M. M. and Gavali, S., "A Multi–Passage Three–Dimensional Navier–Stokes Simulation of Turbine Rotor–Stator Interaction," AIAA Paper #91–2464, 1991; also Private Communication.

Mayle, R. E., "The Role of Laminar–Turbulent Transition in Gas Turbine Engines," ASME Journal of Turbomachinery, Vol. 113, pp. 509–537, 1991.

McDonald, H., and Fish, R. W., "Practical Calculations of Transitional Boundary Layers," International Journal of Heat and Mass Transfer, Vol. 16, No. 9 1972, 1729–1744.

Munk, M., and Prim, R. C., "On the Multiplicity of Steady Gas Flows Having the Same Streamline Pattern," Proceedings of the National Academy of Sciences, U. S. Vol. 33, 1947.

Ni, R. H., "A Rational Analysis of Periodic Flow Perturbations in Supersonic Two–Dimensional Cascades", ASME Paper #78–GT–176, 1978.

Ni, R. H.: A Multiple–Grid Scheme for Solving the Euler Equations, AIAA Journal, Vol. 20, No. 11, Nov. 1982, pp. 1565–1571.

Ni, R. H and Bogoian, J. C., "Prediction of 3D Multistage Turbine Flow Field Using a Multiple–Grid Euler Solvers:, AIAA Paper #89–0203, 1989.

Ni, R., Sharma, O, Takahashi, R. and Bogoian, J., "3D Unsteady Flow Simulation Through a Turbine Stage", Paper Presented at the 1989 Australian Aeronautical Conference – Research and Technology – The Next Decade, Melbourne, Australia, Oct. 9–11, 1989.

Ni, R. and Sharma, O., "Using 3D Euler Flow Simulations to Assess Effects of Periodic Unsteady Flow Through Turbines," AIAA Paper #90–2357, 1990.

Novak, R, A., and Hearsay, R. M. "A Nearly Three Dimensional Intrablade Computing System for Turbomachinery. Pts. I & II," ASME Papers 76–FE–19 and 20, 1976.

Nyland, T. W., Englund, D. R., and Anderson, R. C., "On the Dynamics of Short Pressure Probes: Some Design Factors Affecting Frequency Response," NASA TN D–6151, 1971.

Patankar, S. V., and Spalding, D. B., "Heat and Mass Transfer in Boundary Layers," Intertext Books, London, U. K. 1970.

Pfeil, H and Herbst, R., "Transition Procedure of Instationary Boundary Layers," ASME Paper #79–G7–128 1979.

Pfeil, H., Herbst, R. and Schrader, T., "Investigation of the Laminar–Turbulent Transition of Boundary Layers Disturbed by Wakes", ASME Paper 82–GT–124, 1982.

Pulliam, T. H. and Steger, J. K., "Recent Improvements in Efficiency, Accuracy, and Convergence for Implicit Approximate Factorization Algorithms," AIAA Paper 85–0360, 1985.

Rai, M. M. and Chakravarthy S. R., "An Implicit Form for the Osher Upwind Scheme." AIAA Journal, Vol. 24, No. 5 May 1986, pp. 735–743.

Rai, M. M., "A Conservative Treatment of Zonal Boundaries for Euler Equation Calculations," Journal of Computational Physics, Vol. 62, 1986, pp. 472–503.

Rai, M. M., "An Implicit Conservative Zonal Boundary Scheme for Euler Equation Calculations," Computers & Fluids, Vol. 14, No. 3, 1986, pp. 295–319.

Rai, M. M. and Dring, R. P., "Navier–Stokes Analyses of the Redistribution of Inlet Temperature Distortions in a Turbine," AIAA Paper #87–2146, 1987.

Rai, M. M., "Unsteady Three-Dimensional Simulations of Turbine Rotor-Stator Interaction," AIAA Paper #87-2058, 1987.

Rai, M. M. and Madavan, N.K., 1988, "Multi Airfoil Navier Stokes Simulations of Turbine Rotor-Stator Interaction," Journal of Propulsion and Power, Vol. 5, No. 3, pp. 307-319, 1988.

Rai, M. M., "Three Dimensional Navier-Stokes Simulations of Turbine Rotor-Stator Interactions", Journal of Propulsion and Power, Vol. 5, No. 3, pp. 307-319, 1989.

Rangwalla, A. A., Private Communication.

Rangwalla, A. A., Madavan, N. K., and Johnson P. D., "Application of Unsteady Navier Stokes Solver to Transonic Turbine Design," AIAA Paper #2468, 1991.

Rhie, C. M., "A Pressure Based Navier-Stokes Solver Using the MultiGrid Method," AIAA Paper #86-0207, 1986.

Roe, P. L., "Approximate Riemann Solvers, Parameter Vectors, and Difference Schemes," Journal of Computational Physics, Vol. 43, 1981, pp. 357-372.

Schultz, N., "Aerodynamic of Cascades," AGARDograph #220, 18 1977.

Sharma, O. P., Kopper, F. C., Knudsen, L. K. and Yustinich, J. B., "Energy Efficient Engine (E^3) Low Pressure Turbine Subsonic Cascade Component Development and Integration Program," NASA CR-165592, January, 1982.

Sharma, O. P., Wells, R. A., Schlinker, R. H. and Bailey, D. A., "Boundary Layer Development on Turbine Airfoil Suction Surface," Journal of Engineering for Power, Vol. 104, July 1982, pp 698-706.

Sharma, O. P., Butler, T. L., Joslyn, H. D., and Dring, R. P., "Three-Dimensional Unsteady Flow in an Axial Flow Turbine," Journal of Propulsion and Power, Vol. 1, #1, Jan-Feb. 1985.; also AIAA Paper #83-1170, 1983.

Sharma, O. P. and Graziani, R. A., "Influence of Endwall Flow on Airfoil Suction Surface Mid-Height Boundary Layer Development," Journal of Engineering for Power, Vol. 105, Jan. 1983, pp. 147-155.

Sharma, O. P. and Butler, T. L., "Prediction of Endwall Losses and Secondary Flows in Axial Flow Turbines," Journal of Turbomachinery April 1987.

Sharma, O. P., Renaud, E., Butler, T. L., Milsaps, K., Dring, R. P., and Joslyn, H. D., 1988, "Rotor-Stator Interaction in Multi-Stage Axial-Flow Turbines," AIAA Paper No. 88-3013.

Sharma, O. P., "Momentum and Thermal Boundary Layers on Turbine Airfoil Suction Surfaces," AIAA Paper #87-1918, 1987.

Sharma, O. P., Pickett, G. F. and Ni, R. H., "Assessment of Unsteady Flows in Turbines", ASME Paper #90-GT-150, 1990.

Sharma, O. P. and Syed, S. A., "Turbulence Modeling in Gas Turbine Design & Analysis," AIAA Paper #AIAA-91-0514, 1991.

Sharma, O. P., Belford, K. A., Soderberg, C. R., Gertz, J. B., Staubach, J. B. and Griffin, L. W., "Simulation of Unsteady Flow for an Advanced Gas Generator Turbine at High and Low Subsonic Mach Numbers," Presented at the 1992 ETO Conference in Huntsville, Alabama, 1992.

Staubach, J. B., Private Communication, 1990.

Takahashi, R. and Ni, R. H., "Unsteady Euler Analysis of the Redistribution of an Inlet Temperature Distortion in a Turbine," AIAA Paper 90–2262, 1990.

Townsend, A. A., "Structure of Turbulent Shear Flow," Cambridge University Press, 1956.

van Driest, E. R., "On Turbulent Flow Near a Wall," J. Aero. Sciences, Vol. 23, pp. 1007, 1956.

Vatsa, V. N. and Wedan, B. W., "Navier–Stokes Solutions for Transonic Flow Over a Wing Mounted in a Wind Tunnel," AIAA Paper 88–0102, January, 1988.

Yaras, M. I., Zhu, Y. and Sjolander, S. A., "Flowfield in the Tip Gap of a Planar Cascade of Turbine Blades," ASME Journal of Turbomachinery, July 1989.

Yee, H. C., Warming, R. F., and Harten, A., "Implicit Total Variation Diminishing (TVD) Schemes for Steady–State Calculations," Journal of Computational Physics, Vol. 57, No. 3, 1985, pp. 327–360.

APPENDIX

RAI3DS
User's Manual

Contract NAS8-36950

Prepared for :

National Aeronautics and Space Administration
George C. Marshall Space Flight Center
Marshall Space Flight Center, Alabama 35812

Kelly Belford

Pratt & Whitney Aircraft
East Hartford, Connecticut 06108

Table of Contents

Foreward and Summary

This Document is a manual describing the use of a 3D Navier-Stokes flow solver, RAI3DS, which was developed under NASA Contract NAS8-36950, "Three Dimensional Turbopump Flowfield Analysis". The Program Managers of this contract are Lisa W. Griffin, of NASA/MSFC, and Dr. Om P. Sharma, of Pratt & Whitney Aircraft. This Document accompanies the final report of the contract, in which the methodology of the solution algorithm is presented. The focus of this manual is the mechanics of using the system, accompanied by some samples of jobstreams, input, and output. Some details of major modifications made to the original version of this program, ROTOR 3 (M. M. Rai, NASA/Ames, 1987) are also included.

Overview of RAI3DS System

The purpose of RAI3DS is to solve for the flow through a turbopump. It is the result of work in support of NASA Contract NAS8-36950, the main tasks of which were to verify, enhance, and apply the three-dimensional, unsteady Navier-Stokes flow solver ROTOR3, written by Man Mohan Rai, NASA/Ames. ROTOR3 was designed for a specific experimental single-stage axial turbine, for which it gave good predictions of the experimental data (Ref. 1). In order to utilize the predicitve capability of ROTOR3 as a turbomachinery design tool, modifications were necessary to make the code applicable to general cases, and also to reduce the computational resources required for its execution. As a result of this work, RAI3DS will solve for one, two, or three airfoil rows, up to four airfoils in each row, in two or three dimensions, with or without tip clearance, planar or annular, steady-state or unsteady. It can also be applied to radial flow machines as well as axial. Additional features include capability for imposing a line of symmetry condition in three-dimensional axisymmetric cases; the option to model stream tube contraction effects in two-dimensional cases; and the capability for specifying an incoming wake and/or boundary layer.

RAI3DS consists of three major modules: the grid generator, the flow initializer, and the flow solver, each having different forms of input and output. The grid generator and flow initializer run on the Iris workstation, and the solver runs on the Cray-XMP. In addition, there is a shell script, run on the Iris, that generates the UNICOS job stream needed to run the flow solver on the Cray. Each of these modules are explained in detail, including sample input and output, in the following sections of this manual.

Grid Generator

The solution scheme of the RAI3DS flow solver requires two overlaid grids for each airfoil. A dense inner grid surrounds the airfoil with lines normal to the surface, and is overlaid by a less-dense outer grid of horizontal and vertical lines extending to the boundaries of the solution domain. Between each airfoil, the outer grids are slightly overlaid at the interface. This grid scheme is explained in more detail by Rai (Ref. 2), but here is an example of a radial cross-section of a stage with rotation about the X-axis:

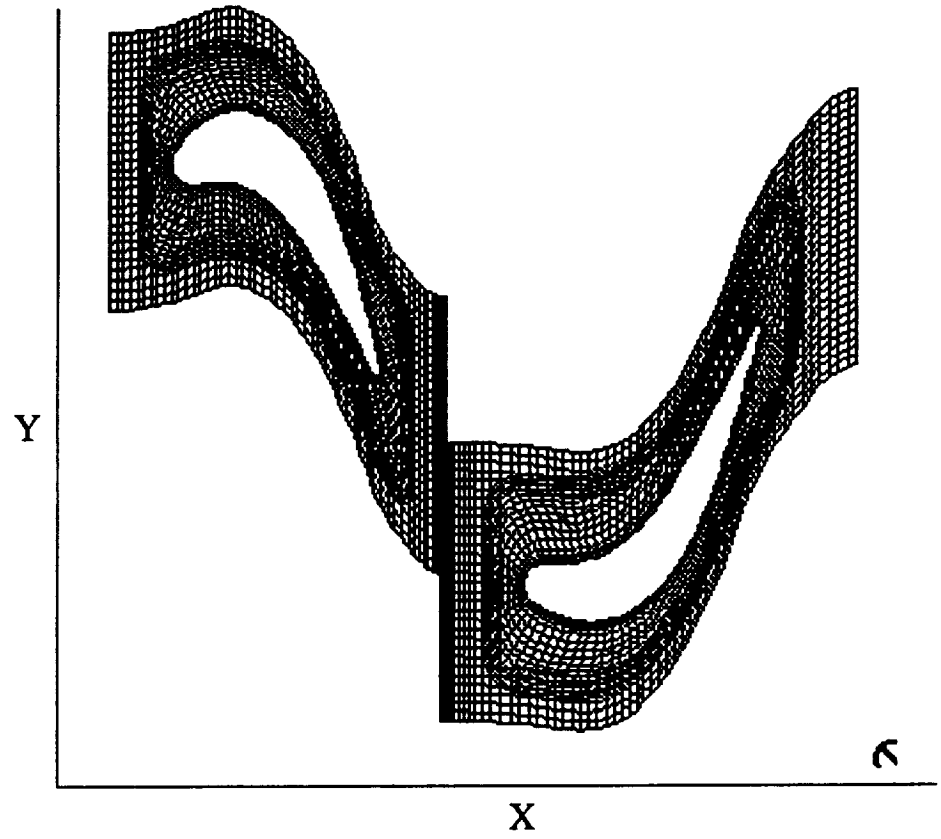

In actuality, the outer H-grid extends throughout the solution domain; the innermost portion is not shown here so as not to obstruct the view of the inner O-grid. The grids are stored in Cartesian coordinates, with X-, Y-, and Z- coordinates for each node, represented by (I,J,K). For the outer grids, I varies with X and J varies with Y; for the inner grids, I varies with airfoil circumference and J varies with distance from the surface; K varies with radius,which is normal to the page.

The procedure to generate these grids is as follows: for each airfoil, the outer H-grid is generated first, it's boundaries in the Y-direction following the curve of the airfoil's camber line, which is generated from the X-Y coordinates of the airfoil surface. The outer boundary of the inner O-grid is then generated, and the O-lines are distributed from the airfoil surface out to the boundary. The O-lines are connected

with lines normal to the airfoil at the surface and curving out to the boundary. This is done at five spanwise locations, and then repeated according to the user-specified radial distribution of the grid. For planar cases, the grid is then "unwrapped" at each radial location so that each grid plane has a constant Z-value. For 2-dimensional cases, all grid planes except that at midspan are eliminated, and the midspan grid plane is copied twice, forming a grid of three identical planes at three different Z-locations. For radial cases, the planar grid (i.e., having constant Z-values at each X-Y plane) is transformed to curve around the Z-axis, as shown here:

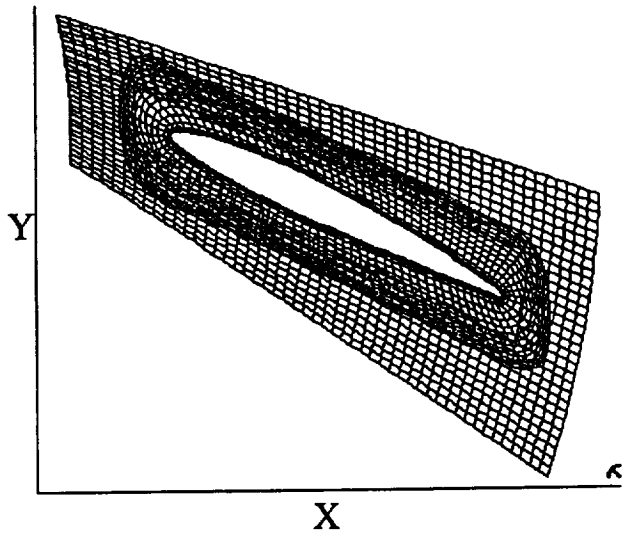

For three-dimensional cases with rotation, RAI3DS will solve for the flow over the tip of the rotor, requiring an extra grid for the clearance region. This grid is also an O-grid, having as its outer boundary the edge of the rotor tip and as its inner boundary an "O" collapsed into a line. The O-lines are connected by lines that are normal to the airfoil surface in the X-Y plane, which are extensions of the normal inner grid lines:

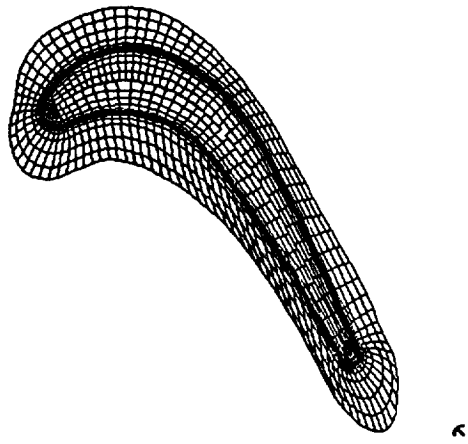

The above shows the first few lines of the inner O-grid meeting with the tip clearance grid at the airfoil surface. A tip clearance grid is generated at each grid plane above

the tip of the rotor, for which the radial distribution is specified by the user.

For some unsteady cases, it is advantageous to use a small H-grid to represent the exit section of an airfoil row, rather than solve for the entire row. This is what is referred to as a "pseudo-airfoil" both in this document and in the RAI3DS system codes. The feature was added for the purpose of simulating first rotor interaction with the wake coming off of a first stator, without having to compute the flow through the first stator. A small, stationary H-grid was generated to represent the exit section of the first stator, and a wake was defined at the inlet and held as the boundary condition. The rotor grids were then moved past this small stationary grid just as they would if there had been a full stator grid upstream of them. This type of simulation saves on computation as well as storage requirements, but is only applicable to cases in which there are no unsteady effects present at the location of the inlet to the pseudo-airfoil grid. Here is an example of a pseudo-stator grid preceding a rotor grid:

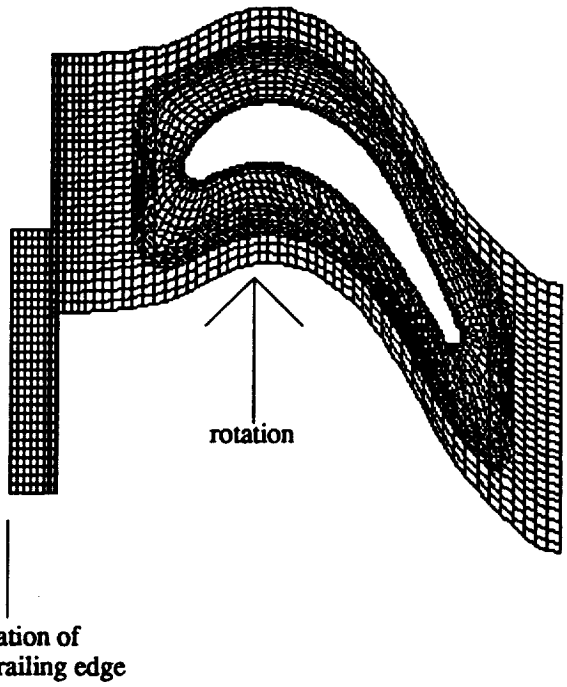

The program requires the following input: the geometry of each airfoil, in X-Y coordinates, at several spanwise locations, the radius at which each of these is defined, the number of blades in each row of airfoils (i.e., the total number of airfoils in the disk), and the upstream and downstream boundaries of the solution domain of each airfoil, although these are subject to change during execution of the program. For each airfoil , this information is read in, and the user is prompted for information to tailor the grid to satisfy the requirements of the particular case. The user will have the opportunity to change grid density in all three directions, scale the airfoils relative to one another, and change upstream and downstream boundaries. Obtaining the optimum grid for a case generally requires several iterations of the program, even for those familiar with the effects of changing each variable. For this reason, the generated grid is output in a PLOT3D-readable file to allow the user to view the grid

and determine the necessary modifications, if any.

To best explain the various options available, a sample run is presented with detailed explanations accompanying each user prompt. This sample is a 3D, planar rotor with tip clearance, its geometry being the same as the first rotor of the United Technologies Research Center Large Scale Rotating Rig (LSRR) (Ref. 3), and a pseudo-stator, meant to demonstrate nearly all possible options of the code. Obviously, much of this would be bypassed in a simpler case. The input file, the format of which is described at the end of this chapter, is expected by the program to be in FORTRAN unit 2. This is the only necessary file assignment, and the user may then invoke the program.

```
% grd3ds
ENTER 1 FOR A RADIAL IMPELLER CASE, RETURN FOR AXIAL

HOW MANY FULL AIRFOIL ROWS ?
1
```

This is the number of full airfoil grids you want to generate, regardless of whether you want a pseudo-airfoil grid upstream. You must have coordinates for this number of airfoils in the input file.

```
ENTER TYPE OF 1ST FULL AIRFOIL ROW, 1=STATOR, 2=ROTOR
2
```

"1st" means leftmost.

```
PSEUDO-AIRFOIL UPSTREAM ? (O=NO, 1=YES)
1
2D OR 3D? (ENTER '2' OR '3')
(NOTE 3D IMPLIES TIP CLEARANCE IF SOLVING FOR A ROTOR)
3
```

Note that if you want to solve for a stationary airfoil with tip clearance, refer to it as a rotor and define rotation speed to be zero (this is done later).

```
PLANAR CASE? (O=NO,1=YES)
1
```

This applies to 2 or 3 dimensions.

```
ENTER NMBR OF AXIAL POINTS FOR PSEUDO-AIRFOIL GRID, I2
10
 ENTER JMAX FOR PSEUDO-AIRFOIL GRID, I2
28
```

The spacing in the Y-direction in the pseudo grid should be as close as possible to that of the neighboring airfoil grid; this will depend on the pitch ratio of the rows.

ENTER 1 TO CHANGE AIRFOIL 2 K-PLANE MESH DIMENSIONS
(INNER: 101,21 DSBOD = .0005
OUTER: 50,31
TIP: 101,11)

1

The above are defaults.

ENTER IMAX (AXIAL PNTS) FOR OUTER GRID, FORMAT=I2
(DEFAULT=50, MAX=61)

ENTER 1 TO CHANGE IBEG AND IEND, OR RETURN

1

This allows changing the axial boundaries of the inner grid relative to the airfoil.

ENTER % AX CHORD FOR IBEG AND IEND (CURRENTLY=.1)

.08

Change them from 10% bx to 8% bx, i.e. closer to the airfoil l.e. and t.e..

ENTER JMAX (CIRCUM. PNTS) FOR OUTER GRID, FORMAT=I2
(DEFAULT=31, MAX=31)

21

This depends on JMAX for the pseudo grid, also pitch ratio; in this case, the pseudo grid will have 28 points, and there will be 3 pseudo-stator grids for 4 rotor grids, so 21 points are chosen so that the spacing will be the same for each row.

ENTER 1 TO CHANGE JBEG AND JEND, OR RETURN

1

This allows moving the circumferential (Y-direction) boundaries of the inner grid.

ENTER % PITCH FOR JBEG AND JEND (CURRENTLY=.25)

.20

Change the distance of the boundaries from the airfoil surface from 25% pitch to 20%, i.e. closer to pressure and suction sides.

ENTER IMAX (AROUND BLADE) FOR INNER GRID, FORMAT=I3
(DEFAULT=101, MAX=101)

ENTER JMAX (NORM TO BLADE) FOR INNER GRID, FORMAT=I2
(DEFAULT=21, MAX=31)

ENTER 1 TO CHANGE DENSITY AT SURFACE

1

Allows changing distance from airfoil surface of 1st O-line of inner grid.

ENTER VALUE OF DSBOD (ORIG, WITH JMX=21, IS .0005)

.0003

ENTER JMAX FOR TIP CLEARANCE REGION, FORMAT=I2
(DEFAULT=11, MAX=11)

Number of O-lines in tip clearance grid.

ENTER KMAX (RADIAL PNTS) BEFORE ADDITION, FORMAT=I2
(DEFAULT=25, MAX=51(NO ADDITION))

45

ENTER KMAX FOR TIP CLEARANCE REGION, FORMAT=I2
(DEFAULT=5, MAX=15)

13

Optimizing K-plane distribution is a trial-and-error process; the numbers chosen here should be less than or equal to final number of K-planes desired. Initially, the program should be run through to the point at which the user has the opportunity to examine the distribution of the chosen number of K-planes. This should be repeated, with modifications made after each examination, until the distribution is satisfactory, at which point the program can be run through its entirety.

CURRENT DIMENSIONS:
NOTE THAT POINTS WILL BE ADDED IF AXIAL SPACING AT
INLET/EXIT BOUND IS CHANGED, AND AGAIN IN OVRLAP,
ALSO RADIAL DISTRIBUTION CAN BE MODIFIED LATER.

AIRFOIL: 1
OUTER: 9, 28 INNER: 1, 1 RADIAL: 45 45

AIRFOIL: 2
OUTER: 49, 21 INNER: 101, 21 RADIAL: 45 33
PAUSE...

Provides an opportunity to make sure dimensions are correct before continuing.

ENTER 1 TO INCREASE CLUSTERING AT T.E. FOR AIRFOIL 2

This will put more grid points around the airfoil trailing edge; note this will take away points from the rest of the airfoil surface.

ENTER 1 TO CHANGE ENDWALL SPACING AND/OR DIST. IN TIP
(DEFAULT: SETA1 = SETA2 = 0.03% SPAN = 1.80000E-03)

1

Unless "1" is entered, radial distance between each endwall and the next closest K-plane will be set to 0.03% of the span, spanwise distribution will be symmetric about the midspan, and the clearance region will be assumed to exist for the last 13 K-planes, i.e., the number entered for "KMAX" for tip clearance. For most cases, it is better to specify the clearance region as a percentage of the total span; to do this, it is necessary to enter "1" at this point.

CHOOSE: 1) SPECIFY TIP CLEARANCE (I.E., %SPAN)
2) TIP CLEARANCE DETERMINED BY GRID

1

If option 2 is chosen, the user will be prompted for new endwall spacing, the same at both endwalls, and the spanwise distribution will be symmetric about the midspan. The tip clearance region will be defined as the top 13 K-planes. In this example, the span is 6 inches; if an endwall spacing of .002 inches is chosen, the geometric distribution of the 45 K-planes would put the 33rd at radius=5.82594, therefore the top 13 K-planes would represent 2.9% of the total span. To get the desired 1% clearance, option 1 must be chosen.

ENTER PERCENT OF TOTAL SPAN FOR CLEARANCE REGION, F5.0
(ENTRY WILL BE DIVIDED BY 100 BEFORE MULTIPLICATION)

1.

This will cause the top 13 of the 45 K-planes to be disributed within the top 1% of the total span.

CHOOSE: 1) K-LINES EVENLY SPACED IN CLEARANCE
2) DENSER AT CASING THAN AT BLADE TIP
3) DENSE AT CASING AND AT BLADE TIP

These are the results of choosing each of the above options:

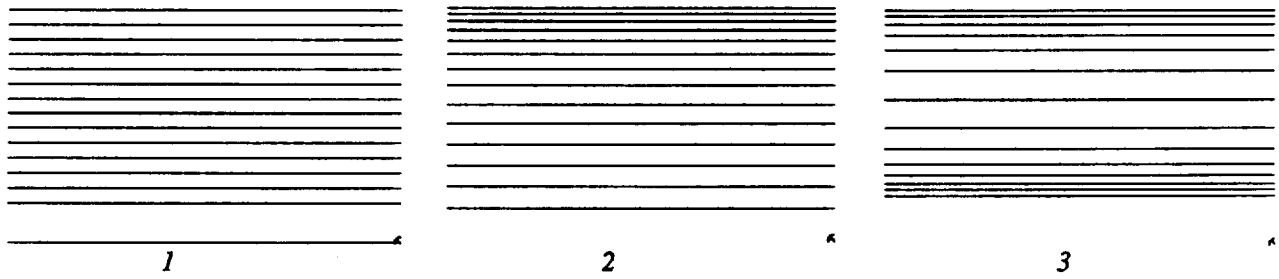

These show only the distribution in the tip clearance; the spacing through the rest of the span varies among the three as well.

3

ENTER SPACING BETWEEN CASING AND NEXT K-PLANE, F5.0

.002

ENTER SPACING BETWEEN BLADE TIP AND NEXT K-PLANE, F5.0

.002

ENTER SPACING BETWEEN HUB AND NEXT K-PLANE (F5.0)
(SPACING AT CASING IS SET TO 0.002000

.002

The above are actual distances in inches.

ENTER 1 IF YOU WANT TO ADD RADIAL LINES AT MIDSPAN

1

Allows filling in sparse area at midspan without taking K-planes away from endwalls; to determine whether this is necessary, a radial distribution should be generated first without excercising this option.

ENTER NUMBER OF POINTS TO BE ADDED, I2
(CURRENT KMX: 45)

04

ENTER KLO & KHI (CURRENT DIST) BETWEEN WHICH TO ADD LINES, 2I3

020027

The above will redistribute the spacing between K-planes 20 and 27 with the addition of four more K-planes, thus bringing the total number to 49.

RADII OF K-PLANES ACCORDING TO ORIGINAL STRETCHING
HAVE BEEN WRITTEN TO A FILE.
HALT EXECUTION OR HIT ENTER TO CONTINUE
PAUSE...

At this point, the program should be exited and the radial distribution should be examined; the output file is in FORTRAN unit 30, and contains the radius defined for each K-plane; these can be plotted as R vs. K - here are the plots resulting from running this program with and without the addition of 4 lines between 20 and 27:

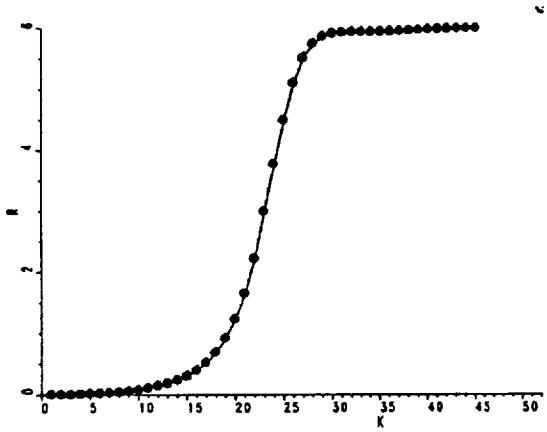

without addition

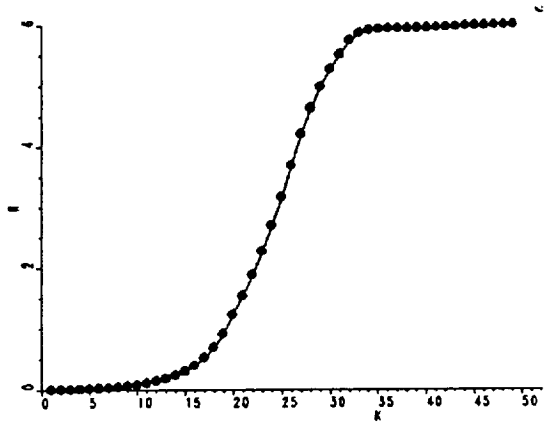

with addition

Note that the distribution below K=20 is the same in both cases, as are the distribution above K=27 in the first plot and that above K=31 in the second.

AXIAL CHORD = 6.34100
L.E. X = 5.00000 T.E. X = 11.3410
UPSTREAM BOUNDARY FROM INPUT FILE IS AT 60.8737% AXIAL CHORD
DWNSTREAM BOUNDARY FROM INPUT FILE IS AT 37.9120% AXIAL CHORD
(FOR VALUES LESS THAN 25, YOU MAY NEED TO REDEFINE IBEG & IEND)
ENTER 1 TO CHANGE BOUNDARIES OR RETURN

1

Allows changing axial boundaries from those specified in the input file.

ENTER 1 TO SPECIFY PERCENTAGES, 2 TO SPECIFY X-VALUES

1

Boundaries can be specified as either percentages of axial chord, or as actual axial location in inches; the latter is easier when generating grids for multi-row cases to ensure alignment of boundaries at the interface.

ENTER % AX CRD AT WHICH TO DEFINE UPSTRM BOUND (F5.0)

45.

ENTER % AX CRD AT WHICH TO DEFINE DWNSTRM BOUND (F5.0)

35.

CURRENT AIRFOIL GRID BEING GENERATED: 2
ENTER 0) NO CHANGE IN AXIAL SPACING
1) CHANGE AXIAL SPACING AT INLET
2) CHANGE AXIAL SPACING AT EXIT

1

For multi-row cases, increasing density of axial lines at interfaces is recommended; in this case, there will be a pseudo-stator upstream of the rotor, so the latter is considered airfoil number 2, and spacing should be reduced at its inlet. This involves specifying a smaller spacing than exists when the domain is divided evenly by the number of axial points in the grid, and adding an appropriate number of axial points to compensate for the reduced spacing at one end.

ENTER AXIAL SPACING AT BOUNDARY (F10.0)
NOTE: EVEN SPACING IS 0.237787

.065

ENTER NUMBER OF NEW POINTS TO BE ADDED (I1)
(Suggestion: 4

4

Determining the proper spacing and number of additional points may require some trial and error, but one-third to one-quarter of the even spacing is a good start; note that the total number of axial points must not exceed program dimensions, also, inlet spacing for an airfoil must match exit spacing of the preceding one.

ENTER 1 TO FURTHER CHANGE SPACING, OR RETURN

ENTER VALUE OF YFRAC(1), OR RETURN FOR -.5

This refers to the distance between the airfoil camber line and the lower circumferential boundary of the outer H-grid in terms of the fraction of the pitch. In almost all cases, the default (i.e. -.5 or 50% pitch below the camber line) will work.

NOTE: IB,IE,JB,JE: 15 46 7 15
CHECK TO MAKE SURE THESE ARE OK BEFORE INITIALIZING.
PAUSE...

At this point, these values should be recorded, and upon completion of the grid, check to make sure the outer H-grid lines defined by I=IB and I=IE for JB-1<J>JE+1, and by J=JB and J=JE for IB-1<I>IE+1, are contained entirely within the boundaries of the inner O-grid; if not, the program should be re-run with appropriate adjustments made to IBEG & IEND and/or JBEG & JEND.

ENTER 1 TO SKIP ELLIPTIC GRID GENERATOR

1

Recommend skipping elliptic grid generator, which requires a significant amount of CPU, until the final run of the program.

ENTER K-INDEX TO BE USED TO DETERMINE PITCH, I2 (KMX: 49

25

*This is required only for a 3D planar case; the pitch will be the same for all K-planes, and will be equal to 2*PI*(radius at chosen K)/(number of blades). In this case, K=25 is approximately at midspan, at which the radius is 27 inches, therefore the pitch will be 2*PI*27/28 = 6.059 inches.*

ENTER PERCENT 2ND ROW BX UPSTREAM OF 2ND ROW AT WHICH PSEUDO-AIRFOIL INLET WILL BE DEFINED
(NOTE: ROTOR INLET BOUNDARY IS DEFINED AT 45.0000

60.

The pseudo-stator inlet will be 15% rotor bx upstream of the rotor inlet.

ENTER FACTOR OF 2ND ROW GAP TO DEFINE PSEUDO-AIRFOIL GAP
(E.G., FOR A 3-VANE, 4-BLADE CASE, ENTER 1.333)

1.333

The pseudo-stator grid pitch will be 4/3 that of the rotor.

ENTER 1 TO SHIFT PSEUDO- GRID, RETURN FOR ALIGNMENT W/2ND ROW

1

For viewing purposes, most useful for 1/1 ratios; shifts pseudo-airfoil grid in circumferential direction.

ENTER % PITCH TO SHIFT GRID (F5.0)
(CAN BE NEGATIVE)

```
-10.
WRITING PLOT3D FILE ...
%
```

The above run produces the following grid:

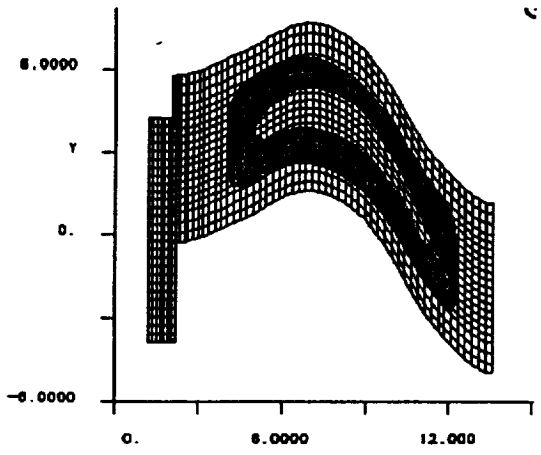

View in radial direction

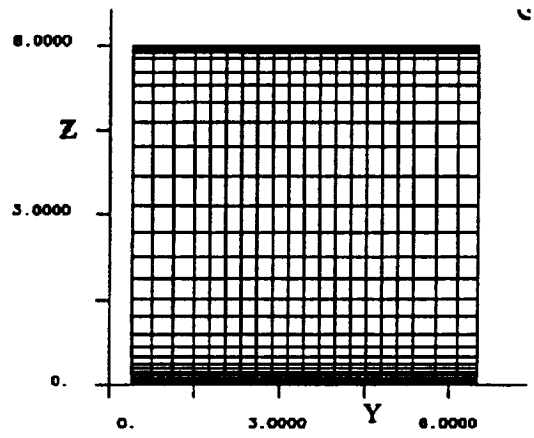

View in axial direction

Note the inner O-grid is not finalized. At this point, if all other aspects of the grid are satisfactory, the program should be run again without skipping the elliptic grid generator.

In summary, the steps to generate a grid are as follows:

1. Create the input file containing the airfoil(s) geometry in unit 2.
2. Invoke the program and, for a 3D case, exit after radial distribution has been written out.

2a. (3D only) Repeat step 2 until desired radial distribution is achieved.

3. Run program through, excercising option to skip elliptic generator.
4. Repeat step 3 until desired inner/outer grid relationship is achieved.
5. Run program through, do not skip elliptic grid generator.

The following is a list of the subroutines and their functions.

MAIN: prompts user for general information about the case; calls:

DIMEN: prompts user for grid dimensions
GNRLAF: main grid generation routine, called for each airfoil; calls:
- GEOM: reads in airfoil geometry from input file
- RSPACE: for 3D cases, prompts user for spanwise grid distribution
- SPLINE: fits a spline to the input airfoil coordinates, defines distribution of grid lines normal to airfoil surface based on curvature
  - CSPLIN: calculates derivatives of X and Y wrt S
- CAMBER: generates airfoil camber line in X-Y coordinates
- TSPLIN: calculates curvature of outer grid boundaries
- ALGEB: generates outer H-grid
- OBOUND: generates outer boundary of the inner O-grid
- ELLIP: elliptic grid generator, generates the inner O-grid
  - TRI: solves the tridiagonal matrix calculated in ELLIP
- REDIST: redistributes inner grid O-lines based on chosen surface spacing

OVRLAP: for multi-row cases, generates patched boundary at each row interface
PSEUDO: for "pseudo-airfoil" cases, generates a small grid upstream of first airfoil grid, representing the exit of the previous airfoil
ROTLID: for cases with tip clearance, generates tip clearance grid
UNWRAP: for planar cases, "unwraps" the annular grid about the X-axis
WRPOUT: for radial cases, "unwraps" the outer H-grid about the Z-axis
GEOMOT: writes grid and case information to file for input to initializer
PLOT3D: writes grid to PLOT3D-readable file

Miscellaneous routines:

SPACE1, SPACE2: geometric point distributors
PUTXYZ, GETXYZ: puts and gets coordinates from temporary storage files
OPNCLO: opens and closes temporary storage files

The format of the input file is described here. All of these lines must be present for every full airfoil for which a grid will be generated. (No input is required for a pseudo-airfoil, its grid will be determined by grid with which it interfaces.)

Card #	Columns	Format	Variable	Description
1	1-80	A80	(dummy)	Title card to separate the airfoils; not used by the program, but line must be present.
2	1-5	I5	NBLADE	Total number of blades in this airfoil row; wll be used in conjunction with radius to

Card #	Columns	Format	Variable	Description
				determine periodic boundaries of solution domain.
3	1-20	G20.8	XU	Axial location of upstream bound.
3	21-40	G20.8	XD	Axial location of downstrm bound.
(Note that XU and XD maybe be changed during program execution.)				
4	1-5	I5	NSPANS	Number of spanwise locations (radii) present to define airfoil geometry; MIN = 2, MAX = 10
4	6-10	I5	NSTR	Number of X-Ycoordinates given to define airfoil geometry at each spanwise location; MAX = 251
(for N=1,NSPANS:)				
5	1-20	G20.8	R(N)	Radius at which the following NSTR lines define the airfoil geometry
(for I=1,NSTR:)				
6	1-20	G20.8	X(N,I)	X-coordinate of Nth point at Ith spanwise location
6	21-41	G20.8	Y(N,I)	Y-coordinate of Nth point at Ith spanwise location

Card type #6 is then repeated to make a total of NSTR lines containing X-Y values. Note the X-Y coordinates must proceed clockwise around the blade

The Card#5/Card#6 combination is repeated to make a total of NSPANS groups of NSTR+1 lines, i.e., one line formatted as Card #5 followed by NSTR lines formatted as Card#6. Each group defines the airfoil geometry at the specified radius. The first radius must be at the hub, and the last must be at the casing. Note that the program will linearly interpolate the coordinates at the given radii to define the geometry at 25%, 50%, and 75% span, and it is those, in addition to the hub and casing geometry, that will be used to generate the grid.

The entire format (i.e., beginning with a title card) is repeated for subsequent airfoils.

The following is the input file accompanying the preceding sample run:

```
LSRR rotor
   28
     1.14                  13.745
    5  136
    0.24000000E+02
    0.50000000E+01    0.28807001E+01
    0.50013294E+01    0.28503103E+01
    0.50052996E+01    0.28201504E+01
    0.50118799E+01    0.27904596E+01
    0.50210295E+01    0.27614498E+01
    0.50326691E+01    0.27333498E+01
     .
     (130 more lines of this format)
     .
    0.25500000E+02
    0.50000000E+01    0.33143501E+01
    0.50013294E+01    0.32839804E+01
    0.50052891E+01    0.32538404E+01
    0.50118694E+01    0.32241602E+01
    0.50210094E+01    0.31951704E+01
    0.50326500E+01    0.31670904E+01
     .
     (130 more lines of this format)
     .
    0.27000000E+02
    0.50000000E+01    0.37861996E+01
    0.50013294E+01    0.37558098E+01
    0.50052996E+01    0.37256498E+01
    0.50118799E+01    0.36959400E+01
    0.50210295E+01    0.36669302E+01
    0.50326691E+01    0.36388197E+01
     .
     (130 more lines of this format)
     .
     0.28500000E+02
     0.50000000E+01    0.42581501E+01
     0.50013294E+01    0.42277298E+01
     0.50052996E+01    0.41975298E+01
     0.50118895E+01    0.41677999E+01
     0.50210495E+01    0.41387596E+01
```

```
0.50327091E+01    0.41106195E+01
.
(130 more lines of this format)
.
0.30000000E+02
0.50000000E+01    0.46918201E+01
0.50013294E+01    0.46614199E+01
0.50052996E+01    0.46312504E+01
0.50118895E+01    0.46015396E+01
0.50210400E+01    0.45725203E+01
0.50326796E+01    0.45444098E+01
.
(130 more lines of this format)
.
```

Flow Initializer

The purpose of the flow initializer is to define an initial guess at the solution of the flow to give the flow solver something to start with. In addition, it is in this program that the boundary conditions that will be applied in the solver are defined. It requires, as input, the aerodynamic conditions at the inlet and exit of the solution domain; also, the number of airfoils in each row for which a solution is desired, the speed of rotation, Reynolds number, and Prandtl numbers for the case. The computational grid, i.e. the file "GEOM", output from the GRIDGEN, is the only other input, and there is no interactive user input. Output is in two forms: 1) a binary "restart" file to be input to the flow solver, 2) a PLOT3D file for viewing the initial flowfield and boundary conditions.

The method of initialization is slightly modified from Rai's original version. Static pressure and density are linearly interpolated between the inlet and exit of the solution domain, axial and radial velocities are constant across the domain, and tangential velocities are linearly interpolated between the inlet and exit of each airfoil based on the general curvature of the airfoils. A no-slip condition is then applied to all surfaces, which was not done by Rai. This is done by defining the (relative) velocity on each surface to be zero, then linearly interpolating to a pre-defined distance from the surface along grid lines that are normal to the surface. Another added feature not present in Rai's original code is the dependency of boundary values on radial and tangential location. This allows specification of an incoming endwall boundary layer (if desired) in three dimensions, and/or an incoming wake to simulate the presence of an airfoil upstream of the inlet to the solution domain, in either two or three dimensions. The same flexibility applies to the exit plane, where measured static pressure data may be held across the plane if the case so warrants.

The following is a list of subroutines and their functions:

MAIN:	main driver, calls:
GEOMIN:	reads file "GEOM", containing grid coordinates and case info.
AEROIN:	reads file containing aerodynamic and viscous parameters
BCDEF:	interpolates and nondimensionalizes inlet and exit flow properties
INIT:	interpolates between inlet and exit to initialize flowfield, imposes no-slip condition on surfaces
INITOT:	writes file "INIT", restart file for input to flow solver RAI3DS
PLOT3D:	writes grid and initial flow in PLOT3D format for viewing

Miscellaneous routines:

SHIFT: applies periodic shift to airfoil grids for multi-blade cases

PUTXYZ,
GETXYZ: puts and gets grid coordinates from temporary storage files

PUTQ,
GETQ: puts and gets flow properties from temporary storage files

OPNCLO: opens and closes temporary storage files

The format of the aerodynamic input file is described here. There are two possibilities for defining the inlet and exit conditions. The first is to specify inlet aerodynamic conditions and exit static pressures at specific radii. These will then be linearly interpolated onto the radii of the computational grid, and will not vary in the circumferential (tangential) direction . Flow properties will then be calculated from the aerodynamic conditions and nondimensionalized according to the scheme expected by the solver. The other option is to input dimensional values of the flow properties themselves (density, velocity components, and pressure) at every computational grid point in the inlet plane, along with dimensional static pressure at every grid point in the exit plane. These will then be nondimensionalized according the the scheme expected by the solver. The latter option will allow specification of an incoming wake, but it is much more difficult, particularly in three dimensions. It requires interpolation of the flow properties from some other source, whether it be experimental data or output from a flow solver, etc., onto the grid coordinates. A method of accomplishing this interpolation is not provided in the RAI3DS system. This file must be in FORTRAN unit 2; here is its format:

Card#	Columns	Format	Variable	Description
1	1-80	A80	(dummy)	Title card to identify case; not used by program but must be present.
2	1	I1	IVARY	=0: aerodynamic input is specified at radii, does not vary across pitch; =1: flow properties are defined at grid points.
3	1-2	I2	NBLDS(1)	Number of blades in row 1 for which solver will calculate flow (MAX = 4).
3	3-4	I2	NBLDS(2)	Number of blades in row 2 for which solver will calculate flow (MAX = 4).

Card#	Columns	Format	Variable	Description
3	5-6	I2	NBLDS(3)	Number of blades in row 3 for which solver will calculate flow (MAX = 4).
(Note: NBLDS(1)+NBLDS(2)+NBLDS(3) must not exceed 7.)				
4	1-10	F10.0	RPM	Speed of rotation in revolutions per minute (=0.0 for stationary cases); can be negative.
4	11-20	F10.0	GAMMA	Specific heat ratio.
4	21-30	F10.0	CP	Specific heat at constant pressure in ($ft^2/sec^2/^\circ R$).
4	31-40	F10.0	REYNIN	Reynolds number per inch based on inlet conditions.
4	41-50	F10.0	PRKIN	Laminar Prandtl number.
4	51-60	F10.0	PRTUR	Turbulent Prandtl number.
If IVARY=0:				
5	1-2	I2	KUP	Number of radii at which inlet aerodynamic conditions will be defined; MIN=1, MAX=50.
6	1-10	F10.0	RADUP	Radius at which the conditions on this line apply.
6	11-20	F10.0	P0INF	Absolute total pressure at inlet, in (lb/in^2).
6	21-30	F10.0	T0INF	Inlet total temperature in ($^\circ R$).
6	31-40	F10.0	AMACH	Absolute Mach number at inlet.
6	41-50	F10.0	ALPHA	Absolute inlet flow angle in degrees,defined as $\tan^{-1}$(V/U), where V=tangential velocity and U=axial velocity.
6	51-60	F10.0	PHI	Absolute inlet flow angle in degrees, defined as $\tan^{-1}$(W/U), where W=radial velocity and

Card#	Columns	Format	Variable	Description
				U=axial velocity.
	Card 6 is then repeated to make a total of KUP lines.			
7	1-2	I2	KDW	Number of radii at which exit static pressure will be defined; MIN=1, MAX=50.
8	1-10	F10.0	RADDWN	Radius at which the static pressure on this line applies.
8	11-20	F10.0	PDWN	Exit static pressure in (lb/in^2).
	Card 8 is then repeated to make a total of KDW lines.			

If IVARY=1:

For n=1,NBLDS(1):

For k=1,KMX, where KMX=number of radial planes in grid:

For j=1,JMX(1), where JMX(1)=number of tangential points in 1st row grid:

5	1-15	G15.8	RINF(n,j,k)	Inlet density in ($lb\text{-}sec^2/in^4$).
5	16-30	G15.8	UINF(n,j,k)	Inlet axial velocity in (in/sec).
5	31-45	G15.8	VINF(n,j,k)	Inlet tangential velocity in (in/sec); note this is tangential velocity for annular cases, Y-vel. for planar.
5	46-60	G15.8	WINF(n,j,k)	Inlet radial velocity in (in/sec); note this is radial velocity for annular cases, Z-vel. for planar.
5	61-75	G15.8	PINF(n,j,k)	Inlet static pressure in (lb/in^2).

(This card will appear a total of NBLDS*KMX*JMX times)

For n=1,NBLDS(last row):

For k=1,KMX, where KMX=number of radial planes in grid:

For j=1,JMX(last row), where JMX=number of tangential points in last row grid:

6	1-15	G15.8	PDWN(n,j,k)	Exit static pressure in (lb/in^2).

(This card will appear a total of NBLDS*KMX*JMX times)

Note that if the case is planar, either two- or three-dimensional, the geometry will have been translated in the grid generator so that the first K-plane has a constant Z-value of 0.0. The values of RADUP and RADDWN, however, must correspond with the original radii input to the grid generator. The following is a sample input file corresponding to the sample run of the grid generator previously shown:

```
LSRR rotor
0
 1 1
410.00      1.4        6007.120  41000.0   0.72       0.90
20
  24.00000  14.60446 540.00000   0.15500  68.2272   0.20240
  24.30000  14.68998 540.00000   0.17721  67.32001  0.44000
  24.40021  14.68890 540.00000   0.18047  66.87000 -0.89000
  24.49980  14.68432 540.00000   0.18016  66.62000 -1.21000
  24.70020  14.67641 540.00000   0.17641  65.99001 -1.55000
  24.89999  14.67336 540.00000   0.17474  65.78999 -2.01000
  25.30020  14.69601 540.00000   0.18069  67.33000 -2.65000
  25.80000  14.69550 540.00000  0.17372  67.05000  -0.26000
  26.39999  14.69499 540.00000   0.17143  67.39000 -0.77000
  27.00000  14.69397 540.00000  0.16894  68.39000  -2.95000
  27.60120  14.69056 540.00000  0.17413  68.27000  -3.12000
  28.20000  14.68664 540.00000  0.16231  67.27000  -3.44000
  28.50121  14.68991 540.00000   0.16094  67.13000 -1.47000
  28.70100  14.69310 540.00000  0.16065  67.39000  -1.37000
  28.90021  14.69557 540.00000   0.16098  67.22000 -1.15000
  29.10120  14.69477 540.00000   0.16118  67.14000 -1.07000
  29.30099  14.69441 540.00000   0.16004  68.41000 -0.70000
  29.49120  14.69419 540.00000   0.15836  71.52000 -0.24000
  29.71730  14.63597 540.00000   0.14163  72.33858 -0.13300
  30.00000  14.60228 540.00000   0.12944  73.58221 -0.07090
 2
  24.00000  14.2018
  30.00000  14.21483
```

Note that the boundary values and initial flowfield should be in absolute frame and Cartesian coordinates. This should be checked using PLOT3D before running the flow solver. When viewing the flowfield, also note that density has been nondimensionalized by the gap-averaged inlet density at midspan, call it RNDF; pressure, by the gap-averaged inlet pressure at midspan, call it PNDF; velocity components have been nondimensionalized by $\sqrt{(PNDF/RNDF)}$.

Flow Solver

The flow solver's main input is a "restart file", which contains all geometric and aerodynamic information about the case, including flow properties at each node that were calculated at the end of the solver's previous run. In addition, a small amount of input affecting a particular run, such as number of time steps, size of time step, frequency of printing convergence information, etc., is required. (For two-dimensional cases, a file defining h-ratio is also necessary.) For each time step, the solver runs through the solution algorithm for each airfoil grid separately, interpolating at grid boundaries, explicitly enforces boundary conditions, and records convergence information. For unsteady cases, this is repeated (usually twice) before the rotating grid(s) is moved relative to the stationary grid according to the size of the time step. After the last time step, the restart file is updated with the latest flowfield and output. For unsteady cases, there is additional output consisting of files containing pressure distributions on airfoil surfaces, and total pressure across the exit plane, which have been written at specified time intervals. This allows analysis of unsteady behavior as a function of time, in addition to the instantaneous solution recorded in the restart file.

The program solves the unsteady, three-dimensional, compressible Navier-Stokes equations, supplemented by an equation of state and an energy equation, all of which are first transformed from Cartesian coordinates into a (ξ, η, ς) coordinate system. In this coordinate system, ξ is the direction tangent to the airfoil surface, η is the direction normal to the airfoil surface, and ς is the direction normal to the hub surface. The thin-layer assumption is made, that is, the viscous terms evaluated as derivatives in the direction tangent to the body surface are assumed to be negligible. The transformed equations then take the following form:

$$Q_t + E_\xi + F_\eta + G_\varsigma = Re^{-1}(S_\eta + T_\varsigma) \qquad (1)$$

where

$$\begin{aligned} Q &= \mathbf{Q}/J \\ E(\mathbf{Q},\xi) &= (\xi_t \mathbf{Q} + \xi_x \mathbf{E} + \xi_y \mathbf{F} + \xi_x \mathbf{G})/J \\ F(\mathbf{Q},\eta) &= (\eta_t \mathbf{Q} + \eta_x \mathbf{E} + \eta_y \mathbf{F} + \eta_x \mathbf{G})/J \\ G(\mathbf{Q},\varsigma) &= (\varsigma_t \mathbf{Q} + \varsigma_x \mathbf{E} + \varsigma_y \mathbf{F} + \varsigma_x \mathbf{G})/J \end{aligned} \qquad (2)$$

$\mathbf{Q}$ is the dependent variable vector, (ρ, ρu, ρv, ρw, e) in Cartesian coordinates, where ρ is density, u, v, and w are velocities in the x-, y-, and z-directions, respectively, and e is energy; $\mathbf{E}$, $\mathbf{F}$, and $\mathbf{G}$ are flux vectors in the x-, y-, and z-directions, respectively; S and T are the viscous flux vectors in the η- and ς-directions, respectively; J is the Jacobian of the coordinate transformation; Re is Reynolds number. The integration scheme used to solve the set of equations is described in detail in Ref. 1. It's final form is as follows:

$$[I + \frac{\Delta\tau}{\Delta\xi}(\nabla_\xi A^+_{i,j,k} + \nabla_\xi A^-_{i,j,k})]^p$$

$$[I + \frac{\Delta\tau}{\Delta\eta}(\nabla_\eta B^+_{i,j,k} + \nabla_\eta B^-_{i,j,k} - Re^{-1}\delta_\eta M)]^p$$

$$[I + \frac{\Delta\tau}{\Delta\varsigma}(\nabla_\varsigma C^+_{i,j,k} + \nabla_\varsigma C^-_{i,j,k} - Re^{-1}\delta_\varsigma N)]^p \times$$

$$(Q^{p+1}_{i,j,k} - Q^p_{i,j,k})$$

$$= -\Delta\tau\left(\frac{Q^p_{i,j,k} - Q^n_{i,j,k}}{\Delta\tau} + \frac{E^p_{i+1/2,j,k} - E^p_{i-1/2,j,k}}{\Delta\xi}\right.$$

$$+ \frac{F^p_{i,j+1/2,k} - F^p_{i,j-1/2,k}}{\Delta\eta} + \frac{G^p_{i,j,k+1/2} - G^p_{i,j,k-1/2}}{\Delta\varsigma}$$

$$\left. - \frac{S^p_{i,j+1/2,k} - S^p_{i,j-1/2,k}}{Re\Delta\eta} - \frac{T^p_{i,j,k+1/2} - T^p_{i,j,k-1/2}}{Re\Delta\varsigma}\right) \qquad (3)$$

where

$$\begin{aligned} A^\pm &= (\partial E/\partial Q)^\pm \\ B^\pm &= (\partial F/\partial Q)^\pm \\ C^\pm &= (\partial G/\partial Q)^\pm \\ M &= (\partial S/\partial Q) \\ N &= (\partial T/\partial Q) \end{aligned} \qquad (4)$$

and Δ, ∇, and δ are forward, backward, and central difference operators, respectively. The $E_{i+1/2,j,k}$, $F_{i,j+1/2,k}$, $G_{i,j,k+1/2}$, $S_{i,j+1/2,k}$, and $T_{i,j,k+1/2}$ are numerical fluxes consistent with their corresponding physical fluxes, and are evaluated using Roe's scheme (Ref. 4). The superscript n refers to the time step, and the superscript p refers to the iteration per time step. The subscripts i,j,k refer to the grid node. As mentioned before, the derivation of this scheme and it's limitations are fully described in Ref. 1; it is presented here only for reference.

The following is a general list of subroutines and their functions; a detailed version can be found in Appendix 1. Key features and modifications made to some of these routines, i.e., enhancements to Rai's original ROTOR3 code, are documented in some detail following the list. They are categorized according to the general feature which was modified, which may have required implementation in several

routines, as opposed to simple listing of the changes made to each routine.

RAI3DS (main routine): reads indicators to dictate run: calls:

RESTIN:	reads initial flow file or restart file from previous RAI3DS run
JACBIN:	calculates Jacobians for the variable transformation
TRIANG:	calculates interpolation factors at inner/outer interface
HDATA:	(2D only) reads H-ratio input data
EIGEN:	(steady only) calculates "time" step

(for each iteration)

CONTRL:	controlling routine for each solution iteration; calls:
GMOVE:	(multirow only) moves rotating grids relative to stationary grids
PGRID:	defines solution above and below periodic bounds for use in RHS
RHS:	control routine for computing the right hand side of Eq. (3); calls:
SRINT:	(outer grids only) interpolates at inner/outer interface
MUKN:	calculates kinematic viscosity (Sutherland's law)
MUTR:	calculates eddy viscosity (Baldwin-Lomax with modifications)
FLUXR:	computes the numerical flux vectors E^p, F^p, and G^p in Eq. (3)
VFLUX:	computes the viscous flux vectors S^p and T^p in Eq. (3)
STCONT:	(2D only) adds stream tube contraction terms in place of G^p
LHS:	control routine for computing the left hand side of Eq. (3) and solving for Q^{p+1}; calls:
SMATRX:	computes the matrices $A^{\pm}$, $B^{\pm}$, and $C^{\pm}$ in Eq. (3)
VMAT:	computes the matrices M and N in Eq. (3)
BTRI:	inverts the matrix equation (3), solving for Q^{p+1}
CORREC:	imposes explicit boundary conditions at all boundaries
CONVRG:	calculates change in solution from previous iteration
WRTPS:	writes out pressure distribution at midspan
WRTEXT:	writes out exit total pressure across pitch at midspan
RESTOT:	writes out restart file containing updated solution

2D or 3D solution: RAI3DS has the capability for either two- or three-dimensional solutions. Its algorithms work with three dimensions, and for this reason, even if a two-dimensional solution is desired, a three-dimensional grid is required. The grid for a two-dimensional solution must consist of three identical grid planes at three separate Z-locations. A maximum K-index of 3 will signal the solver to compute the solution at only the middle plane and copy it to the planes above and below it. This will ensure zero flux in the Z-direction. In addition, the solver will skip evaluation of terms with respect to Z, i.e., vectors G^p and T^p and matrices $C^{\pm}$ and N in Eq (3), saving on computation time. (Affected subroutines: CORREC, all RHS

and LHS; also, routine MUTR2D will be called instead of other MUTR routines.)

Stream tube contraction terms: Some three-dimensional effects have been shown to be effectively captured in a two-dimensional solution by adding stream tube contraction terms (Rangwalla, Ref. 5). The calculation of these terms and their incorporation in the solution algorithm have been added to RAI3DS. (Affected subroutines: all RHS routines and VFLUX, plus addition of HDATA and STCONT.)

Planar or annular configuration: Although RAI3DS always works in Cartesian as opposed to cylindrical coordinates, the configuration of the geometry may be either a plane or an annulus. Obviously, a two-dimensional case must be planar, but a three-dimensional case may have either configuration. (Affected subroutines: GMOVE, PGRID, CORREC; logical variable PLANE is indicator.)

Symmetry condition: For axisymmetric three-dimensional cases, more grid resolution can be obtained by using the solver's full grid capacity for the region between the hub and the midspan of the airfoil and imposing a symmetry condition at the uppermost K-plane. This, in effect, doubles the spanwise resolution. Obviously, this is applicable only to planar three-dimensional cases with no tip clearance. It has been demonstrated with such a case, however (Ref. 6), that finer spanwise grid resolution significantly improves the solver's capability for predicting three-dimensional effects. For details on this feature and instructions on how to use it, see Appendix 2. (Affected subroutines: all RHS, all LHS, and all MUTR routines, CORREC; logical variables HAFSYM and FULSYM are indicators.)

Multi-blade, multi-row capability: Current limitations in the solver are four blades per row and three total rows. (Affected subroutines: GMOVE, PGRID, outer LHS routines, CORREC; variables NBLADS and NROWS are indicators.)

Radial flow capability: While ROTOR3 was applicable only to axial flow machines, in which rotation occurs in the plane normal to the direction of the incoming flow, RAI3DS can be used to solve cases in which the rotation occurs in the same plane as the incoming flow vector. Specifically, for axial flow cases, rotation is about the X-axis, and for radial cases, rotation is about the Z-axis; in both cases, flow convects along the X-axis. The current version of the code can be used for impellers without tip clearance or inlet guide vanes/diffusers. (Affected subroutines: CORREC, GMOVE, PGRID, TRIANG, SHIFT, EIGEN, all RHS, all LHS, all MUTR; logical variable RADIAL is indicator.)

Inlet/exit boundary conditions: The initial values of entropy, pitch angle, yaw angle, and total enthalpy are held at the inlet, accompanied by a Reimann invariant that is extrapolated from the interior. Holding both the enthalpy and entropy results in holding total pressure, which is a property commonly specified by design engineers at the inlet. In addition to allowing total pressure specification, this is a less stiff condition than that in ROTOR3, which held initial entropy, tangential and radial velocities, an initial Reimann invariant, and a Reimann invariant extrapolated from the interior. The relaxed conditions reduce the occurence of pressure waves, which may slow the convergence of the calculation in some cases. Specified static pressure is

held at every point in the exit plane, modified from the radial equilibrium condition in ROTOR3. Both the inlet and exit conditions may vary in both the tangential and radial directions, allowing specification of more general conditions than were possible in ROTOR3. The derivation of the inlet boundary condition is presented in Appendix 3. (Affected subroutine: CORREC.)

Surface boundary conditions: Capability of specifying wall temperature or heat flux on solid boundaries was added to ROTOR3. These options may be chosen, or an adiabatic wall condition may be used. The implementation of specified wall temperature was derived by Griffin (Ref. 7), and the implementation of specified heat flux is presented in Appendix 3. (Affected subroutines: LHS, CORREC, plus addition of BCSURF; ISURF is indicator.)

Turbulence model: The Baldwin-Lomax turbulence model in ROTOR3 was modified to account for surface curvature, three-dimensionality and Coriolis force. These modifications, deduced by interrogating transport equations for the turbulent kinetic energy and total Reynolds shear stress, are similar to those termed by various investigators as 'algebraic stress models' (Ref. 8). A transition model has also been implemented that accounts for the influence of upstream airfoil wakes on the onset and the extent of the transition on the downstream airfoils. This model is primarily applicable on the suction sides of airfoils operating at moderate Reynolds number. (Affected subroutines: all MUTR routines.)

Pseudo-airfoil: This capability was added to allow solution for a rotor moving past a stationary wake without having to solve for the upstream stator. Conditions are specified at the inlet of a small H-grid, which remains stationary and is treated as an "outer" grid by the code. The following rotor moves past the H-grid as it would a stator grid. (Affected subroutines: CONTRL, CORREC, JACBIN, TRIANG, RHSSO; variable IPSEUD is indicator.)

To create the necessary input and execute the flow solver, the user should run the shell script, RAIJOB. This script is run on the Iris and will prompt the user for all information necessary for defining the input files, setting up the file environment, and executing the flow solver. The output from the script is a UNICOS jobstream, which is then submitted to the Cray. Presented below is a sample run of the shell script corresponding to the three-dimensional pseudo-stator/rotor case for which a sample run of the grid generator was previously shown. Note that in order for the script to execute, the file "skel.job" must exist in the current directory.

```
% RAIJOB

**************************************************************************
*                                                                        *
*                        RAI3DS                                          *
*                                                                        *
**************************************************************************
```

This shell script creates a UNICOS jobstream for running RAI3DS on the NASA/MSFC Cray.
You will be asked questions about your job, and the file "skel.job" will be edited.
The file "skel.job" must be in the current directory.

(Enter "q" to quit or Carriage Return to continue.)

Please enter Cray userid
ckab196
Please enter Cray password
passwd
Please enter job name (7 characters max)
lsrr

Information about the case size is required to request SSD space

Please enter number of airfoil rows in the case
2
Note this includes the pseudo-stator.
2D OR 3D? (Enter 2 OR 3)
3
How many airfoils in row 1 ?
1
Tip clearance in row 1? (y or n)
n
How many airfoils in row 2 ?
1
Tip clearance in row 2? (y or n)
y
Please enter KMAX
49

Please enter numer of k-planes in tip clearance

13

Please enter name of input restart file residing in $HOME on the Cray

lsrrinit

The script is set up to copy the file '$HOME/lsrrinit' into FORTRAN unit 8, which the solver expects to contain the input restart file. This can be changed by editing the UNICOS jobstream if the input file does not reside in the user's home directory on the Cray.

Please enter name of output file to be written to $HOME, or
Carriage Return if you do not want to save the file on the Cray.
(Either way, the file will be disposed back to the IBM.)

lsrr200

Please enter number of steps per rotation through one rotor passage.

3000

This determines the time step. The number is case-dependent, and for some cases in which the grid is particularly dense, the solver may blow up if the time step is too large. It is safest to use at least 2000 steps per rotor passage. For steady-state cases, the time step is based on grid density and the flowfield, and can be increased to speed up convergence of the solver.

Please enter number of iterations per time step

3

This is usually 3 for unsteady cases and 1 for steady-state cases.

Do you want to change frequency of eddy viscosity calculation? (y or n)

y

If yes, eddy viscosity will be calculated at the first time step, then only as often as is specified. Between updates, the most recently calculated value is used at each grid point. This saves on CPU, since eddy viscosity calculation is very time-consuming, and does not adversely affect the solution as long as the viscosity is updated reasonably often (every 50 or 100 time steps).

Please enter iteration interval at which eddy viscosity will be calculated
(e.g., for "50", eddy viscosity will be updated every 50 iter)

100

Please enter iteration number at which to impose this frequency
(e.g., for "500", eddy viscosity will be calculated at every iteration
until number 500, after that, every 100 iterations

1000

Do you want to force transition? (y or n)

y

This requires knowing where the transition points are on the airfoil in terms of grid indices. The turbulence model will calculate the natural transition point using empirical correlations, which may be inaccurate. If the transition point is

known (from experimental data), best results are obtained by specifying it.

Please enter I-indices of inner O-grid between which eddy viscosity
will be turned on (same for all rows)
(e.g., for "37 81", eddy viscosity will be set to zero for I=1,37 and for I=81,IMAX)

56 92

Please enter K-planes between which calculation will be transitional
(e.g., for "7 25", calculation will be fully turbulent
around entire blade for K=1,7 and for K=25,KMAX).
Hit Carriage Return for full span transitional.

Enter:
0) Surface boundary condition will be 1st-order, adiabatic
1) Surface b.c. will be 1st-order, specified wall temp
2) Surface b.c. will be 2nd-order, specified wall temp
3) Surface b.c. will be 2nd-order, specified heat flux

3

See Appendix 3 for descriptions of these.

Enter heat flux on blade, hub, casing, separated with spaces; must be reals with
not less than 1 digit before the decimal point and 5 digits after the decimal point
(e.g., 0.41500);
see Users Manual for instructions on how to calculate these in proper units.

0.41500 0.52500 0.52500

See Appendix 3.

Enter:
0) No line of symmetry will be imposed
1) Restart file contains full span
(program will solve for K=1 to midspan, then impose symmetry)
2) Restart file contains half span
(program will solve for K=1 to KMAX with modified b.c. at KMAX)

0

See Appendix 2 for details.

How many time steps?

200

How often do you want convergence info written out? (every _ time steps)?

10

This consists of the maximum change in energy over each grid for each airfoil and its grid indices. It should be noted that this information can be used to insight into the convergence rate of a case and/or to locate trouble spots in the flowfield. To decide whether a case is converged, however, requires thorough examination of the flowfield, particularly surface static pressures and exit total pressure contours. For this reason, there is no predefined convergence

criterion built in to the solver.

How often do you want midspan Ps dist. written out? (0 = not at all)?

50

This is useful in unsteady cases for plotting pressure amplitudes. The (nondimensional) surface static pressures at midspan are written as a function of time step, I-index of the O-grid, and percent axial chord downstream of the leading edge. This format can be modified in the routine WRTPS to produce proper input formats for various plotting packages. In this case, the information will be written out every 50 time steps.

How often do you want exit Pt written out? (0 = not at all)?

50

Same as above, except total pressure across the exit plane at midspan will be written out; format is in routine WRTEXT.

Please enter CPU time in seconds

5000

This is best determined by trial and error; a typical 2D cascade requires less than 1/2 second per iteration, whereas a 3D stage may require over 30 seconds per solution iteration (90 seconds per time step), depending on grid size.

The file lsrr.job has been created.

%

The above run produces the following jobstream:

```
# USER=ckab196 PW=passwd
# QSUB -r lsrr
# QSUB -eo
# QSUB -lm 4.0mw
# QSUB -lt 4990
# QSUB -lT 5000
#
# CREATE TEMPORARY DIRECTORY AND TEMPORARY SSD
#
set -x
cd $TMPDIR
SSD=`tmpdir /ssd`
#
#  CLEAN-UP IF JOB TERMINATES ABNORMALLY
#
```

```
trap "cd ..; exit" 0 2 3 15 26
#
# BUILD SEGLDR INPUT COMMAND FILE AND LINK
#     fetch the object file from the Cray;  to create the object file,
#     compile the source using cft77 with the -b option
#
fetch slvr.o -f TR -t'dsn=CKAB196.UNIC.OBJECT.RAI3DS,DISP=SHR'
#
cat >seg.input<<eofseg
bin=slvr.o
abs=a.slvr
xfer=RAI3DS
eofseg
segldr seg.input
#
# DEFINE FILE 3  - main input file
#
cat >fort.3<<eof3
25
00200000100005000050
2000300003
01.0099999
01001000
056092
001049
3
0000.415000000.525000000.52500
0
eof3
#
# DEFINE FILE 4 - hratio values (this file is not used for 3d cases)
#
cat >fort.4<<eof4
nvals:  2
    x       h
-100.      1.0
 100.      1.0
nvals:  2
    x       h
-100.      1.0
 100.      1.0
eof4
#
```

```
# DEFINE FILE 8 (input restart file)
#
cp $HOME/lsrrinit fort.8
#
# RUN JOB
#
FILENV=.assign
# Export the file environment:
export FILENV
# Assign statements for unformatted restart files coming from Iris:
assign -a fort.8 -F f77 -N ieee -C ascii FORT8
assign -a fort.9 -F f77 -N ieee -C ascii FORT9
# SSD files
# Export the SSD environment variable
export SSD
# See if there's enough space on SSD for all the files; if not,
# use disk for all the files.
if setf -n 34868b $SSD/dummyfil
then
 rm $SSD/dummyfil
 FILDIR=$SSD
else
 FILDIR=$TMPDIR
fi
# The number in the -n option is how many blocks of 512 WORDS will be
# written to the file;  e.g. if 2 arrays of dimension (512,3) will be
# written to the file, then the assign statement would have "-n 6."
#
#******note - there are only files for 2 rows here!!*********
#
# DEFINE SSD FILES FOR Q ARRAYS - 1 FOR EACH ROW AND GRID TYPE
#  TOTAL SIZE OF EACH OF THESE WILL BE nAIRFOILS*5*nia*nja*nka
assign -a $FILDIR/fort51 -n 1499   -s u FORT51
assign -a $FILDIR/fort52 -n 1499   -s u FORT52
assign -a $FILDIR/fort53 -n 1  -s u FORT53
assign -a $FILDIR/fort54 -n 1499   -s u FORT54
assign -a $FILDIR/fort55 -n 1499   -s u FORT55
assign -a $FILDIR/fort56 -n 1499  -s u FORT56
# DEFINE SSD FILES FOR QOLD ARRAYS - 1 FOR EACH ROW AND GRID TYPE
#  TOTAL SIZE OF EACH OF THESE WILL BE nAIRFOILS*5*nia*nja*nka
assign -a $FILDIR/fort61 -n 1499   -s u FORT61
assign -a $FILDIR/fort62 -n 1499   -s u FORT62
assign -a $FILDIR/fort63 -n 1  -s u FORT63
```

```
assign -a $FILDIR/fort64 -n 1499   -s u FORT64
assign -a $FILDIR/fort65 -n 1499   -s u FORT65
assign -a $FILDIR/fort66 -n 1499  -s u FORT66
# DEFINE SSD FILES FOR AJA ARRAYS - 1 FOR EACH ROW AND GRID TYPE
#  TOTAL SIZE OF EACH OF THESE WILL BE nia*nja*KMX
assign -a $FILDIR/fort71 -n 300   -s u FORT71
assign -a $FILDIR/fort72 -n 300   -s u FORT72
assign -a $FILDIR/fort73 -n 1  -s u FORT73
assign -a $FILDIR/fort74 -n 300   -s u FORT74
assign -a $FILDIR/fort75 -n 300   -s u FORT75
assign -a $FILDIR/fort76 -n 80  -s u FORT76
# DEFINE SSD FILES FOR PERMANENT XYZ ARRAYS - 1 FOR EA ROW AND GRID
TYPE
#  TOTAL SIZE OF EACH OF THESE WILL BE 3*nia*nja*KMX
assign -a $FILDIR/fort41 -n 899   -s u FORT41
assign -a $FILDIR/fort42 -n 899   -s u FORT42
assign -a $FILDIR/fort43 -n 1  -s u FORT43
assign -a $FILDIR/fort44 -n 899   -s u FORT44
assign -a $FILDIR/fort45 -n 899   -s u FORT45
assign -a $FILDIR/fort46 -n 239  -s u FORT46
# DEFINE SSD FILES FOR WORKING XYZ ARRAYS - 1 FOR EACH ROW AND GRID
TYPE
#  TOTAL SIZE OF EACH OF THESE WILL BE 3*nia*nja*KMX
assign -a $FILDIR/fort81 -n 899   -s u FORT81
assign -a $FILDIR/fort82 -n 899   -s u FORT82
assign -a $FILDIR/fort83 -n 1  -s u FORT83
assign -a $FILDIR/fort84 -n 899   -s u FORT84
assign -a $FILDIR/fort85 -n 899   -s u FORT85
assign -a $FILDIR/fort86 -n 239  -s u FORT86
# DEFINE SSD FILES FOR TMP ARRAYS - 1 FOR EACH ROW OUTER AND TIP
#  TOTAL SIZE OF EACH OF THESE WILL BE 5*nia*nja*nka
assign -a $FILDIR/fort91 -n 1499   -s u FORT91
assign -a $FILDIR/fort92 -n 1  -s u FORT92
assign -a $FILDIR/fort93 -n 1499   -s u FORT93
assign -a $FILDIR/fort94 -n 1499  -s u FORT94
# DEFINE SSD FILE FOR STR ARRAY - ONLY ROTOR INNER GRID
#  TOTAL SIZE WILL BE 5*nia*nja*nka
assign -a $FILDIR/fort97 -n 1499    -s u FORT97
# DEFINE SSD FILE FOR INTERP ARRAYS - 1 FOR EACH ROW
#  TOTAL SIZE OF EACH WILL BE 3*(4*nka*nia*3 + nka*nia*3)
assign -a $FILDIR/fort31 -n 435 -s u FORT31
assign -a $FILDIR/fort32 -n 435 -s u FORT32
# DEFINE SSD FILE FOR H-RATIO ARRAYS - 1 FOR EACH ROW
```

```
# TOTAL SIZE OF EACH WILL BE (nia*nja)
assign -a $FILDIR/fort34 -n 1   -s u FORT34
assign -a $FILDIR/fort35 -n 1   -s u FORT35
#
time ./a.slvr
#
# cat the unsteady Ps and Pt files
cat fort.21
cat fort.22
cat fort.24
cat fort.25
#
# COPY OUTPUT FILE TO CRAY
cp fort9 $HOME/lsrr200
ls -l $HOME
#
# SEND RESTART FILE TO FRONTEND
#
# dispose fort9   ?????????
```

The dispose command must be edited in the file 'skel.job' to send the output file back to the frontend.

For two-dimensional cases in which H-ratio is to be specified, it is necessary to edit the here document defined as 'fort.4' in the above jobstream. The format is the same as is already contained in the here document: for each airfoil, simply edit the number following 'nvals:' to tell the code how many values of x and h to read (must be a two-digit number in columns 9 and 10, not greater than 25 for each airfoil), then list that many lines of format (F10.0) to define h as a function of x. The x-values should be in increasing order, beginning with a value that is not greater than the inlet boundary of the airfoil's outer H-grid, and ending with a value that is not less than the exit boundary. The values of h can be defined by using results from either a streamline or a three-dimensional inviscid analysis of the airfoil row (Ref. 9). For two-dimensional cases with no stream tube contraction, no modifications to the here document are necessary, assuming the solution domain does not lie outside the range ($-100.0 < x > 100.0$).

In addition to the restart file, the output file from the UNICOS jobstream will be sent to the frontend. This file will contain all output from writes to Unit 6 in the solver, including convergence information and listings of the files containing midspan pressure distributions and exit total pressures.

Experience with the solver has revealed several somewhat common problems that occur when a calculation is begun from an initial guess. The following is a list of

the most common, along with some possible causes and solutions. For any problem, the first thing that should be checked for is a grid error at the trouble spot, such as a discontinuity or lines crossing over each other. The solutions listed here assume the grid is not the problem.

Symptom	Possible cause/cure
"TROUBLE AT GIVTRI" message at beginning of run	Outer H-grid lines defined by variables IBEG, IEND, JBEG, and JEND are not contained entirely within the inner O-grid; regenerate grid (In some cases, it is possible to visually determine what the values of IBEG, etc should be and simply hardcode them in the routine RESTIN.).
Density and/or energy less than zero on or near the airfoil surface (particularly the trailing edge); may appear in the form of an error message from CONVRG, or a bad argument to mathlib occuring in MUKN	Time step too large; reduce it and continue running. Incorrect Reynolds number has also been a cause; this can be hardcoded in routine RESTIN.
Bad argument to mathlib occuring in MUTR routine	Incorrect Reynolds number, or initial guess problems; less frequent eddy viscosity calculation in beginning has been known to smooth out "bad" points.
Bad argument to mathlib occuring in CORREC	Incorrect or discontinuous inlet boundary values; re-initialize flowfield.

References

[1]Rai, M. M., 1987, "Unsteady Three-Dimensional Navier-Stokes Simulations of Turbine Rotor-Stator Interaction", AIAA Paper No. 87-2058.

[2]Rai, M. M., 1987, "Navier-Stokes Simulations of Rotor-Stator Interaction Using Patched and Overlaid Grids", *Journal of Propulsion and Power*, Vol. 3, No. 5, pp. 387-396.

[3]Sharma, O. P., Butler, T. L., Joslyn, H. D., and Dring, R. P., 1985, "Three-Dimensional Unsteady Flow in an Axial Flow Turbine", *Journal of Propulsion and Power*, Vol. 1, No. 1.

[4]Roe, P. L., 1981, "Approximate Riemann Solvers, Parameter Vectors, and Difference Schemes", *Journal of Computational Physics*, Vol. 43, pp. 357-372.

[5]Rangwalla, A. A., Madavan, N. K., and Johnson, P. D., 1991, "Application of Unsteady Navier-Stokes Solver to Transonic Turbine Design", AIAA Paper No. 2468.

[6]Dorney, D. J., and Davis, R. L., 1991, "Navier-Stokes Analysis of Turbine Blade Heat Transfer and Performance", AGARD CPP-510 Paper No. 22.

[7]Griffin, L. W. and McConnaughey, H. V., 1989, "Prediction of the Aerodynamic Environment and Heat Transfer for Rotor-Stator Configurations", ASME Paper No. 89-GT-89.

[8]Launder, B. E., 1989, "Second Moment Closure: Present... and Future", *International Journal of Heat and Fluid Flows*, Vol. 10, No. 4.

[9]Cumpsty, N. A., 1989, *Compressor Aerodynamics*, pp. 136-140.

RAI3DS Subroutines

RAI3DS (main routine): reads input file in Unit 3; calls:

- RESTIN: reads initial flow file or restart file from previous run
- JACBIN: calculates Jacobians for the variable transformation, i.e. $(x,y,z) \rightarrow (\xi,\eta,\varsigma)$
- TRIANG: calculates factors for interpolation of flowfield at inner O-grid/outer H-grid interface; calls:
  - GIVTRI: for the given point in the given grid, find the triangle in the other grid in which the point lies and determine the weights of the three points for interpolation
- HDATA: (called in 2D cases only) reads H-ratio data in Unit 4, linearly interpolates in x to define H at every grid point
- EIGEN: (called in steady-state cases only) calculates grid-dependent time step
- CONTRL: controlling routine for each solution iteration; calls:
  - GMOVE: (called in multirow cases only) moves rotating grids relative to stationary grids according to size of time step; if rotors have passed stators, i.e., a cycle has been completed, applies periodic shift to rotors to begin new cycle
  - RHSSI: controlling routine for computing right hand side of Eq. 3 (chapter 4) for stator inner O-grids; loop 10 calculates ξ-direction contribution, loop 80 calculates η-direction contribution, loop 160 calculates ς-direction contribution; calls:
    - MUKN: calculates kinematic viscosity for stator inner O-grid
    - MUTRSI: (called in 3D cases only) calculates eddy viscosity for stator inner O-grid in η-direction and ς-direction; loop 10 calculates viscosity below midspan away from the wall; loop 210 calculates it above midpsan away from the wall; loop 410 calculates it below midspan close to wall; loop 610, above midspan close to wall
    - MUTR2D: (called in 2D cases only) calculates eddy viscosity for stator inner O-grid in η-direction only
    - FLUXR: computes the numerical flux vectors E^p, F^p, and G^p in Eq. 3 (chapter 4) using Roe's scheme for stator inner O-grid
    - VFLUX: computes viscous flux vectors S^p and T^p for stator inner grid
    - STCONT: (called in 2D cases only) calculates stream tube contraction terms (H-ratio) instead of the G^p vector
  - LHSSI: controlling routine for computing the left hand side of Eq. 3

(chapter 4) and solving for Q^{p+1}; loop 10 inverts the solution matrix in the ξ-direction, loop 120 inverts in the η-direction, loop 250 inverts in the ς-direction; implicit inlet/exit boundary conditions are applied within the ξ-direction loop, implicit surface boundary conditions are applied within the η-direction loop; calls:

SMATRX: computes the matrices $A^{\pm}$, $B^{\pm}$, and $C^{\pm}$ in Eq. (3) for stator inner grids; called once in each loop

VMAT: computes the matrices M and N in Eq. (3) for stator inner grids; called only in η- and ς-direction loops

BTRI: inverts the given matrix; called once in each loop

RHSRI:
MUKN
MUTRRI
MUTR2D
FLUXR
VFLUX
STCONT
} see above descriptions under RHSSI; all are the same here except they are applied to rotor inner O-grids instead of stator grids

LHSRI
SMATRX
VMAT
BTRI
} see above descriptions under LHSSI; all are the same here except they are appiled to rotor inner O-grids insead of stator grids

PGRID: defines solution above and below periodic boundaries of the outer H-grid, i.e. the boundaries in the circumferential direction, for use in RHSSO

RHSSO: controlling routine for computing right hand side of Eq. 3 (chapter 4) for stator outer H-grids; loop 10 calculates ξ-direction contribution, loop 180 calculates η-direction contribution, loop 340 calculates ς-direction contribution: calls:

SRINT: interpolates flowfield onto outer H-grid at inner O-grid interface from the inner grid flowfield, using interpolation factors calculated in TRIANG

MUKN: calculates kinematic viscosity for stator outer H-grid

MUTRSO: (called in 3D cases only) calculates eddy viscosity for stator outer H-grid in η-direction and ς-direction; loop 10 calculates viscosity below midspan; loop 210 calculates it above midpsan

FLUXR: computes the numerical flux vectors E^p, F^p, and G^p in Eq. 3 (chapter 4) using Roe's scheme for stator outer H-grid

STCONT: (called in 2D cases only) calculates stream tube contraction terms (H-ratio) instead of the G^p vector

VFLUX: computes viscous flux vectors S^p and T^p for stator outer grid

LHSSO: controlling routine for computing the left hand side of Eq. 3 (chapter 4) and solving for $Q^{p+\frac{1}{2}}$; loop 10 inverts the solution matrix in the ξ-direction, loop 190 inverts in the η-direction, loop 330 inverts in the ς-direction; implicit inlet/exit boundary conditions are applied within the ξ-direction loop, implicit surface boundary conditions are applied within the η-direction loop; calls:

SMATRX: computes the matrices $A^{\pm}$, $B^{\pm}$, and $C^{\pm}$ in Eq. (3) for stator outer grids; called once in each loop

VMAT: computes the matrices M and N in Eq. (3) for stator outer grids; called only in η- and ς-direction loops

BTRI: inverts the given matrix; called once in each loop

PGRID: see above description

RHSRO
SRINT
MUKN
MUTRRO
FLUXR
VFLUX
STCONT

} see above descriptions for RHSSO; all are the same here except they are applied to rotor outer H-grids instead of stator grids

LHSRO
SMATRX
VMAT
BTRI

} see above descriptions for LHSSO; all are the same here except they are applied to rotor outer H-grids instead of stator grids

RHSRL
MUKN
FLUXR
VFLUX
LHSRL
SMATRX
VMAT
BTRI

} see above descriptions for RHSSI and LHSSI; all are the same here except they are applied to tip clearance grids; note there is no call to an eddy viscosity routine - eddy viscosity is assumed to be zero in the clearance region

CORREC: applies explicit boundary conditions at all boundaries, including all solid surfaces, periodic boundaries, inlet/exit boundaries, inner/tip grid interface for cases with tip clearance, and row interfaces for multirow cases; calls:

WALTMP: calculates temperature on solid surfaces; called only if the option was chosen to specify wall temperature

BCSURF: imposes solid surface boundary condition, either adiabatic

	wall, specified wall temperature, or specified heat flux
CONVRG:	calculates and prints out change in solution from previous time step, specifically, change in energy
WRTPS:	prints out blade surface static pressure distribution at midspan
WRTEXT:	prints out exit total pressure across pitch at midspan
RESTOT:	writes restart file with new solution
PLOT3D:	writes grid and solution in PLOT3D format for viewing

Miscellaneous routines:

SHIFT:	applies periodic shift to airfoil grids for multiblade cases; this saves on storage, as only one copy of the grid must be stored
PUTXYZ,GETXYZ:	puts/gets grid arrays on SSD
PUTAJA,GETAJA:	puts/gets Jacobian arrays on SSD
PUTQ,GETQ:	puts/gets current Q arrays on SSD
PUTOLD,GETOLD:	puts/gets differential (QD) arrays on SSD
PUTH,GETH:	puts/gets H-ratio arrays on SSD
PUTSTR,GETSTR:	puts/gets inner QD grid (for use in RHSRL) on SSD
PUTTMP,GETTMP:	puts/gets Q or QD arrays to be stored temporarily on SSD
PUTTRP,GETTRP:	puts/gets outer/inner interface interpolation factors on SSD

Symmetry Condition

A symmetry condition may be used in the solver for axisymmetric cases in order to, in effect, increase grid resolution in the spanwise direction. There were two options for imposing symmetry implemented in the solver, only one of which was successfully used. The other was left in with the intention of later debugging, but the problem was never resolved and this option should not be used. This is symmetry option number 2 in the RAIJOB shell script. The intent of this option is to allow the full grid capability of the program to be used for half the span, and modify the boundary condition applied at the uppermost K-line to assume a symmetry condition. That is, the geometry contained in the computational grid is only half of the actual airfoil. The difference between this and option number 1, which was run successfully, is that option 1 requires the full airfoil to be present and accounted for by several K-lines. In this case, most, but not all, of the K-lines are distributed below the midspan, the solution is calculated from hub to midspan, and a symmetry condition is applied at the midspan.

To generate a grid to which the symmetry option is applicable, the user should have a three-dimensional axisymmetric configuration in the input file, and run the grid generator as usual up to this point:

ENTER KMAX (RADIAL PNTS) BEFORE ADDITION, FORMAT=I2
(DEFAULT=25, MAX=51(NO ADDITION))

The number of K-lines specified here should be based on the total number of lines desired for the half-span. The number that is chosen here will determine how many lines will be retained in the UPPER half of the span, that is, those that will not be used in the calculation. The remaining K-lines allowed in the solver will be distributed between the hub and midspan. For example, choosing 15 here will result in a final grid with 7 K-lines above midspan and 42 lines below midspan (due to the maximum K-dimension being set to 49 in the current version of the RAI3DS system). Continuing with this example, in which a three-dimensional airfoil with a total span of 6.0 inches was used,

15
CURRENT DIMENSIONS:
NOTE THAT POINTS WILL BE ADDED IF AXIAL SPACING AT
INLET/EXIT BOUND IS CHANGED, AND AGAIN IN OVRLAP,
ALSO RADIAL DISTRIBUTION CAN BE MODIFIED LATER.

AIRFOIL: 1
OUTER: 50, 31 INNER: 101, 21 RADIAL: 15 15

PAUSE...

ENTER 1 TO INCREASE CLUSTERING AT T.E. FOR AIRFOIL 1

ENTER 1 TO CHANGE K-LINE SPACING AND/OR DIST. IN TIP
(DEFAULT: SETA1 = SETA2 = 0.03% SPAN = 1.80000E-03)
1

This option must be excercised to re-distribute the K-planes.

ENTER 1 TO DISTRIBUTE K-LINES FOR A SYMMETRY CONDITION
1

The above question will be asked only for a three-dimensional, planar stator.

SPAN = 6.00000 KMAX = 15

ENTER DIF BTWN HUB AND 2ND K-LINE, F10.0
.002

With this input, the program will use a spacing of 0.002 inches at the hub, and a spacing of 6.0/(NKA-KMAX) at the midspan, where NKA is currently set to 49, and KMAX for this case is 15.

RADII OF K-PLANES ACCORDING TO ORIGINAL STRETCHING
HAVE BEEN WRITTEN TO A FILE.
HALT EXECUTION OR HIT ENTER TO CONTINUE
PAUSE..

At this point, the plot of radii as a function of K-index looks like this:

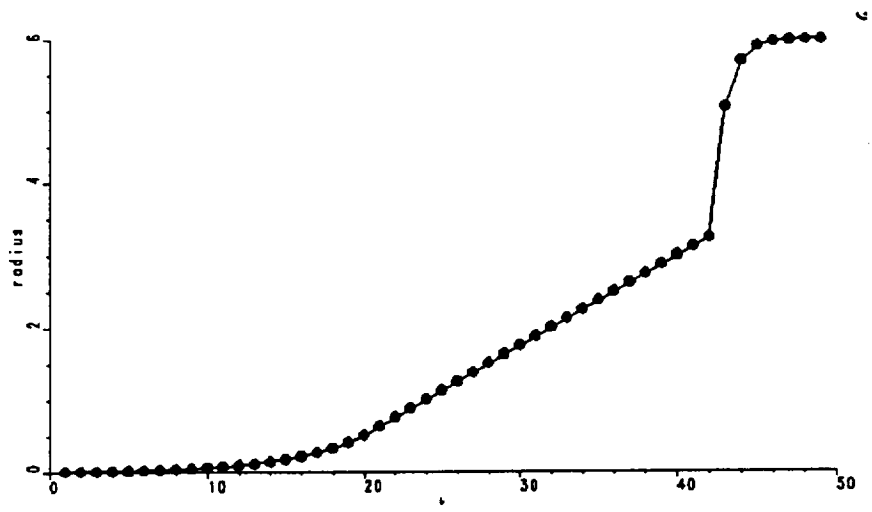

Note that there are two points above midspan that mirror the two points below midspan. This is necessary for the implementation of the line of symmetry boundary condition in the solver. The following is a view in the axial direction of the final grid generated by continuing the above example:

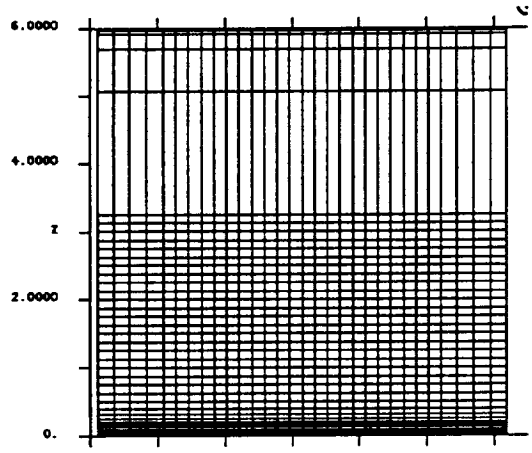

Note that K-line 40 is at Z=3.0, which is the midspan. This is what should appear in the first line of FORTRAN unit 3, input to the flow solver. Unit 3 is defined by the here document 'fort.3' in the UNICOS jobstream created by RAIJOB. If the value of KMID (in this case, 40) is not properly specified, the symmetry condition will not be implemented properly.

Boundary Conditions

Inlet Boundary Condition

In the following expressions, *u,v,w* are velocities in the *x*-, *y*-, and *z*-directions, *p* is static pressure, ρ is density, *c* is speed of sound, *s* is entropy, and *h* is total enthalpy, α is *arctan(v/u)* and φ is *arctan(w/u)*; boldface type indicates a new updated value, subscript 0 indicates an initial value, and subscripts of 1 and 2 indicate a current value at inlet and one point downstream of inlet, respectively.

The inlet boundary condition in ROTOR3 was the following:

$$\text{Reimann invariant 1} = R_1 = u_0 + \frac{2}{\gamma-1}\left(\frac{\sqrt{\gamma p_0}}{\sqrt{\rho_0}}\right)$$

$$\text{Reimann invariant 2} = R_2 = u_2 - \frac{2}{\gamma-1}\left(\frac{\sqrt{\gamma p_2}}{\sqrt{\rho_2}}\right)$$

$$u_1 = (R_1 + R_2)/2$$
$$v_1 = v_0$$
$$w_1 = w_0$$

$$c_1 = \frac{\gamma-1}{4}(R_1 - R_2)$$

$$s_1 = s_0$$

$$\rho_1 = \left(\frac{c_1}{\gamma s_1}\right)^{1/(\gamma-1)}$$

$$p_1 = \frac{\rho_1 c_1^2}{\gamma}$$

The following modifications were made to, in effect, hold inlet total pressure, in addition to reducing the stiffness of the boundary condition:

FIrst define the variable h' as follows:

$$h' = \frac{2c^2}{\gamma-1} + u^2 = 2h - (v^2 + w^2) \qquad (1)$$

Assuming $h_1 = h_0$, that is, inlet total enthalpy is held at its initial value,

$$h'_1 = 2h_0 - (v_1^2 + w_1^2) \qquad (2)$$

It can be shown that (2), together with the assumption

$$u_1 - \frac{2c_1}{\gamma-1} = u_2 - \frac{2c_2}{\gamma-1} = R_2 , \qquad (3)$$

yields:

$$\frac{2}{\gamma-1}(1+\frac{2}{\gamma-1})c_1^2 + \frac{4R_2}{\gamma-1}c_1 - (h'_1 - R_2^2) = 0$$

This is a quadratic equation for c_1 that can be solved with the quadratic formula. Then,

$$u_1 = R_2 + \frac{2c_1}{\gamma-1}$$

$$v_1 = u_1 \tan(\alpha_0)$$
$$w_1 = u_1 \tan(\varphi_0)$$

$$s_1 = s_0$$

$$\rho_1 = (\frac{c_1}{\gamma s_1})^{1/(\gamma-1)}$$

$$p_1 = \frac{\rho_1 c_1^2}{\gamma}$$

Surface boundary conditions

The surface boundary condition in ROTOR3 was a first-order adiabatic wall condition, that is, in addition to the no-slip condition for velocity, zero normal pressure and density gradients were imposed. Options were added to specify either wall temperature or heat flux on the surfaces, which modified the density condition.

The specified wall temperature condition that was implemented was developed by Griffin (Ref. 7). It requires an additional input file containing adiabatic wall temperatures on the surfaces, and the wall temperature is prescribed as a percentage of the adiabatic wall temperature. The percentage is input in the RAIJOB shell script. The adiabatic wall temperature file can obtained by running RAI3DS with the adiabatic wall condition; the file will get written out in routine WALTMP, which will also read the file if the option to specify wall temperature is chosen. The UNICOS jobstream will need modification to assign these files to the file environment.

The following is the derivation of the second-order density condition allowing specified heat flux. Here, Q is heat flux, k is the coefficient of thermal conductivity, R is the specific gas constant, T is temperature, p is static pressure, ρ is density, and y is distance from the wall.

Assume

$$Q = -k\frac{dT}{dy} = -k\frac{d\left(\frac{p}{\rho R}\right)}{dy} = \frac{-k}{R}\frac{\left(\frac{dp}{dy}\right)\rho - p\left(\frac{d\rho}{dy}\right)}{\rho^2}$$

Assuming a zero normal pressure gradient, this yields

$$Q = \frac{k\,p}{R\rho^2}\left(\frac{d\rho}{dy}\right) \quad \Rightarrow \quad \frac{d\rho}{dy} = \frac{\rho^2 Q'}{p}, \quad where\ Q' = \frac{QR}{k}$$

Now assume that ρ is some quadratic function of y, given by

$$\rho = ay^2 + by + c$$

Then, values of ρ at y1, y2, and y3 are given by the system

$$ay_1^2 + by_1 + c = \rho_1$$

$$ay_2^2 + by_2 + c = \rho_2$$

$$ay_3^2 + by_3 + c = \rho_3$$

Assuming y_1 is zero, that is, at the wall, the system reduces to

$$b = \frac{(\rho_2 - \rho_1) y_3^2 - (\rho_3 - \rho_1) y_2^2}{y_2 y_3^2 - y_2^2 y_3}$$

Differentiating the quadratic equation for ρ,

$$\frac{d\rho}{dy} = 2ay + b \quad \Rightarrow \quad \frac{d\rho}{dy} = b \text{ at the wall.}$$

From the previous expression for $\frac{d\rho}{dy}$,

$$\frac{(\rho_2 - \rho_1) y_3^2 - (\rho_3 - \rho_1) y_2^2}{y_2 y_3^2 - y_2^2 y_3} = \frac{\rho^2 Q'}{p}$$

Algebraically solving for ρ_1,

$$\rho_1 = \frac{\rho_2 y_3^2 - \rho_3 y_2^2}{y_3 2 - y_2 2} - \frac{\rho^2 Q' (y_2 y_3^2 - y_2^2 y_3)}{p (y_3^2 - y_2^2)}.$$

The values of p and ρ at y_2 is used in the implementation of the condition. To define the value of Q' (note the solver will expect the given heat flux value to be properly nondimensionalized and to contain the factors of R and k), divide the dimensional Q by the dimensional k, and use a value of 1.0 for R to be consistent with the solver's nondimensionalization scheme. This will result in a value with units of degrees over length. Divide by inlet total temperature and convert remaining length unit to inches to obtain the value of Q' in inches^{-1}. This is what should be input to the RAIJOB shell script.

NASA
National Aeronautics and Space Administration

Report Documentation Page

1. Report No.	2. Government Accession No.	3. Recipient's Catalog No.

4. Title and Subtitle

Three-Dimensional Turbopump Flowfield Analysis

5. Report Date
April 27, 1992

6. Performing Organization Code

7. Author(s)

O. P. Sharma, K. A. Belford and R. H. Ni

8. Performing Organization Report No.
PWA-6142-43

10. Work Unit No.

9. Performance Organization Name and Address

UTC-Pratt & Whitney
Commercial Engineering
400 Main Street
East Hartford, Connecticut 06108

11. Contract or Grant No.
NAS8-36950

13. Type of Report and Period Covered
Final Report - 2/88-4/92

12. Sponsoring Agency Name and Address

George C. Marshall Space Flight Center
National Aeronautics and Space Administration
Marshall Space Flight Center, AL 35812

14. Sponsoring Agency Code

15. Supplementary Notes

Principal Contracting Officer's Representative: Janice Burrough AP-29-F
Marshall Space Flight Center, AL 35812

16. Abstract

A program was conducted to develop a flow prediction method applicable to rocket turbopumps. The complex nature of a flowfield in turbopumps is described and examples of flowfields are discussed to illustrate that physics based models and analytical calculation procedures based on computational fluid dynamics (CFD) are needed to develop reliable design procedures for turbopumps. A CFD code developed at NASA ARC was used as the base code. The turbulence model and boundary conditions in the base code were modified, respectively, to: 1) compute transitional flows and account for extra rates of strain, e.g. rotation, and 2) compute surface heat transfer coefficients and allow computation through multistage turbomachines. Benchmark quality data from two and three-dimensional cascades were used to verify the code. The predictive capabilities of the present CFD code were demonstrated by computing the flow through a radial impeller and a multistage axial flow turbine. Results of the program indicate that the present code operated in a two-dimensional mode is a cost effective alternative to full three-dimensional calculations, and that it permits realistic predictions of unsteady loadings and losses for multistage machines.

17. Key Words (Suggested by Author(s))

Multistage
Computational Fluid Dynamics
Heat Transfer Coefficients
Boundary Layer
Tip Leakage
Two-Dimensional
Three-Dimensional
Turbopump
Axial Flow Turbines
Cascades
Radial Impellers

18. Distribution Statement

19. Security Classif. (of this report)	20. Security Classif. (of this page)	21. No. of pages	22. Price
Unclassified	Unclassified	180	

NASA FORM 1626 OCT 86